INVESTIGATING THE ROLE OF THE CENTRAL METABOLISM IN THE GUT-BRAIN AXIS OF FAMILIAL DYSAUTONOMIA

by

Stephanann Marin Costello

A dissertation submitted in partial fulfillment
of the requirements for the degree

of

Doctor of Philosophy

in

Biochemistry

MONTANA STATE UNIVERSITY
Bozeman, Montana

December 2023

©COPYRIGHT

by

Stephanann Marin Costello

2023

All Rights Reserved

DEDICATION

To all my friends and family who have loved and supported me along my entire academic journey.

To my parents, Shawn and Craig Costello, and brother, Paul Costello, for helping me become the individual I am, and so proudly supporting me throughout life and college.

To my best friend Erin, who never allowed me to quit when things were hard during my PhD and for being an incredible friend who was instrumental in me achieving this goal.

To the Brush and Robison Families who have loved and supported me and celebrated all the successes along the way.

To Jeremy, my Fiancé and soon to be husband - I never imagined I would find you during my time at MSU, but I am so lucky to complete this chapter of my life with you. Jeremy, you have loved me so well and made the final process of completing my PhD far more exciting and full of joy than would have been possible without you.

And to the FD patients and their families, for being a bright shining community amidst a devastating disease; your resilience and hope are an incredible inspiration.

ACKNOWLEDGEMENTS

I would like to begin by thanking God for guiding me to MSU to complete my PhD. The community of MSU, the Chemistry and Biochemistry department, SIGP, INBRE, and Bozeman have provided me so many more opportunities than I ever could have imagined. I thank all the mentors, friends, and strangers who became my family during my PhD, I could not have done it without all of you.

Dr. Valérie Copié, thank you for being a mentor that has your sights set on doing great science, and enabling people to succeed. You believed in me when I didn't, challenged me to grow, supported me when I needed it most, and helped me become the scientist I am now proud to be. Thank you, Dr. Frances Lefcort, for your passion for FD research – you were an incredible teacher and scholar to be co-mentored by. And thank you to all the present and former members of the Copié and Lefcort labs for your incredible support, particularly Galen O'Shea-Stone, Shawn Hartney, Amanda Fuchs, Annie Waldum, Daniel Horan, Brian Tripet, Seth Pincus, Tami Peters, Anastasia Schultz, Martha Chaverra, and Heini Miettinen – you have been a wonderful community of scientists to learn from and with.

Thank you to the SIGP program, and INBRE NAGF for providing additional funding and support throughout my PhD. Thank you especially Craig Ogilvie, Sweeney Windchief, Barbara Komlos (our Sloan Auntie), Aaron Thomas, and Kevin Gibson for opening doors, providing resources for our success as scholars, and creating a great community.

Finally, thank you to ALL of the friends I made through MSU and the Christian communities during my time in Bozeman, you brought so much joy to my PhD experience.

TABLE OF CONTENTS

1. INTRODUCTION 1

Metabolomics 1
NMR Based Metabolomics 2
Statistical Workflow and Pathway Analysis 6
Complexities of Metabolomics Data Comprehension 8
Familial dysautonomia 9
Gut-Brain-Metabolism Axis 14
Models of FD 16
Cellular and Non-Mammalian 16
Mouse Models 16
Tuba1a-Cre^{+};Elp1$^{LoxP/LoxP}$ 18
Pax6-Cre^{+};Elp1$^{LoxP/LoxP}$ 19
Research Question, Hypothesis, and Research Aims 20
References 24

2. GUT MICROBIOME DYSBIOSIS DRIVES METABOLIC DYSFUNCTION IN FAMILIAL DYSAUTONOMIA 33

Contribution of Authors and Co-Authors 33
Manuscript Information 36
Results 38
Altered gut-metabolism axis in FD 38
Patient factors associated with dysbiosis 39
Neuronal Elp1 controls gut-metabolism axis 40
Discussion 40
Methods 43
Human subjects 43
Mice 43
Sool microbiome sequencing 43
Preparation of serum and stool samples for metabolomics 44
NMR-based metabolomics 44
TMA and TMAO analysis LCMS 44
Statistics 45
Reporting summary 45
Data availability 45
Code availablity 45
References 45

TABLE OF CONTENTS CONTINUED

3. A COMPREHENSIVE NMR ANALYSIS OF SERUM AND FECAL METABOLITES IN FAMILIAL DYSAUTONOMIA PATIENTS REVEALS SIGNIFICANT METABOLIC PERTURBATIONS 49

Contribution of Authors and Co-Authors 49
Manuscript Information 51
Abstract 52
1. Introduction 52
2. Materials and Methods 54
2.1 Participants and Sampling Scheme 54
2.2 Blood Serum and Stool Sample Collection 54
2.3 Human Serum Sample Preparation and Serum Metabolite Extraction 55
2.4 Human Fecal Sample Preparation and Stool Metabolite Extraction 55
2.5 NMR Spectra Acquisition and Preprocessing 55
2.6 NMR Spectra Profiling and NMR Signal and Metabolite Annotation Validation 55
2.7 Unpaired Univariate and Multivariate Statistical Analyses 56
2.8 Paired Multivariate Statistical Analyses 56
2.9 Metabolic Pathway Impact Analysis 57
3. Results 57
3.1 Metabolite Concentration Differences Separate FD Patients from Their Healthy Control Relative Populations 57
3.2 The Serum and Stool Metabolomes of the FD Patient Group Differ Significantly from the Metabolomes of the Healthy Relative Control Group 58
3.3 Paired Analyses of FD Patient and Healthy Relative Serum and Stool Metabolomes Further Highlights Metabolic Changes Associated with FD 62
4. Discussion 63
4.1 Amino Acid Catabolism Suggests an Overall Energy Deficit 65
4.2 Purine Salvage and Nucleotide Degradation Pathways 66
4.3 Tyrosine Degradation 67
4.4 Metabolites Implicated in Gut Microbiome Changes 67
4.5 Neuronal Associated Metabolites 69
4.6 Taurine Metabolism and a Potential Dietary Deficit with Systemic Consequences 70
5. Conclusion 70
References 72

TABLE OF CONTENTS CONTINUED

4. CHARACTERIZATION OF THE METABOLIC DEFICITS IN A RETINAL SPECIFIC *ELP1* KNOCKOUT MOUSE MODEL 77

Contribution of Authors and Co-Authors 77
Manuscript Information 79
Abstract 80
1. Introduction 81
2. Materials and Methods 84
2.1 Mice 84
2.2 Retina Sample Collection for NMR and MS Metabolite Extractions 84
2.3 Metabolite Extraction for 1D 1H NMR Analysis 85
2. Acquisition and Processing of 1D ^{1}H NMR spectra 86
2.5 Chenomx Spectral Signal Annotation and Quantitation 86
2.6 NMR and Statistical Analyses 88
2.7 Extraction of Mouse Retinae for Dopamine Isolation 88
2.8 UHPLC/Q-TOF-MS Analysis for Relative Dopamine Quantitation 88
2.9 Retinal Histology for Flat Mount Preparations 89
3. Results 91
3.1 Retina Metabolomic Differences Emerged at 2 Months of Age 91
3.2 Alterations in dopaminergic amacrine cell population in CKO retinae. 97
3.3 Reduced Dopamine Levels at P30 in CKO Retina 98
4. Discussion 101
4.1 ^{1}H NMR data indicate that metabolic disturbances align with *Elp1* induced RGC degeneration. 102
4.2 Taurine is fundamental for mitochondrial electron transport chain (ETC) complex 1 function and RGC health. 103
4.3 Alterations in the levels of metabolites involved in the Cahil (alanine-glucose) and mini-Krebs cycles point to energetic (ATP) deficits in CKO retinae 104
4.4 Reduced levels of membrane phospholipid associated metabolites myo-inositol and choline are associated with retinopathy. 108
4.5 Alterations in dopaminergic cell populations 112
5. Conclusion 113
Supplementary Info 115
Acknowledgements 119
References 120

TABLE OF CONTENTS CONTINUED

5. *TUBA1A-CRE*$^{+}$*;ELP1*$^{LOXP/LOXP}$ SUCCINATE SUPPLEMENTATION 126

Phenotype Scores 128
Gut Transit Assay 131
NMR Metabolomics Analysis 132
Conclusion 133

6. CONCLUSION 136

Avenues Inspired by the Human Metabolomics Analysis 136
Choline 137
Taurine 139
Conclusion 142

APPENDICES 145

GUT MICROBIOME DYSBIOSIS DRIVES METABOLIC DYSFUNCTION IN FAMILIAL DYSAUTONOMIA: SUPPLEMENTARY MATERIAL 146

A COMPREHENSIVE NMR ANALYSIS OF SERUM AND FECAL METABOLITES IN FAMILIAL DYSAUTONOMIA PATIENTS REVEALS SIGNIFICANT METABOLIC PERTURBATIONS: SUPPLEMENTARY MATERIAL 158

WESTERN BLOT TROUBLESHOOTING FOR THE CHOLINE TRANSPORTERS 186

Standard Western Blot Methods 187
Protein Extraction from Tissue 187
Bicinchoninic acid (BCA) Assay 188
Gel Electrophoresis 189
Semi-Dry Transfer and Blot 191
Blot Development on Photopaper 193
General Troubleshooting Notes: 195
Reagents 195
Choline Transporters 196
OCT1/Slc22a1 196
Trial 1 196
Trial 2 197
Trial 3 199
Trial 4 201
Summary 205

TABLE OF CONTENTS CONTINUED

CTL1/Slc44a1 206
Trial 1 206
Trial 2 207
Trial 3 208
Trial 4 209
Summary 210

REFERENCES CITED 212

LIST OF TABLES

Table Page

1. Table 3.1 Unpaired volcano plot analysis of serum and stool metabolite concentrations between the FD patient and control relative sample groups 61

2. Table 3.2 Paired volcano analysis of serum and stool metabolite profiles obtained from the v.1 and v.2 list of FD patient–relative control pairs 62

3. Table S4.1 P7 Retina Metabolites Identified and Quantified by NMR: Concentrations, Standard Deviation and Fold Change 115

4. Table S4.2 P60 Retina Metabolites Identified and Quantified by NMR: Concentrations, Standard Deviation and Fold Change 116

5. Table S4.3 Volcano plot analysis of P60 retinae metabolite concentrations between CKOs and controls 117

6. Table A1.3 Pathology scoring method used to quantify clinical phenotype in FD (Tuba1a-cre^{+};ELP1$^{loxp/loxp}$) and control (Tuba1a-cre^{-};ELP1$^{+/loxp}$) mice 156

7. Table A2.1 Patient and control relative sample and clinical data summary 160

8. Table A2.2 Human Serum Metabolites Identified and Quantified by NMR: Concentrations and Percent Differences 162

9. Table A2.3 Stool Polar Metabolites Identified and Quantified by NMR: Concentrations and Percent Differences 164

10. Table A2.4 Variable Importance in Projection (VIP) scores associated with components 1, 2, and 3 of the PLS-DA model generated from the distinct serum metabolite profiles of the FD patients and healthy control relatives 166

11. Table A2.5 Variable Importance in Projection (VIP) scores associated with components 1, 2, and 3 of the PLS-DA model generated from the distinct stool metabolite profiles of the FD patients and healthy control relatives 168

12. Table A3.1 BCA Assay Standards 188

13. Table A3.2 Recipes for 10 mL of Separating gel and 4 mL of 4% Stacking gel 190

LIST OF FIGURES

Figure Page

1. Figure 1.1 The genetic origins and tissue specific splicing defects of ELP1 that give rise to reduced ELP1 protein and Elongator Complex function in the nervous system and promote FD 10

2. Figure 2.1 FD alters the microbiome and metabolome 38

3. Figure 2.2 Microbiome OTU and metabolite differences in FD 39

4. Figure 2.3 Neuron-specific Elp1 deletion drives progressive microbiome and metabolome divergence in mice 41

5. Figure 2.4 Cohousing ameliorates gut transit deficit and disease in FD mice 42

6. Figure 3.1. Multivariate statistical analyses of serum and fecal metabolic profiles separate the FD patient population (orange) from the control relative group (blue), with panels (A,B) presenting the 3D-PCA and 3D-PLS-DA scores plots from the analyses of serum metabolite patterns, and panels (C,D) those from fecal sample analyses 59

7. Figure 3.2. Variable importance in projection (VIP) score plots corresponding to the first two components of the 3D-PLS-DA models obtained from serum and stool metabolite profiles 60

8. Figure 3.3 Simplified schematic of amino acid catabolic pathways used for ATP production 65

9. Figure 3.4 Simplified schematic of the purine salvage pathway 66

10. Figure 3.5 Choline is obtained primarily from the diet and contributes to four metabolic pathways employed by gut microbes and the host 68

11. Figure 4.1 Principal component (PCA) multivariate statistical analyses of the metabolic profiles of P7 and P60 retinas indicate that the CKO group (gold) cluster separately from control group (blue) by P60 92

12. Figure 4.2 Hierarchical clustering analysis (HCA) and heatmap visualizations of (A) P7 and (B) P60 CKO (gold) and control (blue) retina samples 94

LIST OF FIGURES CONTINUED

Figure Page

13. Figure 4.3 The two-sample t-test of the P60 retinae metabolomic profiles identified 13 metabolites that significantly discriminated the CKOs from controls....96

14. Figure 4.4 Changes in TH+ cell number throughout disease progression....100

15. Figure 4.5. An illustration of how the Cahill and mini-Krebs cycle both contribute to rapid energy production in the retina....106

16. Figure 4.6 Phosphatidylcholine production and catabolism. Blue boxes indicate metabolites with significantly lower levels measured in the Pax6 CKO retina compared to controls....111

17. Figure S4.1 Representative 1D 1H NMR spectrum of retina metabolite extracts from a P60 sample....118

18. Figure 5.1 Succinate and water consumption (μL*mouse/hour) for mutants and controls....128

19. Figure 5.2 Total phenotype scores for MW and CW groups plotted for each mouse based on (A) treatment group and (B) treatment group partitioned by sex....130

20. Figure 5.3 Total gut transit time for mutants and controls treated with either succinate or water....132

21. Figure 6.1. Summary of the NMR metabolomics-based analysis of FD patients' stool samples, and the associated disruptions of choline and taurine metabolism to FD....137

22. Figure A1.1 Gut microbiome diversity of FD patients is significantly different from healthy relatives....147

23. Figure A1.2 Gut microbiome enterotypes of FD patients....148

24. Figure A1.3 Differentially abundant microbiome members among FD patients and....149

25. Figure A1.4 Gut microbiome diversity of FD relatives and patients compared to two cohorts of healthy adults from other studies....150

LIST OF FIGURES CONTINUED

Figure Page

26. Figure A1.5 NMR-based metabolomic differences between FD patients and healthy relatives 151

27. Figure A1.6 Pathology score for FD mice housed separately or cohoused with control mice 152

28. Figure A1.7 Gut transit times for FD mice housed separately or cohoused with control mice 153

29. Figure A1.8 Stool metabolite diversity of FD and control mice 154

30. Figure A1.9 Unique and shared OTUs observed in laboratory mice and human subjects 155

31. Figure A2.1 Results from Clinical Blood Tests that measured (A) blood urea nitrogen (BUN) levels, (B) creatinine levels, (C) BUN per creatinine ratio, and (D) estimated glomerular filtration rate (eGFR) levels in de-identified FD patient samples 170

32. Figure A2.2 Results from FD patient liver enzyme blood tests and measurements of (A) Alanine aminotransferase (ALT) levels; (B) aspartate transaminase (AST) levels; (C) AST/ALT ratio; and (D) alkaline phosphatase levels (ALP) 172

33. Figure A2.3 Human serum mixed metabolite 1D 1H-NMR (600 MHz) spectra 174

34. Figure A2.4 Human fecal metabolite 1D 1H-NMR spectra 175

35. Figure A2.5 Validation metrics associated with the PLS-DA modeling of serum metabolite profiles of FD patients and healthy controls 176

36. Figure A2.6 Validation Metrics associated with the PLS-DA modeling of stool metabolite profiles of FD patients and healthy controls 177

37. Figure A2.7 Scree plots associated with unsupervised PCA analyses of (A) serum and (B) stool metabolite profiles 178

38. Figure A2.8 Random forest analysis of the FD patient vs Control relative groups 179

39. Figure A2.9 Tyrosine pathways yield tyramine, p-cresol, fumarate, and dopamine 181

LIST OF FIGURES CONTINUED

Figure Page

40. Figure A2.10 Beta-alanine and malonate metabolism connect via the intermediate malonate semialdehyde....182

41. Figure A2.11 Taurine is obtained primarily from the diet but can also be synthesized endogenously via degradation of homocysteine and participates in 3 primary host metabolic functions 183

42. Figure A2.12 The four neural signaling molecules identified in elevated concentrations in the stool of FD patients compared to their control relatives....184

43. Figure A3.1 Trial 1 of the OCT1 antibody with an exposure time of ~1 second 197

44. Figure A3.2 Trial 2 of OCT1 antibody with exposure times of (A) ~45 seconds and (B) < 1 second 198

45. Figure A3.3 Trial 3 of OCT1 antibody with a 10 second exposure time....200

46. Figure A3.4 OCT1 western blot for RIPA extracted liver tissue with a (A) 10 minute exposure for OCT1 and (B) a 5 second exposure for GAPDH 202

47. Figure A3.5 OCT1 western blot for RIPA extracted liver tissue with a (A) 2 minute exposure for OCT1 and (B) a 3 second exposure for GAPDH 204

48. Figure A3.6 Trial 1 CTL1 western blot for RIPA extracted gut tissue with a (A) ~45 second exposure for CTL1 and (B) a ~15 second exposure for GAPDH....207

49. Figure A3.7 Trial 2 CTL1 western blot for RIPA extracted liver tissue with a (A) 2 minute exposure for CTL1 and (B) a ~1 second exposure for GAPDH....208

50. Figure A3.8 Trial 4 CTL1 western blot for standard extracted retina tissue with a (A) 10 second exposure for CTL1 (upper) and ~1 second exposure for GAPDH (lower) and (B) 1 minute exposure for CTL1 (upper) and ~1 second exposure for GAPDH (lower) 210

ABSTRACT

Familial dysautonomia (FD) is a rare, highly debilitating, developmental, and progressive neurodegenerative disease, with recessive heritability, and primary penetrance among Eastern European Jewish populations. The disease affects both the central and peripheral nervous systems, with primary deficits in the autonomic and sensory divisions. Patients thus present with numerous complex neurological phenotypes, and those of primary interest include severe gastrointestinal dyscoordination, cardiovascular instability, baroreceptor imbalances that promote autonomic "crises" marked by uncontrollable retching, and progressive visual decline leading to blindness. There is no cure for FD, and patients are still subject to a poor quality of life despite current advances in understanding the cellular mechanisms mediating the disease.

The nervous system, gut-microbial ecosystem, and central metabolism are individually complex, but ever more intricate due to the crosstalk between these systems. Thus, dysregulation or damage in one system could facilitate disruption in another, thus creating a negative feedback loop between the gut-brain-metabolism axis and ultimately perpetuating neurodegeneration, gut dysbiosis, and a dysfunctional metabolism. Understanding how each individual system is affected by the FD founder mutation could lead to methods for restoring healthy function to one of the branches of the gut-brain-metabolism axis, thus arresting the negative feedback loop and disease perpetuation. In this work, nuclear magnetic resonance-based metabolomics was employed along with targeted mass spectrometry techniques to characterize the metabolic changes of FD patients, and subsequently to interrogate the retinal metabolome of a retina specific FD mouse model (Pax6).

Insights into the critical changes in FD patients' fecal metabolites were found and associated with neuronal networks and the gut-microbiome. Further avenues exploring these results and the role of metabolic dysfunction in FD led to the interrogation of the retinal metabolome of the Pax6 mouse model, and identification of altered metabolites associated with energy circuits of the eye, mitochondrial function, and retinal ganglion cell health. These data demonstrate metabolic dysfunction in FD patients, and the Pax6 model, with disruptions being analogous to clinical phenotypes, gut-dysbiosis, and the cellular degeneration of FD patients, thus providing foundational information for the generation of novel therapeutic options targeting the cellular metabolic pathways of the gut-brain-metabolism axis.

CHAPTER ONE

INTRODUCTION

Metabolomics

Genomics, transcriptomics, proteomics, and metabolomics comprise the "-omics" fields that enable a holistic methodological molecular approach to studying a biological system. Genetic expression encompasses the transcription of a gene into mRNA and downstream translation into proteins, which in turn, through specialized effector functions, facilitate transport, and catabolic and biosynthetic reactions of small molecules called metabolites. Amino acids, fatty acids, sugars, steroids, vitamins, and lipids are examples of metabolite classes that are widely studied using metabolomics [1]. Given their interconnected nature, each "-omics" field is sequentially interdependent and builds upon the last, with metabolomics representing the cellular response to changes in genes, transcripts, and proteins. However, metabolomics not only reports on internal cellular changes imparted by genomics, transcriptomics, or proteomics perturbations monitored via the other "-omics" approaches, but is also mediated by environmental stressors and lifestyle changes [2].

Genomics, transcriptomics, and proteomics are associated with ~20,000 genes, ~140,000 mRNA transcripts, and ~100,000 proteins, respectively [3,4]. Being the final readout and subject to changes in genes, mRNA, proteins, and environment, the number of total metabolites that mediate cellular responses were originally thought to reduce analyte complexity. A total of ~3,000 unique metabolites were originally thought to comprise all the cellular pathways in the body, a number that is strikingly fewer than the total constituents of the other "-omics" field [4]. This number is now believed to be closer to ~218,000 compounds [5]. Though analyte

complexity may yet be comparable to the other "-omics" fields, metabolomics still captures the vast amount of information that can be garnered from changes in biological phenomena, and environmental stimuli into valuable datasets that contain direct information about cellular status of tissues, organs, or organisms.

The basic principles of the field of metabolomics are to identify small molecules with altered levels representative of a biological phenotype and then attempt to establish the mechanism associated with these changes [1]. These small molecules can originate from the host, microbial, dietary, or other exogenous sources and support an array of cellular functions including energy production and storage, and regulation of gene expression, cell signaling, growth, and differentiation [6]. Metabolomics applications have thus garnered more attention for cancer, metabolic, and neurodegenerative disease research for their ability to elucidate the pathophysiological mechanisms underlying a disease on a comprehensive scale [1]. The term "biomarker" has thus emerged as a result of metabolomic studies that identify small molecules indicative of disease diagnosis, inform on disease mechanisms, and lay the foundation for developing novel therapeutics that target specific molecules and pathways to mitigate the disease or associated symptoms [1,2,7]. Given the rise in metabolomics for disease research, specified workflows have emerged to isolate, identify, and quantify groups of metabolites and discern mechanistic relevance.

NMR Based Metabolomics

The field of metabolomics primarily utilizes the two following analytical techniques: 1) Nuclear Magnetic Resonance (NMR) spectroscopy and 2) Mass Spectrometry (MS) [1–3]. Each technique bears its own advantages and disadvantages, though herein, those of NMR are

discussed. NMR is the most common approach to elucidate the three dimensional structures of organic small molecules [4], and as such, is a valuable tool for untargeted metabolomics methods. NMR spectroscopy is built upon the principle of energy absorption and re-emission by atomic nuclei due to excitation with an external magnetic field [5]. Nuclei with a nuclear spin $I \neq 0$ (where I = the nuclear spin quantum number, which is dependent upon the number of protons and neutrons) are NMR active [6]. Thus, by subjecting NMR active nuclei to a strong constant magnetic field, exciting the spin state to a different energy state with a radio frequency pulse, and allowing the nuclei to precess back to their equilibrium state in the magnetic field, an electromagnetic signal with a frequency characteristic of that nucleus can be captured [5,6]. The local magnetic field surrounding an atom in a molecule changes the nuclear spin resonance frequency, thus informing on the electronic structure of a molecule and its individual functional groups. The frequency measured for nuclei of interest is thus unique for individual compounds, and as such, results in characteristic spectral splitting patterns and chemical shifts, as observed in an NMR spectrum. These spectral characteristics can thus be used to identify unknown molecules in a complex metabolite mixture and allow for direct identification and quantification of metabolites [2,3,5].

The nondestructive nature of NMR allows for the collection of multiple spectra for a single sample, and the near absence of NMR spectrometer variations for a given magnetic field strength enables NMR experiments to be a highly reproducible [2,4,5]. NMR can be used to probe the magnetic properties of diverse spin ½ nuclei: proton (^{1}H), carbon (^{13}C), nitrogen (^{15}N), and phosphorus (^{31}P) [4]. ^{1}H NMR predominates metabolomics-based experiments because protons are contained within the structure of almost every organic compound, and as such, every known metabolite [4,5]. Additionally, ^{1}H nuclei are present at 99.98% natural abundance, have a

large gyromagnetic ratio, compared to, for example, ^{13}C nuclei, which are present ~1% abundance and whose gyromagnetic ratio is a 1/4 of g (^{1}H) [4]. This results in ^{1}H NMR experiments being intrinsically more sensitive than ^{13}C NMR, and potentially being more suitable for untargeted NMR metabolomics studies.

The limited sensitivity of NMR experiments is one of the drawbacks of the approach, which in turn places a restriction on sample size and results in a limit of detection of 5 mM for metabolites present in a typical sample metabolite mixture. Spectral crowding and overlap of resonance signals is inherently limiting in untargeted NMR analyses of complex metabolite mixtures, although 2D ^{1}H-^{1}H NMR and ^{1}H-^{13}C correlation experiments can be used to alleviate the spectral complexity observed in a 1D ^{1}H NMR spectrum. Lastly, there is an intrinsic limitation to the diversity of metabolites that are visible with any metabolomics technique, and NMR is no exception. The extraction method and solvent used tailor any experiment to observe a select group of metabolites, such as in the case of using water as a solvent, thus only enabling the observation of polar metabolites. Despite the limitations of 1D ^{1}H NMR, 50-200 metabolites with concentrations >1 μM can be identified and quantified using this technique [3,7], informing on many substrates, intermediates, and products of central metabolic pathways.

Given the increase of metabolomics-based research for diseases, there exists several highly effective platforms for aiding in the identification and quantification of metabolites in complex biological samples. One such program for NMR metabolomics is the Chenomx™ NMR suite software [5,8]. This software enables further processing of 1D ^{1}H NMR spectra and the identification of metabolites through an automated or manual peak-based fit style. Both methods for identifying compounds within the spectra consider the characteristics signatures of each ^{1}H resonance including the chemical shift and spectral splitting patterns, and quantitation of

metabolites is obtained by measuring signal intensities. The software is equipped with a small molecule reference spectral database and allows the use of additional small molecule reference spectral libraries, including the Human Metabolome Database (HMDB) [9]. Metabolite identification and quantitation is then achieved by fitting the spectral patterns and ^{1}H chemical shifts of reference compounds to those observed in the 1D ^{1}H NMR spectra of the sample metabolite mixtures, similar to solving a jigsaw puzzle.

Though direct compound identifications and quantifications is achieved using 1D ^{1}H NMR, the overlap of NMR signals, or less distinct splitting patterns of a molecule may lead to ambiguous metabolite annotations. Metabolite ID ambiguity may thus necessitate metabolite ID validation via spiking of a pure compound, 2D NMR experiments, or use of an orthogonal analytical method such as liquid chromatography-mass spectrometry (LC-MS).

Due to the non-destructive nature of NMR, validation of compound IDs can be done by spiking a known concentration of a standard compound into the sample and confirming the increase in ^{1}H signal intensities for the annotated metabolite in question. Although more time intensive, a valuable method for spectral deconvolution can be accomplished by collecting 2D NMR spectra that plot data with two frequency axes rather than one. The two dimensions of the 2D NMR spectrum can consist of homonuclear or heteronuclear correlation experiments that inform on interactions across single and multiple bonds within the molecule. ^{1}H-^{1}H correlation spectroscopy (COSY) and total correlation spectroscopy (TOCSY) provide information on proton interactions between neighboring, or all hydrogen atoms in a molecule, respectively. Heteronuclear Single Quantum Correlation (HSQC) and Heteronuclear Multiple Bond Correlation (HMBC) experiments inform on a single bond or multi-bond level, respectively, but between two different nuclei, most commonly proton-carbon connections [4].

One of the strengths of NMR spectroscopy is that it is highly complementary with mass spectrometry to broaden the coverage of metabolites identified and quantified in metabolomics experiments. Many advances in the field have helped improve sensitivity, which has been considered a significant limitation of this analytical technique [10]. Sensitivity issues have been ameliorated through the design of sensitivity-enhanced NMR cryoprobes, ultra-high field NMR magnets, and improved spectrometer electronics [4,11,12]. As such, NMR spectroscopy is a valuable tool in the metabolomics workflow that allows for efficient high-throughput analyses of serum, fecal, and tissue samples to garner valuable information about molecular markers indicative of disease phenotypes and the cellular mechanisms underlying disease pathology.

Statistical Workflow and Pathway Analysis

MetaboAnalyst is a widely used online platform designed for metabolomic data analysis and interpretation with an aim to "enable high-throughput analysis for both targeted and untargeted metabolomics, and to narrow the gap from raw spectra to biological insights" [13]. The software is capable of statistically normalizing metabolomics datasets and subsequently performing univariate and multi-variate statistical analyses. Of the available features, the statistical tests most common used for metabolomics datasets include univariate *t*-tests and analysis of variances (ANOVAs) and multivariate unsupervised principal component (PCA), supervised partial least squared discriminant (PLS-DA), random forest, and hierarchical clustering (HC) analyses [1,14]. MetaboAnalyst is further equipped to perform validation and correction tests to ensure that the statistical models generated do not lead to false positives or overfit the data. False discovery rate correction (FDR) is available for t-tests and ANOVAs, and multiple metrics can be used to assess the validity of the PLS-DA modeling, including: leave-

one-out validation test for predictive variability metrics (Q^2) and predicted residual sum of squares (PRESS) error (R^2), and separation distance and prediction accuracy permutation tests (n = 1000) [15,16]. MetaboAnalyst is also available as an R package that allows users to further personalize their metabolomics data analysis through integration with MetaboAnalyst-associated packages, allowing for the application of additional statistical metrics, including assessments of classification error rates (CER), and area under the receiver operating characteristic curve (AUROC) [5].

The final stage in the analysis of metabolomics data is a functional examination of the small molecules that achieved significance based on statistical parameters such as *p* values and validation metrics, by interrogating the metabolites of interest based on their biological context and their role in central metabolic pathways and cellular functions. These pathways impact analyses enable the identification of physiological and pathophysiological associations of metabolites for specific disease states. MetaboAnalyst has a pathway enrichment analysis module in which users input a list of metabolites of interest and the program maps the metabolite to known biochemical pathways based on public databases such as HMDB [9], the Kyoto Encyclopedia of genes and Genomes (KEGG) [17], and the Small Molecule Pathway (SMP) database [5,18]. The pathway impact analysis provides an impact score based on a topological analysis, thereby indicating pathways that may be most impacted based on the number of metabolites identified and belonging to specific biochemical networks. This tool can then help establish, together with a thorough review of published findings, the relevance of metabolites and specific pathways of interest, yielding information that demonstrate the significance of the metabolomics observations and provide molecular insights into mechanisms of disease or study model.

Complexities of Metabolomics Data Comprehension Challenges in the field of metabolomics often arise due to the single time points of sampling of the metabolomes, which provide only a snapshot of the biological systems of interest that are subject to change and highly dynamic. Profiling of metabolites yields valuable information that can inform on the biological and environmental changes of an organism, though the redundancy and complexity of metabolic networks and the cross talk between metabolism, cell signaling, gene expression and regulation can be challenging to interpret. Moreover, the lack of linearity in response of biological metabolic networks adds to the challenge of data interpretation in terms of biological significance and impacted cellular networks. Among the central metabolic pathways exist many branch points that interconnect pathways via commonly used substrates and/or intermediates. Additionally, many pathways are subject to feedback regulation by intermediates of coupled metabolic pathways, which can lead to the shuttling of metabolites to alternative pathways or cellular fates. As such, a single change in a metabolite level cannot be easily linked to a specific pathological process. Metabolite patterns are most informative when clusters of metabolites are found to be altered. Given the complexity and interconnected nature of metabolic pathways and cellular networks, subsequent analyses are usually necessary to fully comprehend the biological consequences of the observed metabolic perturbations, though the regulation and activity of enzymes involved in a given metabolic pathway can usually be postulated, especially when observed changes in metabolite levels correspond to metabolites that are part of the same pathway, contribute to the regulation of that pathway, or are related to a disease hallmarks as assessed by analysis of metadata that has been recorded in parallel with metabolomics data.

Metabolomics based techniques can be used to inform on the cellular mechanisms mediating disease progression, and have gained more attention recently as a valuable tool for

studying neurodegenerative diseases such as Alzheimer's and Parkinson's [19,20]. As such, metabolomics presents as an equally valuable tool to elucidate the cellular mechanisms mediating neurodegeneration and inform on the clinical phenotypes and alterations of familial dysautonomia patients.

Familial dysautonomia

Familial dysautonomia (FD) is a rare, highly debilitating, developmental and progressive neurodegenerative disease and first coined Riley-Day syndrome by the New York pediatricians who discovered it in 1949 [21,22]. FD has since been classified as Hereditary Sensory Autonomic Neuropathy (HSAN) Type-lll given that patients present with complex neurological phenotypes reflective of peripheral autonomic and sensory deficits, which begin at birth [22,23]. Children are diagnosed with FD based on the following features: 1) absence of axon flare following intradermal histamine injection; 2) pain and temperature perception deficits; 3) defective tear production; 4) smooth underdeveloped fungiform papillae of the tongue; 5) low muscle tone and absence of deep tendon reflexes; and 6) Ashkenazi Jewish heritage [22].

FD is inherited among eastern European, Ashkenazi Jewish descent with a carrier rate ranging from 1:27-1:32, and 1:18 for those with Polish heritage [21–23]. Both parents must carry a mutated copy of the gene that causes FD (Figure 1), thus classifying it as an autosomal recessive disease. Unlike many neurodegenerative diseases such as Alzheimer's, Parkinson's, or amyotrophic lateral sclerosis (ALS) that are multifactorial in origin, FD is caused by a single point "founder mutation" in >99% of patients. The founder mutation traces back to the Pale of Settlement, a demarcated boundary where Jewish individuals were exiled to in the former Russian Empire between 1791-1917 [21,23,23]. The rapid endogamous population expansion

within the tight geographical constraints lent itself to a genetic bottleneck among the population and increased the carrier frequency of autosomal recessive disease such as FD.

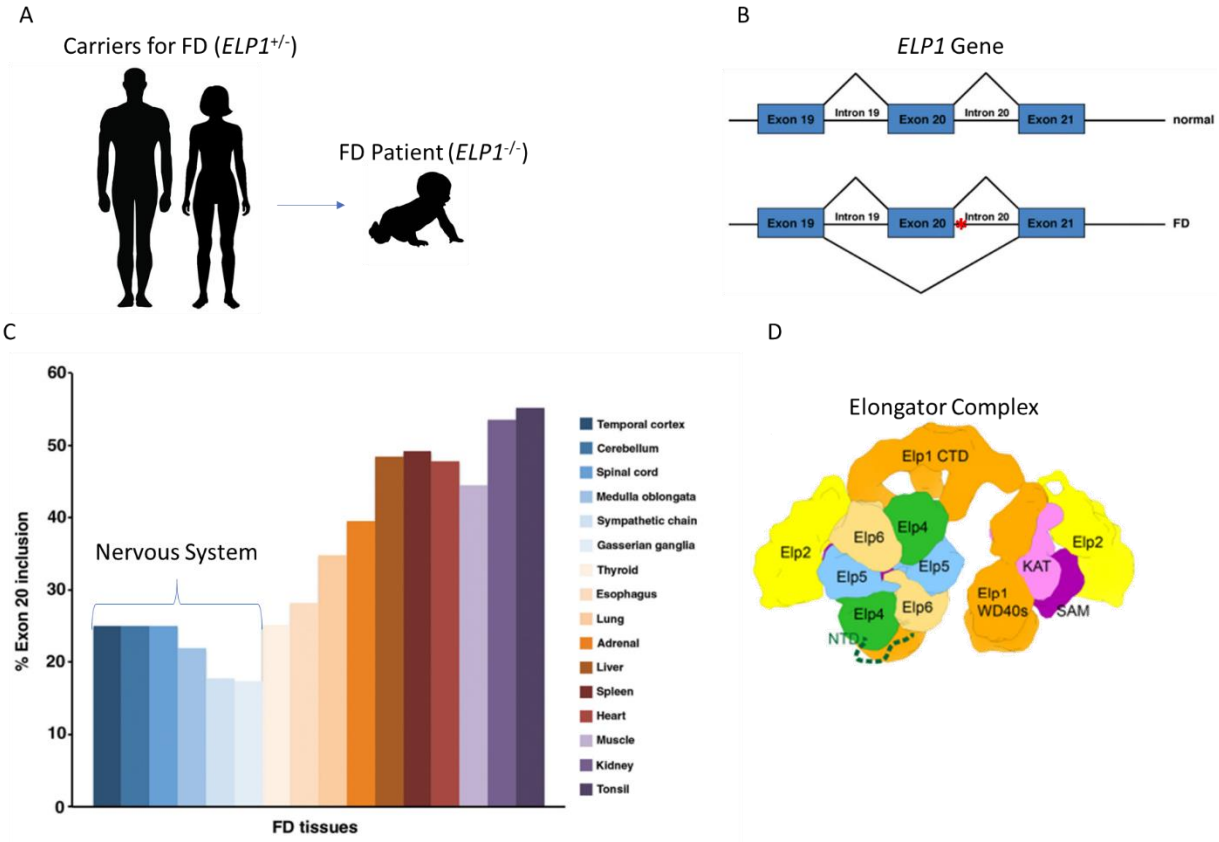


Figure 1. The genetic origins and tissue specific splicing defects of *ELP1* that give rise to reduced ELP1 protein and Elongator Complex function in the nervous system and promote FD. (A) An illustration of the autosomal recessive heritability of FD, indicating both parents must carry one copy of the *ELP1* FD founder mutation, and their children must inherit two copies of the mutated allele to be born with FD. (B) The relevant regions of the *ELP1* gene for both a normal and FD transcript, depicting exon 19-20, the associated introns, and the FD *ELP1* point mutation (red star) in intron 20. (C) Represents various tissue types from FD patients that were measured for their percent of exon 20 inclusion and highlights the deficit of exon 20 inclusion primarily in tissue types of the nervous system. (D) The quaternary structure of the Elongator Complex, where Elp1 acts as the scaffold protein (orange), enabling assembly of the Elp1 subunits 1-6. Panels (B-D) were adapted from Dietrich & Dragatsis (2016), and Dauden, *et al.* (2017)[22,24].

The mutation that causes FD is in the gene that encodes elongator protein 1 (*ELP1,* formerly *IKBKAP*), and corresponds to a single thymine (T) to cytosine (C) base pair substitution within the region of chromosome 9 associated with nucleotide position 2,204 and base pair 6 of intron 20 (c.2204 + 6T > C) (Figure 1) [21,23]. This single base pair substitution causes a splicing defect when the mRNA transcript is undergoing processing to remove noncoding introns. As a result of impaired mRNA splicing, exon 20 is excised along with introns 19 and 20, and a truncated form of the *ELP1* mRNA transcript results [22,25]. The miss-spliced mRNA contains a frameshift mutation that introduces a premature stop codon, thus preventing the proper translation of a fully functional ELP1 protein [25]. The truncated mRNA is thus targeted for nonsense mediated decay, leading to a reduced production of functional ELP1 protein [22]. Interestingly, this splicing defect occurs in a tissue specific manner, with neurons being the prime tissue type that contains the smallest levels of functional ELP1 protein as a result of a greater frequency of impaired splicing in these tissues (Figure 1) [22,25,26].

ELP1 is the scaffold protein of the 6-subunit elongator complex comprised of ELP 1-6 (Figure 1). The elongator complex, and thus ELP1, are necessary for the development and survival of neurons due to the role of the elongator complex in modifying tRNA wobble uridines and facilitating the translational expression of AA- and AG- codon-biased genes [27–30]. Lysine, glutamate, and glutamine are the amino acids with redundant codons ending in either AA- or AG-. The elongator complex facilitates interpretation of redundant codons by chemically modifying transfer RNAs (tRNAs) with the addition of a thiol (s^2) and 5’ methoxy-carbonyl-methyl (mcm^5) modification to the uridine in the wobble position at nucleotide number 34 of the tRNA molecule [28,31]. *Goffena, J. et al* demonstrated that the mcm^5s^2 elongator complex modification increases translational efficiency of large AA- biased codons and decreases the

efficiency of small AG- biased codons [28]. When the translational cellular machinery encounters an AA- ending codon without the mcm^5s^2 modification, ribosome stalling occurs in the translational process and leads to protein misfolding. As a result, lack of ELP1 and elongator complex assembly negatively impacts the production of several cellular proteins of varying sizes and AA:AG ratios. Proteins most impacted include those involved in DNA repair, histone acetylation, and actin cytoskeleton organization for cell migration [27,28,32]. Neurons impacted by the loss of ELP1 comprise both the central (CNS) and peripheral nervous system (PNS) in FD [21–23,26,30].

The central nervous system includes the brain, spinal cord, and retina [33], and all the nerves that innervate the limbs and organs of the body comprise the peripheral nervous system and transmit sensory input (afferent) to, and motor (efferent) signals from, the central nervous system [22,34]. The motor division of the peripheral nervous system can be further divided into the somatic (skeletal muscle innervation) and autonomic (smooth muscle, cardiac muscle, and glands) nervous systems. The autonomic nervous system has both a sympathetic and parasympathetic component which mediates the “fight-or-flight”, and “rest-and-digest” responses, respectively [22,34]. Though the parasympathetic nervous system is responsible for conserving energy and digestion, it regulates all involuntary acts such as breathing, blood pressure, sweating, salivating, tear production, temperature regulation, and many more [22,34]. The sensory and autonomic nervous systems are most impacted by the FD ELP1 mutation, and as such, patients develop highly diverse symptoms with variable hallmark features including: low body mass index (BMI) accompanied with low muscle tone; dysphagia and frequent aspiration of food or drink promoting chronic lung infections; gastrointestinal dyscoordination; cardiovascular instability; breath-holding spells and sleep apnea; spinal curvature; and baroreflex

instability that promotes autonomic “crises” marked by vomiting, nausea, hypertension, tachycardia and blotching [21–23,29,35]. The most debilitating clinical symptoms of FD are the progressive neurodegenerative features of the disease which include optic atrophy and worsening gait ataxia [21,35].

FD was once considered a fatal pediatric disorder, but advances in clinical care have improved patient longevity and quality of life [21,22,35], though many current treatments still focus on symptom management rather than prevention, and are not viable for long term use as they are highly invasive and often have difficult-to-tolerate off target effects [22,35,36]. Increasing the expression of wild type *ELP1* has been a primary focus for developing therapeutic treatment options for FD patients using small molecules splicing modulators (SMSMs), antisense oligonucleotides (AOs), or adeno-associated virus (AAV) mediated gene therapy [37–41]. However, these methods are still in their infancy, and some of the earliest therapeutic interventions aimed at enhancing the amount of functional ELP1 protein in diverse tissues resulted in detrimental effects to patients health [35,38]. Although these methods are not devoid of off target effects, SMSMs, AOs, and AAV-mediated gene therapies present a very promising therapeutic approach for FD [37,40,41]. A third avenue for developing novel and viable therapeutic options for FD patients includes characterizing the gut microbiome and central metabolism disturbances; in so doing, these systems that are part of the gut-brain-metabolism axis of FD could be targeted to develop novel, non-invasive therapeutics to treat or mitigate neurodegeneration.

Gut-Brain-Metabolism Axis

Extensive bi-directional cross talk between neurons, the gut microbiome, and central metabolism highlight the gut-brain-metabolism axis as a valuable network of cellular processes that can be targeted through any of the given branches for preventing and treating neurodegenerative disease [42–44]. Communication between two of these axes (i.e., the gut-brain, metabolism-brain, or gut-metabolism axis) has been explored, but studies involving all three are only beginning to emerge.

Recent advances in neurodegenerative research regarding Alzheimer's, Parkinson's, ALS, and autism spectrum disorder (ASD) have highlighted the profound role the gut microbiome plays in the progression of these neurological diseases and disorders [45–47]. Proper gut microbial health is vital for maintaining overall host metabolic homeostasis and organ function, as gut microbes can out-compete the host for important bio nutrients [48], or produce compounds that are necessary for maintaining proper host health, and influencing the pathophysiology of the whole body [49–53]. Indeed, several neurological disorders and metabolic diseases have been associated with dysbiotic gut microbial communities [42,45,53,54].

Though not as well explored as the gut microbiome, central metabolism is equally important for understanding the pathophysiological mechanisms underlying disease onset and progression of neurodegenerative diseases and disorders [44,55–57]. Pathological markers of neurodegenerative diseases include deficits in mitochondrial function and energy production and oxidative stress, which are direct consequences of abnormal central metabolic regulations which can worsen neurological symptoms [57–59]. FD shares many hallmark features with Alzheimer's, Parkinson's, ALS, and ASD , including the disruption of elongator complex

function [58–61], and current evidence for FD patients suggests that metabolic dysfunction and gut microbiome dysbiosis is present and exacerbating disease progression [62,63].

Vagal nerve innervation is reduced in the gastrointestinal (GI) tract of FD patients [64], which likely promotes the manifestation of severe GI dyscoordination including impaired gastric emptying, diarrhea, constipation, and gastroesophageal reflux [65]. Accompanying the physiological GI symptoms experienced by FD patients is the recurrence of *Clostridium difficile (C. diff.)* infections [35]. These debilitating characteristics indicate that FD patients may experience overall gut dysbiosis, *i.e.* global compositional changes of the microbial population including reduced gut microbiota biodiversity and complexity, and alterations in composition [49]. Accompanying the signs for gut dysbiosis are clinical symptoms indicating a deficit in metabolic homeostasis, especially regarding ATP (adenosine triphosphate) energy levels. Beginning in infancy, FD patients have characteristically high metabolisms, low fat content, and uncoordinated eating. These characteristics can result in malnutrition and failure to thrive, a status that translates to adolescence and adulthood, and is reflected in extremely low BMI, and reduced muscle tone partnered with increased incidences of Rhabdomyolysis, a chronic muscle wasting disease [22,65,66]. Further, mitochondria of muscle and retinal ganglion cells (RGCs) of FD patients exhibit structural abnormalities, and functional deficits of the electron transport chain [67–70]. Considerable progress in understanding the clinical and scientific etiology of FD has laid the groundwork for investigating the gut-brain-metabolism axis of FD, and a significant portion of that foundation includes the development of many useful cellular and animal models that recapitulate hallmarks of the FD disease at the cellular and phenotypic levels.

Models of FD

Cellular and Non-Mammalian Non-mammalian animal models of FD have been particularly valuable for teasing apart the effect of *Elp1* absence in promoting developmental deficits of the peripheral nervous system [29]. *Elp1* loss of function studies have been conducted in *Caenorhabditis elegans*, chick, zebrafish, *Zenopus,* and *Drosophila*, which have allowed researchers to identify deficits in neural cell migration, axonal branching, tissue innervation, vesicle trafficking along microtubules, and synaptic function [22,29,71–74]. In addition to these studies, cellular models of FD patient-derived lymphoblast and fibroblast have been used to investigate therapeutic options, such as the usage of the small molecule splicing compound kinetin [38,75]. However, most of FD research has relied on diverse FD mouse models to gain mechanistic understanding of the CNS and PNS deficits in FD, and to test novel interventions and therapeutics targeting restoring Elp1 levels and arresting or delaying progressive neurodegeneration.

Mouse Models Variants of Elp1 mice were made by conditionally knocking out *Elp1*, generating humanized transgenic mice, and by genetically combining both conditional knockouts (CKOs) and transgenics [22,29]. Each FD mouse model yielded insightful information at the cellular and phenotypic levels and ultimately guided the development of the Tα (*Tuba1a-Cre; Elp1*$^{LoxP/LoxP)}$ and Pax6 (*Pax6-Cre; Elp1*$^{LoxP/LoxP}$) mouse models used in this work.

The first FD mouse model was a humanized mouse, engineered by introducing the full human mutant *ELP1* gene into the mouse genome via a bacterial artificial chromosome (BAC). This model recapitulated the tissue specific splicing deficits of *ELP1* observed for FD patients, demonstrating that the same mechanism of altered splicing was translatable to mice [76].

However, because mouse *Elp1* was expressed at normal healthy levels, this model did not exhibit phenotypic manifestations of FD. Next, a conventional knockout was made using the LoxP -Cre recombinase system targeting mouse *Elp1,* which demonstrated embryonic lethality, prompting the generation of mice with a loss of *Elp1* function ($Elp1^{3LoxP/3LoxP}$) mutation, and exon 20 *Elp1* deletion ($Elp1^{\Delta 20/\Delta 20}$), though both still demonstrated early embryonic stage lethality [77].

Post-embryonically viable FD mice were generated using a LoxP-flanked *Elp1* gene locus ($Elp1^{flox/flox}$), and by generating a compound heterozygote with both the floxed and Δ20 alleles ($Elp1^{flox/\Delta 20}$), resulting in a 90% and 95% reduction of Elp1 protein levels, respectively. These mice required special care, though they were the first mice to recapitulate many phenotypic attributes of the human FD disease, including: small stature, gait ataxia, loss of fungiform papillae, pain and temperature sensation deficits, spinal curvature, progressive eye and bladder pathology, and reduced lifespan [78]. Interestingly, a 5% increase in Elp1 expression was observed in the $Elp1^{flox/flox}$ mouse model compared to the $Elp1^{flox/\Delta 20}$, demonstrating a fine threshold of Elp1 expression levels which, if met, might be able to resolve neuronal developmental defects [78]. As such, a complex transgenic mouse was engineered, which introduced copies of the FD human *ELP1* gene into the $Elp1^{\Delta 20/flox}$ mouse ($TgFD9;Elp1^{\Delta 20/\mathrm{flox}}$), allowing for low expression levels of properly spliced human and mouse mRNA, meeting the minimum ELP1 (human and mouse) protein threshold, thus generating a viable mouse that most closely models the global tissue-specific altered splicing defect observed in FD patients, and that recapitulates many sensory and autonomic deficits of the disease [79]. Despite being the most representative mouse model in terms of ELP1/Elp1 protein expression, subsequent conditional knockout mice are still highly valuable to investigate specific organ systems, to tease apart the

tissue specific functions of ELP1, and to test the effectiveness of therapeutics aimed at mitigating the loss of specific cell populations.

Tuba1a-Cre^{+}*;Elp1*$^{LoxP/LoxP}$ Conditional knockout (CKO) mice were generated using the LoxP-Cre system to selectively ablate *Elp1* in specific tissues and to characterize the PNS sensory and autonomic developmental deficits associated with FD [80,81]. Following those, a pan-neuronal CNS and PNS CKO was generated using a *Tuba1a* promoter driven Cre recombinase in which Cre was activated in early development (E12.5) and caused *Elp1* ablation in a majority of the CNS and ~40% of the PNS [30]. This mouse was the first to demonstrate a central nervous system requirement for *Elp1* and that loss of Elp1 solely in the nervous system is sufficient to recapitulate many of the hallmark behavioral and phenotypic signatures of FD that are associated with both developmental and progressive neurodegeneration. These mice were smaller in appearance, weighed less than control littermates, were completely devoid of abdominal fat, and experienced shortened lifespan, often dying suddenly [30]. The manifestations of gait ataxia, low grip strength, hindlimb clasping, tremors, and spinal curvature (kyphoscoliosis) were attributed to perturbations in the development and survival of spinal motor neurons and loss of innervation of the neuromuscular junction [30]. Impaired development and subsequent decline of cortical motor neurons appeared to be at the source of abnormal behavioral traits (poor grooming), and impaired spatial learning and memory [30]. Interestingly, this mouse model was the first to recapitulate the slow progressive eye pathology observed in FD patients [30,82].

Tuba1a-Cre expression was detected in ~90% of retinal ganglion cells (RGC), the cell type responsible for visual decline in FD patients [68], and marginal amounts of *Tuba1a-Cre* expression was detected in other neuronal cells: bipolar cells, amacrine cells, photoreceptors and

Müller glia [30]. As such, the *Tuba1a-Cre*$^{+}$*;Elp1*$^{LoxP/LoxP}$ (Tα) mouse model was the first to enable the characterization of the visual impairments including diminished retinal function, and pathology associated with FD. Development of RGCs was not inhibited, demonstrating that differentiation of progenitors into RGCs is not dependent on Elp1 levels. With age however, metabolically active temporal RGCs exhibited slow progressive degeneration, while the melanopsin (intrinsically photosensitive) RGCs were resistant to death, recapitulating the human manifestations of FD retinopathy. RGC degeneration was ultimately followed by optic nerve thinning, disruption of the nerve fiber layers, Müller cell activation, and indirect photoreceptor loss [30].

Though *Tuba1a-Cre*$^{+}$*;Elp1*$^{LoxP/LoxP}$ mice were the first to model slow progressive RGC degeneration, this mouse model limited the understanding of the consequences of Elp1 reduction in mediating FD optic neuropathy due to nearly autonomous expression of *Tuba1a-Cre* in RGCs. Additionally, the model resulted in a pan-neuronal loss of Elp1, suggesting that the progressive neuropathy observed in other tissues could be the cause of the retinal deficits observed. To overcome this limitation, a *Pax6-Cre*$^{+}$*;Elp1*$^{LoxP/LoxP}$ was thus engineered.

Pax6-Cre^{+}*;Elp1*$^{LoxP/LoxP}$ The Pax6 model was developed to assess whether the retinal changes observed in the Tα mouse model of FD were due to a direct requirement for Elp1, or if independent off target effects from other systems promoted disturbances in the retina, and to further probe the health of all retinal cell populations. The retina specific knockout of *Elp1* was generated using the Cre-lox system and the Pax6 reporter gene, generating a *Pax6-Cre*$^{+}$*; Elp1*$^{Loxp/Loxp}$ (Pax6) CKO mouse model of FD [67]. This model confirmed that Elp1 is not required for the development of the retina, and despite the abolishment of *Elp1* expression in all

retinal cell types (i.e., muller glia, amacrine cells, bipolar cells, and intrinsically photosensitive RGC), only RGCs showed progressive decline, followed by optic nerve thinning [67]. Degeneration of RGCs and the temporal optic nerve is reminiscent of Leber's hereditary optic neuropathy (LHON) and dominant optic atrophy (DOA), both of which are visual disorders that stem from mutations affecting electron transport chain function of the mitochondria [83–85]. As such, the functional status of retinal mitochondria of the Pax6 model was interrogated, resulting in the observation that inner mitochondrial membranes were depolarized, and the function of the electron transport chain complex 1 protein and ATP levels were reduced [67]. This study concluded that lack of Elp1 induced cellular changes that affected mitochondrial structure and function, creating cellular stress and ultimately promoting death of RGCs and optic nerve thinning.

Each mouse model developed to interrogate the cellular and pathophysiological mechanisms underlying FD disease phenotypes are unable to completely recapitulate the human form of the disease, as it is impossible to fully translate the *in vivo* FD physiological environment of the human disease to a FD mouse model, and CKO mice selectively delete *Elp1* expression in target tissues instead of cells being subject to the tissue specific altered splicing of *Elp1*. Nevertheless, these FD mouse models have clearly demonstrated the efficacy of Elp1 CKO to identify pathophysiological mechanisms that give rise to the diverse debilitating symptoms of FD, demonstrating their potential value for testing novel therapeutics to treat human FD.

Research Question, Hypothesis, and Research Aims

The research questions addressed in this dissertation and work described herein consisted of the following: 1) Are the serum and fecal metabolomes of FD patients distinct from control

relatives, and if so, which metabolites are indicative of the FD phenotype? 2) Is the gut microbial community of FD patients distinct from that of control relatives and how do these microbiome differences relate to observed metabolome differences? 3) How can the metabolic state of FD patients be probed or redressed to further inform on phenotypic symptoms and ultimately help ameliorate FD disease traits or mitigate disease onset and progression?

The aims of this dissertation research include the comprehensive and detailed metabolomic characterization of stool samples, identification of altered metabolite levels in FD patients, metabolomics studies of the Tα FD mouse model to identify the molecular mechanisms at the source of the FD metabolic traits observed in FD patients, and an in-depth metabolomics characterization of the Pax6 mouse retina. To accomplish these aims, techniques for extracting polar metabolites from human and mouse stool samples were adapted [86,87] and optimized to obtain sufficient amounts of metabolites for NMR studies, optimize signal-noise ratios of the NMR experiments, and to separate proteins and other large molecules (lipids) that can yield broad and undefined NMR signals in 1D ^{1}H NMR spectra of metabolite mixtures and complicate spectral analysis. Additionally, a metabolite extraction method was developed to measure levels of taurine and other high abundancy retinal metabolites, which was adapted from experiments characterizing rabbit lens [88], and rat retina [89], and modified to demonstrate use, for the first time, of a perchloric acid extraction for NMR metabolomics studies of mouse retinae. Optimization of these protocols enabled the characterization of the stool metabolomes of FD patients and Tα mouse model, and Pax6 mouse retinas. Similarities and differences between polar metabolite profiles of FD patients and control relatives were evaluated and recapitulation of these profiles in the Tα FD mouse model was examined. Altered levels of metabolites

identified in the FD patients that were implicated in optic nerve pathology were also assessed in the Pax6 FD mouse retinae.

In conjunction to the effort directed towards stool sample and retina tissue metabolomics method development, significant training was received in mouse handling and experimentation at the BSL1 and BSL2 levels. This training was vital to lead mouse experiments that characterized the recapitulation of the human metabolomics data, and intervention experiments that targeted the central metabolism. Substantial effort was dedicated to honing skillsets that enabled mouse experimentation and collection of samples, such as the dissection of mouse retinal tissue for NMR analysis and associated experiments. Lastly, western blots constituted the bulk of experiments completed to interrogate choline (CTL1 and OCT1), and taurine (TAUT) transporters in gut, liver and retinal tissue, which required substantial troubleshooting and parameter optimization for each specific antibody.

A better understanding of the crosstalk between gut microbes, neuronal health, and metabolic homeostasis may provide novel avenues by which to guide the development of efficacious metabolism-based interventions and treatment strategies aimed at mitigating neurodegeneration and neurodegenerative disease progression. The metabolome analyses conducted herein on FD patients identified key metabolic disturbances indicative of many phenotypic deficits experienced by FD patients and informed on altered metabolic pathways, which may be worth exploring further to fully delineate gut-brain-metabolism interactions in FD. One such exploration led to the identification of elevated gut-microbial processing of choline and altered bile acid metabolism involving taurine in FD patients. Additionally, implications of taurine in eye health inspired the characterization of retinal metabolic deficits that present as likely candidates for non-invasive therapeutic methods to prevent the progressive decline of

RGCs. Many other avenues that interrogate the metabolites identified in the original fecal metabolomic analysis, or fully tease apart the contribution of altered choline and taurine metabolism to the mechanisms mediating FD disease progression are promising future studies that can be explored based on the foundational work presented herein. The metabolomics findings presented in this PhD dissertation are the first detailed metabolome studies of FD patients and FD mouse models, providing the first direct evidence that altered metabolic pathways contribute to neurodegeneration through the gut-brain-metabolism axis in FD.

References

1. Trifonova, O.P.; Maslov, D.L.; Balashova, E.E.; Lokhov, P.G. Current State and Future Perspectives on Personalized Metabolomics. *Metabolites* **2023**, *13*, 67, doi:10.3390/metabo13010067.

2. Gowda, G.A.N.; Raftery, D. NMR Metabolomics Methods for Investigating Disease. *Anal. Chem.* **2023**, *95*, 83–99, doi:10.1021/acs.analchem.2c04606.

3. Emwas, A.-H.; Roy, R.; McKay, R.T.; Tenori, L.; Saccenti, E.; Gowda, G.A.N.; Raftery, D.; Alahmari, F.; Jaremko, L.; Jaremko, M.; et al. NMR Spectroscopy for Metabolomics Research. *Metabolites* **2019**, *9*, 123, doi:10.3390/metabo9070123.

4. Sinclair, G.M.; Oakes, S.M.; Warden, A.C.; Paten, A.M.; Jones, O.A.H. Exploring the Potential Application of Alternative Nuclei in NMR Based Metabolomics. *Metabolomics* **2023**, *19*, 42, doi:10.1007/s11306-023-02003-z.

5. Chen, Y.; Li, E.-M.; Xu, L.-Y. Guide to Metabolomics Analysis: A Bioinformatics Workflow. *Metabolites* **2022**, *12*, 357, doi:10.3390/metabo12040357.

6. Levitt, M.H. *Spin Dynamics: Basics of Nuclear Magnetic Resonance*; John Wiley & Sons, 2013; ISBN 978-1-118-68184-8.

7. Wishart, D.S. Quantitative Metabolomics Using NMR. *TrAC Trends Anal. Chem.* **2008**, *27*, 228–237, doi:10.1016/j.trac.2007.12.001.

8. Wishart, D.S. Bioinformatic Tools for Clinical Metabolomics. In *Clinical Metabolomics Applications in Genetic Diseases*; Abdel Rahman, A.M., Ed.; Springer Nature: Singapore, 2023; pp. 71–96 ISBN 978-981-9951-62-8.

9. Wishart, D.S.; Feunang, Y.D.; Marcu, A.; Guo, A.C.; Liang, K.; Vázquez-Fresno, R.; Sajed, T.; Johnson, D.; Li, C.; Karu, N.; et al. HMDB 4.0: The Human Metabolome Database for 2018. *Nucleic Acids Res.* **2018**, *46*, D608–D617, doi:10.1093/nar/gkx1089.

10. Wishart, D.S.; Cheng, L.L.; Copié, V.; Edison, A.S.; Eghbalnia, H.R.; Hoch, J.C.; Gouveia, G.J.; Pathmasiri, W.; Powers, R.; Schock, T.B.; et al. NMR and Metabolomics—A Roadmap for the Future. *Metabolites* **2022**, *12*, doi:10.3390/metabo12080678.

11. Marion, D. An Introduction to Biological NMR Spectroscopy *. *Mol. Cell. Proteomics* **2013**, *12*, 3006–3025, doi:10.1074/mcp.O113.030239.

12. Lee, J.H.; Okuno, Y.; Cavagnero, S. Sensitivity Enhancement in Solution NMR: Emerging Ideas and New Frontiers. *J. Magn. Reson. San Diego Calif 1997* **2014**, *241*, 18–31, doi:10.1016/j.jmr.2014.01.005.

13. Pang, Z.; Chong, J.; Zhou, G.; de Lima Morais, D.A.; Chang, L.; Barrette, M.; Gauthier, C.; Jacques, P.-É.; Li, S.; Xia, J. MetaboAnalyst 5.0: Narrowing the Gap between Raw Spectra and Functional Insights. *Nucleic Acids Res.* **2021**, *49*, W388–W396, doi:10.1093/nar/gkab382.

14. Lamichhane, S.; Sen, P.; Dickens, A.M.; Hyötyläinen, T.; Orešič, M. An Overview of Metabolomics Data Analysis: Current Tools and Future Perspectives. In *Comprehensive Analytical Chemistry*; Elsevier, 2018; Vol. 82, pp. 387–413 ISBN 978-0-444-64044-4.

15. Szymańska, E.; Saccenti, E.; Smilde, A.K.; Westerhuis, J.A. Double-Check: Validation of Diagnostic Statistics for PLS-DA Models in Metabolomics Studies. *Metabolomics* **2012**, *8*, 3–16, doi:10.1007/s11306-011-0330-3.

16. Ruiz-Perez, D.; Guan, H.; Madhivanan, P.; Mathee, K.; Narasimhan, G. So You Think You Can PLS-DA? *BMC Bioinformatics* **2020**, *21*, 2, doi:10.1186/s12859-019-3310-7.

17. Ogata, H.; Goto, S.; Sato, K.; Fujibuchi, W.; Bono, H.; Kanehisa, M. KEGG: Kyoto Encyclopedia of Genes and Genomes. *Nucleic Acids Res.* **1999**, *27*, 29–34.

18. Frolkis, A.; Knox, C.; Lim, E. SMPDB: The Small Molecule Pathway Database - PMC. *Nucleic Acids Res* **2010**, *38*, 480–487.

19. Kori, M.; Aydın, B.; Unal, S.; Arga, K.Y.; Kazan, D. Metabolic Biomarkers and Neurodegeneration: A Pathway Enrichment Analysis of Alzheimer's Disease, Parkinson's Disease, and Amyotrophic Lateral Sclerosis. *OMICS J. Integr. Biol.* **2016**, *20*, 645–661, doi:10.1089/omi.2016.0106.

20. Havelund, J.F.; Heegaard, N.H.H.; Færgeman, N.J.K.; Gramsbergen, J.B. Biomarker Research in Parkinson's Disease Using Metabolite Profiling. *Metabolites* **2017**, *7*, 42, doi:10.3390/metabo7030042.

21. Norcliffe-Kaufmann, L.; Slaugenhaupt, S.A.; Kaufmann, H. Familial Dysautonomia: History, Genotype, Phenotype and Translational Research. *Prog. Neurobiol.* **2017**, *152*, 131–148, doi:10.1016/j.pneurobio.2016.06.003.

22. Dietrich, P.; Dragatsis, I. Familial Dysautonomia: Mechanisms and Models. *Genet. Mol. Biol.* **2016**, *39*, 497–514, doi:10.1590/1678-4685-GMB-2015-0335.

23. González-Duarte, A.; Cotrina-Vidal, M.; Kaufmann, H.; Norcliffe-Kaufmann, L. Familial Dysautonomia. *Clin. Auton. Res.* **2023**, *33*, 269–280, doi:10.1007/s10286-023-00941-1.

24. Dauden, M.I.; Kosinski, J.; Kolaj-Robin, O.; Desfosses, A.; Ori, A.; Faux, C.; Hoffmann, N.A.; Onuma, O.F.; Breunig, K.D.; Beck, M.; et al. Architecture of the Yeast Elongator Complex. *EMBO Rep.* **2017**, *18*, 264–279, doi:10.15252/embr.201643353.

25. Slaugenhaupt, S.A.; Blumenfeld, A.; Gill, S.P.; Leyne, M.; Mull, J.; Cuajungco, M.P.; Liebert, C.B.; Chadwick, B.; Idelson, M.; Reznik, L.; et al. Tissue-Specific Expression of a Splicing Mutation in the IKBKAP Gene Causes Familial Dysautonomia. *Am. J. Hum. Genet.* **2001**, *68*, 598–605, doi:10.1086/318810.

26. Cuajungco, M.P.; Leyne, M.; Mull, J.; Gill, S.P.; Lu, W.; Zagzag, D.; Axelrod, F.B.; Maayan, C.; Gusella, J.F.; Slaugenhaupt, S.A. Tissue-Specific Reduction in Splicing Efficiency of IKBKAP Due to the Major Mutation Associated with Familial Dysautonomia. *Am. J. Hum. Genet.* **2003**, *72*, 749–758.

27. Dalwadi, U.; Yip, C.K. Structural Insights into the Function of Elongator. *Cell. Mol. Life Sci.* **2018**, *75*, 1613–1622, doi:10.1007/s00018-018-2747-6.

28. Goffena, J.; Lefcort, F.; Zhang, Y.; Lehrmann, E.; Chaverra, M.; Felig, J.; Walters, J.; Buksch, R.; Becker, K.G.; George, L. Elongator and Codon Bias Regulate Protein Levels in Mammalian Peripheral Neurons. *Nat. Commun.* **2018**, *9*, 1–10, doi:10.1038/s41467-018-03221-z.

29. Lefcort, F.; Mergy, M.; Ohlen, S.B.; Ueki, Y.; George, L. Animal and Cellular Models of Familial Dysautonomia. *Clin. Auton. Res.* **2017**, *27*, 235–243, doi:10.1007/s10286-017-0438-2.

30. Chaverra, M.; George, L.; Mergy, M.; Waller, H.; Kujawa, K.; Murnion, C.; Sharples, E.; Thorne, J.; Podgajny, N.; Grindeland, A.; et al. The Familial Dysautonomia Disease Gene IKBKAP Is Required in the Developing and Adult Mouse Central Nervous System. *Dis. Model. Mech.* **2017**, *10*, 605–618, doi:10.1242/dmm.028258.

31. Karlsborn, T.; Tükenmez, H.; Chen, C.; Byström, A.S. Familial Dysautonomia (FD) Patients Have Reduced Levels of the Modified Wobble Nucleoside mcm5s2U in tRNA. *Biochem. Biophys. Res. Commun.* **2014**, *454*, 441–445, doi:10.1016/j.bbrc.2014.10.116.

32. Cameron, B.; Lehrmann, E.; Chih, T.; Walters, J.; Buksch, R.; Snyder, S.; Goffena, J.; Lefcort, F.; Becker, K.G.; George, L. Loss of Elp1 Perturbs Histone H2A.Z and the Notch Signaling Pathway. *Biol. Open* **2021**, *10*, bio058979, doi:10.1242/bio.058979.

33. Purves, D.; Augustine, G.J.; Fitzpatrick, D.; Katz, L.C.; LaMantia, A.-S.; McNamara, J.O.; Williams, S.M. The Retina. In *Neuroscience. 2nd edition*; Sinauer Associates, 2001.

34. Wehrwein, E.; Orer, H.S.; Barman, S. Overview of the Anatomy, Physiology, and Pharmacology of the Autonomic Nervous System. In *Comprehensive Physiology*; 2016; Vol. 6, pp. 1239–1278 ISBN 978-0-470-65071-4.

35. Palma, J.-A.; Kaufmann, L.; Fuente, C.; Percival, L.; Mendoza, C.; Kaufmann, H. Current Treatments in Familial Dysautonomia. *Expert Opin. Pharmacother.* **2014**, *15*, 2653–2671, doi:10.1517/14656566.2014.970530.

36. Axelrod, F.B.; Liebes, L.; Gold-von Simson, G.; Mendoza, S.; Mull, J.; Leyne, M.; Norcliffe-Kaufmann, L.; Kaufmann, H.; Slaugenhaupt, S.A. Kinetin Improves IKBKAP mRNA Splicing in Patients With Familial Dysautonomia. *Pediatr. Res.* **2011**, *70*, 480–483, doi:10.1203/PDR.0b013e31822e1825.

37. Ajiro, M.; Awaya, T.; Kim, Y.J.; Iida, K.; Denawa, M.; Tanaka, N.; Kurosawa, R.; Matsushima, S.; Shibata, S.; Sakamoto, T.; et al. Therapeutic Manipulation of IKBKAP Mis-Splicing with a Small Molecule to Cure Familial Dysautonomia. *Nat. Commun.* **2021**, *12*, 4507, doi:10.1038/s41467-021-24705-5.

38. Slaugenhaupt, S.A.; Mull, J.; Leyne, M.; Cuajungco, M.P.; Gill, S.P.; Hims, M.M.; Quintero, F.; Axelrod, F.B.; Gusella, J.F. Rescue of a Human mRNA Splicing Defect by the Plant Cytokinin Kinetin. *Hum. Mol. Genet.* **2004**, *13*, 429–436, doi:10.1093/hmg/ddh046.

39. Morini, E.; Gao, D.; Montgomery, C.M.; Salani, M.; Mazzasette, C.; Krussig, T.A.; Swain, B.; Dietrich, P.; Narasimhan, J.; Gabbeta, V.; et al. ELP1 Splicing Correction Reverses Proprioceptive Sensory Loss in Familial Dysautonomia. *Am. J. Hum. Genet.* **2019**, *104*, 638–650, doi:10.1016/j.ajhg.2019.02.009.

40. Schultz, A.; Cheng, S.-Y.; Kirchner, E.; Costello, S.; Miettinen, H.; Chaverra, M.; King, C.; George, L.; Zhao, X.; Narasimhan, J.; et al. Reduction of Retinal Ganglion Cell Death in Mouse Models of Familial Dysautonomia Using AAV-Mediated Gene Therapy and Splicing Modulators. *Sci. Rep.* **2023**, *13*, 18600, doi:10.1038/s41598-023-45376-w.

41. Romano, G.; Riccardi, F.; Bussani, E.; Vodret, S.; Licastro, D.; Ragone, I.; Ronzitti, G.; Morini, E.; Slaugenhaupt, S.A.; Pagani, F. Rescue of a Familial Dysautonomia Mouse Model by AAV9-Exon-Specific U1 snRNA. *Am. J. Hum. Genet.* **2022**, *109*, 1534–1548, doi:10.1016/j.ajhg.2022.07.004.

42. Wachsmuth, H.R.; Weninger, S.N.; Duca, F.A. Role of the Gut–Brain Axis in Energy and Glucose Metabolism. *Exp. Mol. Med.* **2022**, *54*, 377–392, doi:10.1038/s12276-021-00677-w.

43. Savidge, T.C. Epigenetic Regulation of Enteric Neurotransmission by Gut Bacteria. *Front. Cell. Neurosci.* **2016**, *9*, 503, doi:10.3389/fncel.2015.00503.

44. Procaccini, C.; Santopaolo, M.; Faicchia, D.; Colamatteo, A.; Formisano, L.; Candia, P. de; Galgani, M.; Rosa, V.D.; Matarese, G. Role of Metabolism in Neurodegenerative Disorders. *Metab. - Clin. Exp.* **2016**, *65*, 1376–1390, doi:10.1016/j.metabol.2016.05.018.

45. Quigley, E.M.M. Microbiota-Brain-Gut Axis and Neurodegenerative Diseases. *Curr. Neurol. Neurosci. Rep.* **2017**, *17*, 94, doi:10.1007/s11910-017-0802-6.

46. Forssberg, H. Microbiome Programming of Brain Development: Implications for Neurodevelopmental Disorders. *Dev. Med. Child Neurol.* **2019**, *61*, 744–749, doi:10.1111/dmcn.14208.

47. Mirzaei, R.; Bouzari, B.; Hosseini-Fard, S.R.; Mazaheri, M.; Ahmadyousefi, Y.; Abdi, M.; Jalalifar, S.; Karimitabar, Z.; Teimoori, A.; Keyvani, H.; et al. Role of Microbiota-Derived Short-Chain Fatty Acids in Nervous System Disorders. *Biomed. Pharmacother.* **2021**, *139*, 111661, doi:10.1016/j.biopha.2021.111661.

48. Arias, N.; Arboleya, S.; Allison, J.; Kaliszewska, A.; Higarza, S.G.; Gueimonde, M.; Arias, J.L. The Relationship between Choline Bioavailability from Diet, Intestinal Microbiota Composition, and Its Modulation of Human Diseases. *Nutrients* **2020**, *12*, 2340, doi:10.3390/nu12082340.

49. Antonio, N.; Andrea, T.; Claudio, T.; Beatrice, P.; Pamela, C.; Chiara, M.; Gian, L. de' A.; Francesco, D.M.; Tiziana, M. Digestive Disorders and Intestinal Microbiota. *Acta Bio Medica Atenei Parm.* **2018**, *89*, 47–51, doi:10.23750/abm.v89i9-S.7912.

50. Kelly, C.J.; Zheng, L.; Campbell, E.L.; Saeedi, B.; Scholz, C.C.; Bayless, A.J.; Wilson, K.E.; Glove, L.E.; Kominsky, D.J.; Magnuson, A.; et al. Crosstalk between Microbiota-Derived Short-Chain Fatty Acids and Intestinal Epithelial HIF Augments Tissue Barrier Function. *Cell Host Microbe* **2015**, *17*, 662–671, doi:10.1016/j.chom.2015.03.005.

51. Markowiak-Kopeć, P.; Śliżewska, K. The Effect of Probiotics on the Production of Short-Chain Fatty Acids by Human Intestinal Microbiome. *Nutrients* **2020**, *12*, 1107, doi:10.3390/nu12041107.

52. Han, J.; Antunes, L.C.M.; Finlay, B.B.; Borchers, C.H. Metabolomics: Towards Understanding Host–Microbe Interactions. *Future Microbiol.* **2010**, *5*, 153–161, doi:10.2217/fmb.09.132.

53. Oluwatobi, P.E.; Ese, I.G.; Oluwatumininu, P.A.; Eghosa, M. Microbiota Gut-Brain Axis and Neurodegenerative Disease. *Romanian Neurosurg.* **2020**, 110–116.

54. Gwak, M.-G.; Chang, S.-Y. Gut-Brain Connection: Microbiome, Gut Barrier, and Environmental Sensors. *Immune Netw.* **2021**, *21*, e20, doi:10.4110/in.2021.21.e20.

55. Vascellari, S.; Palmas, V.; Melis, M.; Pisanu, S.; Cusano, R.; Uva, P.; Perra, D.; Madau, V.; Sarchioto, M.; Oppo, V.; et al. Gut Microbiota and Metabolome Alterations Associated with Parkinson's Disease. *mSystems* **2020**, *5*, mSystems.00561-20, e00561-20, doi:10.1128/mSystems.00561-20.

56. Konjevod, M.; Nikolac Perkovic, M.; Sáiz, J.; Svob Strac, D.; Barbas, C.; Rojo, D. Metabolomics Analysis of Microbiota-Gut-Brain Axis in Neurodegenerative and Psychiatric Diseases. *J. Pharm. Biomed. Anal.* **2021**, *194*, 113681, doi:10.1016/j.jpba.2020.113681.

57. Muddapu, V.R.; Dharshini, S.A.P.; Chakravarthy, V.S.; Gromiha, M.M. Neurodegenerative Diseases – Is Metabolic Deficiency the Root Cause? *Front. Neurosci.* **2020**, *14*, 213, doi:10.3389/fnins.2020.00213.

58. Chen, C.; Turnbull, D.M.; Reeve, A.K. Mitochondrial Dysfunction in Parkinson's Disease—Cause or Consequence? *Biology* **2019**, *8*, 38, doi:10.3390/biology8020038.

59. Moreira, P.I.; Carvalho, C.; Zhu, X.; Smith, M.A.; Perry, G. Mitochondrial Dysfunction Is a Trigger of Alzheimer's Disease Pathophysiology. *Biochim. Biophys. Acta BBA - Mol. Basis Dis.* **2010**, *1802*, 2–10, doi:10.1016/j.bbadis.2009.10.006.

60. Kojic, M.; Wainwright, B. The Many Faces of Elongator in Neurodevelopment and Disease. *Front. Mol. Neurosci.* **2016**, *9*, doi:10.3389/fnmol.2016.00115.

61. Simpson, C.L.; Lemmens, R.; Miskiewicz, K.; Broom, W.J.; Hansen, V.K.; van Vught, P.W.J.; Landers, J.E.; Sapp, P.; Van Den Bosch, L.; Knight, J.; et al. Variants of the Elongator Protein 3 (ELP3) Gene Are Associated with Motor Neuron Degeneration. *Hum. Mol. Genet.* **2009**, *18*, 472–481, doi:10.1093/hmg/ddn375.

62. Cheney, A.M.; Costello, S.M.; Pinkham, N.V.; Waldum, A.; Broadaway, S.C.; Cotrina-Vidal, M.; Mergy, M.; Tripet, B.; Kominsky, D.J.; Grifka-Walk, H.M.; et al. Gut Microbiome Dysbiosis Drives Metabolic Dysfunction in Familial Dysautonomia. *Nat. Commun.* **2023**, *14*, 218, doi:10.1038/s41467-023-35787-8.

63. Costello, S.M.; Cheney, A.M.; Waldum, A.; Tripet, B.; Cotrina-Vidal, M.; Kaufmann, H.; Norcliffe-Kaufmann, L.; Lefcort, F.; Copié, V. A Comprehensive NMR Analysis of Serum and Fecal Metabolites in Familial Dysautonomia Patients Reveals Significant Metabolic Perturbations. *Metabolites* **2023**, *13*, 433, doi:10.3390/metabo13030433.

64. Bar-Shai, A.; Maayan, C.; Vromen, A.; Udassin, R.; Nissan, A.; Freund, H.R.; Hanani, M. Decreased Density of Ganglia and Neurons in the Myenteric Plexus of Familial Dysautonomia Patients. *J. Neurol. Sci.* **2004**, *220*, 89–94, doi:10.1016/j.jns.2004.02.017.

65. Palma, J.-A.; Roda, R.; Norcliffe-Kaufmann, L.; Kaufmann, H. Increased Frequency of Rhabdomyolysis in Familial Dysautonomia. *Muscle Nerve* **2015**, *52*, 887–890, doi:10.1002/mus.24781.

66. Cotrina, M.L.; Morgenstein, B.; Perez, M.; Norcliffe-Kaufmann, L.; Palma, J.-A.; Kaufmann, H. Height, Weight, and Body Mass Index in Patients with Familial Dysautonomia. *PLOS ONE* **2023**, *18*, e0293800, doi:10.1371/journal.pone.0293800.

67. Ueki, Y.; Shchepetkina, V.; Lefcort, F. Retina-Specific Loss of Ikbkap/Elp1 Causes Mitochondrial Dysfunction That Leads to Selective Retinal Ganglion Cell Degeneration in a Mouse Model of Familial Dysautonomia. *Dis. Model. Mech.* **2018**, *11*, doi:10.1242/dmm.033746.

68. Mendoza-Santiesteban, C.E.; Palma, J.-A.; Hedges, T.R.; Laver, N.V.; Farhat, N.; Norcliffe-Kaufmann, L.; Kaufmann, H. Pathological Confirmation of Optic Neuropathy in Familial Dysautonomia. *J. Neuropathol. Exp. Neurol.* **2017**, *76*, 238–244, doi:10.1093/jnen/nlw118.

69. Mendoza-Santiesteban, C.E.; Hedges, T.R.; Norcliffe-Kaufmann, L.; Warren, F.; Reddy, S.; Axelrod, F.B.; Kaufmann, H. Clinical Neuro-Ophthalmic Findings in Familial Dysautonomia. *J. Neuro-Ophthalmol. Off. J. North Am. Neuro-Ophthalmol. Soc.* **2012**, *32*, 23–26, doi:10.1097/WNO.0b013e318230feab.

70. Mendoza-Santiesteban, C.E.; Hedges III, T.R.; Norcliffe-Kaufmann, L.; Axelrod, F.; Kaufmann, H. Selective Retinal Ganglion Cell Loss in Familial Dysautonomia. *J. Neurol.* **2014**, *261*, 702–709, doi:10.1007/s00415-014-7258-2.

71. Abashidze, A.; Gold, V.; Anavi, Y.; Greenspan, H.; Weil, M. Involvement of IKAP in Peripheral Target Innervation and in Specific JNK and NGF Signaling in Developing PNS Neurons. *PLoS ONE* **2014**, *9*, e113428, doi:10.1371/journal.pone.0113428.

72. Hunnicutt, B.J.; Chaverra, M.; George, L.; Lefcort, F. IKAP/Elp1 Is Required In Vivo for Neurogenesis and Neuronal Survival, but Not for Neural Crest Migration. *PLoS ONE* **2012**, *7*, e32050, doi:10.1371/journal.pone.0032050.

73. Cheng, W.W.-C.; Tang, C.S.-M.; Gui, H.-S.; So, M.-T.; Lui, V.C.-H.; Tam, P.K.-H.; Garcia-Barcelo, M.-M. Depletion of the IKBKAP Ortholog in Zebrafish Leads to Hirschsprung Disease-like Phenotype. *World J. Gastroenterol. WJG* **2015**, *21*, 2040–2046, doi:10.3748/wjg.v21.i7.2040.

74. Singh, N.; Lorbeck, M.T.; Zervos, A.; Zimmerman, J.; Elefant, F. The Histone Acetyltransferase Elp3 Plays in Active Role in the Control of Synaptic Bouton Expansion and Sleep in Drosophila. *J. Neurochem.* **2010**, *115*, 493–504, doi:10.1111/j.1471-4159.2010.06892.x.

75. Hims, M.M.; Ibrahim, E.C.; Leyne, M.; Mull, J.; Liu, L.; Lazaro, C.; Shetty, R.S.; Gill, S.; Gusella, J.F.; Reed, R.; et al. Therapeutic Potential and Mechanism of Kinetin as a Treatment for the Human Splicing Disease Familial Dysautonomia. *J. Mol. Med. Berl. Ger.* **2007**, *85*, 149–161, doi:10.1007/s00109-006-0137-2.

76. Hims, M.M.; Shetty, R.S.; Pickel, J.; Mull, J.; Leyne, M.; Liu, L.; Gusella, J.F.; Slaugenhaupt, S.A. A Humanized IKBKAP Transgenic Mouse Models a Tissue Specific Human Splicing Defect. *Genomics* **2007**, *90*, 389–396, doi:10.1016/j.ygeno.2007.05.012.

77. Chen, Y.-T.; Hims, M.M.; Shetty, R.S.; Mull, J.; Liu, L.; Leyne, M.; Slaugenhaupt, S.A. Loss of Mouse Ikbkap, a Subunit of Elongator, Leads to Transcriptional Deficits and Embryonic Lethality That Can Be Rescued by Human IKBKAP. *Mol. Cell. Biol.* **2009**, *29*, 736–744, doi:10.1128/MCB.01313-08.

78. Dietrich, P.; Yue, J.; E., S.; Dragatsis, I. Deletion of Exon 20 of the Familial Dysautonomia Gene Ikbkap in Mice Causes Developmental Delay, Cardiovascular Defects, and Early Embryonic Lethality. *PLoS ONE* **2011**, *6*, e27015, doi:10.1371/journal.pone.0027015.

79. Morini, E.; Dietrich, P.; Salani, M.; Downs, H.M.; Wojtkiewicz, G.R.; Alli, S.; Brenner, A.; Nilbratt, M.; LeClair, J.W.; Oaklander, A.L.; et al. Sensory and Autonomic Deficits in a New Humanized Mouse Model of Familial Dysautonomia. *Hum. Mol. Genet.* **2016**, *25*, 1116–1128, doi:10.1093/hmg/ddv634.

80. George, L.; Chaverra, M.; Wolfe, L.; Thorne, J.; Close-Davis, M.; Eibs, A.; Riojas, V.; Grindeland, A.; Orr, M.; Carlson, G.A.; et al. Familial Dysautonomia Model Reveals Ikbkap Deletion Causes Apoptosis of Pax3+ Progenitors and Peripheral Neurons. *Proc. Natl. Acad. Sci.* **2013**, *110*, 18698–18703, doi:10.1073/pnas.1308596110.

81. Jackson, M.Z.; Gruner, K.A.; Qin, C.; Tourtellotte, W.G. A Neuron Autonomous Role for the Familial Dysautonomia Gene ELP1 in Sympathetic and Sensory Target Tissue Innervation. *Development* **2014**, *141*, 2452–2461, doi:10.1242/dev.107797.

82. Ueki, Y.; Ramirez, G.; Salcedo, E.; Stabio, M.E.; Lefcort, F. Loss of Ikbkap Causes Slow, Progressive Retinal Degeneration in a Mouse Model of Familial Dysautonomia. *eNeuro* **2016**, *3*, doi:10.1523/ENEURO.0143-16.2016.

83. Kirches, E. LHON: Mitochondrial Mutations and More. *Curr. Genomics* **2011**, *12*, 44–54, doi:10.2174/138920211794520150.

84. Sadun, A.A.; Morgia, C.L.; Carelli, V. Leber's Hereditary Optic Neuropathy. *Curr. Treat. Options Neurol.* **2011**, *13*, 109–117, doi:10.1007/s11940-010-0100-y.

85. Zanna, C.; Ghelli, A.; Porcelli, A.M.; Karbowski, M.; Youle, R.J.; Schimpf, S.; Wissinger, B.; Pinti, M.; Cossarizza, A.; Vidoni, S.; et al. OPA1 Mutations Associated with Dominant Optic Atrophy Impair Oxidative Phosphorylation and Mitochondrial Fusion. *Brain* **2008**, *131*, 352–367, doi:10.1093/brain/awm335.

86. Wu, J.; An, Y.; Yao, J.; Wang, Y.; Tang, H. An Optimised Sample Preparation Method for NMR-Based Faecal Metabonomic Analysis. *The Analyst* **2010**, *135*, 1023–1030, doi:10.1039/b927543f.

87. Deda, O.; Gika, H.G.; Wilson, I.D.; Theodoridis, G.A. An Overview of Fecal Sample Preparation for Global Metabolic Profiling. *J. Pharm. Biomed. Anal.* **2015**, *113*, 137–150, doi:10.1016/j.jpba.2015.02.006.

88. Midelfart, A.; Dybdahl, A.; Gribbestad, I.S. Detection of Different Metabolites in the Rabbit Lens by High Resolution ^{1}H NMR Spectroscopy. *Curr. Eye Res.* **1996**, *15*, 1175–1181, doi:10.3109/02713689608995153.

89. Santiago, A.R.; Garrido, M.J.; Cristóvão, A.J.; Duarte, J.M.N.; Carvalho, R.A.; Ambrósio, A.F. Evaluation of the Impact of Diabetes on Retinal Metabolites by NMR Spectroscopy. *Curr. Eye Res.* **2010**, *35*, 992–1001, doi:10.3109/02713683.2010.500113.

90. Han, T. (Kevin); Everett, R.S.; Proctor, W.R.; Ng, C.M.; Costales, C.L.; Brouwer, K.L.R.; Thakker, D.R. Organic Cation Transporter 1 (OCT1/mOct1) Is Localized in the Apical Membrane of Caco-2 Cell Monolayers and Enterocytes. *Mol. Pharmacol.* **2013**, *84*, 182–189, doi:10.1124/mol.112.084517.

CHAPTER TWO

GUT MICROBIOME DYSBIOSIS DRIVES METABOLIC DYSFUNCTION IN FAMILIAL DYSAUTONOMIA

Contribution of Authors and Co-Authors

Manuscript in Chapter 2

Author: Alexandra M. Cheney

Contributions: A.M.C., S.M.C., and N.V.P. contributed equally to this work, including acquisition, analysis and interpretation of data and drafting of this manuscript.

Co-First Author: Stephanann M. Costello

Contributions: A.M.C., S.M.C., and N.V.P. contributed equally to this work, including acquisition, analysis and interpretation of data and drafting of this manuscript.

Co-First Author: Nicholas V. Pinkham

Contributions: A.M.C., S.M.C., and N.V.P. contributed equally to this work, including acquisition, analysis and interpretation of data and drafting of this manuscript. N.V.P. generated new software used to analyze results.

Co-Author: Annie Waldum

Contributions: Data acquisition (sample preparation and metabolite profiling using NMR).

Co-Author: Susan C. Broadaway

Contributions: Sample and data acquisition, including obtaining samples from FD patients and their relatives.

Co-Author: Maria Cotrina-Vidal

Contributions: Sample and data acquisition, including obtaining samples from FD patients and their relatives.

Co-Author: Marc Mergy

Contributions: Involved in experimental design, data acquisition, and drafting of this manuscript.

Co-Author: Brian Tripet

Contributions: Data acquisition and analysis and drafting of this manuscript.

Co-Author: Douglas J. Kominsky

Contributions: Involved in experimental design, data acquisition, and drafting of this manuscript.

Co-Author: Heather. M. Grifka-Walk

Contributions: Involved in experimental design, data acquisition, and drafting of this manuscript.

Co-Author: Horacio Kaufmann

Contributions: Contributed to all clinical aspects of the study, including data acquisition and interpretation of results, and drafting of this manuscript.

Co-Author: Lucy Norcliffe-Kaufmann

Contributions: Contributed to all clinical aspects of the study, including data acquisition and interpretation of results, and drafting of this manuscript.

Co-Author: Jesse T. Peach

Contributions: Data acquisition and analysis and drafting of this manuscript.

Co-Author: Brian Bothner

Contributions: Data acquisition and analysis and drafting of this manuscript.

Co-Author: Frances Lefcort

Contributions: F.L., V.C., and S.T.W. contributed to all aspects of the study and led the team's efforts in overall conception of the project, data analysis and interpretation, and drafting of this manuscript.

Co-Author: Valérie Copié

Contributions: F.L., V.C., and S.T.W. contributed to all aspects of the study and led the team's efforts in overall conception of the project, data analysis and interpretation, and drafting of this manuscript.

Co-Author: Seth T. Walk

Contributions: F.L., V.C., and S.T.W. contributed to all aspects of the study and led the team's efforts in overall conception of the project, data analysis and interpretation, and drafting of this manuscript.

Manuscript Information

Alexandra M. Cheney, Stephanann M. Costello, Nicholas V. Pinkham, Annie Waldum, Susan C. Broadaway, Maria Cotrina-Vidal, Marc Mergy, Brian Tripet, Douglas J. Kominsky, Heather M. Grifka-Walk, Horacio Kaufmann, Lucy Norcliffe-Kaufmann, Jesse T. Peach, Brian Bothner, Frances Lefcort, Valérie Copié, and Seth T. Walk

Nature Communications

Status of Manuscript:

☐ Prepared for submission to a peer-reviewed journal

☐ Officially submitted to a peer-reviewed journal

☐ Accepted by a peer-reviewed journal

☒ Published in a peer-reviewed journal

Nature Portfolio

Manuscript published January 13th, 2023

Issue 14, January 2023

doi: https://doi.org/10.1038%2Fs41467-023-35787-8

nature communications

Article

https://doi.org/10.1038/s41467-023-35787-8

Gut microbiome dysbiosis drives metabolic dysfunction in Familial dysautonomia

Received: 13 June 2022

Accepted: 18 December 2022

Published online: 13 January 2023

Check for updates

Alexandra M. Cheney[1,4], Stephanann M. Costello[1,4], Nicholas V. Pinkham[2,4], Annie Waldum[1], Susan C. Broadaway[2], Maria Cotrina-Vidal[3], Marc Mergy[2], Brian Tripet[1], Douglas J. Kominsky[2], Heather M. Grifka-Walk[2], Horacio Kaufmann[3], Lucy Norcliffe-Kaufmann[3], Jesse T. Peach[1], Brian Bothner[1], Frances Lefcort[2] ✉, Valérie Copié[1] ✉ & Seth T. Walk[2] ✉

Familial dysautonomia (FD) is a rare genetic neurologic disorder caused by impaired neuronal development and progressive degeneration of both the peripheral and central nervous systems. FD is monogenic, with >99.4% of patients sharing an identical point mutation in the elongator acetyltransferase complex subunit 1 (*ELP1*) gene, providing a relatively simple genetic background in which to identify modifiable factors that influence pathology. Gastrointestinal symptoms and metabolic deficits are common among FD patients, which supports the hypothesis that the gut microbiome and metabolome are altered and dysfunctional compared to healthy individuals. Here we show significant differences in gut microbiome composition (16 S rRNA gene sequencing of stool samples) and NMR-based stool and serum metabolomes between a cohort of FD patients (~14% of patients worldwide) and their cohabitating, healthy relatives. We show that key observations in human subjects are recapitulated in a neuron-specific *Elp1*-deficient mouse model, and that cohousing mutant and littermate control mice ameliorates gut microbiome dysbiosis, improves deficits in gut transit, and reduces disease severity. Our results provide evidence that neurologic deficits in FD alter the structure and function of the gut microbiome, which shifts overall host metabolism to perpetuate further neurodegeneration.

From 1791 to 1917, Jews living in the Russian Empire were forced to live inside the prescribed Pale of Settlement, a region spanning present day Ukraine, Poland, Slovakia, Hungary, Republic of Moldova, and Romania. This oppression created generations of endogamy within the region and a genetic bottleneck that enriched a deleterious allele of the *ELP1* gene such that today, between 1 in 18 to 1 in 27 Ashkenazi Jews carry the original *ELP1* founder mutation (c2204 + 6 T > C)[1–3]. The allele is highly penetrant and results in impaired splicing of *ELP1* (formerly called *IKBKAP*[4,5]), leading to a devastating neurologic disease first described in 1949[6] and now called Familial dysautonomia (FD). FD patients are homozygous for the mutant allele and have tissue-specific reductions in Elp1 protein, primarily in the nervous system[7,8]. Elp1 is a key scaffolding subunit of the six-protein Elongator complex and is required for codon-biased mRNA translation with additional reports of a role in transcript elongation[9–13]. FD symptoms result largely from dysfunctional neuronal development and neurodegeneration of sensory and autonomic neurons in the peripheral nervous system, leading to widespread deficits in organ innervation[3]. FD patients have reduced body mass index (BMI), high metabolic rate, and low fat content indicative of metabolic deficits[14]. In addition, patients have severe

[1]Department of Chemistry and Biochemistry, Montana State University, Bozeman, MT, USA. [2]Department of Microbiology and Cell Biology, Montana State University, Bozeman, MT, USA. [3]Department of Neurology, New York University School of Medicine, New York, NY, USA. [4]These authors contributed equally: Alexandra M. Cheney, Stephanann M. Costello, Nicholas V. Pinkham. ✉e-mail: lefcort@montana.edu; vcopie@montana.edu; seth.walk@montana.edu

cardiovascular, respiratory, and gastrointestinal (GI) dysfunction due to innervation deficits[3,15,16]. GI complaints are frequently reported by FD patients and these symptoms significantly impact their quality of life[17]. Similarly, patients with other neurological disorders, such as autism spectrum disorder (ASD), also suffer from debilitating GI symptoms and share hallmark neurological impairments with FD[18–20]. The ultimate therapeutic goal for FD is to develop strategies to increase levels of Elp1 (protein) in the affected cell populations and tissues, but no such treatments are clinically available. Since the peripheral nervous system senses and responds to both the gut microbiome and liver – and in response to these signals regulates digestion and metabolism, we sought to answer the basic question: Is the gut-metabolism axis involved in FD pathology?

To address this question, we recruited FD patients and healthy, cohabitating relatives to help control for lifestyle factors known to influence comparisons[21], such as environment (cohabitants share a built environment), diet (cohabitants are more likely to eat the same food), and genetics (parents carry one copy of the deleterious *ELP1* allele and siblings have a 50% chance of carrying the mutant allele). In total, 49 patients and 54 relatives provided at least one sample for microbiome ($n = 51$ patient-relative combinations) or metabolome analyses (n = 58 patient-relative combinations for stool; n = 50 patient-relative combinations for serum; Supplementary Table 1a, b in Supplementary Data 1). Given an estimated 350 FD patients worldwide, this sampling effort represents ~14% of all known FD patients and a sample size comparable to those reported in previous gut microbiome studies of autism spectrum disorder (ASD), Alzheimer's disease, and Parkinson's disease[22–25]. Here, we present evidence that the gut-metabolism axis is an important factor in FD progression and can be at least partially reversed by microbiome homogenization via co-housing in a mouse model of the disease.

Results

Altered gut-metabolism axis in FD

Gut microbiome diversity was quantified from stool samples using Illumina sequencing of the bacterial 16 S rRNA encoding gene (V4 region) and polar metabolites (serum and stool) were identified and quantified using ^{1}H NMR-based metabolomics. Results from such '-omics' technologies are typically considered with respect to diversity, meaning the presence-absence and relative abundance of observations (taxa for microbiome sequencing and metabolites for metabolomics). Both within the sample (alpha-) and between group (beta-) diversity estimates are important. All microbiome and metabolome samples were plotted using ordination to visually compare groups (Fig. 1a, e, f). Statistical tests were then performed to evaluate the significance and identify key bacterial operational taxonomic units (OTUs; ≥97% 16 S rRNA gene sequence identity) or specific metabolites that explained observed differences between FD patients and relatives. Clear groupwise differences were apparent in all ordinations, which were supported by PERMANOVA testing. FD patient microbiomes were more variable (greater dispersion, Fig. 1b; distance to group centroid, Supplementary Fig. 1b) and represented only a subset of species found in paired relatives (i.e., FD patients shared more OTUs with relatives than their relatives shared with them, and FD patients had an average of 45 fewer bacterial taxa compared to paired relatives; Fig. 1d). Alpha-diversity was also lower in FD patient microbiomes compared to paired relatives (Fig. 1a inset and Supplementary Fig. 1a, c). We observed a positive trend between alpha diversity of FD patients and their relatives (size of connected dots in Fig. 1a), and while intriguing, this did not reach statistical significance (linear mixed effects model, Chi-square = 3.110, df = 1, $p = 0.078$). Partition around medoids (PAM) clustering of OTU-based diversity suggested that microbiomes from all subjects (i.e., patients and relatives) represented two distinct community types, or enterotypes (Supplementary Fig. 2a) with FD patients significantly associated with cluster 1 and relatives with cluster 2 (Fisher's exact test, Odds ratio = 9.388, 95% confidence interval of odds ratio = 2.444 to 54.000); Supplementary Fig. 2b). The cluster 1 enterotype exhibited significantly lower alpha diversity compared to cluster 2 (inverse-Simpson's index, t-test, t-statistic = −7.028, df = 67.78, $p < 0.0001$, mean difference between patients and relatives = −7.884, 95% confidence interval of the difference between patients and relatives = −10.123 to −5.646). Also, the abundance of seven OTUs

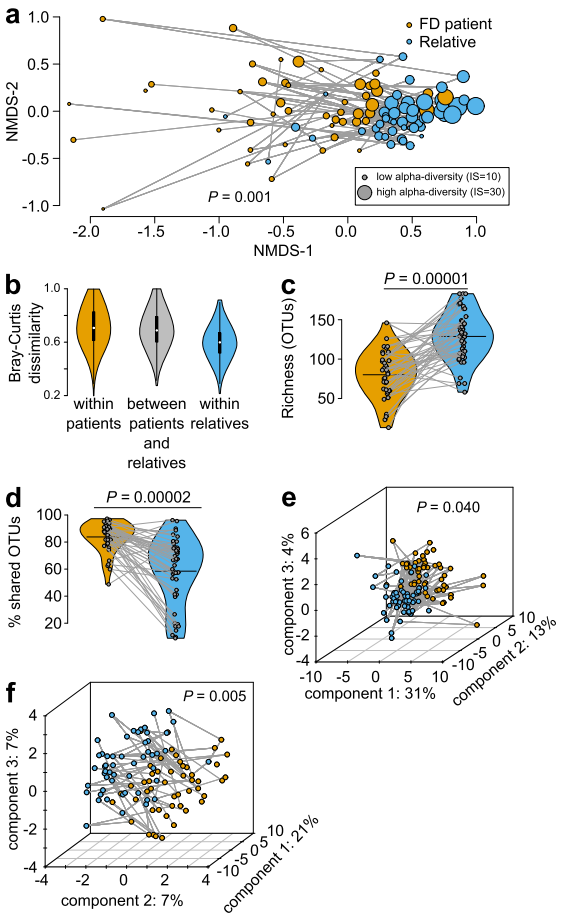


Fig. 1 | FD alters the microbiome and metabolome. a Non-metric multi-dimensional scaling (NMDS) of 16 S rRNA-based stool microbiome diversity in FD patients and healthy relatives (all patient-relative pairs connected with lines). IS, inverse-Simpson's index. **b**, Microbiome beta-diversity (Bray-Curtis dissimilarity) within and between FD patients and paired relatives (each violin plot contains a box and whisker plot here a white dot = median, box = interquartile range (IQR), whiskers = 1.5 times IQR). **c**, **d**, Microbiome richness (**c**) and percentage (%) of shared operational taxonomic units (OTUs) (**d**) between FD patient and healthy relatives (colors as in **a**; bars = mean; lines connect patients and relatives). **e**, **f** Partial least-squares discriminant analysis (PLSDA) of ^{1}H-NMR-based stool (**e**) and serum (**f**) metabolome diversity in FD patients and healthy relatives (colors as in **a**, **b**). n = **a**, **b**, 48 patients, 51 relatives; **c**, **d**, 38 patients, 47 relatives, 47 pairs; **e**, 54 patient, 58 relatives; **f**, 49 patients, 53 relatives. PERMANOVA of Bray-Curtis dissimilarity (**a**, F = 6.847, df = 1, $R^2 = 0.066$) or Euclidean distance (**e**, F = 2.153, df = 1, $R^2 = 0.0191$; **f**, F = 2.506, df = 1, $R^2 = 0.0245$); permutational paired t-testing, two-sided (**c**, mean t-statistic = −5.423, df = 29, mean difference between group means = −45.114, mean 95% confidence interval of the difference between the group means = −62.130 to −28.100; **d**, mean t-statistic = 5.220, df = 29, mean difference between group means = 24.944, mean 95% confidence interval of the difference between the group means = 15.16 to 34.73).

 https://doi.org/10.1038/s41467-023-35787-8

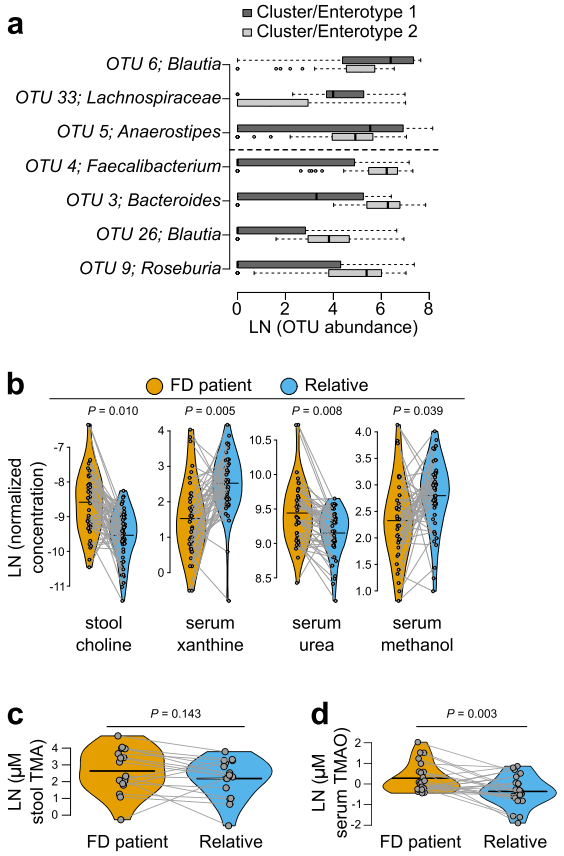


Fig. 2 | Microbiome OTU and metabolite differences in FD. a OTUs responsible for observed partition around medoids (PAM) clusters/enterotypes identified by random forest analysis. OTUs defining cluster/enterotype 1 are shown above the dotted line. OTUs defining cluster/enterotype 2 are shown below the dotted line (centrality line = median, boxes = IQR, whiskers = 1.5 times IQR, dots beyond whiskers = outliers). **b** Metabolites showing significantly different abundances in FD patients compared to relatives (line = mean). **c** Targeted analyses of TMA in stool (line = mean). **d** Targeted analysis of TMAO in serum (line = mean). n = **a**, 48 patients, 51 relatives; **b**, stool, 54 patient, 58 relatives; serum, 49 patients, 53 relatives; **c**, **d**, 24 patient-relative pairs. Random forest analysis (**a**); Natural log (LN) transformed metabolite concentration, permutational paired t-testing (two-sided) with FDR correction (**b**, choline, mean t-statistic = 0.1485, df = 33, mean difference between patient-relative pairs = 0.9860, mean 95% confidence interval of difference between patient-relative pairs = 0.5281 to 1.4440; xanthine, mean t-statistic = 2.9527, df = 33, mean difference between patient-relative pairs = −0.9591, mean 95% confidence interval of difference between patient-relative pairs = −1.4051 to −0.5130; urea, mean t-statistic = 0.9269, df = 33, mean difference between patient-relative pairs = 0.7281, mean 95% confidence interval of difference between patient-relative pairs = 0.3527 to 1.1036; methanol, mean t-statistic = −1.5497, df = 33, mean difference between patient-relative pairs = −0.7295, mean 95% confidence interval of difference between patient-relative pairs = −1.1875 to −0.2716); Paired t-testing, two-sided) (**c**, TMA, t-statistic = 1.5423, df = 16, difference between patient-relative pairs = 0.4499, 95% confidence interval of difference between patient-relative pairs = −0.1685 to 1.0682; **d**, TMAO, t-statistic = 3.3197, df = 23, difference between patient-relative pairs = 0.6418, 95% confidence interval of difference between patient-relative pairs = 0.2419 to 1.0417).

identified by random forest analysis and typically associated with human health were altered, four of which were less abundant in cluster 1 (Fig. 2a and Supplementary Fig. 3) and among FD patients in general, including *Faecalibacterium*[26] (OTU 4; permutational paired t-test, mean t-statistic = −2.247, df = 29, mean $p = 0.0360$, mean difference between patient-relative pairs = −220.51, mean 95% confidence interval of the difference between patient-relative pairs = −421.102 to −19.918) and *Roseburia*[27] (OTU 9; permutational paired t-test, mean t-statistic = −2.093, df = 29, mean p = 0.0496, mean difference between patient-relative pairs = −173.801, mean 95% confidence interval of the difference between patient-relative pairs = −343.562 to −4.040). Overall, these results suggest that many FD patients lacked common "healthy" microbiome members.

All relatives of FD patients that participated in this study as matched controls were known to carry one copy of the *ELP1* founder mutation (previously screened at the Dysautonomia Center, NYU Langone Health) and even though carriers are asymptomatic with respect to typical FD symptoms[3], there is a possibility that the founder allele is penetrant at the level of microbiome diversity. If true, microbiomes of FD relatives would be different from those of other healthy adults. To test this hypothesis, we evaluated 16 S rRNA sequencing data from healthy subjects of two previously published studies[28,29]. Subjects from the first study[28] ($n = 172$) were part of a large, multicenter, cross-sectional design and subjects from the second study[29] ($n = 8$) were sampled longitudinally for an average of 512 days (average of 49 samples per subject), thereby allowing us to consider both between- and within-subject microbiome diversity. When raw reads from these studies were combined and compared to FD relatives (Supplementary Fig. 4,a, c) and FD patients (Supplementary Fig. 4,b, c), beta-diversity (Bray-Curtis dissimilarity) was significantly different. However, when analyzed separately and compared, the microbiome diversity between all cohorts was significantly different (Supplementary Fig. 4,d) and based on the distance to group centroids (the weighted average microbiome diversity of each group, Supplementary Fig. 4,e), differences were greater between healthy individuals and FD patients compared to FD relatives, regardless of study. Collectively, these results provide little evidence that the gut microbiome diversity of FD relatives is significantly different from that of healthy subjects in other studies, where the frequency of the *ELP1* founder mutation is presumably low. Moreover, based on the observed distances to group centroids, the microbiome of FD patients is the most different of all cohorts analyzed, supporting a significant deviation from the microbiome diversity typically observed in healthy subjects.

Similar to microbiome diversity, metabolite levels were consistently different between patients and relatives (Fig. 1e, f). Of the 55 polar serum metabolites identified, FD patients had significantly lower levels of xanthine and methanol, and elevated levels of urea (Fig. 2b, Supplementary Fig. 5,a). Of the 73 polar stool metabolites identified, the only significant difference was an elevated level of choline in FD patients (Fig. 2b, Supplementary Fig. 5,b). Among FD patients, increased choline levels in stool were significantly correlated with lower microbiome alpha diversity, decreased richness, and fewer shared OTUs among patient-relative pairs (Supplementary Table 2 in Supplementary Data 1). Dietary choline is a precursor for microbiome-driven production of trimethylamine[30], which can be converted in the liver to the well-known risk factor for cardiovascular[31] and renal[32,33] disease, trimethylamine N-oxide (TMAO). To investigate whether elevated choline correlated with increased TMAO levels, we used a targeted liquid-chromatography mass-spectrometry (LCMS) method on a sub-set of patient-relative pairs ($n = 24$) and found that serum TMAO levels were indeed significantly elevated in FD patients (Fig. 2d), while TMA in stool trended in the same direction but did not reach statistical significance (Fig. 2c).

Patient factors associated with dysbiosis

Important factors specific to FD and/or FD treatment likely contributed to differences in microbiome and metabolome diversity between FD patients and relatives and especially to the heterogeneity observed among FD patient samples. As might be expected of a

progressive neurodegenerative disease, patient age was statistically associated with several microbiome attributes (Supplementary Table 2 in Supplementary Data 1). In fact, of all factors evaluated in univariate analyses, patient age was the strongest correlate of microbiome diversity. Positive relationships were observed between both age and overall FD patient microbiome variability (dispersion) and similarity to the microbiome of relatives (beta-diversity between patient-relative pairs). A negative relationship was observed between age and the number of OTUs shared with relatives.

As FD progresses, most patients become unable to ingest food orally due to problems swallowing and a gastrostomy tube (G-tube) is placed as standard of care therapy. This procedure did have a significant effect (Supplementary Table 2 in Supplementary Data 1) on the level of choline in stool as FD patients with a G-tube ($n = 42$) had ~2-fold increased levels of choline compared to patients without a G-tube ($n = 8$), although the sample size of the latter group was low. Most FD patients continue to eat food orally for some time even after having a G-tube in place. As the inability to eat progresses, patients use a G-tube exclusively, and this factor (exclusive use of a G-tube) had a significant impact on gut microbiome diversity. Patients who used a G-tube exclusively had less diverse microbiomes compared to those able to consume food orally, shared fewer OTUs with relatives, and were 4.8 times as likely to have an FD-associated cluster 1 microbiome enterotype (Supplementary Table 2 in Supplementary Data 1). Given the progressive nature of FD, however, patient age and exclusive use of a G-tube are covariates and their independent effects are difficult to disentangle.

Antibiotic history also impacted microbiome diversity as patients taking antibiotics within three months prior to sampling were 4.4 times more likely to host an FD-associated cluster 1 microbiome compared to patients that were not treated with antibiotics (Supplementary Table 2 in Supplementary Data 1). Fundoplication, a gastric surgery to decrease acid reflux, was significantly associated with stool choline (Supplementary Table 2 in Supplementary Data 1). Sex, weight, and body mass index (BMI) were also evaluated as a potentially important factor but did not reach statistical significance for either microbiome or metabolome diversity. Finally, results from a clinical chemistry panel were available for some patients and levels of several analytes were associated with microbiome diversity (Supplementary Table 2 in Supplementary Data 1), including creatinine (positively correlated with beta diversity between patient-relative pairs; negatively correlated with the proportion of shared OTUs between patient-relative pairs); estimated glomerular filtration rate (positively correlated with richness; the number of OTUs shared with relatives; and the number of unique OTUs); and alanine aminotransferase (positively correlated with the proportion of shared OTUs between patient-relative pairs). As expected, blood urea nitrogen (BUN) was significantly associated with serum urea, serving as a type of internal control for NMR-based metabolomics results (Fig. 2b). Aspartate aminotransferase and alkaline phosphatase were also evaluated but not significantly associated. Collectively, these results suggest that both the progressive neurodegenerative effects of FD and the clinical history of patients are important determinants of gut-metabolism axis function.

Neuronal Elp1 controls gut-metabolism axis

To more directly address the impact of Elp1-driven neurodegeneration on the gut-metabolism axis, we leveraged a previously described murine model of FD where *Elp1* is specifically ablated in approximately half of peripheral neurons (including enteric neurons) and in the vast majority of neurons of the central nervous system (*Tuba1a-cre*$^{+}$*;Elp1*$^{loxp/loxp}$ hereafter referred to as FD mice[34,35]). Compared to littermate controls (*Tuba1a-cre*$^{-}$*;Elp1*$^{+/loxp}$), we found that the microbiome diversity of FD mice began diverging within 14 days post-weaning (DPW) when housed separately according to genotype (i.e., separately from control littermates; Fig. 3a, b). Similar to FD patients, the microbiome of FD mice became more variable (greater dispersion) compared to controls by 54 DPW (Fig. 3c) and stool metabolite diversity, represented by 68 metabolites, was significantly divergent by 162 DPW (Fig. 3d). Collectively, results from these mice indicate that reduction of neuronal-Elp1 disrupts gut-metabolism homeostasis.

To address whether mutant *Elp1*-driven dysfunction can be rescued by controlling or restraining microbiome divergence, we compared FD mice in our colony that were reared in the presence or absence of littermate controls for different amounts of time (several cages per time point). This approach takes advantage of natural rodent coprophagy among cohoused animals known to homogenize microbiome diversity and recently shown to support normal metabolic functions, neurochemical homeostasis, and cognitive function[36]. These experiments were carried out for up to 329 days post-weaning so that signs of disease, if present, could be observed and quantified (early signs of disease in FD mice are typically observable around 3 months of age (~71 DPW). Similar to previous results (Fig. 3), the stool microbiome and metabolome of separately housed FD and control mice diverged in a statistically significant manner. In contrast, no differences were observed among cohoused mice at the same time point (79 DPW; Fig. 4a, b). Differences in microbiome diversity progressively increased over the next 200 days (increasing F-statistic) regardless of housing conditions but were far greater when the FD mice were housed separately from littermate controls (Fig. 4a). This divergence, even when cohoused, is noteworthy because it likely reflects the strength of the neuronal *Elp1* genetic deletion on the gut ecosystem. Differences in stool metabolite patterns between cohoused FD and control mice also increased with time, but never reached statistical significance throughout the experiment (Fig. 4b). Thus, it appears that cohousing did have a significant impact on the gut-metabolism axis in this murine model. Because FD mice, like FD patients, vary in their clinical phenotype[34,35], we developed a pathology scoring metric to quantify hallmark signs of the disease, such as abnormal/unhealthy body condition, hind limb clasping, and kyphosis (Supplementary Table 3) with sicker mice receiving higher numerical scores. Interestingly, cohousing significantly lowered pathology scores observed among FD mice (Fig. 4c; Supplementary Fig. 6). Moreover, cohousing ameliorated a deficit in FD mouse gut function : we found that gut transit time was significantly slower in separately housed FD mice compared to controls, but was significantly increased when FD and control mice were cohoused (Fig. 4d; Supplementary Fig. 7). Age (DPW) did not appear to contribute significantly to this effect (mouse age was not a significant factor when included in the analysis). Several metabolite level differences were observed between separately housed and cohoused FD mice that could account for differences in disease and gut pathology (Supplementary Fig. 8), including the observation that separately housed FD mice had elevated choline levels at the final time point (Day 279 DPW) compared to the same mice that were cohoused with control mice (Supplementary Fig. 8,a). We also observed elevated levels of the microbiome-derived choline metabolite, methylamine, at both 179 and 279 DPW (Supplementary Fig. 8,a), further supporting altered choline metabolism when FD mice were housed separately from controls. Since stool choline and TMAO were increased in human FD patients (Fig. 2b), this result suggests that despite the marked differences in diet and gut microbiome diversity between lab mice and humans, the impact of neuronal *Elp1* deletion on microbial choline metabolism may be conserved. Together, these results add experimental evidence that at least some of the neuronal *Elp1*-driven pathology and perturbation of the gut ecosystem in FD mice is modifiable by controlling microbiome-metabolome divergence.

Discussion

Currently, the only treatment for FD is palliative care (pain and symptom management), and until therapies can be developed that

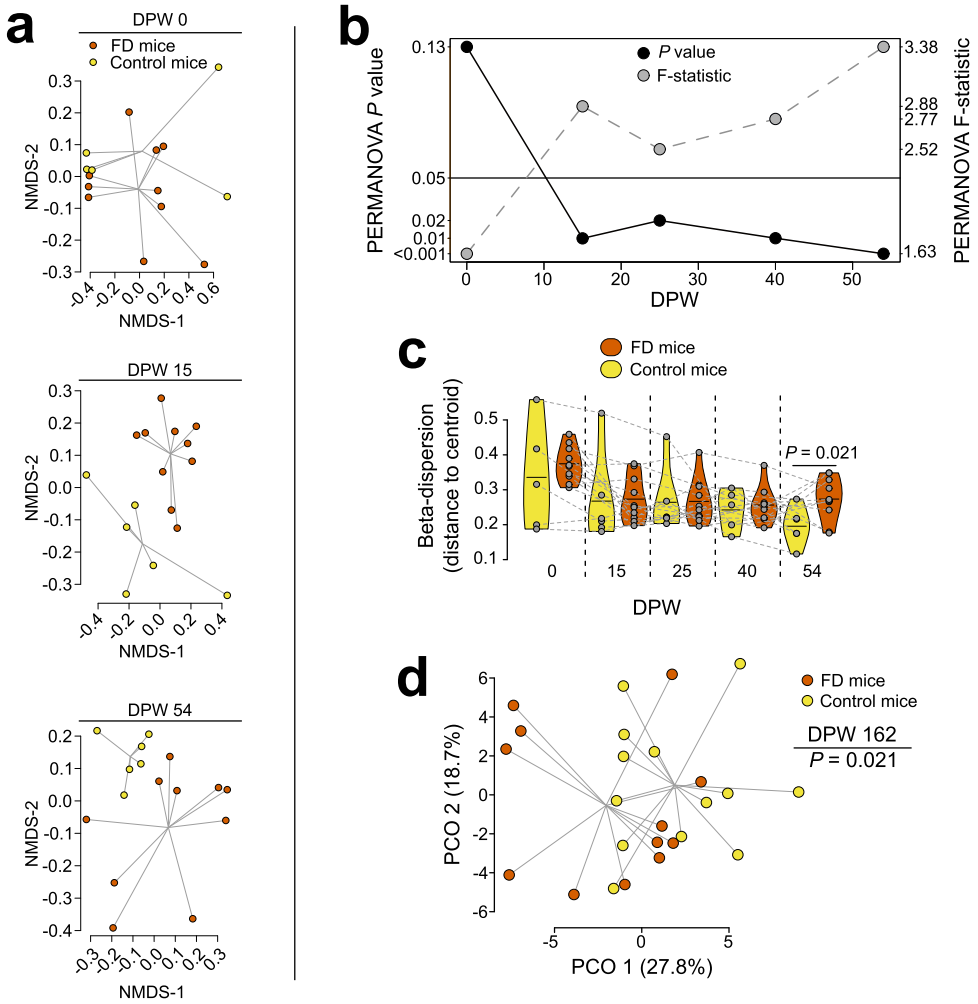


Fig. 3 | Neuron-specific Elp1 deletion drives progressive microbiome and metabolome divergence in mice. a Nonmetric multidimensional scaling (NMDS) of 16 S rRNA-based stool microbiome diversity of FD (*Tuba1a-cre*$^{+}$*; Elp1*$^{loxp/loxp}$) and control (*Tuba1a-cre*$^{-}$*; Elp1*$^{+/loxp}$) mice when housed separately by genotype (group colors same for all panels; DPW = days postweaning). **b** Progressive groupwise differences in microbiome beta-diversity (Bray-Curtis dissimilarity) and (**c**) dispersion of beta-diversity (beta-dispersion) in FD mice (dotted lines connect individual mice, solid line in violin plots = mean). **d** Principal coordinates analysis of stool metabolome in mice at 162 DPW. n = **a**, **b**, **c** 10 FD mice (4 female, 6 male; 3 cages), 6 control mice (4 female, 2 male; 2 cages); **d**, 12 FD mice, 13 control mice (all female; 3 cages per genotype); PERMANOVA (**a**, **b**, day 0, df = 1, R^2 = 0.1099; day 15, df = 1, R^2 = 0.1664; day 25, df = 1, R^2 = 0.1458; day 40, df = 1, R^2 = 0.1836; day 54, df = 1, R^2 = 0.1927; **d**, F = 2.2086, df = 1, R^2 = 0.0876); Welch's two-sample t-test (**c**, t-statistic = −2.6589, df = 12.05, difference between FD and control mice = −0.0777, 95% confidence interval of difference between FD and control mice = −0.1414 to −0.0141).

correct or replace the underlying genetic mutation and/or cellular dysfunction, identifying modifiable factors that slow pathology is paramount. Unlike other more common neurodegenerative diseases (Alzheimer's disease, Parkinson's disease, and amyotrophic lateral sclerosis, ALS), the genetic basis for FD is monogenic, highly penetrant, and recapitulated in neuron-specific mouse models. We have provided evidence that the FD-associated *ELP1* mutation promotes a dysfunctional gut-metabolism axis that in turn promotes pathology reminiscent of more common neurodegenerative diseases and other neurologic/neuropsychiatric conditions. Elp1 is an evolutionarily conserved protein among eukaryotes and a key component of the elongator complex that chemically modifies the wobble uridines in specific tRNA anticodon loops[10,37]. Loss of these modifications leads to translation inefficiency, altered proteome, and consequently cellular dysfunction and premature cell death. Reduction of another elongator subunit, Elp3, also directly alters metabolism in yeast[38].

This is the first evaluation of the gut-metabolism axis in FD and the first of a disease involving degeneration of the peripheral nervous system. Several studies have investigated the contribution of the gut microbiome and/or metabolome to outcomes in other neurodegenerative diseases and at least three included patients' relatives as control subjects[39–41]. However, these previous studies were designed as cohort comparisons, and we are unaware of other microbiome or metabolomics studies in neurodegenerative diseases that compared patients with healthy relatives in a case-control design. As shown recently[21], host factors can confound gut microbiome studies and so matching or pairing is important to minimize spurious associations. Our results are consistent with clinical studies showing that virtually all FD patients have GI symptoms, including constipation, diarrhea and

https://doi.org/10.1038/s41467-023-35787-8

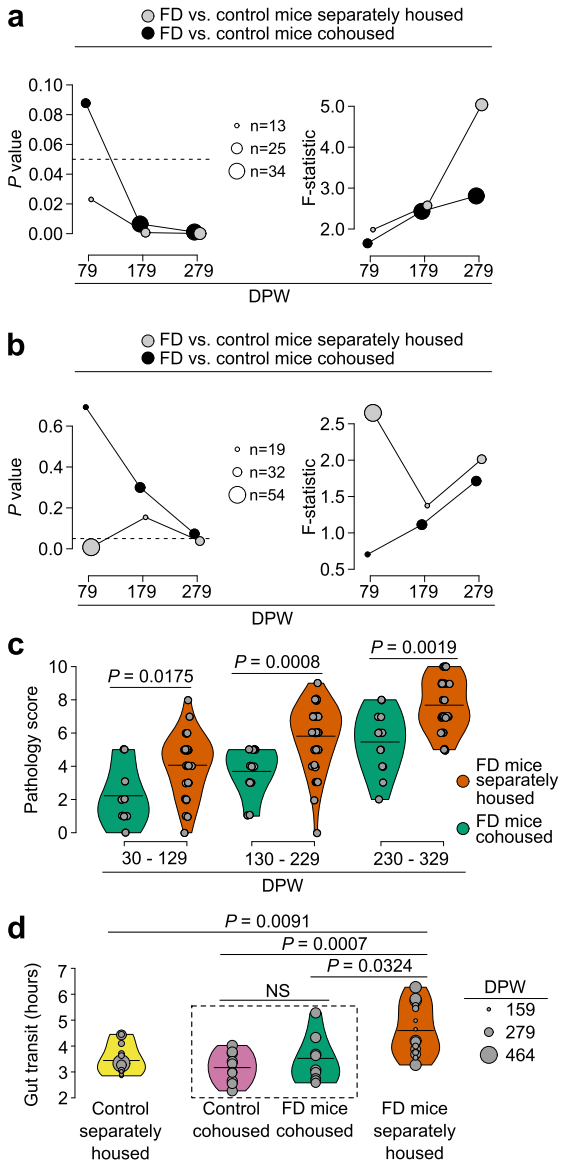


Fig. 4 | Cohousing ameliorates gut transit deficit and disease in FD mice. **a**, **b** Progressive changes in microbiome (**a**) and metabolome (**b**) diversity in FD mice compared to control mice when separately housed or cohoused (size of circles = number of mice sampled at each time; DPW = days post-weaning; dotted line represents $p = 0.05$). **c** Pathology score of FD mice when housed separately or cohoused with control mice. **d** Carmine red-based gut transit for each mouse group. Groups in dotted box were cohoused. n = **a**, 79 DPW separately housed: 10 FD (4 female, 6 male; 3 cages) vs. 3 control (female; 1 cage); 79 DPW cohoused: 9 FD (6 female, 3 male; 3 cages) vs. 12 control (7 female, 5 male; 3 cages); 179 DPW separately housed: 10 FD (5 female, 5 male; 2 cages) vs. 11 control (5 female, 6 male; 3 cages); 179 DPW cohoused: 13 FD (6 female, 7 male; 4 cages) vs. 21 control (7 female, 14 male; 5 cages); 279 DPW separately housed: 13 FD (6 female, 7 male; 4 cages) vs. 21 control (7 female, 14 male; 5 cages); 279 DPW cohoused: 13 FD (7 female, 6 male; 4 cages) vs. 8 control (5 female, 3 male; 2 cages). **b** 79 DPW separately housed: 25 FD (14 female, 11 male; 6 cages) vs. 29 control (18 female, 11 male; 7 cages) mice; 79 DPW cohoused: 9 FD (6 female, 3 male; 3 cages) vs. 11 control (6 female, 5 male; 3 cages); 179 DPW separately housed: 10 FD (6 female, 4 male; 3 cages) vs. 9 control (7 female, 2 male; 3 cages); 179 DPW cohoused: 13 FD (6 female, 7 male; 4 cages) vs. 21 control (7 female, 14 male; 5 cages); 279 DPW separately housed: 15 FD (9 female, 6 male; 4 cages) vs. 12 control (5 female, 7 male; 3 cages); 279 DPW cohoused: 13 FD (6 female, 7 male; 4 cages) vs. 20 control (7 female, 13 male; 5 cages). **c**, 30–129 DPW: 86 separately housed (60 female, 26 male; 18 cages) vs. 21 cohoused (13 female, 8 male; 5 cages); 130–229 DPW: 66 separately housed (47 female, 19 male; 14 cages) vs. 34 cohoused (13 female, 21 male; 8 cages); 230–329 DPW: 40 separately house (22 female, 18 male; 9 cages) vs. 34 cohoused (13 female, 21 male; 8 cages); **d**, 15 FD (12 female, 3 male; 3 cages) and 11 control (all female; 3 cages) mice separately housed; 9 FD (6 female, 3 male; 3 cages) and 10 control (7 female, 3 male; 3 cages) mice cohoused. PERMANOVA (**a**, separately housed, day 79, df = 1, $R^2 = 0.1528$, day 179, df = 1, $R^2 = 0.1193$, day 279, df = 1, $R^2 = 0.1941$; cohoused, day 79, df = 1, $R^2 = 0.0799$; day 179, df = 1, $R^2 = 0.0706$; day 279, df = 1, $R^2 = 0.0807$; **b**, separately housed, day 79, df = 1, R^2=, day 179, df = 1, R^2=, day 279, df = 1, R^2 = ; cohoused, day 79, df = 1, R^2=; day 179, df = 1, R^2=; day 279, df = 1, R^2=); Welch's two-sample t-testing with FDR correction (**c**, DPW 30–129, t-statistic = −2.7203, df = 13.018, difference between FD cohoused and separately housed mice = −1.8403, 95% confidence interval of difference between FD cohoused and separately housed mice = −3.3015 to −0.3790; DPW 130–229, t-statistic = −4.1497, df = 28.434, difference between FD cohoused and separately housed mice = −2.1185, 95% confidence interval of difference between FD cohoused and separately housed mice = −3.1635 to −1.0735; DPW 230–329, t-statistic = −3.7242, df = 20.515, difference between FD cohoused and separately housed mice = −2.2170, 95% confidence interval of difference between FD cohoused and separately housed mice = −3.4568 to −0.9772; **d**, FD cohoused vs. separately housed, t-statistic = −2.9745, df = 18.025, difference between group means = −1.1576, 95% confidence interval of difference between group means = −1.9751 to −0.3400; control cohoused vs. FD separately housed, t-statistic = −4.6345, df = 22.825, difference between group means = −1.4317, 95% confidence interval of difference between group means = −2.0710 to −0.7923; control separately housed vs. FD separately housed, t-statistic = −3.5146, df = 23.385, difference between group means = −1.0759, 95% confidence interval of difference between group means = −1.7087 to −0.4432).

gut dysmotility[17], and comparative pathology shows a reduced number of enteric neurons in FD patients as well as vagal nerve deficits in those with fundoplication[17]. Given the complex clinical histories of FD patients, including antibiotic treatments and GI procedures, it is reasonable to expect that the microbiome and metabolome would be significantly altered. Yet, neuron-specific deletion of *Elp1* in mice resulted in the progressive microbiome and metabolome alteration, suggesting that a neuronal FD mutation is sufficient to cause changes similar to that observed in human FD patients. It is also interesting that despite obvious differences between mice and humans (genetics, environment, diet, microbiome membership; Supplementary Fig. 9), choline metabolism was dysregulated in both human FD patients and the FD mouse model, suggesting a potentially important overlap in the mechanism of pathology.

While it is well known that FD patients suffer from frequent GI dysfunction[17], at least one imaging study found delayed esophageal transit times and delayed gastric emptying among FD patients compared to healthy control subjects, implicating a dysfunctional myenteric plexus of the upper GI tract in FD[42]. These results are consistent with two case studies that isolated and visually compared the esophageal, gastric and/or appendiceal myenteric plexus of FD patients and age-matched control subjects[43]; these studies showed significant reductions in the neuronal number and/or ganglion complexity. Collectively, these results suggest that dysfunctional gut motility in FD patients is most likely due to alterations in neuronal density throughout the GI tract. Like FD patients, our non-cohoused FD mice also had reduced gut transit time, yet co-housed mice did not, suggesting this outcome is not only malleable, but may be useful as a clinical readout for FD therapies.

The increased level of TMAO observed in FD patient serum is noteworthy given the positive predictive value of this metabolite for cardiovascular and kidney diseases[31,32]. Both diseases are leading causes of death among FD patients and together are the most

common non-acute cause of death[3] (acute forms being sudden death during sleep, aspiration, and complications due to aspiration, like pneumonia and sepsis). TMAO can directly alter neuronal physiology, such as increasing brain aging in mice by increasing the senescence of primary neurons[44]. As recently reviewed[45], TMAO is currently the most important microbial metabolite associated with Alzheimer's Disease and increased levels in cerebrospinal fluid was recently shown to be associated with dementia and pathology[46]. Future studies are needed to directly address whether TMAO accelerates neurodegeneration of the peripheral nervous system and whether decreasing TMAO levels is therapeutic. For example, dietary interventions like the choline-restricted diet used to treat the genetic disorder, trimethylaminuria (fish odor syndrome)[47], may help modify TMAO-mediated pathologies.

Elp1 is one of six subunits of the elongator holoenzyme, and in addition to the *ELP1* mutation giving rise to FD, polymorphisms in four other subunit loci have been associated with neurologic diseases, including intellectual disability (*ELP2, ELP4, ELP6*), ALS (*ELP3*), and ASD and Rolandic epilepsy (*ELP4*)[48–52]. Whether these non-*ELP1* mutations in the elongator complex influence the gut-metabolism axis has not been experimentally addressed to our knowledge, but therapeutic modification of the microbiome via fecal microbiome transplantation (FMT) has been evaluated in ASD and found effective for ameliorating both short- and long-term outcomes and both GI and neurologic symptoms[23,24,53]. Our results indicate that the progressive nature of *Elp1*-driven microbiome-metabolome dysbiosis is modifiable, and when controlled, can ameliorate deficits in gut function and pathology. We believe this finding provides rationale for clinical interventions like FMT that has been shown to prevent or lessen debilitating symptoms of other neurologic diseases, including ASD. Our results also suggest that gut function, microbiome diversity, and metabolic function may be clinically useful as empirical indicators of FD disease severity. Finally, given the fact that variants in other Elongator complex subunits have been associated with human cognitive function, ALS, ASD and/or epilepsy[48–52], our results may have broader therapeutic impacts for more common neurologic disorders.

Methods

Human subjects

Samples were obtained from enrolled participants under Institutional Review Board approved protocols at both Montana State University and the New York University School of Medicine (NYU Langone Health). FD patients and their relatives were recruited in a case-control design through the Dysautonomia Center at New York University (NYU) Langone Health. Patients were approached at annual clinic visits to NYU Langone Medical Center. If interested, cohabitating relatives were also approached about the study. All subjects (patients and relatives) were recruited with informed consent following IRB-approved protocols. The potential for self-selection bias was deemed minimal due to the genetic predisposition and highly penetrant nature of the disease. The Dysautonomia Center at NYU Langone serves the majority of FD patients around the world and given the prevalence of the disease in the Ashkenazi Jewish community, we assumed minimal potential of bias due to sample size. Participants received no compensation for participation in this study.

A single relative was enrolled for 27 FD patients; two relatives were enrolled for 13 patients; three relatives were enrolled for 1 patient; and no relatives were enrolled for 7 FD patients. All human samples were collected through the Dysautonomia Center at NYU Langone Health. Patients and relatives were not required to fast prior to any sample collection due to the fragile condition of some patients. Peripheral venous blood samples were collected in test tubes containing clot activator, allowed to coagulate for 30 min, and centrifuged at 1,000–2000× *g* for 10 min for serum separation. Serum was then aliquoted into 15 mL vials and frozen at −20 °C until it was shipped overnight on dry ice to Montana State University where it was stored at −80 °C. Stool samples were self-collected using collection kits (commode/hat) containing gloves and a sterile tongue depressor and placed into a sterile 50 mL conical tube. These samples were requested to be collected as close as possible to blood samples. Tubes were sealed in zip-lock bags and frozen at −20 °C within 24 h. For most subjects, stool collection kits were sent to enrollees just prior to scheduled annual clinic visits so they could bring samples with them to their visit. Some subjects were recruited (potentially during these visits) and a stool collection kit was sent home. Samples collected at home were immediately frozen for at least 12 h and shipped overnight on ice and inside a small Styrofoam cooler box to the clinical team at NYU Langone. Samples were kept frozen at NYU (−20 °C), batched, and shipped overnight on dry ice to Montana State University and stored at −80 °C until processing. Patient metadata were pulled from medical charts or clinical laboratory values and evaluated as categorical predictor variables (Supplementary Table 2 in Supplementary Data 1). Pairing of patient and relative samples was done as much as possible with the only exclusion criterion being if samples were collected >90 days apart. All possible pairs were considered in analyses using permutation analyses (see Statistics below).

Mice

All mouse experiments were conducted in the AALAC-accredited Animal Resource Center at Montana State University under local IACUC-approved protocols (MSU protocol no. 2021-35-81). Specific Pathogen Free (SPF) C57BL/6 mice carrying the *Tuba1a-Cre*$^{+}$*; Elp1*$^{loxp/loxp}$ mutation were used as the disease model (FD mice) and *Tuba1a-Cre*$^{-}$*; /Elp1*$^{+/loxp}$ littermates were used as controls. The creation and description of these genotypes have been described[34]. All experiments included both sexes and mouse age ranged from 21 days (0 days post-weaning; DPW) to 485 days (465 DPW) of age. Mice were housed under a 14-h light/10-h dark cycle with temperatures of 18–23 °C and 40–60% humidity, with food (irradiated PicoLab® Rodent Diet 20, 5053 LabDiet®, Land O'Lakes, Inc., Arden Hills, MN, USA) and water given ad libitum. To avoid cage effects, mice from at least two different cages per experimental group were analyzed. To test the effect of housing, groups of FD mice were either separated from littermate control siblings at weaning or left together.

For stool collection, mice were individually scruffed and freshly voided stool was collected into a sterile microcentrifuge tube, flash frozen in an ethanol dry ice bath, and frozen at −80 °C. To quantify disease in mice, a scoring system was devised based on eight factors (hind limb clasping, evidence of grooming, presence of cataracts, presence of kyphosis, motor function/movement, presence of tremors, observed jumping activity, and body condition) and scored via ordinal bins (Supplementary Table 3). Scores ranged from 0 (no disease) to 12 (severe disease). To quantify gut transit time, mice received an oral gavage of 150 μL of a solution comprised of 6% carmine red dye and 0.5% methylcellulose in water. A white paper towel was place on the floor of cages and mice were individually monitored every ten minutes for evidence of red stool. Gut transit time was calculated as the time between gavage and the presence of red stool.

Stool microbiome sequencing

DNA was extracted from stool (human and mouse) using a DNeasy Powersoil kit (Qiagen, Hilden, Germany) following the manufacturer's instructions. DNA was submitted for 16 S rRNA gene sequencing at the University of Michigan Center for Microbial Systems (dual-index, paired-end sequencing[54]; 250 bp reads of variable region 4). Raw reads (forward and reverse) were processed using mothur[55] v.1.46.1 and assembled into contigs following published protocols[29,54]. Contigs with ambiguous bases or homopolymers of ≥8 bp were discarded. Identical sequences were combined and aligned to the V4 region of the 16 S rRNA alignment of the SILVA database (version

128, https://www.arb-silva.de/documentation/release-128). Chimeric sequences were identified with VSEARCH[56,57] and discarded. Contigs were classified within mothur using the Ribosomal Database Project's Bayesian classifier (training set 16, https://sourceforge.net/projects/rdp-classifier/files/RDP_Classifier_TrainingData). Contigs that classified as mitochondria, chloroplasts, or Eukaryota or were unclassified at the domain level were discarded. The remaining contigs were clustered into operational taxonomic units (OTUs) at ≥97% sequence identity using VSEARCH[57]. OTUs represented by fewer than 100 reads in the data set were removed. Human and mouse samples were rarefied to 9,848 and 5,308 reads, respectively, corresponding to the sample in each dataset with the least number of reads.

Partitioning around medoids (PAM) clustering was conducted using cluster analysis (cluster, version 2.1.3[58]) in R (version 4.1.0). Alpha diversity was estimated using the inverse Simpson index and ordinations (nonmetric multidimensional scaling; NMDS) were used to visualize between beta-diversity (Bray-Curtis dissimilarity). Diversity estimates were generated in R using vegan (version 2.6-2)[59], labdsv (version 2.0-1)[60], and custom scripts. Significance between groups in ordinations was evaluated using permutational multivariate analysis of variance (PERMANOVA) with the Adonis function in vegan and 9999 permutations.

Preparation of serum and stool samples for metabolomics

Serum samples stored at −80 °C were thawed on ice and 400 μL serum was added to 1600 μL acetone (4:1 v/v ratio). Samples were mixed by inversion and incubated at room temperature (25 °C) for 20 min, followed by a second incubation at −20 °C for 1 h and centrifugation at 10,000× I for 10 min. Supernatant was transferred to a microcentrifuge tube and dried using a speed vacuum concentrator overnight, without heat. Dried metabolite mixtures were then reconstituted in 600 μL of serum NMR buffer consisting of 0.25 mM sodium 2, 2-Dimethyl-2-silapentane-5-sulfonic (DSS) in 90% H_2O/10% D_2O, 0.4 mM imidazole, 25 mM NaH_2PO_4/Na_2HPO_4, pH 7, and transferred to a 5 mm Bruker NMR tube.

Stool metabolite extraction from human samples was performed using methods adapted from previous publications[61,62] and is described in detail here. Samples were thawed at room temperature and homogenized by spatula stir mixing in their original 50 mL collection tubes. Aliquots of 500 mg were placed into 2 mL twist cap centrifuge tubes, flash-frozen and stored again at −80 °C. Further processing was done in batches. Samples were thawed and stool NMR buffer solution (0.1 M Na_2HPO_4/KH_2PO_4, pH 7.37, 0.25 mM sodium DSS, 0.4 mM Imidazole, 0.01% sodium azide, in 90% H_2O/10% D_2O, pH 7.0) was added at a 1:2 w/v ratio (wet stool-weight to buffer-volume). Homogenization and lysing were carried out using a bead-beating tissue lyser (Millipore FastPrep-24™ 5 G bead beating tissue lyser set at 6.0 m/s for 40 s), followed by centrifugation at 10,000× *g* for 10 min. Resulting supernatants were transferred to a new 2 mL centrifuge tube and the pellet subjected to a subsequent round of extraction. Supernatant from two rounds of bead beating per sample were combined and centrifuged at 21,000× *g* for 10 min, followed by filtration (4 μm syringe filter), followed by a second centrifugation step (21,000 × *g* for 10 min). The resulting solution was filtered using a 3 kDa filter to remove additional large particulates, and the final pH was adjusted to 7.0. 600 μL of filtered supernatant was transferred to a 5 mm Bruker NMR tube for NMR analysis. A separate aliquot of 500 mg of each human stool sample was lyophilized to determine water-weight percent, and dry weight of extracted samples. Mouse stool samples were prepared similarly to human stool samples with the following exceptions: NMR Buffer was added to achieve a 1:10 w/v (40–180 mg wet stool-weight to buffer-volume) ratio; samples were filtered with only a 3 kDa filter; 600 μL of filtrate was dried overnight under vacuum without heat and resuspended in 600 μL of 90% H_2O to 10% D_2O.

NMR-based metabolomics

All NMR spectra were collected at 300 K using a Bruker 600 MHz (^{1}H Larmor frequency) AVANCE III solution NMR spectrometer equipped with a 5 mm triple resonance (^{1}H, ^{13}C, ^{15}N) liquid helium-cooled cryoProbe, automatic sample loading system (SampleJet), and TopSpin software (Bruker version 3.2). Spectral acquisition of 1D ^{1}H NMR experiments was performed using the Bruker gradient-based water suppression "zgesgp" pulse sequence[1,2], and 1D 1H NMR spectra were recorded using 256 scans, a ^{1}H spectral window of ~12 ppm, 64 K data points, and a dwell time of 69 microseconds between points, resulting in an FID (free induction decay) data acquisition time period of ~4.5 s. Recovery delay time (i.e., D1 parameter) between acquisitions was set to 2 s, resulting in a total relaxation recovery delay of ~6.5 s between scans. DSS chemical shift referencing and phase correction of 1D ^{1}H NMR spectra were conducted using TopSpin (Bruker version 3.2)[63]. Additional manual processing of 1D ^{1}H NMR spectra and metabolite profiling were conducted using the Chenomx NMR Suite software (version 8.4; Chenomx Inc., Edmonton, Alberta, Canada). Baseline correction of NMR spectra following an import of preprocessed '1r' NMR spectral files into the Chenomx software was performed using the automatic cubic spline function (Chenomx Spline) in Chenomx, and subsequent manual breakpoint adjustment to obtain a flat, well-defined baseline, following guidelines from Chenomx application notes and reported methods[63–65]. ^{1}H chemical shifts were referenced to the most upfield signal of DSS, set to 0.0 ppm, and the ^{1}H NMR resonance of imidazole was used to correct for small chemical shift variations arising from slight changes in sample pH. Metabolite identification and quantitation were performed by fitting 1D ^{1}H spectral splitting patterns, chemical shifts, and spectral intensities to reference spectra of small molecules accessible through the Chenomx small molecule spectral database for 14.1 T (600 MHz ^{1}H Larmor frequency) magnetic field strength NMR instruments and the human metabolome database (HMDB). In addition, small spectral adjustments were made using a manual peak-based fit style in Chenomx to achieve optimal fits for compound peak cluster location and spectral intensity matching[66]. Relative intensities were calibrated to DSS concentration (0.25 mM), which was used as an internal reference to quantify metabolite levels and to determine metabolite concentrations. Confirmation of metabolite ID was achieved by spiking of pure metabolite standards into samples, as needed. Metabolite profiles were exported from the Chenomx software and converted from μM to nanomoles/mL for serum, nanomoles/gram for human stool, and nanomoles/mg for mouse stool by normalizing to serum volume, fecal dry mass for human stool, and fecal wet mass for mouse stool, respectively, and taking into account the NMR sample volume (600 μL). Metabolite data were log-transformed and auto-scaled (mean centered and divided by standard deviation) with mouse stool data being additionally normalized by sum, using MetaboAnalyst 4.0[67].

Metabolomic diversity (i.e., the presence/absence and abundance of metabolites) was visualized using ordination (partial least square-discriminant analysis, PLSDA; principal coordinates analysis) in R version 4.1.0 using vegan[59] (version 2.6-2), vegan3d[68] (version 1.1-2), labdsv[60] (version 2.0-1), mixOmics[69], and custom scripts. Axes in ordinations were labeled in ascending order corresponding to the amount of described variation (greatest to least). The validity of the PLSDA models were assessed using MetaboAnalyst version 3.0 and custom R scripts with a leave-one-out validation test for predictive variability (Q^2) metrics and predicted residual sum of squares (PRESS) error (R^2), prediction accuracy and separation distance permutation tests (n = 1000), classification error rates (CER), and area under the receiver operating characteristic curve (AUROC) analyses[70].

TMA and TMAO analysis LCMS

Human serum samples were thawed at room temperature and 20 μL was added to 80 μL of −20 °C acetone in a clean vial and incubated

overnight at −80 °C to precipitate protein[71]. Following centrifugation, the metabolite-containing supernatant was removed and concentrated to dryness using an Eppendorf Concentrator Plus (Eppendorf, Hamburg, Germany) at 30 °C for ~30 min. 50 μL of MeOH:H_2O (50:50) was added to the dried layer and vortexed to reconstitute the metabolite fraction. The sample was split into two 25 μL aliquots for each targeted LCMS analysis.

Stool metabolites were extracted for LCMS analysis using standard methods[72]. Approximately 500 mg of stool was thawed at room temperature and kept on ice for the remainder of the extraction. Three volumes of HPLC-grade water were added to stool samples, vortexed for 30 s, and homogenized using an Ultrasonic Homogenizer 3000 (Biologics, Manassas, VA) set at a 40% duty cycle for five minutes. An equal volume of MeOH, ~1 mL, was added to the slurry, vortexed for 30 s, and centrifuged (20,000 × g for 30 min). The metabolite-containing supernatant was removed and the cell debris pellet was washed. Washes consisted of the addition of MeOH:H_2O to cover the debris pellet and agitation via vortexing. Following centrifugation (20,000 g for 30 min), the supernatant was removed and added to the previously collected supernatant. Acetone precipitation was conducted overnight (5 volumes of −20 °C acetone stored at −80 °C) and the supernatant was filtered using a 3Kda spin filter. Eluent was concentrated to dryness (Eppendorf Concentrator Plus at 30 °C for 2–3 h) and dried samples were reconstituted in 100 μL of MeOH:H_2O (50:50) when ready for LCMS analysis. The sample was divided into two 50 μL aliquots, one for each targeted LCMS analysis.

One of the fecal metabolite extracts from each original sample was derivatized with dansyl chloride for TMA analysis[73]. To begin, 2 μL of 166 mM NaOH was added to each extract and the pH was verified to be between 9 and 9.5 using a pH probe. To this solution, 46 μL of 20 mg/mL dansyl chloride was added and incubated at room temperature for 30 min. After 30 min, 2 μL of 10% formic acid was added to quench the reaction and the pH was verified to be ~4 using a pH probe. Derivatized samples were placed in a clean vial for LCMS analysis.

LCMS analysis for derivatized and underivatized serum and fecal samples was completed on a Waters Synapt-XS Q-IMS-TOF (quadrupole-ion mobility spectrometry-time of flight) mass spectrometer coupled to a Waters I-Class UHPLC (ultra-high-performance liquid chromatography) (Waters, Milford, MA). Separation was achieved with a 130 Å, 1.7 um, 2.1 mm × 100 mm Acquity BEH-HILIC column in a column compartment kept at 30 °C. 5 μL of sample was injected and ionized using electrospray ionization in positive mode. Total method runtime was 6 min with mobile phase A consisting of 15 mmol/L ammonium formate while mobile phase B was acetonitrile. The gradient used was 10% A from 0–2 min, 10–40% A from 2–3.5 min, 40% A from 3.5–4.5 min and 10% A from 4.5–6 min[74]. Authentic standards were used to verify the m/z value and retention time as well as create standard curves for all analytes. Data analysis and normalization was completed in Progenesis QI version 3.0 and statistical analysis was performed in R version 4.1.0.

Statistics

No statistical methods were used to predetermine sample sizes. Data were visually assessed for normality with quantile-quantile plots and, when possible, transformed for normality. The exact number (*n*) of replicates used in each experiment are reported in the respective figure legends. Statistical analyses were conducted in R version 4.1.0. PERMANOVA was used to test for significant difference observed between patients and relatives in ordinations (NMDS and principal coordinates analysis) or PAM clustered defined enterotypes (R package cluster, version 2.1.3). Random forest analysis (R packages randomForest version 4.7-1[75] and rfutilities version 2.1-5[76]) was used to identify both OTUs and individual metabolites responsible for significant differences. Visualization tools in R, including gplots (version 3.1.3)[77], RColorBrewer (version 1.1-3)[78], and dplyr (version1.1.10)[79], were used to generate figures. Paired relative samples were not available for all FD patients and for other FD patients, multiple relatives provided samples within the required 90-day window (i.e., samples outside of this window were excluded). To leverage as many samples (and statistical power) as possible, pairs were randomly selected during permutation analyses performed in R. The number of pairs selected during each permutation was equal to the total number of patients for which a relative sample was available (FD patient samples without a paired relative sample were excluded from paired permutation analyses). FDR-corrected *p* values were generated for all tests with multiple comparisons as described in the respective figures legends. Linear mixed-effects models were generated and evaluated using R package lme4, version 1.1–29[80]. Data distribution was evaluated and displayed for some factors using violin plots (R package vioplot, version 0.3.7[81]).

Reporting summary

Further information on research design is available in the Nature Portfolio Reporting Summary linked to this article.

Data availability

All sequencing reads generated in this study have been deposited in the National Center for Biotechnology Information (NCBI) BioProject database under accession number PRJNA785599. All metabolomics data generated in this study have been deposited in the MetaboLights repository under accession number MTBLS5138 and are also available at GitHub (https://github.com/nvpinkham/Dysautonomia). The data and analyses generated in this study are available as a single compressed Source Data file on GitHub (https://github.com/nvpinkham/Dysautonomia). The Silva 16 S rRNA database used for alignment is available at https://www.arb-silva.de/documentation/release-128 and the RDP training set used is available at https://sourceforge.net/projects/rdp-classifier/files/RDP_Classifier_TrainingData. Microbiome (16 S rRNA sequencing) datasets used for comparisons are available at the NCBI BioProject database accession numbers PRJNA505353 (Martinson et al.) and PRJNA290926 (Baxter et al.). Source data are provided with this paper.

Code availability

Custom code was used to generate figures and statistical comparisons has been deposited in the Zenodo repository (https://doi.org/10.5281/zenodo.7384390) and is available at GitHub (https://github.com/nvpinkham/Dysautonomia)[82].

References

1. Blumenfeld, A. et al. Precise genetic mapping and haplotype analysis of the familial dysautonomia gene on human chromosome 9q31. *Am. J. Hum. Genet.* **64**, 1110–1118 (1999).
2. Carmi, S. et al. Sequencing an Ashkenazi reference panel supports population-targeted personal genomics and illuminates Jewish and European origins. *Nat. Commun.* **5**, 4835 (2014).
3. Norcliffe-Kaufmann, L., Slaugenhaupt, S. A. & Kaufmann, H. Familial dysautonomia: History, genotype, phenotype and translational research. *Prog. Neurobiol.* **152**, 131–148 (2017).
4. Anderson, S. L. et al. Familial dysautonomia is caused by mutations of the IKAP gene. *Am. J. Hum. Genet.* **68**, 753–758 (2001).
5. Slaugenhaupt, S. A. et al. Tissue-specific expression of a splicing mutation in the IKBKAP gene causes familial dysautonomia. *Am. J. Hum. Genet.* **68**, 598–605 (2001).
6. Riley, C. M. et al. Central autonomic dysfunction with defective lacrimation; report of five cases. *Pediatrics* **3**, 468–478 (1949).
7. Cuajungco, M. P. et al. Tissue-specific reduction in splicing efficiency of IKBKAP due to the major mutation associated with familial dysautonomia. *Am. J. Hum. Genet.* **72**, 749–758 (2003).
8. Dietrich, P. & Dragatsis, I. Familial Dysautonomia: Mechanisms and Models. *Genet. Mol. Biol.* **39**, 497–514 (2016).

9. Bauer, F. & Hermand, D. A coordinated codon-dependent regulation of translation by Elongator. *Cell Cycle* **11**, 4524–4529 (2012).
10. Goffena, J. et al. Elongator and codon bias regulate protein levels in mammalian peripheral neurons. *Nat. Commun.* **9**, 889 (2018).
11. Johansson, M. J. O., Xu, F. & Bystrom, A. S. Elongator-a tRNA modifying complex that promotes efficient translational decoding. *Biochim Biophys. Acta Gene Regul. Mech.* **1861**, 401–408 (2018).
12. Karlsborn, T. et al. Elongator, a conserved complex required for wobble uridine modifications in eukaryotes. *RNA Biol.* **11**, 1519–1528 (2014).
13. Otero, G. et al. Elongator, a multisubunit component of a novel RNA polymerase II holoenzyme for transcriptional elongation. *Mol. Cell* **3**, 109–118 (1999).
14. Bar Aluma, B. E. et al. Resting Energy Expenditure in Patients With Familial Dysautonomia: A Preliminary Study. *J. Pediatr. Gastroenterol. Nutr.* **68**, 422–427 (2019).
15. Bar-Shai, A. et al. Decreased density of ganglia and neurons in the myenteric plexus of familial dysautonomia patients. *J. Neurol. Sci.* **220**, 89–94 (2004).
16. Palma, J. A. et al. Current treatments in familial dysautonomia. *Expert Opin. Pharmacother.* **15**, 2653–2671 (2014).
17. Ramprasad, C. et al. Frequency and burden of gastrointestinal symptoms in familial dysautonomia. *Clin. Auton. Res.* **31**, 109–116 (2021).
18. Adams, J. B., Johansen, L. J., Powell, L. D., Quig, D. & Rubin, R. A. Gastrointestinal flora and gastrointestinal status in children with autism-comparisons to typical children and correlation with autism severity. *BMC Gastroenterol.* **11**, 22 (2011).
19. Kojic, M. & Wainwright, B. The Many Faces of Elongator in Neurodevelopment and Disease. *Front Mol. Neurosci.* **9**, 115 (2016).
20. Wang, L. et al. Elevated fecal short chain fatty acid and ammonia concentrations in children with autism spectrum disorder. *Dig. Dis. Sci.* **57**, 2096–2102 (2012).
21. Vujkovic-Cvijin, I. et al. Host variables confound gut microbiota studies of human disease. *Nature* **587**, 448–454 (2020).
22. Bicknell, B., Liebert, A., McLachlan, C. S. & Kiat, H. Microbiome Changes in Humans with Parkinson's Disease after Photobiomodulation Therapy: A Retrospective Study. *J Pers Med.* **12**, https://doi.org/10.3390/jpm12010049 (2022).
23. Kang, D. W. et al. Long-term benefit of Microbiota Transfer Therapy on autism symptoms and gut microbiota. *Sci. Rep.* **9**, 5821 (2019).
24. Kang, D. W. et al. Microbiota Transfer Therapy alters gut ecosystem and improves gastrointestinal and autism symptoms: an open-label study. *Microbiome* **5**, 10 (2017).
25. Vogt, N. M. et al. Gut microbiome alterations in Alzheimer's disease. *Sci. Rep.* **7**, 13537 (2017).
26. Leylabadlo, H. E. et al. The critical role of Faecalibacterium prausnitzii in human health: An overview. *Micro. Pathog.* **149**, 104344 (2020).
27. La Rosa, S. L. et al. The human gut Firmicute Roseburia intestinalis is a primary degrader of dietary beta-mannans. *Nat. Commun.* **10**, 905 (2019).
28. Baxter, N. T., Ruffin, M. T. T., Rogers, M. A. & Schloss, P. D. Microbiota-based model improves the sensitivity of fecal immunochemical test for detecting colonic lesions. *Genome Med.* **8**, 37 (2016).
29. Martinson, J. N. V. et al. Rethinking gut microbiome residency and the Enterobacteriaceae in healthy human adults. *ISME J.* **13**, 2306–2318 (2019).
30. Rath, S., Heidrich, B., Pieper, D. H. & Vital, M. Uncovering the trimethylamine-producing bacteria of the human gut microbiota. *Microbiome* **5**, 54 (2017).
31. Roncal, C. et al. Trimethylamine-N-Oxide (TMAO) Predicts Cardiovascular Mortality in Peripheral Artery Disease. *Sci. Rep.* **9**, 15580 (2019).
32. Pelletier, C. C. et al. Elevation of Trimethylamine-N-Oxide in Chronic Kidney Disease: Contribution of Decreased Glomerular Filtration Rate. *Toxins (Basel)* **11**, https://doi.org/10.3390/toxins11110635 (2019).
33. Zhang, W. et al. Inhibition of microbiota-dependent TMAO production attenuates chronic kidney disease in mice. *Sci. Rep.* **11**, 518 (2021).
34. Chaverra, M. et al. The familial dysautonomia disease gene IKBKAP is required in the developing and adult mouse central nervous system. *Dis. Model Mech.* **10**, 605–618 (2017).
35. Ueki, Y., Ramirez, G., Salcedo, E., Stabio, M. E. & Lefcort, F. Loss of Ikbkap Causes Slow, Progressive Retinal Degeneration in a Mouse Model of Familial Dysautonomia. *eNeuro* **3**, https://doi.org/10.1523/ENEURO.0143-16.2016 (2016).
36. Bo, T. B. et al. Coprophagy prevention alters microbiome, metabolism, neurochemistry, and cognitive behavior in a small mammal. *ISME J.* **14**, 2625–2645 (2020).
37. Huang, B., Johansson, M. J. & Bystrom, A. S. An early step in wobble uridine tRNA modification requires the Elongator complex. *RNA* **11**, 424–436 (2005).
38. Karlsborn, T., Mahmud, A., Tukenmez, H. & Bystrom, A. S. Loss of ncm(5) and mcm(5) wobble uridine side chains results in an altered metabolic profile. *Metabolomics* **12**, 177 (2016).
39. Johansen, K. K. et al. Metabolomic profiling in LRRK2-related Parkinson's disease. *PLoS One* **4**, e7551 (2009).
40. Vascellari, S. et al. Gut Microbiota and Metabolome Alterations Associated with Parkinson's Disease. *mSystems* **5**, https://doi.org/10.1128/mSystems.00561–20 (2020).
41. Wu, L. et al. Altered Gut Microbial Metabolites in Amnestic Mild Cognitive Impairment and Alzheimer's Disease: Signals in Host-Microbe Interplay. *Nutrients* **13**, 10228 (2021).
42. Krausz, Y. et al. Scintigraphic evaluation of esophageal transit and gastric emptying in familial dysautonomia. *Eur. J. Radio.* **18**, 52–56 (1994).
43. Ariel, I. & Wells, T. R. Structural abnormalities of the myenteric (Auerbach's) plexus in familial dysautonomia (Riley-Day syndrome) as demonstrated by flat-mount preparation of the esophagus and stomach. *Pediatr. Pathol.* **4**, 89–98 (1985).
44. Li, D. et al. Trimethylamine-N-oxide promotes brain aging and cognitive impairment in mice. *Aging Cell* **17**, e12768 (2018).
45. Praveenraj, S. S. et al. The Role of a Gut Microbial-Derived Metabolite, Trimethylamine N-Oxide (TMAO), in Neurological Disorders. *Mol. Neurobiol.* **59**, 6684–6700 (2022).
46. Vogt, N. M. et al. The gut microbiota-derived metabolite trimethylamine N-oxide is elevated in Alzheimer's disease. *Alzheimers Res. Ther.* **10**, 124 (2018).
47. Phillips, I. R. & Shephard, E. A. in *GeneReviews((R))* (eds M. P. Adam et al.) (1993).
48. Gaik, M. et al. Functional divergence of the two Elongator subcomplexes during neurodevelopment. *EMBO Mol. Med.* **14**, e15608 (2022).
49. Kojic, M. et al. Elp2 mutations perturb the epitranscriptome and lead to a complex neurodevelopmental phenotype. *Nat. Commun.* **12**, 2678 (2021).
50. Russo, A. et al. ELP2 compound heterozygous variants associated with cortico-cerebellar atrophy, nodular heterotopia and epilepsy: Phenotype expansion and review of the literature. *Eur. J. Med. Genet.* **64**, 104361 (2021).
51. Simpson, C. L. et al. Variants of the elongator protein 3 (ELP3) gene are associated with motor neuron degeneration. *Hum. Mol. Genet.* **18**, 472–481 (2009).

52. Strug, L. J. et al. Centrotemporal sharp wave EEG trait in rolandic epilepsy maps to Elongator Protein Complex 4 (ELP4). *Eur. J. Hum. Genet.* **17**, 1171–1181 (2009).
53. Li, N. et al. Fecal Microbiota Transplantation Relieves Gastrointestinal and Autism Symptoms by Improving the Gut Microbiota in an Open-Label Study. *Front Cell Infect. Microbiol.* **11**, 759435 (2021).
54. Kozich, J. J., Westcott, S. L., Baxter, N. T., Highlander, S. K. & Schloss, P. D. Development of a dual-index sequencing strategy and curation pipeline for analyzing amplicon sequence data on the MiSeq Illumina sequencing platform. *Appl Environ. Microbiol.* **79**, 5112–5120 (2013).
55. Schloss, P. D. et al. Introducing mothur: open-source, platform-independent, community-supported software for describing and comparing microbial communities. *Appl Environ. Microbiol.* **75**, 7537–7541 (2009).
56. Edgar, R. C., Haas, B. J., Clemente, J. C., Quince, C. & Knight, R. UCHIME improves sensitivity and speed of chimera detection. *Bioinformatics* **27**, 2194–2200 (2011).
57. Rognes, T., Flouri, T., Nichols, B., Quince, C. & Mahe, F. VSEARCH: a versatile open source tool for metagenomics. *PeerJ* **4**, e2584 (2016).
58. Maechler, M. et al. Cluster analysis basics and extensions v. R package version 2.0.7-1 (2018).
59. Oksanen, J. et al. vegan: Community Ecology Package v. R package version 2.5-2 (2018).
60. Roberts, D. W. labdsv: Ordination and multivariate analysis for ecology v. R package version 1.8-0 (2016).
61. Deda, O., Gika, H. G., Wilson, I. D. & Theodoridis, G. A. An overview of fecal sample preparation for global metabolic profiling. *J. Pharm. Biomed. Anal.* **113**, 137–150 (2015).
62. Wu, J., An, Y., Yao, J., Wang, Y. & Tang, H. An optimised sample preparation method for NMR-based faecal metabonomic analysis. *Analyst* **135**, 1023–1030 (2010).
63. Fuchs, A. L. et al. Quantitative (1)H NMR Metabolomics Reveal Distinct Metabolic Adaptations in Human Macrophages Following Differential Activation. *Metabolites* **9**, 110248 (2019).
64. Fuchs, A. L. et al. Pseudomonas aeruginosa Planktonic- and Biofilm-Conditioned Media Elicit Discrete Metabolic Responses in Human Macrophages. *Cells* **9**, 102260 (2020).
65. O'Shea-Stone, G. et al. 1H NMR based metabolic profiling distinguishes the differential impact of capture techniques on wild bighorn sheep.*Sci. Rep.* **11**, 11308 (2021).
66. Xia, J. & Wishart, D. S. Metabolomic data processing, analysis, and interpretation using MetaboAnalyst. *Curr Protoc Bioinformatics* **Chapter 14**, Unit 14 10, https://doi.org/10.1002/0471250953.bi1410s34 (2011).
67. Chong, J. et al. MetaboAnalyst 4.0: towards more transparent and integrative metabolomics analysis. *Nucleic Acids Res.* **46**, W486–W494 (2018).
68. Oksanen, J., Kindt, R., & Simpson, G. L. vegan3d: Static and dynamic 3D plots for the 'vegan' package v. R package 1.1-2 (2018).
69. Rohart, F., Gautier, B., Singh, A. & Le Cao, K. A. mixOmics: An R package for 'omics feature selection and multiple data integration. *PLoS Comput. Biol.* **13**, e1005752 (2017).
70. Szymanska, E., Saccenti, E., Smilde, A. K. & Westerhuis, J. A. Double-check: validation of diagnostic statistics for PLS-DA models in metabolomics studies. *Metabolomics* **8**, 3–16 (2012).
71. Peach, J. T. et al. Temporal metabolic response yields a dynamic biosignature of inflammation. *iScience* **24**, 102817 (2021).
72. Deda, O., Gika, H. G. & Theodoridis, G. A. Rat Fecal Metabolomics-Based Analysis. *Methods Mol. Biol.* **1738**, 149–157 (2018).
73. Wang, Q. et al. Aerobic bacterial methane synthesis. *Proc Natl Acad Sci U S A* **118**, https://doi.org/10.1073/pnas.2019229118 (2021).
74. Awwad, H. M., Geisel, J. & Obeid, R. Determination of trimethylamine, trimethylamine N-oxide, and taurine in human plasma and urine by UHPLC-MS/MS technique. *J. Chromatogr. B Anal. Technol. Biomed. Life Sci.* **1038**, 12–18 (2016).
75. Liaw, A. & Wiener, M. Classification and regression by randomForest. *R. N.* **2**, 18–22 (2002).
76. Evans, J. S. & Cushman, S. A. Gradient modeling of conifer species using random forest. *Landsc. Ecol.* **5**, 673–683 (2009).
77. Warnes, G. et al. gplots: Various R programming tools for plotting data v. R package version 3.1.3 (2022).
78. Neuwirth, E. RColorBrewer: ColorBrewer palettes v. R package version 1.1-3 (2022).
79. Wickham, H., Francois, R., Henry, L. & Muller, K. dplyr: A grammar of data manipulation v. R package version 1.0.10 (2022).
80. Bates, D., Machler, M., Bolker, B. & Walker, S. Fitting linear mixed-effects models using lme4. *J. Stat. Softw.* **67**, 1–48 (2015).
81. Adler, D. & Kelly, S. T. vioplot: violin plot v. R package (2020).
82. Pinkham, N. V. & Walk, S. T. Gut microbiome dysbiosis drives metabolic dysfunction in Familial dysautonomia v. 1.0. https://doi.org/10.5281/zenodo.7384390 (2022).

Acknowledgements

Research reported in this publication was supported by the National Institute of Diabetes and Digestive and Kidney Diseases of the National Institutes of Health under award number R01DK117473 to V.C., F.L., and S.T.W.; a supplement for graduate education R01DK117473-02S1 to V.C., S.T.W, and S.M.C.; and support from the National Institute of General Medical Sciences of the National Institutes of Health under award number P20GM103474 to S.M.C. The content is solely the responsibility of the authors and does not necessarily represent the official views of the National Institutes of Health. Additional graduate training support to S.M.C. was provided by the Alfred P. Sloan Foundation and the Montana INBRE Native American Graduate Fellowship by the National Institute of General Medical Sciences of the National Institutes of Health under Award Number P20GM103474. The content is solely the responsibility of the authors and does not necessarily represent the official views of the National Institutes of Health. Additional graduate stipend and training support for A.M.C. from the Molecular Biosciences Program at Montana State University (MSU). Funding for the Proteomics, Metabolomics and Mass Spectrometry Facility used in this publication was made possible in part by the MJ Murdock Charitable Trust, the National Institute of General Medical Sciences of the National Institutes of Health under Award Numbers P20GM103474 and S10OD28650, and the MSU Office of Research, Economic Development and Graduate Education to B.B., S.M.C., and V.C. Financial support for the NMR instruments and operations of MSU's NMR Core Facility has been provided in part by the NIH Shared Instrumentation Grant (SIG) program (1S10RR13878 and 1S10RR026659), the National Science Foundation (NSF-MRI:DBI-1532078; NSF-MRI:CHE–2018388), the Murdock Charitable Trust Foundation (2015066:MNL), and MSU's Office of the Vice President for Research and Economic Development to V.C. We thank Galen O'Shea-Stone, Christina Lucas, Lynn George, Martha Chaverra, and Vickie Riojas for technical support and all the families that provided samples for this study.

Author contributions

A.M.C., S.M.C., and N.V.P. contributed equally to this work, including acquisition, analysis and interpretation of data and drafting of this manuscript. N.V.P. generated new software used to analyze results. A.W. contributed to data acquisition (sample preparation and metabolite profiling using NMR). S.C.B. and M.C.-V. contributed to sample and data acquisition, including obtaining samples from FD patients and their relatives. M.M., D.J.K., and H.M.G.-W. were involved in experimental design, data acquisition, and drafting of this manuscript. B.T., J.P., and B.B. contributed to data acquisition and analysis and drafting of this

manuscript. H.K. and L.N.-K. contributed to all clinical aspects of the study, including data acquisition and interpretation of results, and drafting of this manuscript. F.L., V.C., and S.T.W. contributed to all aspects of the study and led the team's efforts in overall conception of the project, data analysis and interpretation, and drafting of this manuscript.

Competing interests
The authors declare no competing interests.

Additional information
Supplementary information The online version contains supplementary material available at https://doi.org/10.1038/s41467-023-35787-8.

Correspondence and requests for materials should be addressed to Frances Lefcort, Valérie Copié or Seth T. Walk.

Peer review information *Nature Communications* thanks Nadja Zeltner, and the other, anonymous, reviewers for their contribution to the peer review of this work. Peer reviewer reports are available.

Reprints and permissions information is available at http://www.nature.com/reprints

Publisher's note Springer Nature remains neutral with regard to jurisdictional claims in published maps and institutional affiliations.

Open Access This article is licensed under a Creative Commons Attribution 4.0 International License, which permits use, sharing, adaptation, distribution and reproduction in any medium or format, as long as you give appropriate credit to the original author(s) and the source, provide a link to the Creative Commons license, and indicate if changes were made. The images or other third party material in this article are included in the article's Creative Commons license, unless indicated otherwise in a credit line to the material. If material is not included in the article's Creative Commons license and your intended use is not permitted by statutory regulation or exceeds the permitted use, you will need to obtain permission directly from the copyright holder. To view a copy of this license, visit http://creativecommons.org/licenses/by/4.0/.

© The Author(s) 2023

CHAPTER THREE

A COMPREHENSIVE NMR ANALYSIS OF SERUM AND FECAL METABOLITES IN FAMILIAL DYSAUTONOMIA PATIENTS REVEALS SIGNIFICANT METABOLIC PERTURBATIONS

Contribution of Authors and Co-Authors

Manuscript in Chapter 3

Author: Stephanann M. Costello

Contributions: Conceptualization, Methodology, Validation, Formal analysis, Investigation, Data curation, Writing – original draft, Writing – review & editing, Visualization

Co-First Author: Alexandra M. Cheney

Contributions: Conceptualization, Methodology, Validation, Formal analysis, Investigation, Writing – original draft, Writing – review & editing, Visualization

Co-Author: Annie Waldum

Contributions: Methodology, Formal analysis, Investigation, Writing – review & editing

Co-Author: Brian Tripet

Contributions: Methodology, Software, Resources, Writing – review & editing, Supervision

Co-Author: Maria Cotrina-Vidal

Contributions: Methodology, Resources, Writing – review & editing, Supervision, Project administration

Co-Author: Horacio Kaufmann

Contributions: Investigation, Resources, Writing – review & editing, Supervision, Project administration

Co-Author: Lucy Norcliffe-Kaufmann

Contributions: Methodology, Investigation, Resources, Writing – review & editing, Supervision, Project administration

Co-Author: Frances Lefcort

Contributions: Conceptualization, Resources, Writing – original draft, Writing – review & editing, Supervision, Project administration, Funding acquisition

Co-Author: Valérie Copié

Contributions: Conceptualization, Methodology, Software, Validation, Formal analysis, Investigation, Resources, Data curation, Writing – original draft, Writing – review & editing, Supervision, Project administration, Funding acquisition.

Manuscript Information

Stephanann M. Costello, Alexandra M. Cheney, Annie Waldum, Brian Tripet, Maria Cotrina-Vidal, Horacio Kaufmann, Lucy Norcliffe-Kaufmann, Frances Lefcort, and Valérie Copié

Metabolites

Status of Manuscript:

☐ Prepared for submission to a peer-reviewed journal

☐ Officially submitted to a peer-reviewed journal

☐ Accepted by a peer-reviewed journal

☒ Published in a peer-reviewed journal

Multidisciplinary Digital Publishing Institute (MDPI)

Issue 13, volume 3, March 2023

doi: 10.3390/metabo13030433

metabolites 52 MDPI

Article

A Comprehensive NMR Analysis of Serum and Fecal Metabolites in Familial Dysautonomia Patients Reveals Significant Metabolic Perturbations

Stephanann M. Costello [1,†], Alexandra M. Cheney [1,†], Annie Waldum [1], Brian Tripet [1], Maria Cotrina-Vidal [2], Horacio Kaufmann [2], Lucy Norcliffe-Kaufmann [2], Frances Lefcort [3] and Valérie Copié [1,*]

[1] Department of Chemistry and Biochemistry, Montana State University, Bozeman, MT 59717, USA
[2] Department of Neurology, New York University School of Medicine, New York, NY 10017, USA
[3] Department of Microbiology and Cell Biology, Montana State University, Bozeman, MT 59717, USA
* Correspondence: vcopie@montana.edu; Tel.: +1-406-994-7244
† These authors contributed equally to this work.

Abstract: Central metabolism has a profound impact on the clinical phenotypes and penetrance of neurological diseases such as Alzheimer's (AD) and Parkinson's (PD) diseases, Amyotrophic Lateral Sclerosis (ALS) and Autism Spectrum Disorder (ASD). In contrast to the multifactorial origin of these neurological diseases, neurodevelopmental impairment and neurodegeneration in Familial Dysautonomia (FD) results from a single point mutation in the *ELP1* gene. FD patients represent a well-defined population who can help us better understand the cellular networks underlying neurodegeneration, and how disease traits are affected by metabolic dysfunction, which in turn may contribute to dysregulation of the gut–brain axis of FD. Here, ^{1}H NMR spectroscopy was employed to characterize the serum and fecal metabolomes of FD patients, and to assess similarities and differences in the polar metabolite profiles between FD patients and healthy relative controls. Findings from this work revealed noteworthy metabolic alterations reflected in energy (ATP) production, mitochondrial function, amino acid and nucleotide catabolism, neurosignaling molecules, and gut-microbial metabolism. These results provide further evidence for a close interconnection between metabolism, neurodegeneration, and gut microbiome dysbiosis in FD, and create an opportunity to explore whether metabolic interventions targeting the gut–brain–metabolism axis of FD could be used to redress or slow down the progressive neurodegeneration observed in FD patients.

Keywords: familial dysautonomia; NMR metabolomics; human stool and serum polar metabolite profiles; elongator protein subunit 1; ELP1; metabolism; neurodegenerative diseases; neurological disorders; gut–brain–metabolism axis; multivariate statistical analysis

check for updates

Citation: Costello, S.M.; Cheney, A.M.; Waldum, A.; Tripet, B.; Cotrina-Vidal, M.; Kaufmann, H.; Norcliffe-Kaufmann, L.; Lefcort, F.; Copié, V. A Comprehensive NMR Analysis of Serum and Fecal Metabolites in Familial Dysautonomia Patients Reveals Significant Metabolic Perturbations. *Metabolites* **2023**, *13*, 433. https://doi.org/10.3390/metabo13030433

Academic Editor: Stewart Graham

Received: 6 February 2023
Revised: 6 March 2023
Accepted: 14 March 2023
Published: 16 March 2023

Copyright: © 2023 by the authors. Licensee MDPI, Basel, Switzerland. This article is an open access article distributed under the terms and conditions of the Creative Commons Attribution (CC BY) license (https://creativecommons.org/licenses/by/4.0/).

1. Introduction

The role of the gut–brain axis in neurodegenerative diseases has become increasingly appreciated [1–3]. However, the impact of central metabolism dysfunction on the gut–brain axis of neurodegenerative diseases remains poorly understood. Herein, we have investigated serum and fecal polar metabolite changes exhibited in Familial Dysautonomia (FD) patients, and compared these to the levels of polar metabolites measured in healthy family relatives who served as a reference human control group, and are heterozygous carriers of the *ELP1* gene mutation. This comprehensive interrogation of the serum and fecal metabolomes of FD patients is part of our long-term goal to generate new knowledge about the cross-talk between gut microbes, neuronal health, and metabolism in FD [4]. New insights into the gut–brain–metabolism axis of FD could potentially be employed to redress metabolic deficits, and to guide the development of efficacious metabolism-based interventions and treatment strategies aimed at mitigating neurodegeneration and disease progression.

Familial Dysautonomia, also called Riley-Day syndrome or Hereditary and Sensory Autonomic Neuropathy type III, is a debilitating developmental and progressive neurodegenerative disease that occurs primarily in individuals of Ashkenazi Jewish decent, with >99% of all patients sharing the same homozygous founder mutation (c.2204 + 6T > C). FD results from an autosomal recessive point mutation in the *ELP1* gene encoding the elongator complex subunit 1 (ELP1) protein [5–7]. This mutation causes inefficient splicing of exon 20, which in turn introduces a premature stop codon, leading to nonsense-mediated decay of the messenger RNA (mRNA) *ELP1* transcript and subsequent tissue specific reduction in ELP1 protein expression [6–8]. Although *ELP1* is normally ubiquitously transcribed in all tissues, the protein deficit occurs predominantly in neurons [6,8]. ELP1 functions as a scaffolding protein, for the six-subunit elongator complex that mediates wobble uridine modification of transfer RNAs (tRNAs), and codon-biased regulation of mRNA translation [6,9]. The reduction in ELP1 protein levels decreases translation of mRNAs encoding DNA repair proteins and others involved in histone modification [9]. Reduced ELP1 expression also disrupts mitochondrial integrity and function [10,11], which collectively cause cellular stress and promotes neurodegeneration.

Significant impairments to both the central nervous system (CNS) and peripheral nervous system (PNS) are evident in FD, with the sensory and autonomic nervous systems being most heavily impacted [5,6,12]. Hallmarks and clinical features of the disease include reduced pain and temperature sensation, gastrointestinal dyscoordination and enteropathy, cardiovascular instability, progressive optic neuropathy, proprioception loss, and sudden unexpected death during sleep (SUDS) [5,7]. Unfortunately, there is no cure for FD and the progressive decline in neuronal survival results in a 50% mortality rate of FD patients by the age of 40 [5,6]. Additionally, the quality of life of the patients is devastatingly reduced, with current treatment strategies focusing on symptom mitigation, rather than slowing or redressing disease progression and neurodegeneration [7].

FD shares characteristic clinical features with other complex neurodegenerative diseases including Alzheimer's (AD) and Parkinson's (PD) diseases, Amyotrophic Lateral Sclerosis (ALS), and neurodevelopmental disorders such as Autism Spectrum Disorder (ASD) [13–16]. However, because the cause of FD is a single shared genetic mutation [5–7], the FD patient population is a more homogenous group to examine than patient cohorts suffering from multifactorial neurodegenerative diseases. Interestingly, mutations, and/or variants, in the genes encoding four of the other elongator complex proteins are associated with neurological and cognitive impairment disorders including ALS (with the *C9orf72* ALS associated gene variant giving rise to reduced ELP3 expression) [17], intellectual disability (associated with a mutation in the *ELP2* gene), and Rolandic epilepsy or ASD (associated with a mutation or microdeletion, respectively, in the *ELP4* gene) [13,18].

Characterizing the metabolite profiles of serum and stool samples collected from FD patients offers an opportunity to generate insights into metabolic pathways that are impacted at the systemic level and/or that are influenced by gut microbial activity. Given the rich opportunity that the serum and stool metabolomics data present for gaining new knowledge about molecular networks underlying the FD disease state, we sought to expand upon our analysis of the gut–brain–metabolism axis in FD recently reported by our group [4], by evaluating our proton (^{1}H) nuclear magnetic resonance (NMR)-based serum and fecal metabolome data in a stepwise population and pairwise manner. This comprehensive analysis ensures that noteworthy metabolite patterns relevant to FD are not overlooked, and provides an extended list of metabolites of interest, in addition to the subset originally identified as being significant when using a strictly statistical, random permutation test [4]. Examination of the full range of serum and fecal metabolite changes has provided insightful information about metabolic pathways associated with the gut–brain–metabolism axis in FD that were not readily apparent in our initial study.

Herein, an untargeted one dimensional (1D) ^{1}H NMR metabolomics approach was employed to characterize the polar metabolite profiles of serum and stool samples obtained from FD patients and their matched relatives (who served as a control group) who are

heterozygous carriers for the FD mutation. The present study has uncovered additional, prominent changes in the serum and fecal metabolomes of FD patients compared to those of their healthy relatives, expanding upon those reported in [4]. The significance of these findings, with respect to the gut–brain–metabolism axis of FD and its potential relevance to other neurological diseases, is discussed.

2. Materials and Methods

2.1. Participants and Sampling Scheme

FD patients and their relatives were recruited through the Dysautonomia Center at New York University (NYU) Langone Health. Recruitment for this study began in 2016 and samples used for this metabolite profiling analysis were collected during the patients' clinical visits from September of 2016 through January of 2020. A total of 104 participants were enrolled and involved 50 FD patients and 54 relatives (Supplementary Table S1). Worldwide, there exist only 350 individuals diagnosed with FD to date; the 50 patients recruited for this study thus represent 14.30% of the total population of individuals with this disease, which is a significant percentage. All patients enrolled in the study were homozygous for the FD founder mutation in the *ELP1* gene (c.2204 + 6 T > C) and all relatives were heterozygous, including one sibling who was enrolled as a healthy relative control. Individuals who are heterozygous for the *ELP1* gene mutation do not exhibit any of the FD clinical phenotypes and are neurotypical. Of all enrolled patients, 42 had a corresponding paired relative also enrolled; 8 FD patients were enrolled, but had no samples provided by a relative. Of the 42 FD patients enrolled with a relative, 11 of those were enrolled with an additional relative (i.e., mother or father) and 1 FD patient was enrolled with a mother, father, and sibling. The total number of participants included 45 males and 59 females. Of these, 21 male and 29 female FD patients were represented (Supplementary Table S1).

In 2016 and 2017, only stool samples were collected from the original cohort of 22 FD patients and matched control relatives. In 2018, serum samples and biological replicates were collected, together with additional stool samples from newly enrolled participants. Ideally, stool and serum samples were obtained from every participant, though individual comfort level and ability to donate prevented this in some instances. Additionally, biological replicates were obtained at times, although not very often; only 1 biological replicate at a time was included in any given statistical analysis. A summary of patient and control relative samples provided are listed in Supplementary Table S1. Clinical data (Blood Urea Nitrogen (BUN), Creatine, BUN: Creatine, estimated Glomerular Filtration Rate (eGFR), Alanine Aminotransferase (ALT), Aspartate Transaminase (AST), AST:ALT and Alkaline phosphatase levels) were provided for patients' samples that were de-identified at times of sample collections, and are included as Supplementary Information (Supplementary Figures S1 and S2).

2.2. Blood Serum and Stool Sample Collection

The Dysautonomia Center at NYU Langone Health collected and provided all samples used in this study. Due to the fragile nature of some of the patients' health, and to mitigate additional stress that fasting could have induced on the patients, no sample donors were required to fast prior to any sample collection. Peripheral venous blood samples were collected in test tubes containing clot activator, allowed layer separation for 30 min, and spun at 3000 rpm for 10 min for serum separation. Aliquots of serum were partitioned into 15 mL vials and frozen at −20 °C, batch shipped overnight on dry ice and stored at −80 °C until used for metabolomics analysis. Collection kits (commode/hat) were provided to participants for self-collection of stool samples at home or in-patient visits. Stool samples were collected at the NYU Langone's Dysautonomia Center, transferred to 50 mL conical tubes either fresh, from the same day, or previously frozen at −20 °C by the patient and/or relative. As with the serum samples, stool samples were stored at −20 °C at the clinic until

batch shipped overnight on dry ice and then stored at −80 °C until they were extracted for metabolomics analysis.

2.3. Human Serum Sample Preparation and Serum Metabolite Extraction

Serum samples stored at −80 °C were thawed on ice, partitioned into 400 µL aliquots and 1600 µL of acetone added to each aliquot (1:4 v/v ratio of serum to acetone). Samples were mixed by inversion, incubated at room temperature (25 °C) for 20 min, and then incubated at −20 °C for 1 h. Samples were centrifuged at 10,000× g for 10 min and resulting supernatants were transferred to new 2.0 mL microcentrifuge tubes, and dried using a speed vacuum concentrator overnight, without heat. The dried metabolite mixtures were reconstituted in 600 µL of serum-specific NMR buffer (0.25 mM sodium trimethylsilylpropanesulfonate (DSS) in 90% H_2O/10% D_2O, 0.4 mM imidazole, 25 mM NaH_2PO_4/Na_2HPO_4, pH 7), and transferred to a 5 mm Bruker NMR tube.

2.4. Human Fecal Sample Preparation and Stool Metabolite Extraction

Fecal samples stored at −80 °C were thawed at room temperature (25 °C) and homogenized by spatula stir mixing in their original 50 mL conical tubes. Aliquots of 500 mg were measured into 2 mL twist cap centrifuge tubes, flash frozen and stored at −80 °C until further use. For each aliquot, 1 mL of stool-specific NMR buffer (0.1 M Na_2HPO_4/KH_2PO_4, pH 7.37, 0.25 mM DSS, 0.4 mM imidazole, 0.01% sodium azide, in 90% H_2O/10% D_2O, pH 7.0) was added to achieve a 1:2 w/v (wet fecal-weight to buffer-volume) ratio. Samples were homogenized using a Millipore FastPrep-24^{TM} 5G bead beater, set at 6.0 m/s for 40 s. Samples were centrifuged at 10,000× g for 10 min and the supernatants were transferred to new 2.0 mL microcentrifuge tubes. The stool metabolite extraction process was repeated once more using the centrifuged fecal pellets and a fresh 1 mL of stool NMR buffer to collect a second supernatant fraction for each sample. Both supernatant fractions were combined, centrifuged, and filtered using the following: centrifugation at 21,000× g for 10 min and filtering using a 4 µm syringe filter. Resulting filtrates were then centrifuged at 21,000× g for 10 min and filtered using a 3 kDa filter to remove residual large particulates. The final pH of the sample was adjusted to 7.0, prior to transferring 600 µL of the sample solution into a 5 mm Bruker NMR tube for NMR experiments. A second 500 mg aliquot of stool sample was lyophilized to determine the percent water weight and dry mass for each extracted metabolite stool aliquot.

2.5. NMR Spectra Acquisition and Preprocessing

All NMR spectra were collected using a Bruker 600 MHz (^{1}H Larmor frequency) AVANCE III solution NMR spectrometer equipped with a 5 mm triple resonance (^{1}H, ^{13}C, ^{15}N), liquid helium-cooled cryoProbe, automatic sample loading system (SampleJet), and Topspin software (Billerica, MA, USA, Bruker version 3.2). The Bruker gradient-based water suppression "zgesgp" pulse sequence [19,20] was used for the acquisition of 1D ^{1}H NMR spectra, which were recorded at 300 K with the following parameters: 256 scans, 64K data points, a 69 µs dwell time, and a ^{1}H spectral window of 12.0166 ppm, resulting in a NMR spectrum data acquisition time period of ~4.5 s. A recovery delay time (D1) between acquisitions was set to 2.0 s, resulting in a total relaxation recovery delay of ~6.5 s between scans. Chemical shift referencing using DSS and phase correction of 1D ^{1}H NMR spectra were conducted using Topspin (Billerica, MA, USA, Bruker version 3.2), as previously reported [19,21,22]. Baseline and phase correction were executed in Topspin with 0.80 Hz line broadening for exponential multiplication prior to Fourier transformation to give the preprocessed '1r' NMR file.

2.6. NMR Spectra Profiling and NMR Signal and Metabolite Annotation Validation

Chenomx NMR Suite software (version 8.4; Chenomx Inc., Edmonton, AB, Canada) was used for the additional processing of 1D ^{1}H NMR spectra and metabolite identification (i.e., metabolite ID) and quantification. The preprocessed '1r' NMR spectral files

were imported into the Chenomx software and baseline adjusted using the automatic cubic spline function (Chenomx Spline). Manual breakpoint adjustments were applied to obtain a well-defined, flat baseline that did not bias the area under the spectral signal intensities, following guidelines from Chenomx application notes and previously reported methods [23,24]. The most upfield ^{1}H signal of DSS was set to 0.0 ppm for chemical shift referencing, and the ^{1}H NMR resonance of imidazole was used to correct for small chemical shift variations arising from slight changes in sample pH. Metabolite identification and quantitation was achieved by fitting the spectral patterns present in reference spectra of small molecules, which are part of the Chenomx small molecule spectral database for 14.1 T magnetic field strength NMR spectrometers and the human metabolomics database (HMDB) [25], to the ^{1}H chemical shifts, spectral splitting patterns, and signal intensities present in each stool or serum spectrum. A manual peak-based fit style in Chenomx was applied, which permitted optimal fits for compound peak cluster location and intensity [26]. Characteristic NMR spectra of serum and stool samples, with annotated metabolite IDs, are presented as illustrations in the Supplementary Figures S3 and S4, respectively. Relative intensities were calibrated to DSS (0.25 mM), which was used as an internal standard to quantify metabolite levels and to generate lists of metabolite concentrations. Confirmation of the metabolites' IDs was achieved by spiking of the pure metabolite standards into the metabolite mixture samples, as needed.

2.7. Unpaired Univariate and Multivariate Statistical Analyses

Quantitative metabolite profiles were exported from the Chenomx software, as μM concentrations. Prior to multivariate statistical analyses using MetaboAnalyst v.4.0 (Edmonton, AB, Canada), the metabolite concentrations were normalized to serum volume (nanomoles/mL) and to dry fecal mass (nanomoles/g) for stool samples [27]. The serum metabolite concentrations varied widely, from <10 nmol/mL for some metabolites to >5000 nmol/mL for others (Supplementary Table S2). Stool metabolites also varied in concentrations, ranging from <5 nmol/g to >200,000 nmol/g and varied between and within the sample populations as seen in the standard deviations reported in Supplementary Table S3.

The biomass normalized data were evaluated in terms of percent differences in mean metabolite concentrations between the FD patient group and the healthy relative control group. For multivariate and univariate statistical analyses, metabolite concentrations were statistically normalized using logarithmic transformation (log base 10) to ensure a Gaussian distribution of the data [28] and autoscaling, (i.e., centering of each metabolite concentration around the mean divided by the standard deviation) [29]. The data were then analyzed using unsupervised Principal Component Analysis (PCA), supervised Partial Least Squares-Discriminant Analysis (PLS-DA), random forest, and volcano plot analyses (*t*-tests and fold changes (FC)). Additional validation metrics of the PLS-DA models were applied using MetaboAnalyst v.4.0 package and associated R programs. PLS-DA model validity was assessed using a leave-one-out validation test for predictive variability metrics (Q^2) and predicted residual sum of squares (PRESS) error (R^2), separation distance and prediction accuracy permutation tests (n = 1000), classification error rates (CER), and area under the receiver operating characteristic curve (AUROC) (Supplementary Figures S5 and S6) [30].

2.8. Paired Multivariate Statistical Analyses

To account for variability observed in FD patient serum and stool metabolite profiles, paired analyses were conducted by pairing the metabolite profiles of an FD patient to those of their direct healthy relative(s), who served as control(s). Two lists (referred to as versions 1 and 2) of FD patient-healthy relative pairs were generated, using the following exclusion criteria: (1) data from an FD patient or a relative were omitted if there was no sample to be paired with, i.e., when a patient or relative did not donate a sample with their family member; or (2) when an additional family member donated a sample, resulting in two or more pairing schemes; and (3) biological replicates (i.e., the same donor provided

a sample more than once). These exclusion criteria ensured that samples were always paired and that an individual was only represented once in the dataset by omitting multiple patient–relative pairings and biological replicates. Altogether, this led to the generation of 34 possible unique patient–relative pairs for a given paired dataset, which were used for the paired analysis of either serum or stool metabolite patterns.

In the end, two randomly generated paired datasets were used (referred to as paired versions 1 and 2) and the metabolite patterns were examined for similarities and differences between the FD patient and their healthy relative control. These two lists also enabled us to evaluate whether the metabolites found to exhibit significant level differences between the FD patient and relative, depended on which version of the pairs was employed. Similar to our unpaired data analyses, paired *t*-tests and FC analyses were conducted using MetaboAnalyst v.4.0 (Edmonton, AB, Canada) and evaluated using volcano plots.

2.9. Metabolic Pathway Impact Analysis

Once sets of metabolites were identified from the serum and stool metabolomics data and found to be significant with statistical analyses, metabolite patterns were further investigated for their relevance to both human and gut-microbial metabolic pathways. A literature review was first conducted to mine published reports about established pathway(s) and function(s) associated with each individual metabolite or class of metabolites. A metabolic pathway impact analysis was then performed using MetaboAnalyst v.4.0 (Edmonton, AB, Canada) to ensure that all possible pathways of interest were taken into account or not excluded due to a potential lack of available information in the literature.

3. Results

3.1. Metabolite Concentration Differences Separate FD Patients from Their Healthy Control Relative Populations

A total of 55 serum and 73 stool polar metabolites were identified and quantified from the analysis of 1D ^{1}H NMR spectra obtained from FD patients and control relatives, using the Chenomx 8.6 (Chenomx Inc., Edmonton, AB, Canada) software suite.

Percent differences in metabolite mean concentrations (FD patient/Relative control) were calculated to identify potential metabolites with concentration differences that contribute to group separation between the FD patient and healthy relative (Supplementary Tables S2 and S3) populations. We determined that metabolite level differences < 10% were likely not significant due to the extensive heterogeneity of FD disease phenotypes. Serum metabolites with percent level differences >10% were viewed as potentially informative of serum metabolome changes between patients and controls, and were examined as possible contributors to the distinction between the FD patient and healthy control groups, while mean metabolite level differences $\geq$ 40% were viewed as potentially more discriminatory. A similar classification of fecal metabolites based on percent differences in mean concentrations was conducted. However, a threshold of > 20% difference was used to exclude select stool metabolites for which level differences were most likely too small to discriminate between FD patients and healthy controls, as the heterogeneity of the stool metabolite profiles was higher than the one observed for the serum samples.

Using this approach, 22 serum metabolites were selected as potentially valuable discriminators of the FD disease state (Supplementary Table S2) from the healthy relative control group. Serum metabolites exhibiting $\geq$ 40% mean differences between the FD patient and control groups included: xanthine, 1,7-dimethylxanthine, urea, and π-methylhistidine. Six serum metabolites with mean percent differences ranging between 20% and 40% included: glycolate, propylene glycol, dimethyl sulfone, methanol, glycine, and 2-hydroxybutyrate. Lastly, 12 serum metabolites exhibited 10% to 20% mean concentration differences, and included the following: isopropanol, inosine, betaine, pyruvate, dimethylamine, glycerol, serine, leucine, valine, taurine, isoleucine, and alanine.

Similarly, 21 stool metabolites with a mean percent difference $\geq$40% were identified and included: dopamine, lactate, formate, beta-alanine, choline, malonate, ethanol,

succinate, 5-aminopentanoate, 4-hydroxyphenylacetate, 1,1-dimethylbiguanide, tyramine, taurine, glucitol, ornithine, histidine, trimethylamine, sarcosine, isocaproate, p-cresol, and tryptophan (Supplementary Table S3). Stool metabolites with a mean percent concentration difference between the FD patients and healthy controls ranging between >20% and <40% included: glycine, indole, 2-aminobutyrate, valine, glycerophosphocholine, isovalerate, threonine, phenylalanine, orotic acid, alanine, D-glucose, glutarate, methylsuccinate, lysine, leucine, phenylacetic acid, isoleucine, arginine, xylose, proline, tyrosine, and isobutyrate (Supplementary Table S3).

3.2. The Serum and Stool Metabolomes of the FD Patient Group Differ Significantly from the Metabolomes of the Healthy Relative Control Group

Metabolite concentrations normalized to volume (for serum samples) or dry weight (for stool samples) were further normalized for statistical analyses using the MetaboAnalyst software v.4.0 (Edmonton, AB, Canada) [27] by applying the log transformation and autoscaling functions. A population-wise assessment of the metabolome profiles of the FD patient and control groups was conducted using an unpaired, unsupervised multivariate principal component analysis (PCA), to assess whether the two human subject groups could be separated based on distinct serum or stool polar metabolomes. A three-dimensional (3D) PCA scores plot of the serum metabolite profiles, shown in Figure 1A, revealed a small but noticeable clustering of the FD patient group (orange) from the healthy relative control (blue) group. The extent of the separation of the two groups, based on characteristic serum metabolite profiles, was further examined using a supervised partial least squares-discriminant analysis (PLS-DA) (Figure 1B) [31]. Although the 3D-PCA scores plot of the stool metabolomes displayed little separation between the FD patient and control groups (Figure 1C), the PLS-DA supervised analysis was more informative, revealing a clearer separation between the two groups (Figure 1D). Examination of the scree plots associated with the 3D-PCA analyses provided information regarding the contribution of each principal component (PC) to the total variance, and demonstrated that PC1-3 are most influential (in terms of their % contribution to the total variance) for the separate clustering of the FD patient group from the healthy relative control group (Supplementary Figure S7).

To assess the legitimacy of the PLS-DA models, validation metric analyses, including R^2, Q^2, permutation tests, CER, and AUROC analyses were performed and are included as Supplementary Information (Supplementary Figures S5 and S6) [30]. Results from these validation tests demonstrated the validity of the PLS-DA models, and indicated that the separation of the FD group from the control group based on distinct serum and fecal metabolomes is a real phenomenon, and that the PLS-DA models are not overfit. Some of the validation metrics examined were at what we may consider the validation limit (for example, representing a 25% CER; see Supplementary Information), but within the range of values expected given the nature and variability of the serum and stool samples received, and the fact that the patients and relatives provided serum and stool samples at their convenience rather than at fixed times and were not diet restricted.

Random forest analyses of serum and stool metabolite profiles further supported the separate clustering of the FD and control groups and were consistent with CER results associated with PLS-DA models (Supplementary Figure S8).

Metabolites with concentration differences that contributed most significantly to the separate clustering of the FD patient and healthy relative control groups in the 3D-PLS-DA analyses were further evaluated using variable importance in projection (VIP) score plots (Figure 2), which provided valuable information on useful metabolite discriminators when associated with VIP scores ≥ 1.2 [22]. VIP Scores for component 1-3 (Figure 2 and Supplementary Tables S4 and S5) were examined in terms of which specific metabolites contributed most to the group separation along component 1, 2, or 3. Not surprisingly, several metabolites contributed to group separation along more than one component axis of the 3D-PLS-DA scores plots shown in Figure 1B,D.

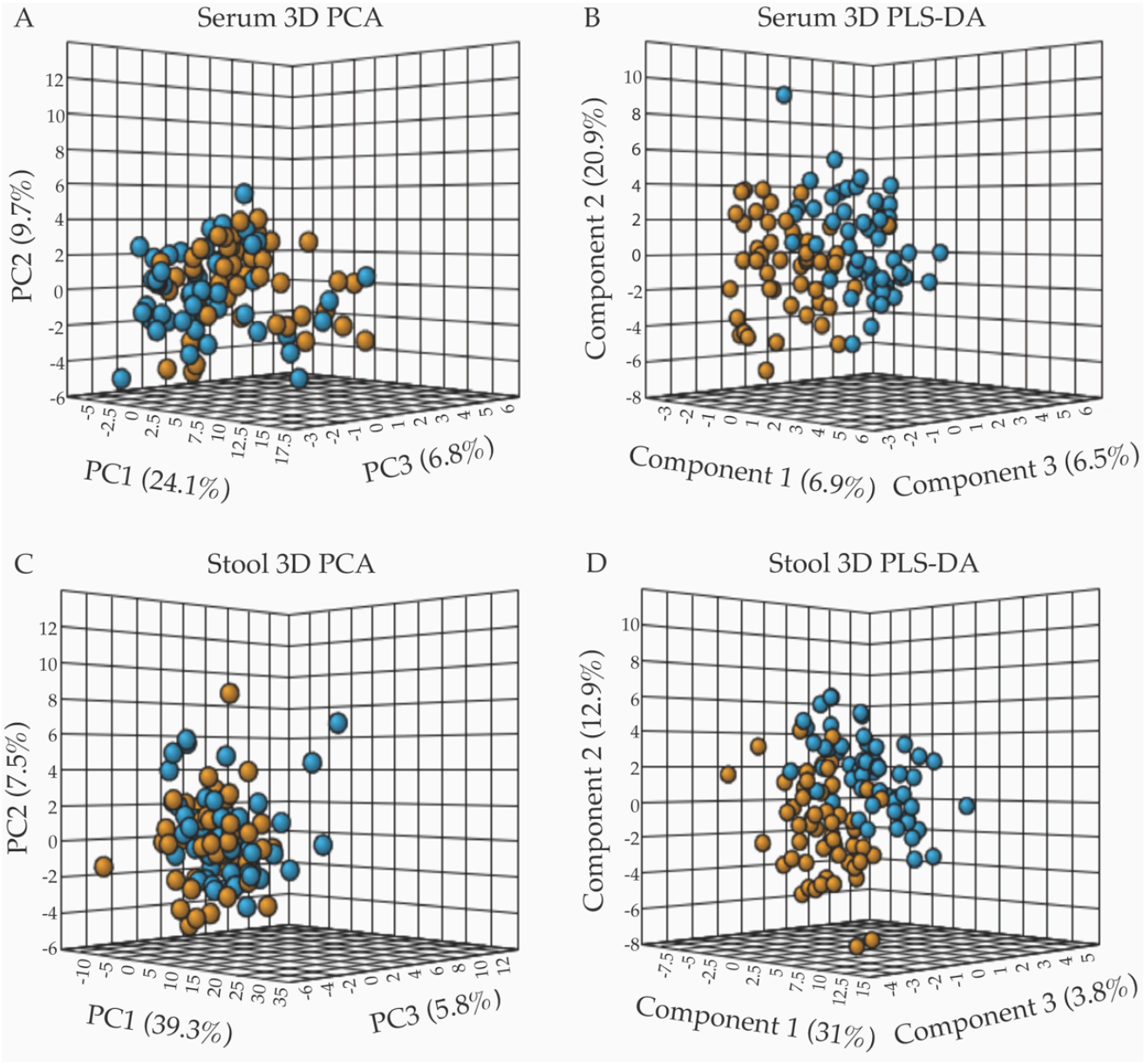


Figure 1. Multivariate statistical analyses of serum and fecal metabolic profiles separate the FD patient population (orange) from the control relative group (blue), with panels (**A**,**B**) presenting the 3D-PCA and 3D-PLS-DA scores plots from the analyses of serum metabolite patterns, and panels (**C**,**D**) those from fecal sample analyses. (**A**) 3D-PCA scores plot obtained from the principal component analysis (PCA) of serum metabolite patterns reveals little separation between the FD patients and healthy control relative groups, with PC1, 2, and 3 accounting for 40.6% of the variance. (**B**) 3D-PLS-DA scores plot obtained from partial least-squares discriminant analysis (PLS-DA) of serum metabolites resulted in the separate clustering of the FD patient and healthy relative control groups, with components 1–3 accounting for 34.3% of the variance. (**C**) 3D-PCA scores plot of stool metabolite profiles, revealing minimal separation between groups, with PC1-3 accounting for 52.6% of the variance. (**D**) 3D-PLS-DA scores plot analysis of stool metabolite profiles indicated a clear separation of the FD patient group from the control group based on distinct fecal polar metabolomes, with components 1–3 accounting for 47.7% of the variance. All data shown in Figure 1 (3D-PCA and PLS-DA scores plots) were generated using the MetaboAnalyst v.4.0 software (Edmonton, AB, Canada).

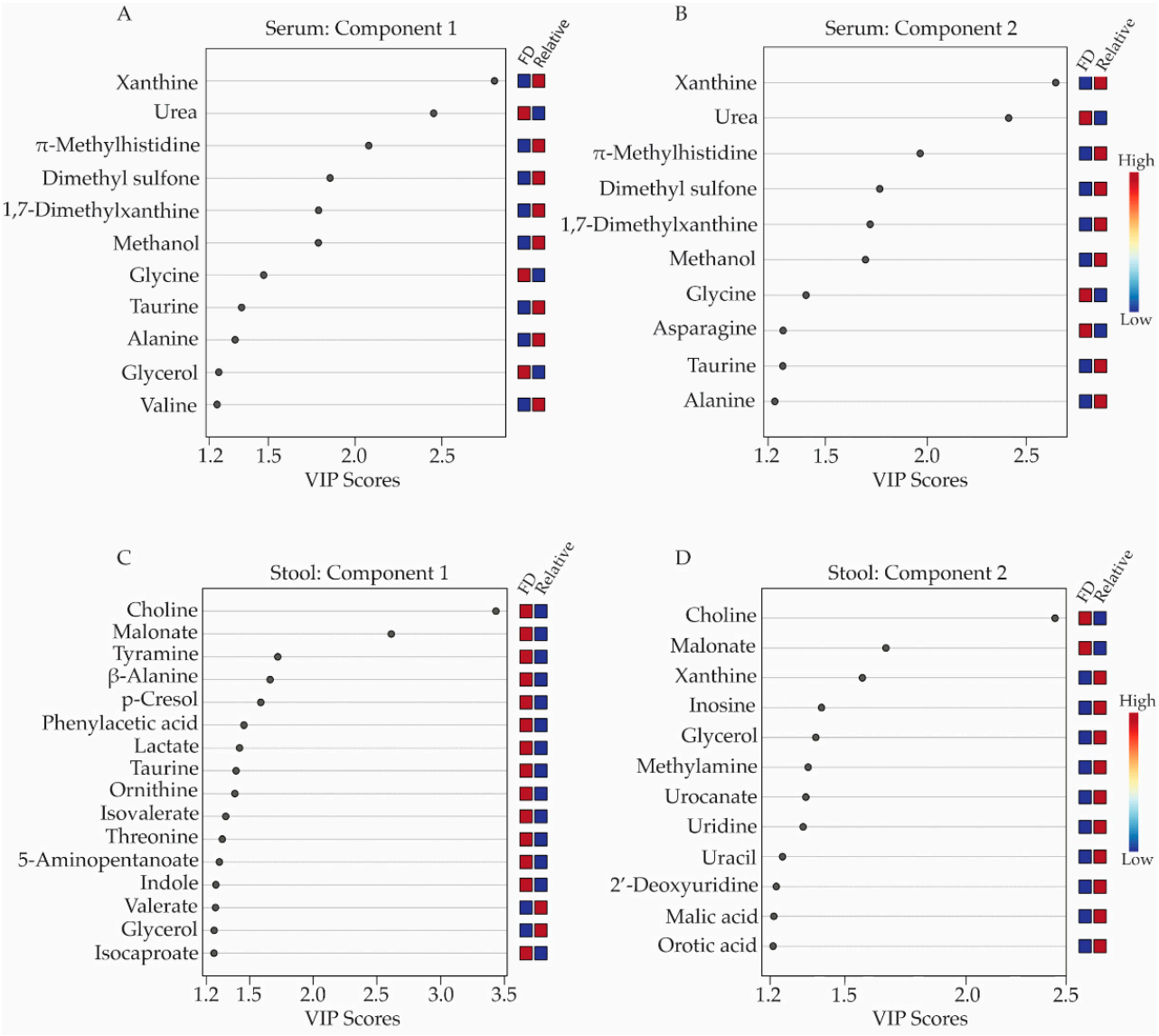


Figure 2. Variable importance in projection (VIP) score plots corresponding to the first two components of the 3D-PLS-DA models obtained from serum and stool metabolite profiles. Metabolites with VIP scores ≥ 1.2 were considered a significant contributor to the distinct clustering of the FD patient and the healthy relative control groups along components 1 and 2 of the 3D-PLS-DA scores plots. Panels (**A**,**B**) display the VIP score plots for the serum metabolites, while panels (**C**,**D**) presents the VIP score plots for the stool metabolite profiles. Relative metabolite levels range from high (red boxes) to low (blue boxes), indicating whether the metabolite concentrations are higher or lower in the FD patient group relative to the levels measured in the healthy relative control group. All VIP scores plots shown in Figure 2 have been generated from PLS-DA modeling conducted in MetaboAnalyst v.4.0 (Edmonton, AB, Canada).

When examining serum metabolites associated with components 1 and 2 of the PLS-DA scores plots, the VIP scores plots identified 11 and 10 serum metabolites, respectively, that were significant contributors (i.e., VIP ≥ 1.2) to the separate clustering of the FD patient and control groups (Figure 2A,B, and Supplementary Table S4), with glycerol and valine being unique to component 1 and asparagine being unique to component 2. Seven of these metabolites were lower in concentrations in the sera of FD patients and included: xanthine, π-methylhistidine, dimethyl sulfone, 1,7-dimethylxanthine, methanol, taurine, alanine,

and valine, while four metabolites, urea, glycine, glycerol, and asparagine were higher in concentration in the FD patient group compared to the healthy relative control group.

For the stool samples, 17 metabolites with VIP scores $\geq$ 1.2 were identified. For component 1 (Figure 2C, Supplementary Table S5), 14 of these were in higher concentration in the stool of FD patients and included choline, malonate, tyramine, beta-alanine, p-cresol, phenylacetic acid, lactate, taurine, ornithine, and isocaproate. Two remaining metabolites with a VIP $\geq$ 1.2 were lower in concentrations in the stool of the FD patients and consisted of valerate and glycerol. Additionally, the VIP scores plot corresponding to component 2 of the PLS-DA model highlighted 10 other stool metabolites that were important for the distinct classification of the two human subject groups and included xanthine, inosine, methylamine, orotic acid, malic acid, urocanate, uracil, 2′-deoxyuridine, uridine and methionine, all exhibiting lower concentrations in the stool samples of FD patients compared to healthy relative controls, except for methionine (Figure 2C and Supplementary Table S5).

Further evaluation of the metabolome differences between the FD patient and healthy relative control groups was performed using an unpaired volcano plot analysis, which takes into account results from both two-sample *t*-tests and fold change (FC) analyses. The unpaired volcano plot analysis (Table 1) identified six significant serum metabolites (false discovery rate (FDR) corrected p value < 0.05 and FC threshold $\geq$ 1.2) consisting of xanthine, urea, π-methylhistidine, 1,7-dimethylxanthine, dimethyl sulfone and methanol, which were all lower in concentrations in the FD group except for urea (Table 1). When using an FDR corrected p value $\leq$ 0.05 and a fold change threshold of $\geq$2.0, only two stool metabolites, choline, and malonate, were found to be significant in the unpaired data analysis. When statistical stringency was relaxed (i.e., using an FDR corrected p value $\leq$ 0.3 and FC $\geq$ 1.2), three additional stool metabolites, tyramine, beta-alanine, and p-cresol were identified as significant, and all five metabolites were higher in concentrations in the stool samples of FD patients compared to the control group (Table 1).

Table 1. Unpaired volcano plot analysis of serum and stool metabolite concentrations between the FD patient and control relative sample groups.

Serum Metabolites	**Fold Change (FC)**	**$\log_2$(FC)**	***p* Value (FDR)**	**$-\mathrm{LOG}_{10}$(p)**
Xanthine	0.53	−0.90	1.90×10^{-4}	3.72
Urea	1.44	0.53	1.69×10^{-3}	2.77
π-Methylhistidine	0.59	−0.75	1.44×10^{-2}	1.84
1,7-Dimethylxanthine	0.55	−0.86	3.80×10^{-2}	1.42
Dimethyl sulfone	0.72	−0.47	3.80×10^{-2}	1.42
Methanol	0.73	−0.46	3.80×10^{-2}	1.42
Stool Metabolites	**Fold Change (FC)**	**$\log_2$(FC)**	***p* Value (FDR)**	**$-\mathrm{LOG}_{10}$(p)**
Choline	3.41	1.77	8.22×10^{-6}	5.08
Malonate	3.17	1.66	3.15×10^{-3}	2.50
β-Alanine	5.42	2.44	0.26	0.58
Tyramine	1.93	0.95	0.26	0.58
p-Cresol	1.42	0.51	0.28	0.54

Unpaired volcano plot analysis indicating fold change (FC) and two-sample *t*-test significance. A fold change threshold of $\geq$1.2 and a p value with FDR correction < 0.05 (serum) and <0.3 (stool) were set as significance criteria. Fold changes were taken as the ratio of the mean metabolite concentrations for the FD patients' group compared to the healthy control relatives' group prior to the application of statistical normalization (log transformation and autoscaling).

3.3. Paired Analyses of FD Patient and Healthy Relative Serum and Stool Metabolomes Further Highlights Metabolic Changes Associated with FD

Next, we conducted paired analyses of the serum and stool metabolite profiles to account for individual patient to relative control pair variability. Pairwise analyses of FD patient-healthy relative pairs were undertaken to examine whether additional metabolite patterns that report on FD could be revealed, and which could have been masked in the population-wise studies due to distinct external factors affecting FD patients or their relatives. These potentially confounding factors could be due to FD patients or relatives experiencing different environments, being on different diets, or in the case of FD patients, exhibiting different disease severity traits.

Based on the exclusion criteria described in the materials and methods section, two sets of 34 possible unique patient–relative pairs were generated for both the serum and stool samples. These two datasets of patient-relative pairs were used to evaluate whether the specific pairs chosen influenced certain metabolites that were found to be significant contributors to the discrimination between FD patients and healthy controls.

Both lists (paired version 1 and 2) of FD patient-relative pairs yielded comparable results when subjected to a paired volcano analysis (FC $\geq$ 1.2, FDR corrected p value < 0.05), identifying two serum metabolites, urea and xanthine, as significant discriminators between FD patient and healthy relative pairs (Table 2). Similar paired analyses were conducted with stool metabolite profiles, which identified three metabolites, choline, malonate, and taurine, as significant discriminators of an FD patient from their respective healthy control relative. All three stool metabolites were in higher concentrations in FD patients' samples compared to their paired relatives' samples (Table 2).

Table 2. Paired volcano analysis of serum and stool metabolite profiles obtained from the v.1 and v.2 list of FD patient–relative control pairs.

Serum Paired Volcano Analysis Version 1:				
	FC	**$\log_2$(FC)**	***p* Value (FDR)**	**$-\mathrm{LOG}_{10}$(p)**
Xanthine	0.40	−1.34	1.44×10^{-2}	1.84
Urea	1.38	0.47	1.44×10^{-2}	1.84
Serum paired volcano analysis version 2:				
	FC	**$\log_2$(FC)**	***p* value (FDR)**	**$-\mathrm{LOG}_{10}$(p)**
Xanthine	0.35	−1.51	3.26×10^{-3}	2.49
Urea	1.39	0.48	1.15×10^{-2}	1.94
Stool paired volcano analysis version 1:				
	FC	**$\log_2$(FC)**	***p* value (FDR)**	**$-\mathrm{LOG}_{10}$(p)**
Choline	3.36	1.75	1.19×10^{-3}	2.92
Stool paired volcano analysis version 2:				
	FC	**$\log_2$(FC)**	***p* value (FDR)**	**$-\mathrm{LOG}_{10}$(p)**
Choline	2.34	1.23	3.58×10^{-2}	1.45
Malonate	2.14	1.10	6.69×10^{-2}	1.17
Taurine	3.04	1.60	8.65×10^{-2}	1.06

Two separate, randomly generated paired datasets for both serum and stool metabolite data. A paired volcano analysis was performed for each paired dataset. Fold change (FC), logarithmic fold change ($\log_2$(FC)), and paired *t*-test *p* values are presented. The fold change threshold was $\geq$1.2 and $\leq$0.8, and the FDR corrected *p* value threshold was <0.05 (serum) and <0.1 (stool). Fold change values for each metabolite were obtained from average values measured in FD patients/Control Relative pair ratios; a negative FC indicates lower levels in FD patients compared to their paired relatives, whereas a positive FC indicates higher levels in FD patients.

Overall, the order and extent of significance (as assessed by FDR corrected *p* values) of the metabolites identified as discriminating between the paired subject groups were

influenced by which list of patient-healthy relative pairs was chosen for analysis. However, similar metabolites were found to be important, irrespective of which paired list was used. In the case of the population-wise (unpaired) analysis, all patients and relatives were represented with a single biological replicate, thus allowing for the identification of a greater number of significant metabolites. Paired ratios have only a subset of the samples, which likely does not provide sufficient statistical power to attribute some of the metabolites as significant in the paired analysis compared to the unpaired analysis.

Considering results from all these analyses and a thorough metabolic pathway review, serum metabolites that were distinct contributors to the separation of the FD patient group from their healthy control relative group, and that alluded to potentially impacted metabolic pathways, could be classified as markers of energy homeostasis pathways (amino acid catabolism, branched chain amino acids (BCAAs), and urea), tricarboxylic acid (TCA) cycle activity and mitochondrial function (taurine), and the purine salvage pathway (xanthine and inosine). Stool metabolites that were consistent discriminators of FD patients from healthy relative controls and connected to distinct metabolic pathways could be grouped as neuronal metabolites (choline, taurine, beta-alanine, and tyramine) and gut-microbial related metabolites (choline, p-cresol, tyramine, beta-alanine, and valerate).

4. Discussion

Our extensive analysis of polar serum and stool metabolite profiles indicated distinct metabolic shifts in FD patients compared to what is observed in healthy control relatives. Due to the rarity of FD, this study achieved a statistically rich sampling of the population of individuals afflicted; herein, we analyzed ~14% of all individuals diagnosed with FD worldwide. Both serum and stool polar metabolite profiles provided snapshots of the systemic and gut/excretory metabolic states of FD patients and resulted in a clear separation of FD patients from healthy relative controls based on distinct metabolic characteristics. These findings are particularly remarkable given that the serum and stool samples were collected from FD patients in uncontrolled environments exhibiting diverse phenotypic traits and different degrees of disease severity.

This analysis extends from work that we recently reported on the gut–brain–metabolism axis in FD [4], providing additional information on the serum and fecal metabolome changes observed in FD patients and their potential significance. The present study analyzes metabolome data by population (FD patients versus control group) and in a pairwise fashion (each FD patient matched to their cohabitating healthy relative control), rather than exclusively using a permutation algorithm of pairwise samples [4]. Comparing results from the population and pairwise analyses aimed to minimize the influence of confounding factors among patients or relatives, which could have included the environment (patients and matched relatives likely share distinct environments); genetics (parents of FD patients have one copy of the *ELP1* gene mutation and are a close genetic match); and diet (cohabitating individuals likely share comparable diets, when possible).

In our previous analysis [4] of microbiome and metabolome changes, additional variables such as sex, weight, body mass index, age, use of antibiotics, fundoplication (a gastric surgery to reduce acid reflux), and use of a gastrostomy tube (G-tube) were all assessed for potential correlations to the changes observed. The only correlations between the metabolite levels and these external parameters involved patients who had received fundoplication surgery and stool choline levels. However, out of 41 patients who donated stool samples, 28 had received fundoplication surgery, representing a larger group than patients without (n = 13). Thus, our results on stool choline levels are unlikely to have been skewed by this association.

In order to prevent adverse health effects from our sampling effort on the patient population, we did not request that stool and serum samples be collected at specific times or restrict patients to the same diet as their control relatives. Patients were permitted flexibility regarding when and where they collected and provided samples, which may have resulted in some of the heterogeneity in the metabolite patterns observed and could subsequently

mask the significance of certain metabolite differences. The population and pairwise analyses were undertaken to ensure that metabolites of interest, which are potentially relevant to FD, would not be overlooked by solely relying on a random selection approach of patient-relative pairs ([4]), while still maintaining an unbiased approach to interrogate the data. Results from the current more detailed analysis of FD patient metabolite profiles clearly demonstrate that the mutation in the *ELP1* gene responsible for FD is associated with multiple notable changes in patient metabolomes, and provides strong support to the physiological data that suggests FD patients experience significant metabolic deficits [32,33].

Of the 55 serum and 73 stool polar metabolites identified and quantified, differences in the levels of eight serum and eight stool metabolites were found to be of significant interest through both unpaired and paired statistical analyses and thorough pathway impact analyses. For serum samples, these metabolites included urea, which was found to be significantly elevated in the FD patient group (Supplementary Table S2). In contrast, the serum metabolites xanthine, inosine, leucine, valine, taurine, isoleucine, and alanine were either significantly decreased (as assessed by statistical FDR corrected p values) or trending toward being in lower concentrations in the sera of FD patients compared to the levels measured in the sera of the healthy control relative group (Supplementary Table S2).

With respect to stool samples, the six metabolites (beta-alanine, choline, malonate, tyramine, taurine, and p-cresol) were found to be significantly elevated in the FD patient group compared to the healthy relative controls. In contrast, levels of fumarate and valerate trended toward being lower in FD patients (Supplementary Table S3).

Examination of the serum and stool metabolite patterns measured in FD patients support previous clinical reports suggesting FD patients experience metabolic energy deficits [7]. In addition, this NMR-based metabolomics study identified other metabolic pathways that are likely implicated in the phenotypic expression of FD. The clinical premise that FD patients suffer from a metabolic energy deficit is supported by our observations that the levels of several serum metabolites associated with energy (ATP) production and nucleotide salvage pathways are altered in FD patients compared to controls. These include metabolites associated with amino acid catabolism (alanine, BCAAs, and urea), the purine salvage pathway (xanthine and inosine), and mitochondrial dysfunction (taurine) (Figures 3 and 4).

A metabolic pathway impact analysis was undertaken for the stool metabolome data using literature information and MetaboAnalyst v.4.0. Such analyses resulted in the grouping of the eight metabolites of interest in four different categories as follows: (1) choline and taurine; (2) tyrosine, fumarate, and p-cresol; (3) beta-alanine and malonate; and (4) valerate (Figure 5 and Supplementary Figures S9–S11). Of these metabolites and pathways impacted, those with relevance to the gut microbiome and nervous system were of primary interest and presented potential insights into how metabolic networks impact FD disease traits through gut-microbe dysbiosis and/or exacerbation of neurodegeneration. Four of the eight stool metabolites identified as being significant and relevant to neural signaling included choline, taurine, beta-alanine, and tyramine (Supplementary Figure S12). Five of these eight metabolites could also be associated with gut microbes, and included tyramine, p-cresol, valerate, beta-alanine and choline. The gut-microbial and metabolic conclusions drawn for these metabolites regarding FD are consistent with published reports highlighting mechanisms by which the gut microbiome contributes to gut health and functionality, disease development, energy homeostasis, bioactive compound production, and the modulation of the communication within the gut–brain axis [1–3,34–37].

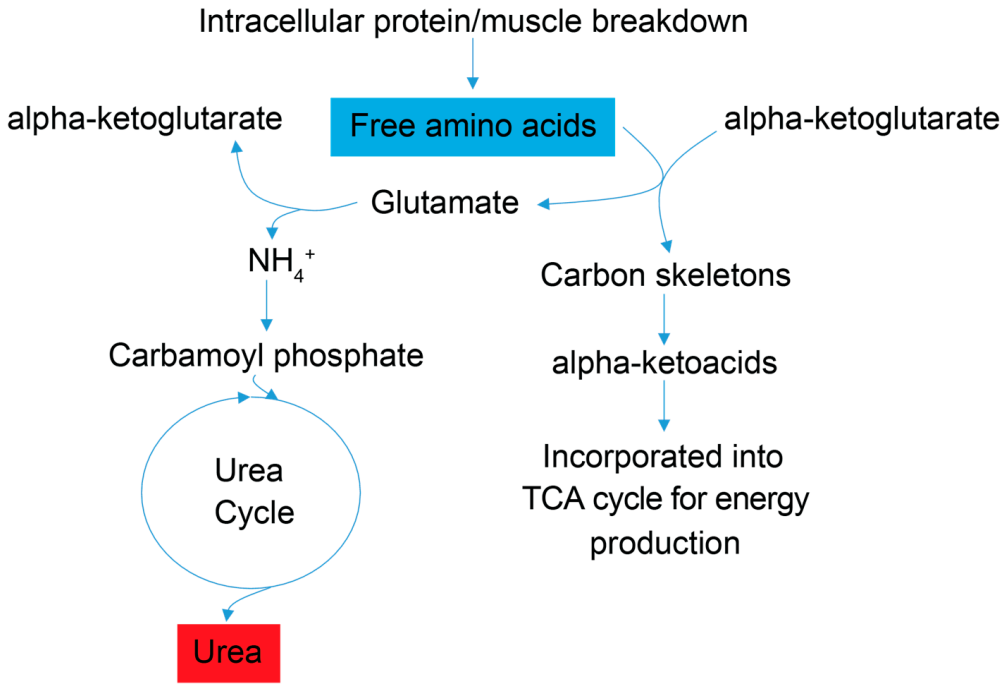


Figure 3. Simplified schematic of amino acid catabolic pathways used for ATP production. Enhanced amino acid degradation, a signature of energetic needs, is supported by an increased concentration of urea in FD patient sera. As indicated by enhanced catabolism of the amino acids alanine and asparagine, and the BCAAs valine, leucine and isoleucine, all trending to be lower (blue). Subsequently, a byproduct of the catabolism of amino acids for energy homeostasis is urea (red), which is then excreted. Red metabolites are increased in FD patient sera, and blue metabolites are decreased.

The distinct serum and stool metabolic profiles of FD patients support clinical observations and revealed metabolic changes in FD disease at the systemic and gut-function levels (discussed further below). Together, these data support the notion that disruption in nutrient absorption and gut microbiome metabolic efficacy contribute to an overall systemic energy deficit, and lead to compensatory metabolic adaptations giving rise to altered polar metabolite patterns, as observed in this study. Lastly, taurine exhibited interesting trends in both serum and stool samples (trending toward a decrease in serum and an increase in stool), suggesting a possible systemic deficit of taurine induced by either diet or gut-absorption capacity with potentially profound impacts on host metabolism.

4.1. Amino Acid Catabolism Suggests an Overall Energy Deficit

Signatures of energy deficits are reflected in the sera of FD patients by observations of lower levels of the amino acid alanine and the branched chain amino acids (BCAAs) valine, leucine, and isoleucine, which suggest increased amino acid catabolism; and by elevated urea concentration, which points to increased nitrogen excretion and is consistent with increased amino acid degradation in FD patients. Degradation of skeletal muscle protein is enhanced under starvation/energy deficient physiological states, and an increase in BCAA catabolism is commonly associated with starvation and muscle wasting, including the debilitating muscle wasting disease rhabdomyolysis [38,39], which has been shown to increase systemic urea levels and can harm kidney function [40]. FD patients are prone to low muscle mass and some suffer from rhabdomyolysis [32]. Blood tests for glomerular filtration rate, blood urea nitrogen content, and creatinine levels (Supplementary Figure S1) indicated that only two FD patients who provided samples displayed signatures of kidney dysfunction. Higher serum urea levels in FD patients, thus, reflect, in all likelihood, increased the deamination of amino acids and the excretion of excess nitrogen associated with amino acid catabolism, while amino acid carbon scaffolds are directed to ATP generating

pathways (Figure 3). Enhanced amino acid catabolism is also a compensatory response to mitochondrial dysfunction (providing amino acid precursors for de novo glucose synthesis and the subsequent use of glucose in glycolysis), impaired oxidative phosphorylation and aerobic ATP energy production, which have been reported to be hallmarks of FD and other neurological diseases including Alzheimer's and Parkinson's [14,16].

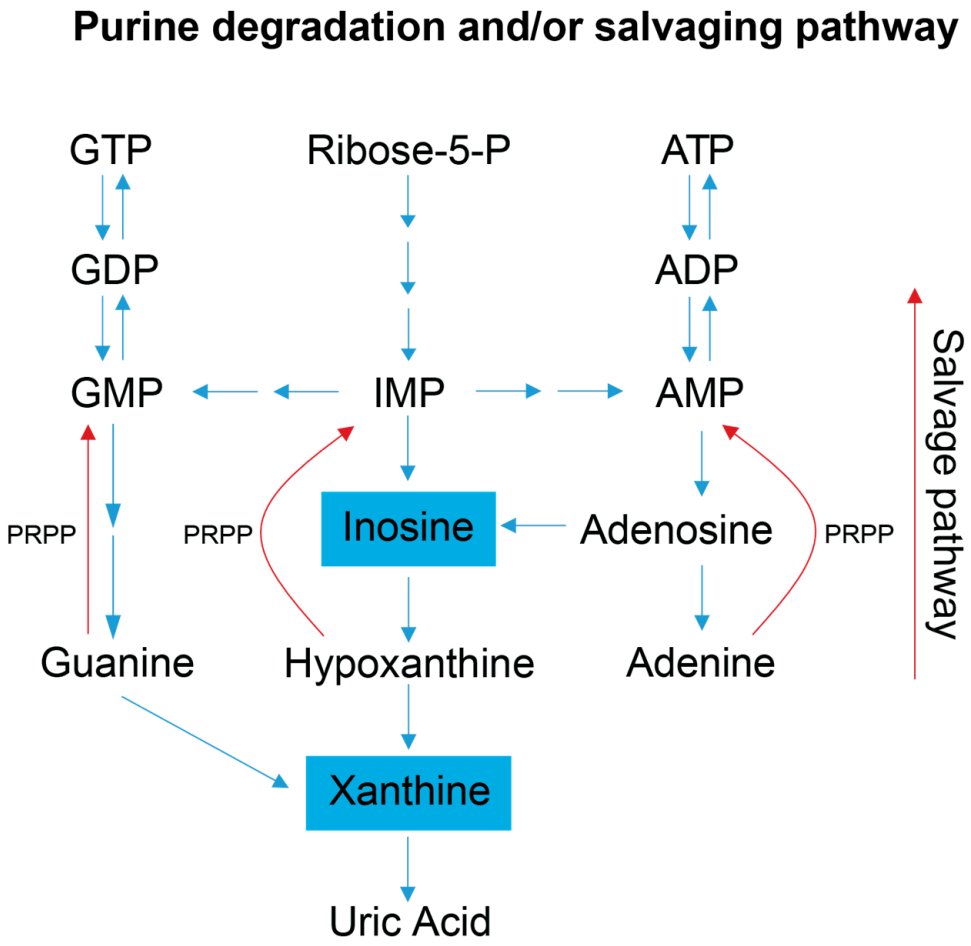


Figure 4. Simplified schematic of the purine salvage pathway. This diagram highlights how a decrease in purine degradation intermediates could reflect the salvaging of purines to preserve energy. Inosine is produced as a result of adenosine deamination via the action of adenosine deaminase and is a key intermediate of purine catabolism in humans, whereas xanthine is generated by the action of xanthine oxidase and is the product of oxidation of hypoxanthine (created via the conversion of inosine) and concomitant reduction of NAD+ to NADH. Additionally, xanthine can be produced via the deamination of guanosine. Xanthine oxidase catalyzes the oxidation of xanthine to uric acid, which is normally excreted in the urine, and was not detected in our metabolite profiling analysis of the serum samples [1,2]. Blue colored metabolites indicate decreased concentration in FD patient sera. Abbreviations: PRPP, phosphoribosyl pyrophosphate; IMP, inosine monophosphate; AMP, adenosine monophosphate; ADP, adenosine diphosphate; ATP, adenosine triphosphate; GMP, guanosine monophosphate; GDP, guanosine diphosphate; GTP, guanosine triphosphate.

4.2. Purine Salvage and Nucleotide Degradation Pathways

FD patient sera have significantly lower xanthine levels, and trend toward lower serum inosine levels, suggesting increased purine salvaging compared to healthy relative controls (Figure 4) [41,42]. Because de novo synthesis of purine nucleotides is an energy expensive process [43,44], decreased levels of the intermediates involved in purine degradation suggest that FD patients may be minimizing the excretion of purine bases and maximizing the purine salvage pathway to minimize the energetic demands of de novo

purine biosynthesis. FD patients are known to undergo hypoxic stress, especially during sleep, and many die due to sudden unexpected death during sleep (SUDS) [45]. Since purine nucleotides (i.e., adenosine) are also salvaged and utilized to cope with hypoxic and oxidative stress, it is reasonable to postulate that this process may also be occurring in FD patients [46]. Decreased purine degradation and enhanced purine salvaging are also observed in other neurological diseases that share hallmark clinical features with FD including AD, PD, ALS, and ASD [47–49].

4.3. Tyrosine Degradation

The tyrosine degradation pathway combines reactions that catalyze the production of tyramine, p-cresol, and fumarate (Supplementary Figure S9). The production of tyramine and p-cresol, both of which are higher in concentration in stool samples of FD patients, are solely dependent on microbial activity in food and the gut [50–53]. Conversely, the production of fumarate, which is lower in concentration in stool samples of FD patients, links to the TCA cycle and the electron transport chain (ETC) of the host and gut-microbes. However, the reduced energetic status of the FD patients, as discussed in Sections 4.1 and 4.2, suggest limited TCA cycle activity, thereby limiting the production of fumarate from this cycle. Bacterial fermentation leads to the production of fumarate as an intermediate, which has low bioavailability due to its extensive utilization by gut bacteria [54]. Changes in fumarate levels in the stool may, thus, reflect altered bacterial activity or the presence of specific microbes, as reported in our previous paper [4].

4.4. Metabolites Implicated in Gut Microbiome Changes

The criteria used in our analyses to establish the association of specific stool metabolites with the gut microbiome were as follows: (1) The metabolites of interest were reported in the literature to be produced or utilized by a genus or species of bacteria; or (2) had been correlated with promoting or impairing the growth of a given genus in published studies; or (3) their presence has been associated with the abundance of a specific microbial genus or species. Interestingly, all five of the metabolites classified as being associated with gut microbes (tyramine, p-cresol, valerate, beta-alanine and choline) were found to be associated with *Clostridium* in other studies [36,37,50,55–58]. Elevated levels of beta-alanine, tyramine and p-cresol were positively correlated with an increase in *Clostridium* genera. Conversely, the gut protective short chain fatty acid (SCFA) valerate has been shown to inhibit the growth of *C. difficile* in vitro [59]. Interestingly, FD patients exhibit elevated levels of tyramine, p-cresol, and beta-alanine in their stool samples, with decreased levels of valerate, findings that are consistent with FD patients being prone to develop *C. difficile* infections [7].

The association between *C. difficile* and p-cresol production is a specific field of research [60–62], in addition to the relevance of p-cresol to Autism Spectrum Disorder (ASD) which has been found to be elevated in stool samples of ASD patients [63–65]. FD patients are prone to *C. difficile* infections [7] and exhibit similar hallmarks to ASD regarding developmental impairments [5,66] and Elongator subunit protein dysfunction [13,18]. This suggests that p-cresol could be a valuable marker of disease that warrants further investigation. Additionally, excess p-cresol has been shown to cause DNA damage in vitro and to compromise colonic epithelial cell integrity [62,63], phenotypes that have been observed in FD mouse models and which are suspected to occur in FD patients as well [10,67]. Though additional gut microbes produce p-cresol and cannot be entirely ruled out for the changes in p-cresol levels observed in this study, the literature regarding p-cresol and *C. difficile* does suggest an interesting link between the susceptibility of FD patients to *C. difficile* infections and the associated downstream effects of p-cresol.

Valerate is a five-carbon SCFA which is produced by a select group of gut microorganisms [68,69]. Similar to the more common SCFAs (acetate, propionate, and butyrate [34]), valerate exhibits strong gastrointestinal (GI) protective effects, stimulates the growth of intestinal epithelium [36,59], and modulates autoimmune inflammation in the CNS [68]. As

with other SCFAs, valerate is relevant to neurological and GI diseases that share hallmarks with FD [59,65,70]. Elevated levels of fecal SCFAs could be due to elevated production of these compounds by the gut microbiome, a reduction in epithelial absorption capacity, or a combination of both [71]. Valerate and other SCFAs present an interesting group of metabolites for further investigations, because they display synergistic relationships with the host metabolism, gut protective effects and, to a lesser extent, are linked to the production of malonate as an intermediate of SCFA biosynthesis [72].

An additional source of malonate in the gut might originate from microbiome-derived beta-alanine metabolism. Beta-alanine is produced from aspartate and uracil, and can be metabolized into malonate and carnosine (Supplementary Figure S10). Muscle carnosine primarily functions as a proton buffer, enhances muscle endurance [73], and is relevant to FD because patients struggle to maintain adequate muscle mass. The elevation of fecal beta-alanine highlights another possible absorption deficit with consequential detrimental effects. However, due to the variety of sources of beta-alanine (dietary, host metabolism, and gut microbiome) and the limited studies on malonate's relevance in fecal samples, the factors that lead to elevated stool beta-alanine and malonate levels in FD patients are not fully understood.

Another metabolite with microbiome relevance is choline, which is obtained from the diet and has four metabolic fates, one of which is initiated by the microbiome [74] with the remaining three pathways subject to influence from the gut microbiome outcompeting the host for the bioavailability of choline [58]. Adequate dietary choline is necessary for phosphatidylcholine, acetylcholine and betaine synthesis (Figure 5), with phosphatidylcholine accounting for 95% of the total choline pool in tissues [75]. Various studies have shown that perturbations of host choline metabolism result in liver damage, elevated markers of DNA damage, kidney dysfunction, and a reduction in mitochondrial membrane potential [37,58,75–79], all symptoms experienced to different degrees by FD patients and/or FD mouse models [5,9,80–82]. Partnering these symptoms with the observation of elevated choline levels in FD patient stool samples, and results reported in [4], suggests that host and/or gut microbial choline metabolism and/or choline absorption is altered in FD.

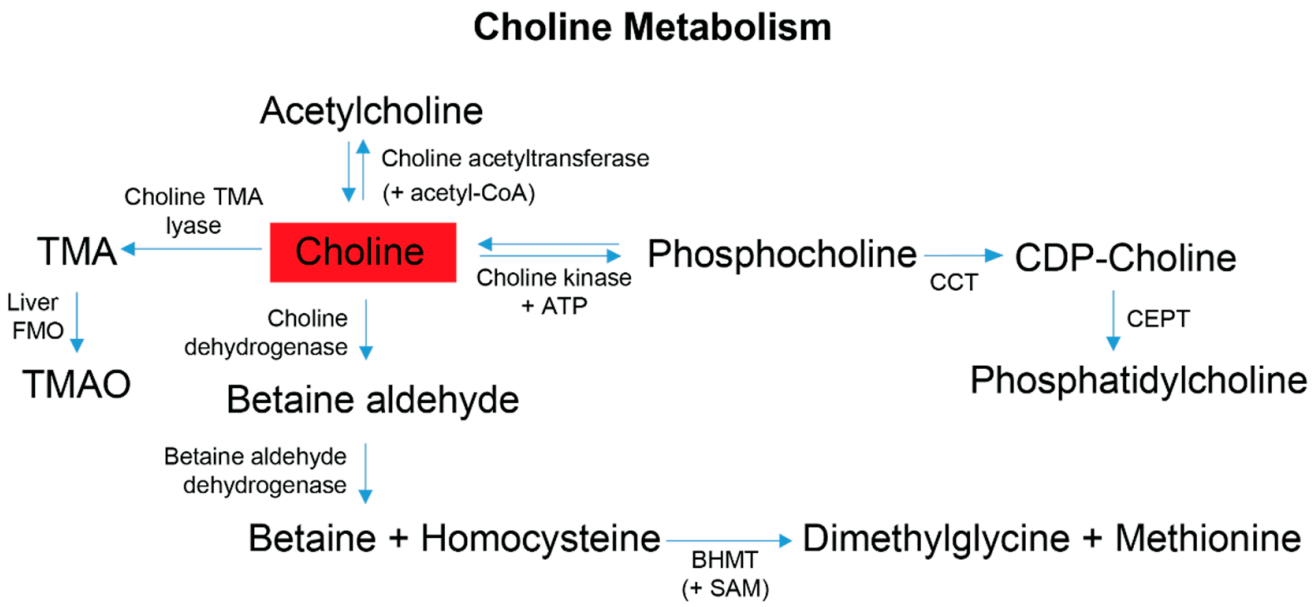


Figure 5. Choline is obtained primarily from the diet and contributes to four metabolic pathways employed by gut microbes and the host. Dietary choline is preferentially committed to the Kennedy

pathway to produce phosphatidylcholine; this process is a 3-step reaction requiring initial ATP expenditure [75]. At the synaptic cleft, choline can also undergo a cyclical reaction to produce acetylcholine for autonomic signaling transduction [66,76,77]. Within the liver and kidneys, choline can be converted to betaine, which is an osmotically active compound and a primary methyl donor that helps facilitate the re-methylation of homocysteine to methionine [66,68]. The production of TMA is mediated by the gut-microbiome. Following gut microbial conversion, TMA is classically absorbed by the gut epithelium, transported to the liver and converted by Flavin-monoxygenases (FMOs) to trimethylamine-N-oxide (TMAO) [51,66]. Red indicates choline was elevated in the stool metabolome of FD patients compared to their healthy relatives. Abbreviations: CoA, coenzyme-A; ATP, adenosine triphosphate; CPT, choline-phosphate cytidyltransferase; CDP, cytidyl-diphosphocholine; CEPT, choline ethanolamine phosphotransferase; BHMT, betaine homocysteine methyl transferase; SAM, S-adenosyl methionine; TMA, trimethylamine; TMAO, trimethylamine-N-oxide.

Though an unambiguous conclusion cannot be made regarding the microbial species' origins of the observed stool metabolite patterns, an inference about gut health can be drawn, as the published studies cited above present important examples of severe gut dysbiosis and include the same metabolites that were identified in FD patients. These findings further substantiate the hypothesis that FD patients experience gut microbiome dysbiosis, which links to impairment of metabolic homeostasis. Our experimental results, which are based on detailed polar metabolite profile analyses, are consistent with microbiome findings that we reported in an earlier publication [4]. Patient antibiotic use was assessed in our previous publication and an association with the use of antibiotics and microbiome diversity was observed. However, no significant correlations with metabolite concentrations were found. The FD mouse study reported in our earlier publication also suggested that neuronal *Elp1* deletion was sufficient to drive microbiome diversity and stool metabolome separation [4]. Therefore, we suspect that the use of antibiotics may influence the microbiome, but from our initial assessment of metabolite patterns and our FD mice results, it does not seem to be a main variable driving the separation observed in the metabolome of FD patients compared to their healthy relatives.

4.5. Neuronal Associated Metabolites

Four metabolites (choline, taurine, beta-alanine, and tyramine) associated with neuronal health, and identified in this study, either contribute directly to nervous system signaling or are precursors of neurotransmitter biosynthesis (Supplementary Figure S12). Choline plays a crucial role in the nervous system through its involvement in the direct production of acetylcholine, a major neurotransmitter (Figure 5 and Supplementary Figure S12), the synthesis of sphingomyelin from phosphatidylcholine for myelination [77,83,84], and choline storage and membrane sustainability through phosphatidylcholine synthesis. Cholinergic parasympathetic neurons modulate function of the GI tract, a process that appears to be greatly impacted in FD patients, as noted by severe gastroenteropathy, abnormal GI tract coordination, and reduced innervation [7,80]. Sphingomyelin is a primary constituent of myelin, which is reduced in large and small sensory axonal fibers in FD patients [5]. Cholinergic neurons are particularly vulnerable to altered choline metabolism, as choline is used both as a membrane lipid for structure and choline storage, and as the neurotransmitter acetylcholine. Given this dependence on choline, failure in its absorption may also contribute to the death of cholinergic neurons in FD based on altered choline metabolism [85]. The production and utilization of choline as acetylcholine is a cyclic process; therefore, a loss of choline in overactive metabolically taxed neurons depletes cellular membrane stores of phosphatidylcholine, further impairing cell functions and promoting neurodegeneration [37,86].

The gamma-aminobutyric acid-a (GABAa) receptor gene is downregulated in stem cells derived from FD patients [87], and GABAa receptor agonists have been used to treat FD crises experienced by patients [7]. Taurine and beta-alanine both bind GABA receptors [88] and beta-alanine can regulate both the GABA [89] and taurine transport

systems [90], which reduce cellular taurine transport, preventing the ability of taurine to improve calcium transport, and to modulate protein phosphorylation and regulate oxidative stress (see Section 4.6) [91].

Lastly, tyramine binds to baroreceptors to increase blood pressure. It has been recommended that FD patients restrict dietary tyramine consumption to help prevent hypertensive crises [92]. Tyramine present in foods and produced by the gut is metabolized by Monoamine Oxidase (MAO) A in the GI tract. However, tyramine is not degraded in individuals taking MAO inhibitors or in patients, including FD patients, who are deficient in MAO [92,93]; this thus allows excess tyramine to enter the systemic circulation through epithelial absorption [94] and ultimately triggers hypertensive crises, through adrenergic norepinephrine production, which are experienced by FD patients [5,93,94].

4.6. Taurine Metabolism and a Potential Dietary Deficit with Systemic Consequences

Taurine is of significant interest as its concentration is both elevated in the stool and lower in the sera of FD patients, suggesting a possible systemic deficit of this crucial metabolite. Taurine is produced endogenously via the degradation of homocysteine (Supplementary Figure S11), is one of the most abundant amino acids in mammals [95], and, similar to choline, is not only produced endogenously but obtained in substantial quantities from the diet. The elevated and decreased levels of taurine observed in the FD patients' stool and serum samples, respectively, could thus reflect an absorption impairment. In addition to the function of taurine in the nervous system (discussed above), another established biological fate of taurine is to enter the hepatic recycling loop via conjugation with bile acids (Supplementary Figure S11). The conjugation of taurine to bile acids enhances their solubility and improves the dietary absorption of lipids and lipid soluble vitamins [96,97]. Following facilitated absorption, bile acids are deconjugated by gut microbe activity, reabsorbed, and recycled. If FD patients do indeed exhibit impaired bile acid deconjugation resulting from microbiome dysbiosis, reduced cycling of taurine-conjugated bile acids could exacerbate GI dysfunction and further promote systemic deficits of taurine and other dietary nutrients.

Taurine deficient phenotypes are characterized by retinal degeneration, cardiomyopathy, and skeletal muscle malfunction [90], as a result of mitochondrial deficits including reduced complex I ETC activity, TCA activity and oxygen consumption and increased ROS production [98]. Mitochondrial dysfunction has been demonstrated in FD mouse models [10,11,67] and observed in an FD patient muscle biopsy which revealed a functional impairment of mitochondrial complexes I, III and IV, which are integral protein components of the ETC [10]. ETC impairment has also been reported to contribute to disease progression in AD, PD, and ASD [14,16,99–101]. Interestingly, characteristics of taurine deficiency are also observed in FD patients [5,32] and FD mouse models [10,67]. Being the most abundant amino acid in the retina, and the fact that taurine deficits cause degeneration of retinal ganglion cells (RGC) [102–104], i.e., the same cell type that dies progressively in FD patients [10,67], taurine levels may be relevant to the progressive blindness experienced by FD patients as they age.

5. Conclusions

In conclusion, our NMR-based metabolomics analyses demonstrated that FD patients exhibit significant changes in their stool and serum polar metabolomes. These metabolic alterations indicate the importance of the gut–brain–metabolism axis in FD, and support recently published microbiome findings [4]. Knowledge gained from these studies in FD may be applicable to other neurodegenerative diseases including AD and PD, which share disease hallmarks with FD [13–16]. Results from our serum polar metabolite profile analyses demonstrated that FD patients present with energetic (ATP) deficiencies, and that metabolic pathways associated with energy generation or metabolite sparing are impacted. From analysis of the serum metabolomics data, we found that the metabolic pathways impacted include enhanced amino acid catabolism, and the purine salvage pathway. Stool

metabolome analyses have identified metabolites associated with pathways involved in neuronal signaling, and indicators of gut-microbiome health and function. Metabolic patterns observed in the profiles of FD patients are consistent with reports from other neurological diseases including PD, AD, ALS, and ASD, suggesting that metabolic impairments observed in FD apply to and/or are relevant to other neurological diseases. New knowledge gained about the mechanisms associated with altered metabolism in FD has the potential to aid in understanding other, more complex, and multifactorial neurological diseases where the gut–brain–metabolism axis plays a prominent role. Knowledge about the key molecular indicators of disease may help guide the design of intervention therapies which, by restoring metabolic homeostasis and/or a healthy gut microbiome, could mitigate disease symptoms, and redress or slow down neurodegeneration.

Supplementary Materials: The following supporting information can be downloaded at: https://www.mdpi.com/article/10.3390/metabo13030433/s1. Table S1: Summary of clinical data from de-identified FD patients and control relatives. Table S2: Polar metabolites identified and quantified in the serum samples of FD patients and healthy relative controls. Table S3: Polar metabolites identified and quantified in the stool samples of FD patients and healthy relative controls. Table S4: Variable Importance in Projection (VIP) scores associated with components 1, 2 and 3 of the PLS-DA model generated from the metabolomics analysis of the serum samples of FD patients and healthy control relatives. Table S5: Variable Importance in Projection (VIP) scores associated with components 1, 2 and 3 of the PLS-DA model generated from the metabolomics analysis of the fecal samples of FD patients and healthy control relatives. Figure S1: Results from clinical blood tests of de-identified FD patients. Figure S2: Results from liver enzyme blood tests and measurements of ALT and AST levels in de-identified blood samples of FD patients. Figure S3: Characteristic 1D 1H NMR spectrum recorded on serum metabolite extracts obtained from FD patients and healthy relative controls. Figure S4: Characteristic 1D 1H NMR spectrum recorded on stool metabolite extracts obtained from FD patients and healthy relative controls. Figure S5: Validation metrics of the PLS-DA modeling of serum metabolite profiles. Figure S6: Validation metrics of the PLS-DA modeling of stool metabolite profiles. Figure S7: Scree plot of the PCA modeling of both serum and stool metabolite profiles. Figure S8: Random forest analysis of the serum and stool metabolite profiles of the FD patient and healthy control relative groups. Figure S9: Schematic diagram of metabolic pathways involved in tyrosine catabolism. Figure S10: Schematic diagram of metabolic pathways involved in beta-alanine and malonate metabolism. Figure S11: Schematic diagram of metabolic pathways involved in taurine metabolism. Figure S12: Schematic diagram of four significant metabolites identified in the stool of FD patients and identified as important neuronal cell signaling molecules. Refs [74,85,89,91,95,105–107] are citied in the Supplementat Materials.

Author Contributions: Conceptualization, S.M.C., A.M.C., F.L. and V.C.; methodology, S.M.C., A.M.C., A.W., B.T. and V.C.; software, S.M.C., A.M.C. and B.T.; validation, S.M.C. and A.M.C.; formal analysis, S.M.C. and A.M.C.; investigation, S.M.C., A.M.C. and A.W.; resources, B.T., M.C.-V., H.K., L.N.-K., F.L. and V.C.; data curation, S.M.C. and A.M.C.; writing—original draft preparation, S.M.C. and A.M.C.; writing—review and editing, S.M.C., A.M.C., A.W., B.T., M.C.-V., H.K., L.N.-K., F.L. and V.C.; visualization, S.M.C. and A.M.C.; supervision, B.T. and V.C.; project administration, M.C.-V., H.K., L.N.-K., F.L. and V.C.; funding acquisition, F.L. and V.C. All authors have read and agreed to the published version of the manuscript.

Funding: This research has been funded by the National Institutes of Health, R01-DK117473 (multi-PI R01 award to F.L. and V.C.) and Diversity Supplement 3R01DK117473-02S1 to V.C. and S.M.C. Additional graduate training support to S.M.C. was provided by the Alfred P. Sloan Foundation program and the Montana INBRE Native American Graduate Fellowship P20GM-103474. Additional graduate training and stipend support to A.M.C. was provided by the Molecular Biosciences Program from Montana State University (MSU). Support for MSU's NMR Core Facility and NMR instrumentation has been provided, in part, by the NIH Shared Instrumentation Grant (SIG) program (1S10RR13878 and 1S10RR026659), the National Science Foundation (NSF-MRI-DBI-1532078; NSF-MRI-CHE-2018388), the Murdock Charitable Trust Foundation (2015066:MNL) and MSU's Office of the Vice President for Research and Economic Development.

Institutional Review Board Statement: The study was conducted in accordance with the Declaration of Helsinki, and approved by the Institutional Review Board of Montana State University (MSU's IRB protocol Title: ELP1 dysfunction in Familial Dysautonomia; IRB Protocol No. 67-2019; PI. Frances Lefcort), and New York University School of Medicine (NYU Langone Health) (IRB protocol code s16-00718).

Informed Consent Statement: Informed and signed consent was obtained for all subjects involved in the study by either personal consent or from a legal guardian.

Data Availability Statement: The data presented in this study are openly available in MetaboLights at https://www.ebi.ac.uk/metabolights/MTBLS5138/descriptors (accessed on 6 December 2022), reference number MTBLS5138.

Acknowledgments: We thank Galen O'Shea-Stone for his R code enabling improved data analysis and graphic design. We also acknowledge Christina Lucas for her contribution of stool sample aliquoting. In addition, we thank the FD treatment center at NYU Langone Health and the FD patients and families enrolled in this study.

Conflicts of Interest: The authors declare no conflict of interest.

References

1. Forssberg, H. Microbiome programming of brain development: Implications for neurodevelopmental disorders. *Dev. Med. Child Neurol.* **2019**, *61*, 744–749. [CrossRef] [PubMed]
2. Quigley, E.M.M. Microbiota-brain-gut axis and neurodegenerative diseases. *Curr. Neurol. Neurosci. Rep.* **2017**, *17*, 94. [CrossRef] [PubMed]
3. Mirzaei, R.; Bouzari, B.; Hosseini-Fard, S.R.; Mazaheri, M.; Ahmadyousefi, Y.; Abdi, M.; Jalalifar, S.; Karimitabar, Z.; Teimoori, A.; Keyvani, H.; et al. Role of microbiota-derived short-chain fatty acids in nervous system disorders. *Biomed. Pharmacother.* **2021**, *139*, 111661. [CrossRef] [PubMed]
4. Cheney, A.M.; Costello, S.M.; Pinkham, N.V.; Waldum, A.; Broadaway, S.C.; Cotrina-Vidal, M.; Mergy, M.; Tripet, B.; Kominsky, D.J.; Grifka-Walk, H.M.; et al. Gut microbiome dysbiosis drives metabolic dysfunction in Familial dysautonomia. *Nat. Commun.* **2023**, *14*, 218. [CrossRef]
5. Norcliffe-Kaufmann, L.; Slaugenhaupt, S.A.; Kaufmann, H. Familial dysautonomia: History, genotype, phenotype and translational research. *Prog. Neurobiol.* **2017**, *152*, 131–148. [CrossRef]
6. Dietrich, P.; Dragatsis, I. Familial Dysautonomia: Mechanisms and Models. *Genet. Mol. Biol.* **2016**, *39*, 497–514. [CrossRef]
7. Palma, J.A.; Norcliffe-Kaufmann, L.; Fuente-Mora, C.; Percival, L.; Mendoza-Santiesteban, C.; Kaufmann, H. Current treatments in familial dysautonomia. *Expert Opin. Pharmacother.* **2014**, *15*, 2653–2671. [CrossRef]
8. Slaugenhaupt, S.A.; Blumenfeld, A.; Gill, S.P.; Leyne, M.; Mull, J.; Cuajungco, M.P.; Liebert, C.B.; Chadwick, B.; Idelson, M.; Reznik, L.; et al. Tissue-specific expression of a splicing mutation in the IKBKAP gene causes familial dysautonomia. *Am. J. Hum. Genet.* **2001**, *68*, 598–605. [CrossRef]
9. Goffena, J.; Lefcort, F.; Zhang, Y.; Lehrmann, E.; Chaverra, M.; Felig, J.; Walters, J.; Buksch, R.; Becker, K.G.; George, L. Elongator and codon bias regulate protein levels in mammalian peripheral neurons. *Nat. Commun.* **2018**, *9*, 889. [CrossRef]
10. Ueki, Y.; Shchepetkina, V.; Lefcort, F. Retina-specific loss of Ikbkap/Elp1 causes mitochondrial dysfunction that leads to selective retinal ganglion cell degeneration in a mouse model of familial dysautonomia. *Dis. Model Mech.* **2018**, *11*, dmm033746. [CrossRef]
11. Ohlen, S.B.; Russell, M.L.; Brownstein, M.J.; Lefcort, F. BGP-15 prevents the death of neurons in a mouse model of familial dysautonomia. *Proc. Natl. Acad. Sci. USA* **2017**, *114*, 5035–5040. [CrossRef]
12. Lefcort, F.; Mergy, M.; Ohlen, S.B.; Ueki, Y.; George, L. Animal and cellular models of familial dysautonomia. *Clin. Auton Res.* **2017**, *27*, 235–243. [CrossRef]
13. Kojic, M.; Wainwright, B. The Many Faces of Elongator in Neurodevelopment and Disease. *Front. Mol. Neurosci.* **2016**, *9*, 115. [CrossRef] [PubMed]
14. Moreira, P.I.; Carvalho, C.; Zhu, X.; Smith, M.A.; Perry, G. Mitochondrial dysfunction is a trigger of Alzheimer's disease pathophysiology. *Biochim. Biophys. Acta* **2010**, *1802*, 2–10. [CrossRef]
15. Simpson, C.L.; Lemmens, R.; Miskiewicz, K.; Broom, W.J.; Hansen, V.K.; van Vught, P.W.; Landers, J.E.; Sapp, P.; Van Den Bosch, L.; Knight, J.; et al. Variants of the elongator protein 3 (ELP3) gene are associated with motor neuron degeneration. *Hum. Mol. Genet.* **2009**, *18*, 472–481. [CrossRef]
16. Chen, C.; Turnbull, D.M.; Reeve, A.K. Mitochondrial Dysfunction in Parkinson's Disease-Cause or Consequence? *Biology* **2019**, *8*, 38. [CrossRef] [PubMed]
17. Bento-Abreu, A.; Jager, G.; Swinnen, B.; Rué, L.; Hendrickx, S.; Jones, A.; Staats, K.A.; Taes, I.; Eykens, C.; Nonneman, A.; et al. Elongator subunit 3 (ELP3) modifies ALS through tRNA modification. *Hum. Mol. Genet.* **2018**, *27*, 1276–1289. [CrossRef] [PubMed]

18. Addis, L.; Ahn, J.W.; Dobson, R.; Dixit, A.; Ogilvie, C.M.; Pinto, D.; Vaags, A.K.; Coon, H.; Chaste, P.; Wilson, S.; et al. Microdeletions of ELP4 Are Associated with Language Impairment, Autism Spectrum Disorder, and Mental Retardation. *Hum. Mutat.* **2015**, *36*, 842–850. [CrossRef]
19. Fuchs, A.L.; Schiller, S.M.; Keegan, W.J.; Ammons, M.C.B.; Eilers, B.; Tripet, B.; Copie, V. Quantitative (1)H NMR Metabolomics Reveal Distinct Metabolic Adaptations in Human Macrophages Following Differential Activation. *Metabolites* **2019**, *9*, 248. [CrossRef] [PubMed]
20. Ramm Sander, P.; Peer, M.; Grandl, M.; Bogdahn, U.; Schmitz, G.; Kalbitzer, H.R. NMR Spectroscopy of Macrophages Loaded with Native, Oxidized or Enzymatically Degraded Lipoproteins. *PLoS ONE* **2013**, *8*, e56360. [CrossRef]
21. Fuchs, A.L.; Miller, I.R.; Schiller, S.M.; Ammons, M.C.B.; Eilers, B.; Tripet, B.; Copie, V. Pseudomonas aeruginosa Planktonic- and Biofilm-Conditioned Media Elicit Discrete Metabolic Responses in Human Macrophages. *Cells* **2020**, *9*, 260. [CrossRef] [PubMed]
22. O'Shea-Stone, G.; Lambert, R.; Tripet, B.P.; Berardinelli, J.; Weeding, J.; White, J.; Thomson, J.; Copié, V.; Garrott, R. 1H NMR Based Metabolic Profiling Distinguishes the Differential Impact of Capture Techniques on Wild Bighorn Sheep. *Nat. Sci. Rep.* **2020**, *11*, 11308. [CrossRef]
23. Fuchs, A.L.; Weaver, A.J., Jr.; Tripet, B.P.; Ammons, M.C.B.; Teintze, M.; Copie, V. Characterization of the antibacterial activity of Bald's eyesalve against drug resistant Staphylococcus aureus and Pseudomonas aeruginosa. *PLoS ONE* **2018**, *13*, e0208108. [CrossRef] [PubMed]
24. Mercier, P.; Lewis, M.J.; Chang, D.; Baker, D.; Wishart, D.S. Towards automatic metabolomic profiling of high-resolution one-dimensional proton NMR spectra. *J. Biomol. NMR* **2011**, *49*, 307–323. [CrossRef] [PubMed]
25. Wishart, D.S.; Feunang, Y.D.; Marcu, A.; Guo, A.C.; Liang, K.; Vázquez-Fresno, R.; Sajed, T.; Johnson, D.; Li, C.; Karu, N.; et al. HMDB 4.0—The Human Metabolome Database for 2018. *Nucleic Acids Res.* **2018**, *46*, D608–D617. [CrossRef] [PubMed]
26. Xia, J.; Wishart, D.S. Metabolomic Data Processing, Analysis, and Interpretation Using MetaboAnalyst. *Curr. Protoc. Bioinform.* **2011**, *34*, 14.10.11–14.10.48. [CrossRef] [PubMed]
27. Chong, J.; Soufan, O.; Li, C.; Caraus, I.; Li, S.; Bourque, G.; Wishart, D.S.; Xia, J. MetaboAnalyst 4.0: Towards more transparent and integrative metabolomics analysis. *Nucleic Acids Res.* **2018**, *46*, W486–W494. [CrossRef]
28. Durbin, B.P.; Hardin, J.S.; Hawkins, D.M.; Rocke, D.M. A variance-stabilizing transformation for gene-expression microarray data. *Bioinformatics* **2002**, *18*, S105–S110. [CrossRef]
29. van den Berg, R.A.; Hoefsloot, H.C.; Westerhuis, J.A.; Smilde, A.K.; van der Werf, M.J. Centering, scaling, and transformations: Improving the biological information content of metabolomics data. *BMC Genom.* **2006**, *7*, 142. [CrossRef]
30. Szymanska, E.; Saccenti, E.; Smilde, A.K.; Westerhuis, J.A. Double-check: Validation of diagnostic statistics for PLS-DA models in metabolomics studies. *Metabolomics* **2012**, *8*, 3–16. [CrossRef]
31. Ruiz-Perez, D.; Guan, H.; Madhivanan, P.; Mathee, K.; Narasimhan, G. So you think you can PLS-DA? *BMC Bioinform.* **2020**, *21*. [CrossRef] [PubMed]
32. Palma, J.-A.; Roda, R.; Norcliffe-kaufmann, L.; Kaufmann, H. Increased frequency of rhabdomyolysis in familial dysautonomia. *Muscle Nerve* **2015**, *52*, 887–890. [CrossRef]
33. Muddapu, V.R.; Dharshini, A.A.P.; Chakravarthy, V.S.; and Gromika, M.M. Neurodegenerative Diseases–Is Metabolic Deficiency the Root Cause? *Front. Neurosci.* **2020**, *14*, 213. [CrossRef] [PubMed]
34. Kelly, C.J.; Zheng, L.; Campbell, E.L.; Saeedi, B.; Scholz, C.C.; Bayless, A.J.; Wilson, K.E.; Glover, L.E.; Kominsky, D.J.; Magnuson, A.; et al. Crosstalk between Microbiota-Derived Short-Chain Fatty Acids and Intestinal Epithelial HIF Augments Tissue Barrier Function. *Cell Host Microbe* **2015**, *17*, 662–671. [CrossRef] [PubMed]
35. Cani, P.D.; Van Hul, M.; Lefort, C.; Depommier, C.; Rastelli, M.; Everard, A. Microbial regulation of organismal energy homeostasis. *Nat. Metab.* **2019**, *1*, 34–46. [CrossRef]
36. Markowiak-Kopec, P.; Slizewska, K. The effect of probiotics on the production of short-chain fatty acids by human intestinal microbiome. *Nutrients* **2020**, *12*, 1107. [CrossRef]
37. Arias, N.; Arboleya, S.; Allison, J.; Kaliszewska, A.; Higarza, S.G.; Gueimonde, M.; Arias, J.L. The relationship between choline bioavailability from diet, intestinal microbiota composition, and its modulation of human diseases. *Nutrients* **2020**, *12*, 2340. [CrossRef]
38. Eley, H.L.; Russell, S.T.; Tisdale, M.J. Effect of branched-chain amino acids on muscle atrophy in cancer cachexia. *Biochem. J.* **2007**, *407*, 113–120. [CrossRef]
39. Holecek, M. Branched-chain amino acids in health and disease: Metabolism, alterations in blood plasma, and as supplements. *Nutr. Metab.* **2018**, *15*, 33. [CrossRef]
40. Torres, P.A.H.; Helmstetter, J.A.; Kaye, A.M.; Kaye, A.D. Rhabdomyolysis: Pathogenesis, Diagnosis, and Treatment. *Ochsner. J.* **2015**, *15*, 58–69.
41. Tang, Z.; Ye, W.; Chen, H.; Kuang, X.; Guo, J.; Xiang, M.; Peng, C.; Chen, X.; Liu, H. Role of purines in regulation of metabolic reprogramming. *Purinergic Signal.* **2019**, *15*, 423–438. [CrossRef]
42. Fasullo, M.; Endres, L. Nucleotide salvage deficiencies, DNA damage and neurodegeneration. *Int. J. Mol. Sci.* **2015**, *16*, 9431–9449. [CrossRef]
43. Dammer, E.B.; Gottle, M.; Duong, D.M.; Hanfelt, J.; Seyfried, N.T.; Jinnah, H.A. Consequences of impaired purine recycling on the proteome in a cellular model of Lesch-Nyhan disease. *Mol. Genet. Metab.* **2015**, *114*, 570–579. [CrossRef]

44. Sonanez-Organis, J.G.; Vazquez-Medina, J.P.; Zenteno-Savin, T.; Aguilar, A.; Crocker, D.E.; Ortiz, R.M. Prolonged fasting increases purine recycling in post-weaned northern elephant seals. *J. Exp. Biol.* **2012**, *215*, 1448–1455. [CrossRef]
45. Palma, J.A.; Norcliffe-Kaufmann, L.; Perez, M.A.; Spalink, C.L.; Kaufmann, H. Sudden Unexpected Death During Sleep in Familial Dysautonomia: A Case-Control Study. *Sleep* **2017**, *40*, zsx083. [CrossRef] [PubMed]
46. Pehar, M.; Harlan, B.A.; Killoy, K.M.; Vargas, M.R. Nicotinamide Adenine Dinucleotide Metabolism and Neurodegeneration. *Antioxid. Redox Signal.* **2018**, *28*, 1652–1668. [CrossRef] [PubMed]
47. Kori, M.; Aydın, B.; Unal, S.; Arga, K.Y.; Kazan, D. Metabolic Biomarkers and Neurodegeneration: A Pathway Enrichment Analysis of Alzheimer's Disease, Parkinson's Disease, and Amyotrophic Lateral Sclerosis. *OMICS J. Integr. Biol.* **2016**, *20*, 645–661. [CrossRef]
48. Glinton, K.E.; Elsea, S.H. Untargeted Metabolomics for Autism Spectrum Disorders: Current Status and Future Directions. *Front. Psychiatry* **2019**, *10*, 647. [CrossRef] [PubMed]
49. Stempler, S.; Yizhak, K.; Ruppin, E. Integrating transcriptomics with metabolic modeling predicts biomarkers and drug targets for Alzheimer's disease. *PLoS ONE* **2014**, *9*, e105383. [CrossRef]
50. van Kessel, S.P.; El Aidy, S. Bacterial Metabolites Mirror Altered Gut Microbiota Composition in Patients with Parkinson's Disease. *J. Parkinson's Dis.* **2019**, *9*, S359–S370. [CrossRef]
51. Wing, M.R.; Patel, S.S.; Ramezani, A.; Raj, D.S. Gut microbiome in chronic kidney disease. *Exp. Physiol.* **2016**, *101*, 471–477. [CrossRef]
52. Gillman, P.K. A reassessment of the safety profile of monoamine oxidase inhibitors: Elucidating tired old tyramine myths. *J. Neural Transm.* **2018**, *125*, 1707–1717. [CrossRef] [PubMed]
53. Burns, C.; Kidron, A. Biochemistry, Tyramine. In *StatPearls*; StatPearls Publishing: Treasure Island, FL, USA, 2022.
54. Rowland, I.; Gibson, G.; Heinken, A.; Scott, K.; Swann, J.; Thiele, I.; Tuohy, K. Gut microbiota functions: Metabolism of nutrients and other food components. *Eur. J. Nutr.* **2018**, *57*, 1–24. [CrossRef] [PubMed]
55. Chiu, C.Y.; Cheng, M.L.; Chiang, M.H.; Kuo, Y.L.; Tsai, M.H.; Chiu, C.C.; Lin, G. Gut microbial-derived butyrate is inversely associated with IgE responses to allergens in childhood asthma. *Pediatr. Allergy Immunol* **2019**, *30*, 689–697. [CrossRef] [PubMed]
56. Armstrong, C.W.; McGregor, N.R.; Lewis, D.P.; Butt, H.L.; Gooley, P.R. The association of fecal microbiota and fecal, blood serum and urine metabolites in myalgic encephalomyelitis/chronic fatigue syndrome. *Metabolomics* **2016**, *13*, 8. [CrossRef]
57. Allman, B.; Biwer, A.; Maitland, C.G.; DiFabio, B.; Coughlin, E.; Smith-Ryan, A.E.; Ormsbee, M. The effect of short term beta alanine supplementation on physical performance and quality of life in parkinson's disease: A pilot study. *J. Exerc. Physiol. Online* **2018**, *21*, 1–13.
58. Romano, K.A.; Vivas, E.I.; Amador-Noguez, D.; Rey, F.E. Intestinal microbiota composition modulates choline bioavailability from diet and accumulation of the proatherogenic metabolite trimethylamine-N-oxide. *mBio* **2015**, *6*, e02481. [CrossRef] [PubMed]
59. Taylor, H.; Serrano-Contreras, J.I.; McDonald, J.A.K.; Epstein, J.; Fell, J.; Seoane, R.C.; Li, J.V.; Marchesi, J.R.; Hart, A.L. Multiomic features associated with mucosal healing and inflammation in paediatric Crohn's disease. *Aliment. Pharmacol. Ther.* **2020**, *52*, 1491–1502. [CrossRef] [PubMed]
60. Kellingray, L.; Gall, G.L.; Defernez, M.; Beales, I.L.P.; Franslem-Elumogo, N.; Narbad, A. Microbial taxonomic and metabolic alterations during faecal microbiota transplantation to treat Clostridium difficile infection. *J. Infect.* **2018**, *77*, 107–118. [CrossRef]
61. Selmer, T.; Andrei, P.I. p-Hydroxyphenylacetate decarboxylase from Clostridium difficile. *Eur. J. Biochem.* **2001**, *268*, 1363–1372. [CrossRef]
62. Saito, Y.; Sato, T.; Nomoto, K.; Tsuji, H. Identification of phenol- and p-cresol-producing intestinal bacteria by using media supplemented with tyrosine and its metabolites. *FEMS Microbiol. Ecol.* **2018**, *94*, fiy125. [CrossRef] [PubMed]
63. Kang, D.W.; Ilhan, Z.E.; Isern, N.G.; Hoyt, D.W.; Howsmon, D.P.; Shaffer, M.; Lozupone, C.A.; Hahn, J.; Adams, J.B.; Krajmalnik-Brown, R. Differences in fecal microbial metabolites and microbiota of children with autism spectrum disorders. *Anaerobe* **2018**, *49*, 121–131. [CrossRef] [PubMed]
64. Angelis, M.D.; Piccolo, M.; Vannini, L.; Siragusa, S.; Giacomo, A.D.; Serrazzanetti, D.I.; Cristofori, F.; Guerzoni, M.E.; Gobbetti, M.; Francavilla, R. Fecal Microbiota and Metabolome of Children with Autism and Pervasive Developmental Disorder Not Otherwise Specified. *PLoS ONE* **2013**, *8*, e76993. [CrossRef] [PubMed]
65. Wang, L.; Christophersen, C.T.; Sorich, M.J.; Gerber, J.P.; Angley, M.T.; Conlon, M.A. Elevated fecal short chain fatty acid and ammonia concentrations in children with autism spectrum disorder. *Dig. Dis. Sci.* **2012**, *57*, 2096–2102. [CrossRef]
66. Nguyen, L.; Humbert, S.; Saudou, F.; Chariot, A. Elongator-An emerging role in neurological disorders. *Trends Mol. Med.* **2010**, *16*, 1–6. [CrossRef]
67. Ueki, Y.; Ramirez, G.; Salcedo, E.; Stabio, M.E.; Lefcort, F. Loss of Ikbkap Causes Slow, Progressive Retinal Degeneration in a Mouse Model of Familial Dysautonomia. *eNeuro* **2016**, *3*. [CrossRef]
68. Luu, M.; Pautz, S.; Kohl, V.; Singh, R.; Romero, R.; Lucas, S.; Hofmann, J.; Raifer, H.; Vachharajani, N.; Carrascosa, L.C.; et al. The short-chain fatty acid pentanoate suppresses autoimmunity by modulating the metabolic-epigenetic crosstalk in lymphocytes. *Nat. Commun.* **2019**, *10*, 760. [CrossRef]
69. Bourriaud, C.; Robins, R.J.; Martin, L.; Kozlowski, F.; Tenailleau, E.; Cherbut, C.; Michel, C. Lactate is mainly fermented to butyrate by human intestinal microfloras but inter-individual variation is evident. *J. Appl. Microbiol.* **2005**, *99*, 201–212. [CrossRef]

70. Adams, J.B.; Johansen, L.J.; Powell, L.D.; Quig, D.; Rubin, R.A. Gastrointestinal flora and gastrointestinal status in children with autism–comparisons to typical children and correlation with autism severity. *BMC Gastroenterol.* **2011**, *11*, 22. [CrossRef] [PubMed]
71. den Besten, G.; van Eunen, K.; Groen, A.K.; Venema, K.; Reijngoud, D.J.; Bakker, B.M. The role of short-chain fatty acids in the interplay between diet, gut microbiota, and host energy metabolism. *J. Lipid Res.* **2013**, *54*, 2325–2340. [CrossRef]
72. Han, J.; Antunes, L.C.M.; Finlay, B.B.; Borchers, C.H. Metabolomics: Towards understanding host–microbe interactions. *Future Microbiol.* **2010**, *5*, 153–161. [CrossRef]
73. Julie, Y.; Culbertson, R.B.K.; Mike Greenwood, and Matthew Cooke. Effects of Beta-Alanine on Muscle Carnosine and Exercise Performance:A Review of the Current Literature. *Nutrients* **2010**, *2*, 75–98.
74. Wiedeman, A.M.; Barr, S.I.; Green, T.J.; Xu, Z.; Innis, S.M.; Kitts, D.D. Dietary Choline Intake: Current State of Knowledge Across the Life Cycle. *Nutrients* **2018**, *10*, 1513. [CrossRef] [PubMed]
75. Ueland, P.M. Choline and betaine in health and disease. *J. Inherit. Metab. Dis.* **2011**, *34*, 3–15. [CrossRef]
76. Zeisel, S.H. Dietary choline deficiency causes DNA strand breaks and alters epigenetic marks on DNA and histones. *Mutat. Res.* **2012**, *733*, 34–38. [CrossRef]
77. Romano, K.A.; Martinez-Del Campo, A.; Kasahara, K.; Chittim, C.L.; Vivas, E.I.; Amador-Noguez, D.; Balskus, E.P.; Rey, F.E. Metabolic, Epigenetic, and Transgenerational Effects of Gut Bacterial Choline Consumption. *Cell Host Microbe* **2017**, *22*, 279–290. [CrossRef]
78. Hensley, K.; Kotake, Y.; Sang, H.; Pye, Q.N.; Wallis, G.L.; Kolker, L.M.; Tabatabaie, T.; Stewart, C.A.; Konishi, Y.; Nakae, D.; et al. Dietary choline restriction causes complex I dysfunction and increased H2O2 generation in liver mitochondria. *Carcinogenesis* **2000**, *21*, 983–989. [CrossRef]
79. Albright, C.D.; Costa, K.-A.d.; Craciunescu, C.N.; Klem, E.; Mar, M.-H.; Zeisel, S.H. Regulation of Choline Deficiency Apoptosis by Epidermal Growth Factor in CWSV-1 Rat Hepatocytes. *Cell Physiol. Biochem.* **2005**, *15*, 59–68. [CrossRef]
80. Bar-Shai, A.; Maayan, C.; Vromen, A.; Udassin, R.; Nissan, A.; Freund, H.; Hanani, M. Decreased density of ganglia and neurons in the myenteric plexus of familial dysautonomia patients. *J. Neurol. Sci.* **2004**, *220*, 89–94. [CrossRef]
81. Chaverra, M.; George, L.; Mergy, M.; Waller, H.; Kujawa, K.; Murnion, C.; Sharples, E.; Thorne, J.; Podgajny, N.; Grindeland, A.; et al. The familial dysautonomia disease gene IKBKAP is required in the developing and adult mouse central nervous system. *Dis. Model. Mech.* **2017**, *10*, 605–618. [CrossRef] [PubMed]
82. Cheishvili, D.; Maayan, C.; Smith, Y.; Ast, G.; Razin, A. IKAP/hELP1 deficiency in the cerebrum of familial dysautonomia patients results in down regulation of genes involved in oligodendrocyte differentiation and in myelination. *Hum. Mol. Genet.* **2007**, *16*, 2097–2104. [CrossRef]
83. Gibellini, F.; Smith, T.K. The Kennedy pathway–De novo synthesis of phosphatidylethanolamine and phosphatidylcholine. *IUBMB Life* **2010**, *62*, 414–428. [CrossRef]
84. Zeisel, S.H.; Klatt, K.C.; Caudill, M.A. Choline. *Adv. Nutr.* **2018**, *9*, 58–60. [CrossRef]
85. Wurtman, R.J. Choline metabolism as a basis for the selective vulnerability of cholinergic neurons. *Trends Neurosci.* **1992**, *15*, 117–122. [CrossRef] [PubMed]
86. Blusztajn, J.K.; Liscovitch, M.; Richardson, U.I. Synthesis of acetylcholine from choline derived from phosphatidylcholine in a human neuronal cell line. *Proc. Natl. Acad. Sci. USA* **1987**, *84*, 5474–5477. [CrossRef]
87. Lefler, S.; Cohen, M.A.; Kantor, G.; Cheishvili, D.; Even, A.; Birger, A.; Turetsky, T.; Gil, Y.; Even-Ram, S.; Aizenman, E.; et al. Familial Dysautonomia (FD) Human Embryonic Stem Cell Derived PNS Neurons Reveal that Synaptic Vesicular and Neuronal Transport Genes Are Directly or Indirectly Affected by *IKBKAP* Downregulation. *PLoS ONE* **2015**, *10*, e0138807. [CrossRef] [PubMed]
88. Ochoa-de la Paz, L.; Zenteno, E.; Gulias-Canizo, R.; Quiroz-Mercado, H. Taurine and GABA neurotransmitter receptors, a relationship with therapeutic potential? *Expert Rev. Neurother.* **2019**, *19*, 289–291. [CrossRef]
89. Tiedje, K.E.; Stevens, K.; Barnes, S.; Weaver, D.F. β-Alanine as a small molecule neurotransmitter. *Neurochem. Int.* **2010**, *57*, 177–188. [CrossRef]
90. Seidel, U.; Huebbe, P.; Rimbach, G. Taurine: A Regulator of Cellular Redox Homeostasis and Skeletal Muscle Function. *Mol. Nutr. Food Res.* **2019**, *63*, e1800569. [CrossRef]
91. Jong, C.J.; Azuma, J.; Schaffer, S. Mechanism underlying the antioxidant activity of taurine: Prevention of mitochondrial oxidant production. *Amino Acids* **2012**, *42*, 2223–2232. [CrossRef] [PubMed]
92. Anderson, M.V. Evidenced Based Elimination Diet Restricting Dairy and Tyramine Foods for Familial Dysautonomia (FD) or Riley-Day Syndrome. *J. Am. Diet. Assoc.* **2006**, *106*, A15. [CrossRef]
93. Anderson, S.L.; Rubin, B.Y. Tocotrienols reverse IKAP and monoamine oxidase deficiencies in familial dysautonomia. *Biochem. Biophys. Res. Commun.* **2005**, *336*, 150–156. [CrossRef]
94. Flockhart, D.A. Dietary restrictions and drug interactions with monoamine oxidase inhibitors: An update. *J. Clin. Psychiatry* **2012**, *73* (Suppl. 1), 17–24. [CrossRef]
95. Wu, J.Y.; Prentice, H. Role of taurine in the central nervous system. *J. Biomed. Sci.* **2010**, *17* (Suppl. 1), S1. [CrossRef]
96. Miyazaki, T.; Sasaki, S.I.; Toyoda, A.; Wei, F.Y.; Shirai, M.; Morishita, Y.; Ikegami, T.; Tomizawa, K.; Honda, A. Impaired bile acid metabolism with defectives of mitochondrial-tRNA taurine modification and bile acid taurine conjugation in the taurine depleted cats. *Sci. Rep.* **2020**, *10*, 4915. [CrossRef]

97. Shao, T.-J.; He, Z.-X.; Xie, Z.-J.; Li, H.-C.; Wang, M.-J.; Wen, C.-P. Characterization of ankylosing spondylitis and rheumatoid arthritis using 1H NMR-based metabolomics of human fecal extracts. *Metabolomics* **2016**, *12*, 70. [CrossRef]
98. Schaffer, S.; Kim, H.W. Effects and Mechanisms of Taurine as a Therapeutic Agent. *Biomol. Ther. (Seoul)* **2018**, *26*, 225–241. [CrossRef] [PubMed]
99. Rossignol, D.A.; Frye, R.E. Mitochondrial dysfunction in autism spectrum disorders: A systematic review and meta-analysis. *Mol. Psychiatry* **2012**, *17*, 290–314. [CrossRef] [PubMed]
100. Kepka, A.; Ochocinska, A.; Chojnowska, S.; Borzym-Kluczyk, M.; Skorupa, E.; Knas, M.; Waszkiewicz, N. Potential Role of L-Carnitine in Autism Spectrum Disorder. *J. Clin. Med.* **2021**, *10*, 1202. [CrossRef]
101. Li, H.; Uittenbogaard, M.; Hao, L.; Chiaramello, A. Clinical Insights into Mitochondrial Neurodevelopmental and Neurodegenerative Disorders: Their Biosignatures from Mass Spectrometry-Based Metabolomics. *Metabolites* **2021**, *11*, 233. [CrossRef]
102. Castelli, V.; Paladini, A.; d'Angelo, M.; Allegretti, M.; Mantelli, F.; Brandolini, L.; Cocchiaro, P.; Cimini, A.; Varrassi, G. Taurine and oxidative stress in retinal health and disease. *CNS Neurosci. Ther.* **2021**, *27*, 403–412. [CrossRef] [PubMed]
103. Garcia-Ayuso, D.; Di Pierdomenico, J.; Hadj-Said, W.; Marie, M.; Agudo-Barriuso, M.; Vidal-Sanz, M.; Picaud, S.; Villegas-Perez, M.P. Taurine Depletion Causes ipRGC Loss and Increases Light-Induced Photoreceptor Degeneration. *Investig. Ophthalmol. Vis. Sci.* **2018**, *59*, 1396–1409. [CrossRef]
104. Ansar, M.; Ranza, E.; Shetty, M.; Paracha, S.A.; Azam, M.; Kern, I.; Iwaszkiewicz, J.; Farooq, O.; Pournaras, C.J.; Malcles, A.; et al. Taurine treatment of retinal degeneration and cardiomyopathy in a consanguineous family with SLC6A6 taurine transporter deficiency. *Hum. Mol. Genet.* **2020**, *29*, 618–623. [CrossRef] [PubMed]
105. Stančíková, M.; Rovenský, J. Metabolism of Aromatic Amino Acids. In *Alkaptonuria and Ochronosis*; Rovensky, J., Urbanek, T., Boldisova, O., Gallagher, J., Eds.; Springer: Malacky, Slovakia, 2015; pp. 9–12. [CrossRef]
106. Eaton, K.K.; Howard, M.; Hunnisett, A. Urinary Beta-Alanine Excretion is a Marker of Abnormal as well as Normal Gut Fermentation. *J. Nutr. Environ. Med.* **2004**, *14*, 121–127. [CrossRef]
107. López-Sámano, M.; Beltrán, L.F.L.; Sánchez-Thomas, R.; Dávalos, A.; Villaseñor, T.; García-García, J.D.; Santos, A.G.L. A novel way to synthesize pantothenate in bacteria involves β-alanine synthase present in uracil degradation pathway. *Microbiologyopen* **2020**, *9*, e1006. [CrossRef]

Disclaimer/Publisher's Note: The statements, opinions and data contained in all publications are solely those of the individual author(s) and contributor(s) and not of MDPI and/or the editor(s). MDPI and/or the editor(s) disclaim responsibility for any injury to people or property resulting from any ideas, methods, instructions or products referred to in the content.

CHAPTER FOUR

CHARACTERIZATION OF THE METABOLIC DEFICITS IN A RETINAL SPECIFIC *ELP1* KNOCKOUT MOUSE MODEL

Contribution of Authors and Co-Authors

Manuscript in Chapter 4

Author: Stephanann M. Costello

Contributions: Conceptualization, Methodology, Validation, Formal analysis, Investigation, Data curation, Writing – original draft, Writing – review & editing, Visualization

Co-First Author: Anastasia Schultz

Contributions: Conceptualization, Methodology, Validation, Formal analysis, Investigation, Data curation, Writing – original draft, Writing – review & editing, Visualization

Co-Author: Donald Smith

Contributions: Methodology, Validation, Formal analysis, Data Curation, Software, Resources

Co-Author: Martha Chaverra

Contributions: Methodology, Formal analysis, Investigation

Co-Author: Brian Tripet

Contributions: Methodology, Software, Resources, Supervision

Co-Author: Lynn George

Contributions: Methodology, Resources, Supervision,

Co-Author: Brian Bothner

Contributions: Resources, Supervision, Project administration, Funding acquisition

Co-Author: Frances Lefcort

Contributions: Conceptualization, Resources, Supervision, Project administration, Funding acquisition

Co-Author: Valérie Copié

Contributions: Conceptualization, Methodology, Software, Validation, Formal analysis, Investigation, Resources, Data curation, Writing – original draft, Writing – review & editing, Supervision, Project administration, Funding acquisition.

Manuscript Information

Stephanann M. Costello, Anastasia Schultz, Donald Smith, Marta Chaverra, Brian Tripet, Lynn George, Brian Bothner, Frances Lefcort, and Valérie Copié

Status of Manuscript:

☒ Prepared for submission to a peer-reviewed journal

☐ Officially submitted to a peer-reviewed journal

☐ Accepted by a peer-reviewed journal

☐ Published in a peer-reviewed journal

Abstract

Neurodegenerative retinal diseases such as glaucoma, diabetic retinopathy, Leber's hereditary optic neuropathy (LHON), and dominant optic atrophy (DOA) are all marked by progressive decline of retinal ganglion cells (RGC). This decline is promoted by structural and functional deficits of mitochondria, including electron transport chain (ETC) dysfunction, increased oxidative stress, and reduced energy (ATP) production [1–5]. The cellular mechanisms associated with progressive optic atrophy have been similarly observed in Familial dysautonomia (FD) patients, who experience progressive loss of visual acuity through neurodegeneration of RGCs, a breakdown in mitochondrial structure, and a disruption in ETC function [6–10]. Overall, retinal metabolism plays a crucial role to meet the elevated energetic demands of this tissue, and recent characterizations of FD patients' serum and stool metabolomes indicate alterations in central metabolic processes and a potential systemic deficit of taurine, a small molecule crucial for eye health [11–14]. This study sought to elucidate the metabolic contributions to the progressive optic atrophy observed in FD. Additionally, dopaminergic amacrine cells make up interneurons within the inner nuclear layer of the retinal fiber layer and mediate integration and modulation of information in a time-dependent manner to RGCs. As these cells have been associated with RGC loss in the neurodegenerative disease Parkinson's [15], a targeted analysis of the dopaminergic amacrine cells and their product, dopamine, was also undertaken. One dimensional (1D) proton (^{1}H) nuclear magnetic resonance (NMR) spectroscopy, mass spectrometry, and retinal histology methods were employed to characterize retinas from the retina specific Elp1 conditional knockout (CKO) FD mouse model (*Pax6-Cre*$^{+}$*; Elp1*$^{flox/flox}$) [9,10]. Metabolite alterations were found to occur in parallel with RGC degeneration

over time, and were associated with reduced mitochondrial function, ATP production via the Cahill and mini-Krebs cycles, and phospholipid metabolism. Dopaminergic amacrine cells were reduced at timepoints P30-P90, and dopamine levels were 25-35% less in the CKO retinae compared to control retinae at P60. Overall, this study has expanded upon the previous understanding underlying the retinal pathology of FD patients. This knowledge may apply to other retinal diseases that share the same hallmark features and help guide new avenues to explore novel non-invasive therapeutics to mitigate the progressive blindness observed in FD.

1. Introduction

Familial dysautonomia (FD) is a rare autosomal recessive, developmental, and progressive neurodegenerative disease that impacts the central and peripheral nervous systems. The disease is caused by a single point mutation (c.2204 + 6T > C) in intron 20 of the elongator protein 1 (ELP1, formerly IKBKAP) gene, resulting in a tissue-specific deficiency of ELP1 transcripts. Neurons are the most impacted, producing little to no functional ELP1 protein [16-18]. FD is classified as the most prevalent hereditary sensory and autonomic neuropathy (HSAN type lll), and patients present with highly variable neurological phenotypes marked by gastrointestinal (GI) dyscoordination, pain and temperature perception deficits, cardiovascular instability, spinal curvature, exacerbated gait ataxia, and progressive visual decline [16,18,19]. FD is highly debilitating, leading to a poor quality of life and 50% mortality rate by the age of 40 [16,17]. The loss of vision is one of the few phenotypes ubiquitous to all patients, and taken together with gait ataxia, visual decline becomes one of the most debilitating symptoms impacting FD patients' quality of life [7].

The visual impairment FD patients develop are marked by a continual loss of retinal ganglion cells (RGCs), resulting in severely decreased visual acuity, a central field of view decline, and color vision defects [6-8]. Clinical findings present reduced papillomacular retinal nerve fiber layer (RNFL) thickness which have been corroborated in mouse models that display mitochondrial dysfunction and reduced ATP [6-9], all indicative of optic neuropathy.

In neurodegenerative retinal diseases such as glaucoma and diabetic retinopathy, RGCs are the primary cell type affected. However, studies have observed cell death in other retinal layers, i.e., the amacrine cells of the inner nuclear layer (INL) [5,20]. Amacrine cells are interneurons that are synaptically active in the inner plexiform layer (IPL), integrating and modulating information in a time-dependent manner to the RGCs [21,22]. There exists a diversity of amacrine cell subtypes, each playing an integral role in signal transmission in the retina. Dopamine neurotransmission in the retina is primarily regulated by a single subpopulation of amacrine cells [22], the dopaminergic amacrine (DA) cells. Dopamine plays a crucial role in the modulation of light adaptation and color vision, along with synaptic formation and transmission [23].

In Parkinson's disease (PD), a neurodegenerative disease characterized by the death of dopaminergic neurons in the Substantia nigra, many patients present with visual impairment similar to what is observed in FD, including decreased visual acuity, color blind defects, and difficulties performing more complex visual tasks [15]. Moreover, PD patients also show a reduction in the RNFL indicative of altered mitochondrial function [15, 25, 25], similar to the clinical findings of axonal loss in the papillo-macular bundle found in Leber hereditary optic neuropathy (LHON), dominant optic atrophy (DOA), and FD. Of particular interest is thus

understanding the overall dysregulation seen in various neural populations in the retina as they relate to optic neuropathy and FD.

We recently characterized FD patients' stool and serum polar metabolite profiles and compared them to those of healthy control relatives using 1D (1-dimensional) ^{1}H (proton) nuclear magnetic resonance (NMR) metabolomics techniques, which has provided valuable insights into the relationship between the central metabolism, progressive neurodegeneration, and clinical phenotypes of FD patients [18,19]. Furthermore, we have shown reduced TH-positive cells in the nodose-petrosal ganglia of three FD mouse models [26].

The retina has inherently increased energetic demands and utilizes characteristic metabolic mechanisms to account for these energetic needs [27]. Given the mitochondrial dysfunction and preferential loss of RGCs seen in FD patients and mouse models [6–10], in conjunction with the energetic deficits indicated by patients' stool and serum metabolomes [11, 12], we sought to investigate the features of the retinal metabolome throughout disease progression using a *Pax6-Cre*$^{+}$*; Elp1*$^{LoxP/LoxP}$ FD mouse model. To address this question, we conducted 1D 1H NMR metabolomics and targeted mass spectrometry analyses, together with retinal histology to determine the metabolic profile of FD mouse retinas and assess whether metabolic dysfunction precedes and promotes RGC, or if the preferential loss of RGCs alters the retinal metabolome, and whether amacrine cell populations are impacted.

Limited energy (ATP) supplies due to mitochondrial dysfunction are associated with retinal disease [1,2,4,20]. It is thus necessary to expand upon our overall understanding of the energetic status of the retina in FD to help discern pathology and provide insights for treatment of retinal diseases including FD [28]. Characterizing the cause and effect of metabolic dysfunction relevant to FD may also provide a translational understanding that could help treat

other optic neuropathies such as LHON, and DOA, which share similar mitochondrial dysfunction with FD.

2. Materials and Methods

2.1 Mice

Mouse studies were conducted in the American Association for Laboratory Animal Care (AALAC) accredited Animal Resource Center at Montana State University under the IACUC-approved protocol (MSU protocol no. 2020-15-51). Retina specific Elp1 knockout mice were generated using Specific Pathogen Free (SPF) C57BL/6 mice, the cre-lox system, and the Pax6 reporter gene, giving *Pax6-Cre*$^{+}$*; Elp1*$^{LoxP/LoxP}$ CKO mice (hereafter referred to as CKO). Littermates (*Pax6-Cre*$^{-}$*; Pax6*$^{+/LoxP}$) were used as controls (hereafter referred to as control). The generation and characterization of the Pax6 mouse is described in Ueki et al [10]. Three time points were used for experimentation to monitor the progression of RGC death, metabolic changes, and changes in other retinal neurons: 7 days (P7), 30 days (P30), and 60 days (P60). P7 and P60 were used to examine the retina metabolome by NMR, and P30 was used for MS experiments. For retinal histology and dopaminergic amacrine cell (DA) counts, the time points included P7, P30, and P90. Mice were housed under a 14-h light/10-h dark cycle with temperatures of 18–23 °C and 40–60% humidity, with food (irradiated PicoLab® Rodent Diet 20, 5053 LabDiet®, Land O'Lakes, Inc., Arden Hills, MN, USA) and water given ad libitum.

2.2 Retina Sample Collection for NMR and MS Metabolite Extractions

P7 mice were humanely euthanized by carbon dioxide (CO2) exposure and decapitation following MSU IACUC approved procedures. A small incision was then made to the eyelid, and

the eyes were enucleated. Retinae were rapidly dissected while eyes were suspended in cold phosphate buffered saline (PBS); the cornea was excised from the sclera, the lens was removed, and the retina was peeled away from the eyecup [9,10,29]. Retina pairs from one mouse were collected in a 1.5 mL microcentrifuge tube and flash-frozen in a 95% ethanol dry ice bath. Thus, each sample consisted of both retinae from a single mouse. Retinae from P30 and P60 mice were collected in the same manner, however, following euthanasia by CO2 exposure, the mice were cervically dislocated and eyes enucleated. Retinae were stored at -80 °C until further processed for NMR or MS metabolite extractions.

2.3 Metabolite Extraction for 1D 1H NMR Analysis

A perchloric acid metabolite extraction optimized to extract taurine that had been used for 1H NMR analysis of rabbit lens [30], and rat retina [31], was adapted and modified for extraction of polar metabolites from FD mouse retinas collected at P7 and P60. Retinas were homogenized with a micro-pestle immediately after removal from storage at -80 °C while the tissue was still frozen. A volume of 500 µL of 7% perchloric acid was added to the homogenized tissue and the samples were vortexed for ~1 minute. Following homogenization, all samples were centrifuged at 4,000 x g for 12 minutes. The supernatant was transferred to a new 1.5 mL microcentrifuge tube, followed by addition of 10 µL of phenol red indicator (1M phenol red in NMR buffer), and pH adjusted to pH 7.0 using a 10 M KOH stock solution and visualization of pH indicator changes and formation of a white KClO4 precipitate. A faint yellow color was observed following addition of ~80 µL of 10 M KOH, indicating a sample pH of ~7.0. The sample was then centrifuged (4,000 x g for 7 minutes) to remove the KClO4 precipitate, and the supernatant was transferred to a new 1.5 mL microcentrifuge tube. Resulting metabolite mixture was

concentrated by drying overnight in a speed vacuum concentrator without heat, and then reconstituted in 600 µL of NMR buffer consisting of 0.25 mM sodium 2, 2-Dimethyl-2-silapentane-5-sulfonic (DSS) in 90% H2O/10% D2O, 0.4 mM imidazole, 25 mM NaH2PO4/Na2HPO4, pH 7, and transferred to a 5 mm Bruker NMR tube.

2. Acquisition and Processing of 1D ^{1}H NMR spectra

Spectral acquisition of each retina metabolite mixture was conducted using a Bruker 600 MHz (^{1}H Larmor frequency) AVANCE III solution NMR spectrometer equipped with a 5 mm triple resonance (^{1}H, ^{13}C, ^{15}N) liquid helium-cooled cryoprobe, Top-Spin software (Billerica, MA, USA, Bruker version 3.2) and an automatic sample loading system (SampleJet). The probe was held a constant temperature of 300 K and a gradient-based water suppression "zgesgp" pulse sequence [11,12,32,33] was employed to acquire the data, using a 12 ppm spectral window, 2048 scans, and 65 K data points. The dwell time between data point acquisition was set to 69 µsec, resulting in a total FID acquisition time of 4.5 sec. The recovery delay time (D1) between acquisitions was set to 2 sec, yielding a total relaxation recovery delay of ~6.5 s between scans. The Topspin (Billerica, MA, USA, Bruker version 3.2) software was used to reference chemical shift to the most up-field 0.0 ppm DSS peak and to apply spectral phase correction, as previously reported [11,12,32-34]. Topspin was also used to execute baseline correction and to apply a 0.80 Hz line broadening EM (exponential multiplication) function, prior to Fourier transformation, to yield the preprocessed '1r' NMR data files.

2.5 Chenomx Spectral Signal Annotation and Quantitation

Additional processing of the 1D ^{1}H NMR spectra and metabolite identification (i.e., metabolite ID) and quantification were performed using the ChenomxTM NMR Suite software

(version 8.4; Chenomx Inc., Edmonton, AB, Canada). Using methods previously reported [35,35], the baseline of the imported '1r' file was further adjusted by applying an automatic cubic spline function (Chenomx Spline), and manually adjusting and placing breakpoints within the Processor module of Chenomx. The resultant baselines were flat and well-defined while preventing the loss of spectral signal intensities during quantification. Chemical shift referencing was achieved using DSS (as mentioned above), and the resonance signals of imidazole were used to account for small discrepancies in chemical shift variations arising from slight pH differences of the samples.

The Profiler module of Chenomx was utilized for metabolite annotation and quantification. Reference spectra from the Chenomx small molecule spectral database for 14.1 T magnetic field strength NMR spectrometers and the human metabolomics database (HMDB) [37], were used to fit ^{1}H chemical shifts, ^{1}H spectral splitting patterns, and signal intensities for each metabolite identified in the 1D ^{1}H NMR spectra of the metabolite mixtures recovered from the FD mouse retinas. Spectral signals were manually fit by visually matching the overall shape and intensity of the NMR signals of standard compounds tabulated in the Chenomx and HMDB databases, allowing for optimal matching of NMR signal location, spectral fit, and signal intensity [38]. Quantitation of metabolite IDs was achieved by referencing intensity to the internal DSS (0.25 mM) standard. An NMR reference spectrum with annotated metabolite IDs is presented as an illustration in the Supplementary Material (Figure S1) for a P60 mutant retina sample.

2.6 NMR and Statistical Analyses

Spectral metabolite IDs were exported from the Chenomx software as μM concentrations. Normalization of the datasets and subsequent univariate and multivariate statistical analyses were carried out using MetaboAnalyst v 5.0. (Edmonton, AB, Canada). Logarithmic transformation (log10) was applied prior to statistical analyses. Metabolite level differences between the CKO and controls were evaluated using Principal Component Analysis (PCA), hierarchical clustering analysis and heatmap visualization, *t*-tests, and a volcano plot analysis that accounts for both fold change and two sample *t*-test *p* values.

2.7 Extraction of Mouse Retinae for Dopamine Isolation

Mice were euthanized as previously described (section 2.2) and the methods described in Pérez-Fernández et al [39] were adapted for the MS analysis of dopamine levels in the retinas of Pax6 mice. Retina pairs were dissected in PBS, collected in a 1.5 mL microcentrifuge tube, flash frozen and stored at -80 °C until further processed. Thus, each sample consisted of both retinae from a single mouse. Upon removal from storage at -80 °C, each retina sample was immediately homogenized with a micro-pestle while still frozen. 40 μL of the extraction mixture (0.5 mM ascorbic acid and 1% formic acid) was added, and the sample homogenized further for 1 minute and placed on ice. Following manual homogenization, all samples were sonicated for 5 minutes and then centrifuged at 14,000 g for 5 minutes. To prevent oxidation of dopamine, the resulting supernatant was subject to MS analysis within 5 hours of the extraction procedure.

2.8 UHPLC/Q-TOF-MS Analysis for Relative Dopamine Quantitation

UHPLC/Q-TOF-MS (ultra-high performance liquid chromatography-quadrupole time-of-flight mass spectrometry) analysis of the FD retina samples was conducted at the Montana State

University Mass Spectrometry Facility. An Agilent 1290 LC coupled to an Agilent 6538 Q-TOF was employed together with an Agilent Eclipse Plus C18 chromatography column (1.8 µm particle size, 2.1 x 50 mm) maintained at 50 °C and operated at a flow rate of 0.6 mL/min for separation, with a sample injection volume of 5 µL. Water (0.1% formic acid) and acetonitrile (0.1% formic acid) were the mobile phase solvents A and B, respectively. Initially, mobile phase conditions of 99% A and 1% B were applied and held constant for 2 minutes, then a linear gradient from 1% to 98% B was applied over 6 minutes, followed by a hold of 1.25 minutes at 99% B, then returned to the initial condition for a 2.75 minutes re-equilibration, resulting in a total run time of 12 minutes. The LC eluent was ionized with electrospray ionization in positive mode and the Agilent 6538 Q-TOF was operated at 2 Hz over a mass range of 50-1000 m/z. A dopamine standard (insert information on standard) was used to verify the m/z value and retention time. Relative quantitation was achieved using the Agilent MassHunter Quantitative Analysis for Q-TOF (v B.07.00/ build 7.0.457.0) software, and values were reported in extracted ion chromatogram (EIC) area. Retinae from 1 month old CKO mice were evaluated based on their concentration of dopamine, relative to age matched litter controls with two separate MS experiments. Due to batch effect variability that can be introduced based on separate MS experiments, the data was not combined and is thus referred to as Run 1 and Run 2. The difference in dopamine levels in the CKOs compared to controls was assessed with a two-tailed t-test for equal variance with a p-value threshold < 0.05.

2.9 Retinal Histology for Flat Mount Preparations

Mice were euthanized as previously described (section 2.2), and the temporal surface of the eye was marked with green dye (Ketchum Manufacturing) prior to enucleation. The tissue

was fixed in 4% paraformaldehyde (PFA) at room temperature (RT) for 1 hour. The retinas were excised, and the temporal region was marked by a small 15-degree cut. The tissue was permeabilized in 1X PBS containing 0.5% Triton-X 100 for 30 minutes at RT with gentle shaking. Non-specific binding was blocked using 1X PBS containing 0.5% Triton-X 100 and 5% bovine serum albumin (BSA) at RT for 3 hours with gentle shaking. All retinae were incubated for 2 nights at 4°C in primary antibodies diluted in 1% BSA, 0.1% Triton X-100 in 1X PBS, followed by overnight incubation at 4°C with secondary antibodies. Four identical radial cuts flattened the tissue into four lobes, leaving the central region intact. The tissue was mounted with the ganglion cell layer (GCL) oriented facing up on microscope slides using ProLongTM Gold Antifade Mountant (Invitrogen, Cat# P36930).

Retinal flat mounts were imaged using a Leica DMi8 THUNDER imaging system using the navigator spiral scan function with a 20X objective under brightfield illumination with false color. Confocal images of flat-mount retinas were obtained using Lecia TSC SP8 with a 20X oil immersion objective with a resolution of 1024 X 1024. A single image 1mm from the peripheral edge of the tissue in each retinal quadrant was obtained.

Retinal images were processed using ImageJ plugin: Fiji. The total TH+ cells in each retina were counted manually. All images were randomized, ensuring the experimenter was blind to the genotype. The data was reported as the total number of TH+ amacrine cells per retina.

For pairwise comparisons, unpaired two-tailed t-tests were used with a $p < 0.05$ indicating significance. All data were expressed as mean ± SEM. Graphs were made using GraphPad Prism (version 9); Column data are plotted as scatter dot-bar plots to show variability, and n shows the sample size for each data set.

3. Results

3.1 Retina Metabolomic Differences Emerged at 2 Months of Age

A total of 14 retina pairs were collected from mice seven days old (P7) (n=7 CKO, n=7 controls), and a total of 28 metabolites were identified and quantified using NMR (Table S1). Similarly, 17 retina pairs were collected from P60 mice (n=9 CKO, n=8 controls). The same 28 metabolites identified in the P7 dataset were found in the P60 dataset (Table S2 & Figure S1).

Differences in metabolic profiles between CKO and control retinas from P7 and P60 retinae were initially assessed using an unsupervised multivariate PCA analysis (Figure 1). The 2-dimensional (2D) PCA scores plot shown in Figure 1A for P7 retinae revealed intermingled clustering of all datapoints, with no obvious separation of the CKO and controls. Analysis of 3D PCA scores plot for the P7 group revealed a marginal though noticeable separation between P7 CKO and control mouse groups (Figure 1 B), suggesting a potential trend in metabolite differences sufficiently strong to distinguish the two animal groups based on distinct retina metabolome profiles.

PCA analysis of the P60 retina samples (Figure 1C, 1D), revealed a more noticeable difference between the CKO and control groups, as assessed by a tight clustering of the control group and reduced overlap of the sample groups in PCA score plots. Examination of the 2D PCA score plot (Figure 1C) group separation along principal component 2 (PC2). When taking into account a third principal component, the resulting 3D PCA scores plot (Figure 1D) demonstrated a distinct clustering of the CKO group separate from the control group, indicating that retina metabolome differences are sufficiently characteristic to result in the separate clustering of the CKO and control mouse samples.

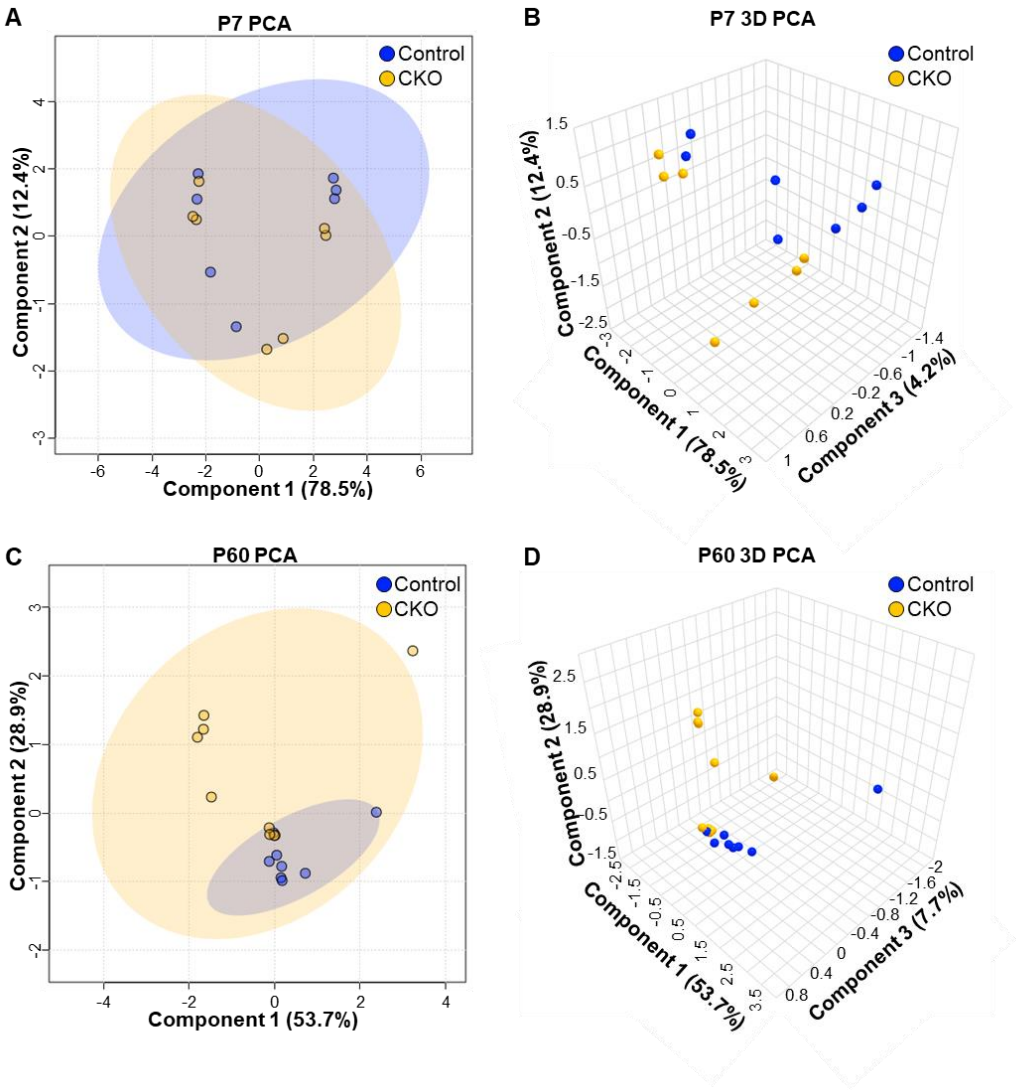


Figure 1. Multivariate Principal component analyses (PCA) of the metabolic profiles of P7 and P60 retinas indicate that the CKO group (gold) cluster separately from control group (blue) by P60. Panels (A,B) present the 2D- and 3D-PCA scores plots of retinae at P7, while panels (C,D) present the 2D- and 3D-PCA scores plots for retinas collected at P60. (A) 2D PCA scores plots of P7 retinas show complete overlap of samples for both groups, indicating any differences in metabolomic profiles are not sufficiently distinct to separate the CKO from controls. (B) Metabolite patterns of the CKO retinas appear to slightly cluster separately from those of control samples in the 3D PCA scores plot of the P7 retinas; however, principal component 3 only accounts for 4.2% of the variance, indicating a marginal group separation. (C) 2D PCA scores plots of the metabolic profiles of P60 retinas reveal that the CKO samples are more variable than controls, but cluster separately from controls when examining the resulting 3D PCA scores plot (D). Each dot on these plots represents each sample generated by collecting the two retinas of each mouse.

Differences between the metabolite profiles of CKO and control mouse retinas were further assessed through a hierarchical cluster analysis (HCA) and visualized using heatmaps. Samples from the CKO group cluster more closely together, based on their characteristic metabolite level patterns, compared to the control group at P60, although this distinction was not so at P7 (Figure 2). This is also consistent with what was observed in the PCA analyses of the P7 and P60 groups. The variation in metabolite levels measured for both CKOs and controls at P7 did not lead to a separate clustering by genotype at that time point (Figure 2A). At P60, the metabolite profiles of the CKO retinas lead to a separate clustering of the CKO samples controls, except for control sample 323whose metabolite patterns appear to more closely resemble that of the CKOs. At P60, the heatmap indicates that there are many metabolites whose levels are lower in the CKO retinas relative to control samples, as shown by the blue and red color blocks associated with each cluster. Metabolites that exhibited the greatest difference in levels in the CKO mice compared to the controls included succinate, alanine, aspartate, acetylcarnitine, choline, glutamine, taurine, glycine, phosphocholine, glycerophosphocholine, glutamate, gamma-aminobutyric acid (GABA) and myo-inositol, all of which were lower in concentration in the CKO group, relative to the control group.

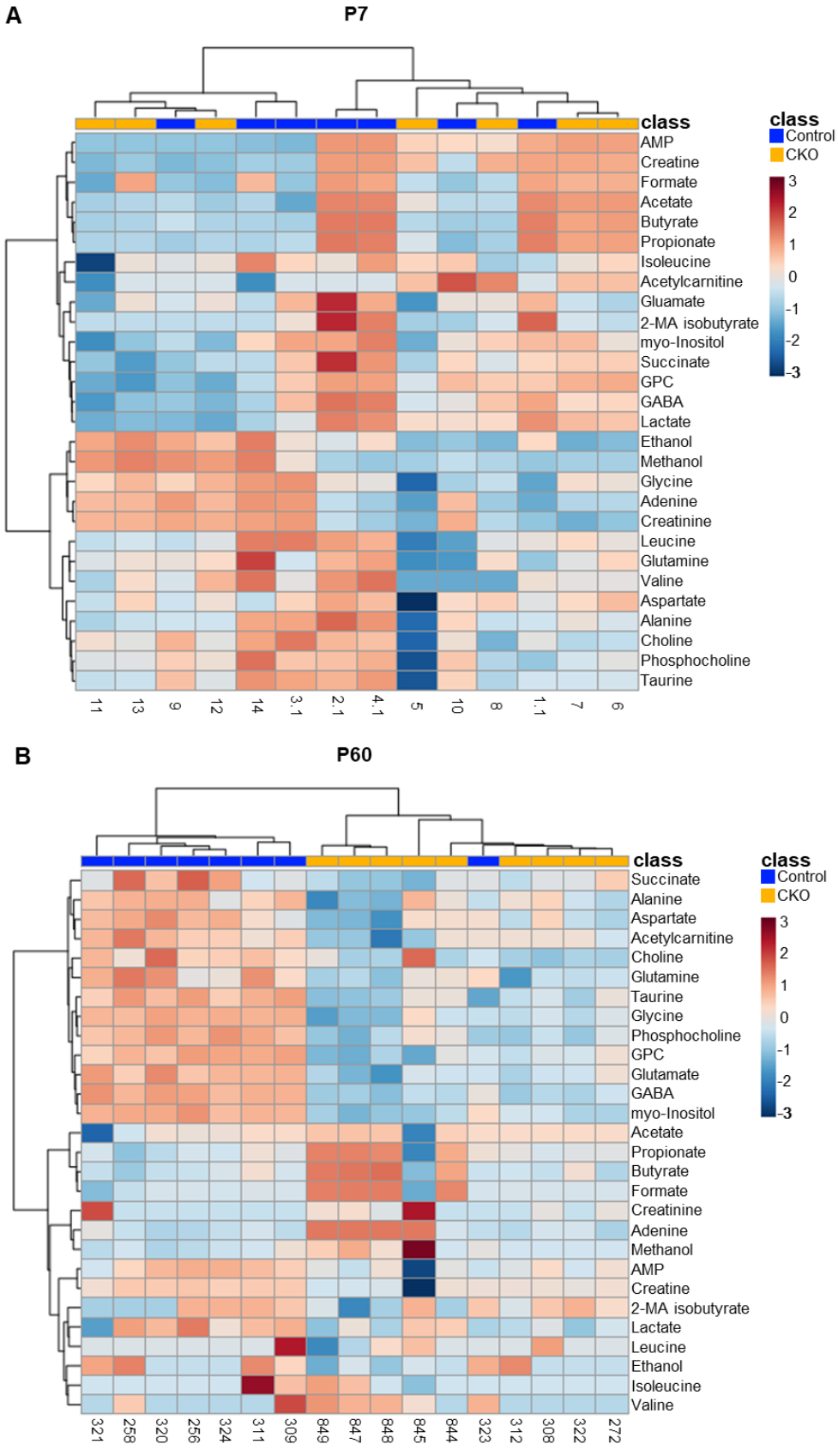

A
P7
class
AMP
Creatine
Formate
Acetate
Butyrate
Propionate
Isoleucine
Acetylcarnitine
Gluamate
2-MA isobutyrate
myo-Inositol
Succinate
GPC
GABA
Lactate
Ethanol
Methanol
Glycine
Adenine
Creatinine
Leucine
Glutamine
Valine
Aspartate
Alanine
Choline
Phosphocholine
Taurine
11 13 9 12 14 3.1 2.1 4.1 5 10 8 1.1 7 6
class
Control
CKO
3 2 1 0 -1 -2 -3
B
P60
class
Succinate
Alanine
Aspartate
Acetylcarnitine
Choline
Glutamine
Taurine
Glycine
Phosphocholine
GPC
Glutamate
GABA
myo-Inositol
Acetate
Propionate
Butyrate
Formate
Creatinine
Adenine
Methanol
AMP
Creatine
2-MA isobutyrate
Lactate
Leucine
Ethanol
Isoleucine
Valine
321 258 320 256 324 311 309 849 847 848 845 844 323 312 308 322 272
class
Control
CKO
3 2 1 0 -1 -2 -3

Figure 2 Hierarchical clustering analysis (HCA) and heatmap visualizations of (A) P7 and (B) P60 CKO (gold) and control (blue) retina samples. The red-blue color spectrum represents the scaled abundance of each metabolite, with dark red and blue indicating high and low abundance, respectively. No distinct clustering based on metabolite levels and genotype are observed until P60. Abbreviations: AMP: adenosine monophosphate; 2-MA isobutyrate: 2-methylamino isobutyrate; GPC: glycerophosphocholine; GABA: gamma-aminobutyric acid.

Conducting an unpaired, two-tailed *t*-test revealed no significant differences between the metabolites measured for the CKO and control retina samples at P7, but the *t*-test for the P60 samples identified 13 metabolites whose levels were significantly (FDR $p < 0.05$) altered between the CKO and control groups (Figure 3). All metabolite levels of those identified from the *t*-test (alanine, aspartate, choline, glutamine, GABA, glycerophosphocholine, glycine, glutamate, acetylcarnitine, phosphocholine, succinate, myo-inositol and taurine) were lower in the CKO compared to the control retina samples.

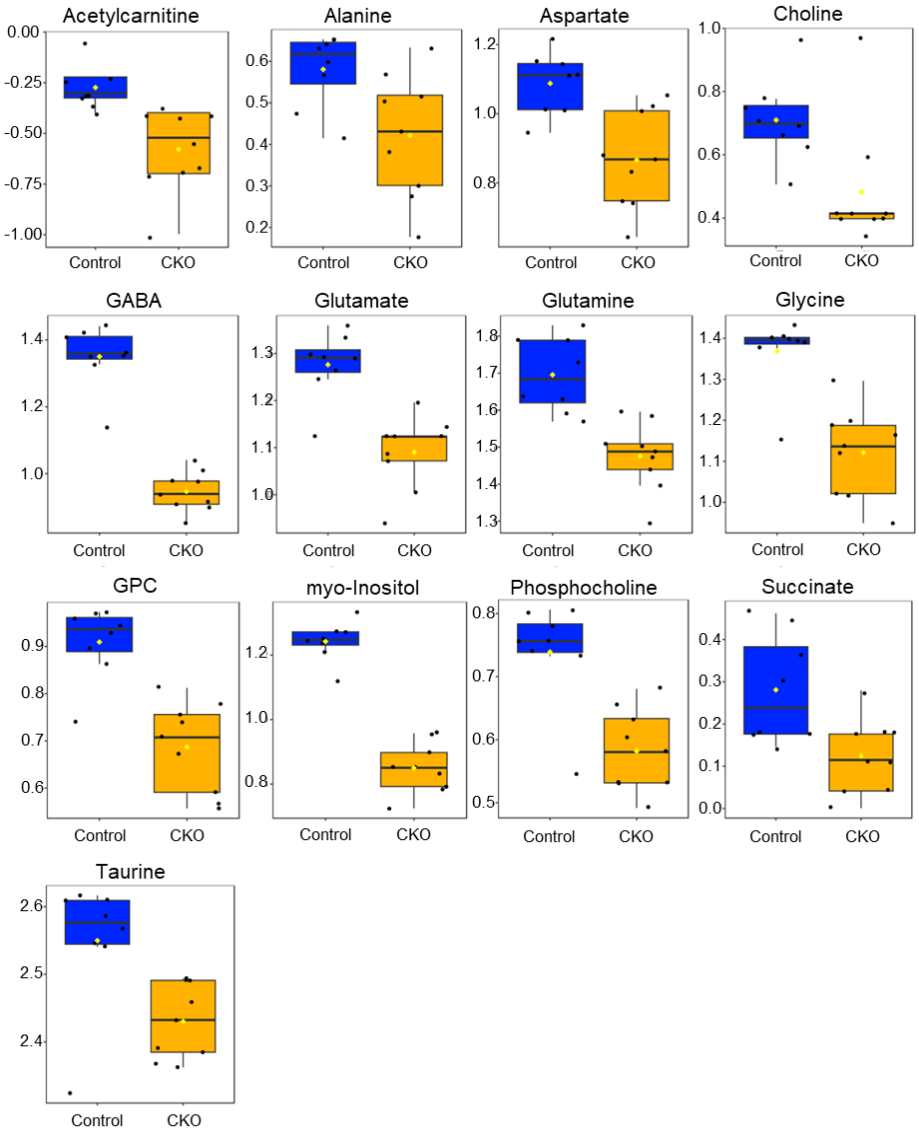


Figure 3. The two-sample *t*-test of the P60 retinae metabolomic profiles identified 13 metabolites that significantly discriminated the CKOs from controls. Normalized concentration is displayed on the y-axes.The *t*-test parameters assumed equal variance and employed a FDR corrected *p* value threshold < 0.05.

A volcano plot analysis of differential metabolite levels was performed for the P60 retina metabolite samples. This analysis was used to examine which metabolites were most different between the CKO and control groups based on fold change (FC) concentration differences, and excluded metabolites that did not reach FDR-corrected *p* value < 0.05 through *t*-test evaluation

(Table S3). This analysis revealed that the levels of myo-inositol and GABA were both ~2.5 times lower in the CKO retinas compared to controls. The reduction in concentration of glycine, glycerophosphocholine, glutamate, glutamine, aspartate, acetyl-carnitine, and choline ranged between 1.7-1.5 folds for the CKO retinas compared to controls, while all other metabolites identified in the two-sample *t*-test were reduced by a FC ≤ 1.5.

Overall, these analyses indicated no statistically significant differences in metabolite levels at P7, but do pointed to significant changes in metabolite levels of the CKO retinas compared to control at P60, with myo-inositol and GABA being the lowest in concentration in the CKO group compared to the control group. Metabolites that most discriminated between the two groups belonged to diverse classes including amino acids, phospholipid metabolism constituents, inhibitory and excitatory neurotransmitters, and metabolites involved in retina energy (ATP) metabolism.

3.2 Alterations in dopaminergic amacrine cell population in CKO retinae.

Dopaminergic amacrine (DA) cells are modulatory retinal interneurons involved in key visual processes such as light adaptation and color vision [21,22]. In the mouse retina, DA cell bodies are strictly positioned within the inner nuclear layer (INL) and extend processes to other retinal layers, in contrast to dopamine receptors which are distributed throughout the retina [40]. Dopamine transmission via DA cells utilize volume transmission allowing for the pan-retinal modulatory affect. Interestingly, the DA cells are one of the sparsest retinal neurons making 0.0001% of all retinal neurons. Despite making up a small percentage of retinal neurons the number the DA cells is a tightly regulated process [41].

Based on the retinal degeneration found in FD patients, and reduced levels of GABA at P60 (Figure 3 and Table S3), the cellular status of the DA cells were evaluated. CKO and control retinas at P7, P30, P60, and P90, were immunolabeled with an antibody to tyrosine hydroxylase (TH) (rabbit anti-Tyrosine Hydroxylase, Millipore, #AB152), as this is the rate limiting step in DA synthesis. Alteration in the number of TH-positive cells in CKO retinas compared to littermate controls was observed at the later timepoints examined (Figure 4). Interestingly, at P7, before mice have opened their eyes and all amacrine cells have been generated, there is no observable difference in the number of TH-positive cells between the CKO and control (Figure 4A & 4B). However, by P30, when substantial RGC death has occurred, significantly fewer TH-positive amacrine cells were observed in the CKO (Figure 4A & 4B; **** $p < 0.0001$). This trend continued until P90, with a similar number of TH-positive cells in the CKO being significantly reduced in the CKO compared to the control (Figure 4A & 4B; **** $p < 0.0001$).

3.3 Reduced Dopamine Levels at P30 in CKO Retina

Dopaminergic amacrine cells are the primary source of dopamine synthesis in the retina [42]. thus, relative dopamine levels in CKO retinas were measured using UHPLC/Q-TOF-MS to determine whether the significant reduction in DA+ amacrine cells is associated with lower dopamine levels. Two MS experiments (Run 1 and Run 2) were conducted as described in section 2.8, and data were analyzed separately as a result of batch variability. Dopamine levels at P30 in Run 1 were significantly (p value < 0.05) reduced by ~35% in CKO retinas compared to controls ($p=0.023$). Though Run 2 did not reach significance ($p < 0.05$), a ~25% reduction in dopamine levels was still observed in CKO retinas, relative to the amount measured in the control retinas. Overall, while there is variability in dopamine levels between the CKO and

control retinas, we can confidently report a ~ 25-35% reduction of total dopamine levels in the CKO mouse retinas compared to control samples at P30. These findings are supported by the reduction in the number of DACs observed in the CKO mice at three different timepoints.

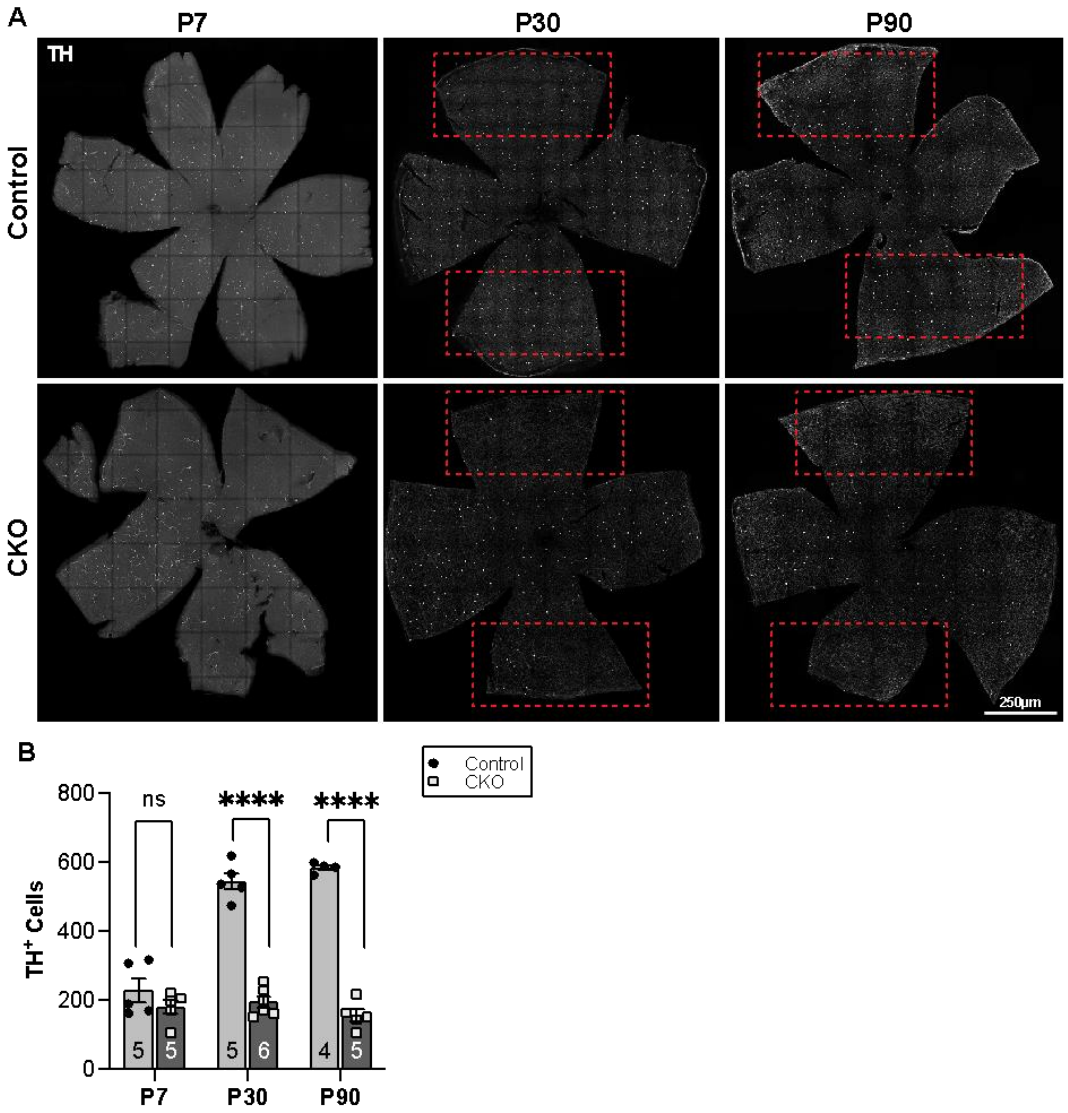


Figure 4. Changes in TH+ cell number throughout disease progression.
(A) Representative retina flat mount stained with anti-TH at three different ages (columns) demonstrating changes in cell number as the disease progresses between control (top panel) and CKO (bottom panel). Red boxes indicate regions with the most prominent reduction in the TH cells in the CKO and corresponding regions in the control retinae. Scale bar, 250µm.
(B) Quantification of TH+ amacrine cells from control mice compared to CKO mice. TH+ cells were counted in the entire retina. ns = 0.2545, **** $p < 0.0001$, unpaired *t*-test. Data are shown as average ±SEM, and each data point represents an individual retina. The sample size for individual groups is represented by n within each bar.

4. Discussion

FD is a highly debilitating neurodevelopmental and neurodegenerative disease, with a ubiquitous clinical phenotype of progressive visual decline that begins around 20 years of age in humans [9]. Previous studies using the FD Pax6 CKO mouse model have reported evidence of mitochondrial dysfunction, reduced ATP production, neuronal stress, and secondary cell types affected by loss of Elp1 [9,10] (data in preparation, and submitted).

The role of mitochondrial dysfunction and reduced energy production in the CKO retina has necessitated to better understand how metabolic impairments affect the function of the retina in FD. Our recent metabolomics analysis of the polar metabolite profiles of FD patients' serum and fecal samples generated insights into the interconnection between FD disease state and the central metabolism, and how the observed metabolic changes potentially report on metabolic processes that may play a role in promoting further neurodegeneration and FD disease progression [11].

A metabolomics analysis of the CKO Pax6 mouse retina was conducted to gain a better understanding of how metabolism may contribute to the optic neuropathy observed in FD patients. In addition, we investigated the phenotypic characteristic of dopaminergic amacrine cells of the retina via immunohistochemistry and targeted mass spectrometry (MS) experiments. Metabolic dysfunction was observed to occur in tandem with *Pax6-cre; Elp1*$^{flox/flox}$ induced RGC degeneration, which was marked by alterations in taurine, Cahill and mini-Krebs cycle intermediates, phospholipid metabolism, and metabolites associated with maintaining proper mitochondrial function. The data demonstrated that Pax6 mouse retinas have a 25-35% reduction

in dopamine levels at P60, data that is accompanied by an overall reduction in DA cell numbers compared to controls beginning at P30.

4.1 ^{1}H NMR data indicate that metabolic disturbances align with *Elp1* induced RGC degeneration.

At postnatal day 7 (P7), the metabolome of retinas from FD mice could not be separated from the control mice as differences in polar metabolite patterns were small and not significant (Figure 1A & 1B, Figure 2A). Metabolite pattern trends appear to be emerging based on slight group differentiation observed in the P7 3D PCA plot (Figure 1B), though when evaluated using a *t*-test, no metabolites were significantly different based on an FDR corrected p value < 0.05. Conversely, by P60, the metabolome of CKO retinas began to diverge from that of controls and enabled the separate clustering of the CKO groups from the control group, as observed in the 2D and 3D PCA scores plots (Figure 1C & 1D). Further analysis using a two-sample *t*-test identified 14 metabolites had significantly different levels (FDR $p \leq 0.05$) in the CKO retinas compared to controls (Figure 3). These data suggest that the onset of RGC decline is associated with metabolic dysfunction. Metabolites with altered levels significantly discriminated between the retina metabolome of CKO and control mice (Figure 3) and were further evaluated based on their associated metabolic pathways, and relevant cellular functions specific to the retina.

The retina is one of the most energy demanding neuronal tissues [4,27], thus requiring efficient metabolism to meet its energetic (ATP)needs, however, causing retinal cells to be highly sensitive to disturbances in energy supplies [28,43]. RGC rely critically on proper mitochondrialfunction for RGC survival, and disruption of mitochondrial metabolism within RGCs has been linked to other optic neuropathies in addition to FD, includingglaucoma, Leber's hereditary optic neuropathy (LHON), and dominant optic atrophy (DOA) [1,2,4]. In this work,

taurine, and other metabolites that contribute to healthy mitochondrial function and energy production, were identified as being key markers of CKO retina pathology when compared to control retinas at P60.

4.2 Taurine is fundamental for mitochondrial electron transport chain (ETC) complex 1 function and RGC health.

In our previous metabolomics analysis of FD patients, taurine levels were lower and implicated in a systemic deficit of FD patients [11]. Herein, taurine was also identified as being significantly decreased in the FD mouse retinas at P60(Figure 3). Compared to any other bodily tissue, the retina is the most enriched in taurine, and deficits of this metabolite cause loss of functional photoreceptors, RGC degeneration, and optic neuropathy [13,14,44-46]. The mechanism by which taurine deficient phenotypes induce retinal damage is thought to occur via functional impairments of the mitochondria, including reduced complex 1 electron transport chain (ETC) activity and oxygen consumption, and leading to increased reactive oxygen species (ROS) production [47,48]. Reduced ETC complex 1 function has been reported in FD patients [10,11] and in Pax6 mouse retinas at 2.5 months of age [10]. Mutations in genes that dysregulate complex 1 are also associated with LHON and DOA [1,2]. As such, this presents an interesting crossroads between taurine deficient phenotypes and a reduction in Elp1, as both cellular states reportedly promote mitochondrial dysfunction through a similar cellular mechanism of mediating translation effectively.

Elp1 is responsible for modifying the wobble uridine of tRNA molecules of glutamate, glutamine, and lysine [49], while adequate taurine levels enable smooth translation of leucine and lysine wobble uridines in the mitochondria [47,50]. Reduction of both Elp1 and taurine in the CKO retina could thus acts in concert and enhance wobble uridine modification deficiencies.

Interestingly, the wobble uridine modification facilitated by taurine are necessary for the synthesis of mitochondrial proteins cytochrome b, ND5, and ND6 (NADH-ubiquinone oxidoreductase chain 5 and 6) [47,50], the latter two being the same proteins that are mutated in LHON and DOA [1,2]. Moreover, all are responsible for maintaining proper complex 1 function, minimizing ROS production and cellular stress, and preventing the breakdown of mitochondrial structure and function. Improving mitochondrial function in dorsal root ganglia (DRG) neurons has been shown to improve neuronal survival in FD [51], suggesting that mitochondria could be a promising target to prevent RGC loss [10]. Taurine has a direct role in protecting mitochondrial function, and taurine supplement studies have shown that it can mitigate metabolic impairments, mitochondrial dysfunction [48], and retinal degeneration [44]. Taurine is thus regarded as a promising metabolite for future studies aimed at elucidating its direct involvement in FD retinal pathology, and may be a good candidate for therapeutic interventions focused on mitigating the progressive optic atrophy observed in FD patients, as well as that of LHON and DOA.

4.3 Alterations in the levels of metabolites involved in the Cahil (alanine-glucose) and mini-Krebs cycles point to energetic (ATP) deficits in CKO retinae.

Retinal tissue, being another constituent of the central nervous system, is closely associated with the brain, and as such, metabolic energy to sustain retinal function is predominantly derived from anaerobic glycolysis [4,27]. Though glucose is the preferred substrate of the retina for energy production, it is possible that other substrates, such as lactate or certain amino acids, can be used, based on the close relationship between the retina and the brain [4]. Metabolic pathways of the brain are characterized by the reliance on glucose for glycolysis, and TCA cycle activity that is fueled by ketone catabolism and the malate-aspartate shuttle that

supplies substrates for replenishing the TCA intermediates [52]. Recent investigations into the energetic needs of the retina identified an uncoupling of glycolysis and the TCA cycle through the “mini-Krebs” (6-step TCA) cycle and the alanine-glucose Cahill cycle (Figure 5), which appears to take place in photoreceptors and Müller glia [27], utilizing similar metabolic pathways as those described for the brain, though unlike the brain, these pathways in the retina are seemingly independent of starvation conditions [52].

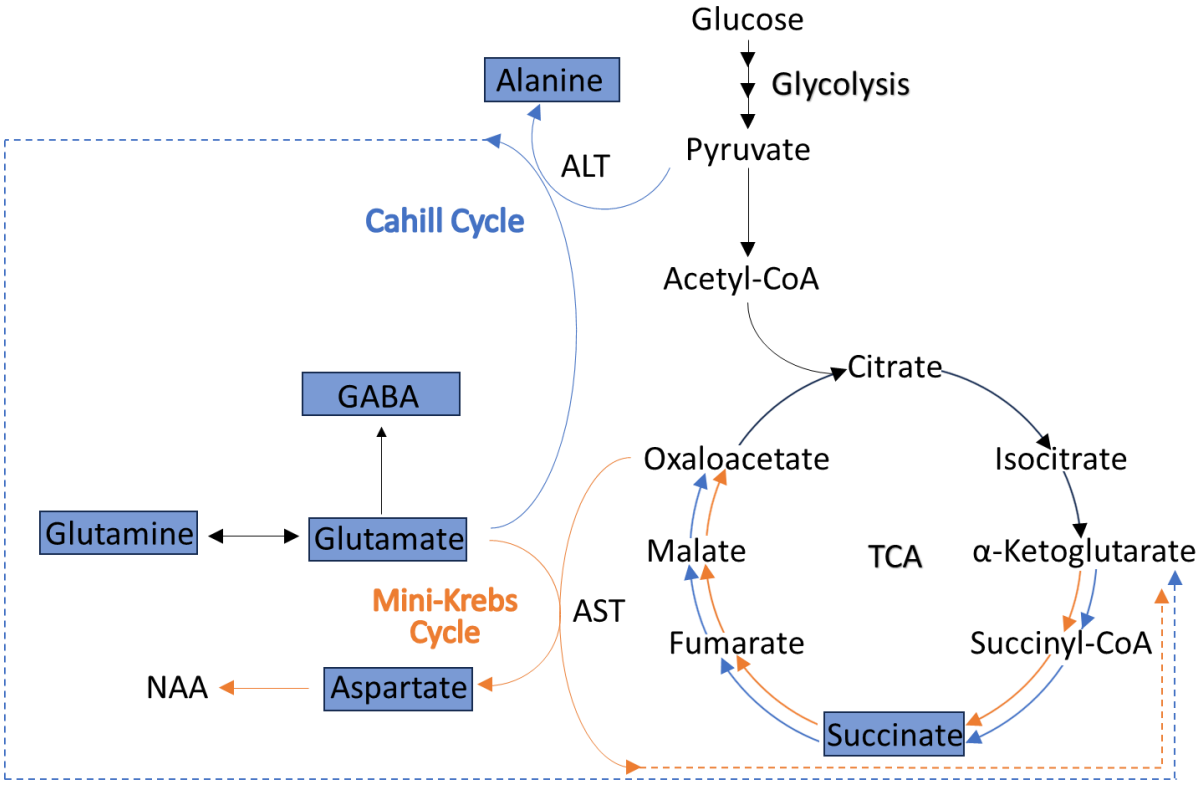


Figure 5. An illustration of how the Cahill and mini-Krebs cycle both contribute to rapid energy production in the retina. The Cahill and mini-Krebs cycles are shown in blue and orange, respectively. Key steps in each cycle are depicted, with ALT initiating the Cahill cycle by converting pyruvate and glutamate to alanine and α-ketoglutarate, respectively, which can then enter the TCA cycle. In a similar manner, glutamate and oxaloacetate can be converted to aspartate and α-ketoglutarate, via AST function, thus entering the TCA cycle as well. Both pathways provide means by which ATP, NADH, GTP and FADH2 can be generated at a more efficient rate than classical glycolysis coupled to aerobic catabolism via the TCA cycle in the retina [27]. The characteristic signature metabolites that indicate Cahill and mini-Krebs cycle activity include alanine (Cahill) and NAA (mini-Krebs cycle) [27]. Blue boxes indicate metabolites in significantly lower concentrations measured in the Pax6 CKO retina compared to controls. Abbreviations: ALT, alanine transaminase; AST aspartate aminotransferase; NAA, n-acetyl aspartate.

In the Cahill cycle of the retina, which is unique compared to how the liver utilizes this cycle, pyruvate produced from glycolysis is transaminated to alanine, and converts glutamate to α-ketoglutarate, which can enter the TCA cycle [27]. In the mini-Krebs cycle, metabolites enter the TCA cycle via the conversion of glutamate and oxaloacetate to α-ketoglutarate and aspartate,

respectively, a reaction mediated by aspartate amino transferase. In both instances, glutamate is a key metabolite for both pathways. In Müller glia, and presumably other retinal cell types, glutamate can be derived from glutamine, or absorbed from the extracellular space [27]. An additional metabolic fate of glutamine, beyond its role in energy metabolism, is its conversion to GABA (gamma amino-butyric acid), the most abundant inhibitory neurotransmitter, which is used by DA cells [23]

Lower levels of alanine, glutamine, glutamate, and aspartate were measured in P60 Pax6 retinas, suggesting a potential deficit or depletion of these key energy-producing substrates. GABA levels were also reduced in the P60 CKO retinae, suggesting the lower levels of glutamate are not a result of GABA production. A third pathway that uncouples glycolysis and the TCA cycle, similarly to the Cahill and mini-Krebs cycle, is the Cori (lactate-glucose) cycle, which reduces pyruvate to lactate to maintain anaerobic glycolysis by regenerating NAD+ [27]. Lactate was profiled in the CKO and control retinas, though no significant difference in lactate levels were observed, suggesting that the Cori cycle may not be substantially upregulated. The fact that succinate levels were not found to be elevated in CKO Pax 6 retinas suggest that the TCA cycle is indeed active and could be fueled through the shuttling of intermediates through the mini-Krebs cycle (Figure 5).

Since the mini-Krebs cycle is an efficient way for retinal cells to produce energy [27], it stands to reason that this pathway may actually be used to a greater extent by the retinal cells in the CKO eye than the control. Such enhanced use of the mini-Krebs cycle could lead to a depletion of available glutamine and glutamate that are used in the Cahill cycle, thus leading to reduced alanine levels, corroborating our observations in the CKO retinae (Figure 3). To confirm

whether the mini-Krebs cycle is being used or not, the end product, N-acetyl aspartate (NAA) would have to be measured, which unfortunately was not detected in our analysis.

Though these pathways have not been directly linked to RGCs, but instead to the function of photoreceptors and Müller glia, RGC (and now DA cells) are the only reported cell types that die in the Pax6 FD mouse model. Photoreceptors die in other FD models, though at a much later age than the P60 timepoint used in this study [9], and there is no evidence that photoreceptors are reduced in the Pax6 FD mouse model [10]. Müller cells in CKO Pax6 retinae, however, have been found to be dysfunctional as they are unable to mount the expected cellular response to mitochondrial damage (data in preparation), though cell numbers for Müller glia in CKO Pax6 retinas remain comparable to controls. These results indicate that the metabolic changes identified in this study are either indicative of alterations specific to RGCs that should be further explored, or these data present evidence of alterations associated with cell types other than RGCs, such as Müller glia, which may not die due to *Elp1* loss, but instead promote disease progression through dysregulation of other cell functions.

4.4 Reduced levels of membrane phospholipid associated metabolites myo-inositol and choline are associated with retinopathy.

Myo-inositol is the most abundant of nine isoforms of inositol and is comprised of a six carbon ring structure, each with an attached hydroxyl group [53]. Myo-inositol is commonly found in tissues with high glucose utilization [53], including the retina, and is a marker for glial cell proliferation [54], although glial cell numbers were unchanged in the CKO Pax6 retinae compared to controls (data in preparation). Both dietary absorption and endogenous synthesis provide sources for myo-inositol. Glucose-6-phosphate is used to synthesize myo-inositol

phosphate, which is then converted to myo-inositol through L-myo-inositol-1-phosphate synthase, and myo-inositol-1-phsophate catalysis. This synthesis occurs in the liver, kidneys and brain [53], but myo-inositol concentrations are primarily maintained in neural tissue by active cellular uptake that can be inhibited by elevated blood glucose levels. Reduced levels of cellular myo-inositol manifest as abnormal phospholipid metabolism [3] of phosphoinositide's, which make up a substantial component of retinal cell membranes [55]. Additionally, reduced levels of myo-inositol can impact cholinergic transmission by improperly mediating assembly and disassembly of microtubules that are involved in neurotransmitter secretion [3]. The cholinergic nervous system is greatly impacted in FD and FD mouse models [56,57][30,64], and as such, suggests a mechanism by which reduced levels of myo-inositol could be exacerbating dysfunction of the cholinergic system in FD.

Within the retina, the distribution of phosphatidylinositols in retinal membranes of cell types other than rod outer segments and the retinal pigment epithelium are ubiquitous [55]. Phosphoinositides are important for numerous cellular functions, including development, proliferation, differentiation, membrane excitability, exocytosis, phagocytosis, cell motility and detection of extracellular signals, as the enzymes mediating these functions contain highly specific phosphoinositide-binding domains. Thus, the pathways regulated by phosphoinositides are essential for the function and health of the retina, and for mediating cellular responses to a disease state [55]. The function of the PTEN (Phosphatase and TENsin homolog) enzyme is thus one that could be altered as a result of reduced myo-inositol levels [55,58]. PTEN is also linked to many important downstream cellular response signals that mediate DNA repair and survival signaling [59] and preliminary data suggests this protein may be reduced in CKO Pax6 retinae (data in preparation). Little is known about phosphoinositide regulation and function in the

retina, but it is understood that dysregulation of phosphoinositide can lead to blindness in human patients and animal models [55]. Given the need for downstream products of myo-inositol metabolism for numerous enzyme functions, restoring myo-inositol levels in FD retinas may be beneficial to ensure proper protein synthesis, DNA repair, and survival signaling through PTEN activity and other phosphoinositide-dependent enzymes [59].

Similar to myo-inositol, choline is a precursor for another crucial phospholipid, phosphatidylcholine, and was identified to be reduced in Pax6 CKO retinae at P30 (Figure 3). In neurons, choline facilitates cellular homeostasis via two primary metabolic fates: phosphatidylcholine synthesis, and acetylcholine production. Phosphatidylcholine functions both as a primary cellular membrane constituent, and as a storage molecule to maintain localized neural pools of choline for acetylcholine synthesis [60,61]. Both acetylcholine and an intermediate of phosphatidylcholine synthesis (citicoline) are crucial for the survival and viability of retinal ganglion cells [62], the cell types that die in FD [6,9,10].

Lower levels of choline, phosphocholine, and glycerophosphocholine were measured in the CKO retinae compared to controls. Choline and phosphocholine are the substrate and product, respectively, of the first reaction of the 4 step Kennedy pathway of phosphatidylcholine synthesis (Figure 6). Glycerophosphocholine is a catabolic product of phosphatidylcholine and an intermediate in *de novo* synthesis of choline. High cell membrane synthesis and an active Kennedy pathway are characterized by low choline and high phosphocholine levels [27,32]. The levels of choline, phosphocholine and glycerophosphocholine measured in this study suggest that phospholipid biosynthesis and catabolism are impaired in the CKO retinae. In our prior untargeted metabolomics analysis of FD patients [11,12], we postulated that disrupted choline metabolism may contribute to disease progression, and the present data suggest that choline may

play an even greater role than previously recognized, especially regarding retinal health and RGC degeneration.

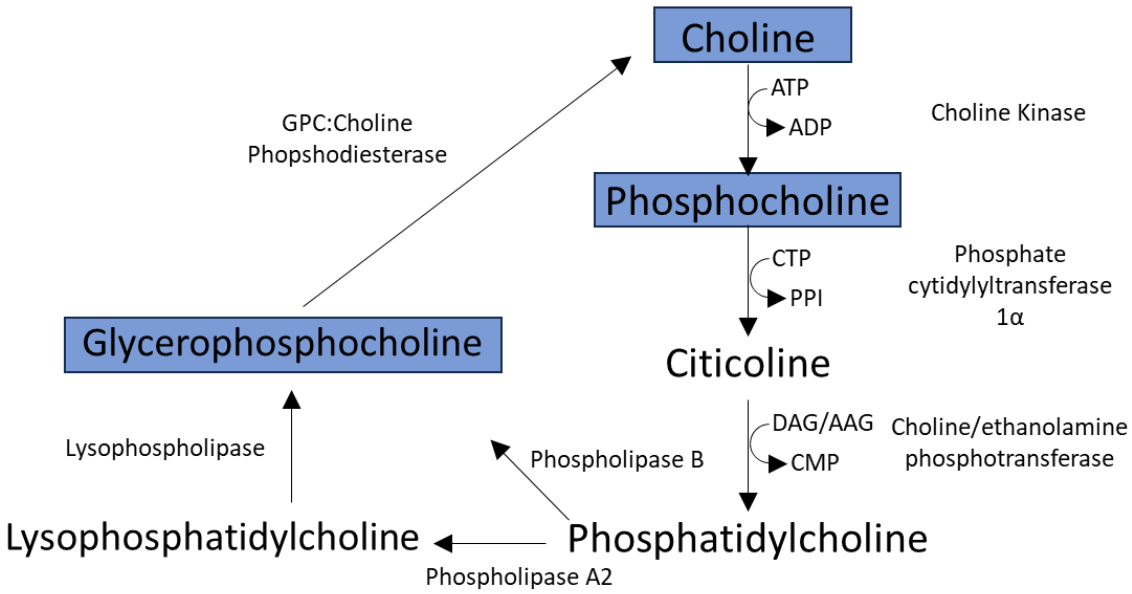


Figure 6. Phosphatidylcholine production and catabolism. Blue boxes indicate metabolites with significantly lower levels measured in the Pax6 CKO retina compared to controls. Abbreviations: ATP, adenosine triphosphate; ADP, adenosine diphosphate; CTP, cytidine triphosphate; PPI, inorganic pyrophosphate; DAG, diacylglycerol; AAG, alkyl-acyl-glycerol; CMP, cytidine monophosphate; GPC, glycerophosphocholine.

Citicoline has been shown to promote acetylcholine and myelin production, restore mitochondrial functions, to have anti-apoptotic effects, stimulate antioxidant activity, prevent neuronal cell death, and to counteract retinal nerve fiber layer thinning [62,63] FD patients and mouse models exhibit reduced myelination of axons, thinning of the retinal nerve fiber layer (NFL), enhanced RGC death, and have deficits in mitochondrial integrity and function [6,7,9,10,16]. Though further studies are needed to evaluate the function of the Kennedy pathway in Pax6 retinas, it may be useful to evaluate levels of citicoline directly, as this metabolite represent a promising neuroprotectant to prevent or reduce RGC death and to limit

visual decline in FD patients. In addition, citicoline has been shown to increase retinal dopamine concentrations [63], which were reduced in the CKO retinae through our MS analysis.

4.5 Alterations in dopaminergic cell populations

This study provides the first evidence that specific subtypes of retinal neurons other than RGCs may also be affected by the loss of *Elp1*. Furthermore, these data might help explain the decline in visual acuity and color-vision deficits in FD patients [6,64]. Interestingly, it does not appear that the DA amacrine cells are dying because the number of TH-positive cells in the CKO is consistent throughout disease progression, whereas in the control, an increase in of~400 cells is observed from P7 to P30. These data are consistent with the targeted MS analysis that found a 25-35% reduction in dopamine levels at P30 (Figure 4). All together, these data have shown that the population of DA cell populations are reduced in the CKO retinae, which is also reflected in the reduced levels of available dopamine.

Amacrine cells are the most diverse cell type of the retina, and despite their morphological differences, most amacrine cells function as inhibitory interneurons, which can be divided into two groups based on whether the cells use GABA or glycine as their primary neurotransmitter. GABAergic cells and glycinergic cells can also express additional neurotransmitters [41,65,66]. Dopaminergic amacrine cells are also GABAergic, while GABAergic amacrine cells are "born" at distinct times. The majority of the TH-positive amacrine cells are born by E16 [41]. Therefore, by P7, all amacrine cells fated to be $GABA^+$ TH^+ should have undergone terminal mitosis and begun differentiating. Taken together, these observations indicate a potential problem with differentiation in a small subtype of neurons in the absence of Elp1. Additionally, lower amacrine cell numbers could lead to altered receptive

properties of RGCs, which may result in additional visual processing dysfunction as seen in FD patients. This preliminary study of retina amacrine cells has yielded exciting results that warrant further investigation to better understand the impact of DA cell deficits in the FD retina, confirm potential defects in neuronal differentiation in the absence of Elp1, and to elucidate yet another important biological function of Elp1 and the Elongator complex.

5. Conclusion

In conclusion, our NMR-based metabolomics analysis of *Pax6-Cre*$^{+}$*; Elp1*$^{loxp/loxp}$ CKO retinae has shown significant changes in polar metabolites which are relevant to mitochondrial function, energy production, and phospholipid metabolism. Accompanying these data are the targeted dopamine MS analysis and histological examination of a subpopulation of retinal amacrine cells, which have shown significant reduction of both cellular dopamine levels and DA cells in CKO retinae compared to control retinae. These data have provided the first untargeted metabolic investigation of *Elp1* CKO retina, and demonstrated for the first time, that a retinal cell population other than RGCs is directly impacted by the loss of *Elp1* in this FD mouse model. Of particular interest for future study are the metabolites taurine, myo-inositol, and constituents of the Kennedy pathway, including citicoline, as these metabolites show great promise as efficacious retinal neurotherapeutics which could be delivered in a non-invasive way. In addition, it would be worthwhile to further explore why levels of dopamine and numbers of DA cells are reduced in Pax6 FD mice, as a better mechanistic understanding of these phenomena could help better understand or treat the visual color decline observed in FD patients. Ultimately, results presented in this study have provided new knowledge on how metabolic deficits impact retinal health and can interfere with the function of not only RGCs but also additional cell types

associated with optic atrophy in FD. These findings may be applicable to other retinal diseases that are associated with mitochondrial and metabolic-mediated deficits.

Supplementary Info

Metabolites	P7					
	CKO		Control			
	Average (uM)	SD (uM)	Average (uM)	SD (uM)	FC	Log2 FC
Acetate	34.40	71.74	79.47	97.22	0.43	-1.21
Adenine	27.31	15.41	36.14	18.90	0.76	-0.40
AMP	6.57	6.30	8.03	8.05	0.82	-0.29
Alanine	11.14	2.22	15.37	3.48	0.72	-0.46
Aspartate	9.07	2.47	9.86	1.36	0.92	-0.12
Butyrate	8.86	20.84	25.19	30.33	0.35	-1.51
Choline	3.40	0.97	5.56	1.61	0.61	-0.71
Creatine	21.97	21.86	24.43	28.83	0.90	-0.15
Creatinine	19.69	24.35	36.60	32.47	0.54	-0.89
Glutamine	88.93	11.75	94.06	8.02	0.95	-0.08
Ethanol	7.34	5.20	9.29	6.45	0.79	-0.34
Formate	19.74	17.85	25.43	20.85	0.78	-0.37
GABA	3.31	1.88	5.56	3.14	0.60	-0.75
Glycine	29.09	6.84	30.17	4.68	0.96	-0.05
Isoleucine	1.17	0.42	1.54	0.37	0.76	-0.40
Glutamate	12.10	2.63	16.07	3.92	0.75	-0.41
Lactate	20.61	18.57	34.93	26.45	0.59	-0.76
Leucine	2.09	0.45	2.66	0.59	0.78	-0.35
Methanol	693.80	599.60	607.06	1040.74	1.14	0.19
2-MA isobutyrate	0.51	0.73	1.47	1.28	0.35	-1.52
Acetylcarnitine	0.26	0.13	0.23	0.08	1.13	0.17
Phosphocholine	17.54	3.31	21.70	2.29	0.81	-0.31
Propionate	7.59	17.25	20.74	24.72	0.37	-1.45
Succinate	1.13	0.41	1.89	1.26	0.60	-0.74
Taurine	125.87	24.76	172.86	27.44	0.73	-0.46
Valine	2.26	0.47	2.77	0.69	0.81	-0.30
myo-Inositol	5.43	1.67	7.44	1.85	0.73	-0.46
GPC	3.06	1.94	4.26	2.26	0.72	-0.48

Table S1 P7 Retina Metabolites Identified and Quantified by NMR: Concentrations, Standard Deviation and Fold Change. 28 metabolites were identified in retinae from 7 CKO and 7 control P7 mice. Column 1 indicates the quantified metabolite, and columns 2 and 3 report the average metabolite concentrations and standard deviations (SD) measured in the retinas from CKO and control mice, respectively. Columns 4 and 5 reports fold change (FC) and Log_2 FC of metabolite concentrations between CKO and control mice. A negative percent value indicates an average lower in CKO mice compared to control mice, and a positive percent value is higher in CKOs compared to controls. Abbreviations: GPC, glycerophosphocholine; GABA, gamma-

aminobutyric acid. AMP, adenosine monophosphate; 2-MA isobutyrate, 2-methylamino isobutyrate.

Metabolites	P60					
	CKO		Control			
	Average (uM)	SD (uM)	Average (uM)	SD (uM)	FC	Log2 FC
Acetate	133.54	71.59	67.76	37.41	1.97	0.98
Adenine	29.18	23.39	9.41	2.05	3.10	1.63
AMP	7.67	3.94	13.08	4.77	0.59	-0.77
Alanine	2.78	0.96	3.88	0.78	0.72	-0.48
Aspartate	7.70	2.46	12.48	2.57	0.62	-0.70
Butyrate	7.27	5.90	2.73	0.46	2.67	1.42
Choline	3.41	2.34	5.35	1.92	0.64	-0.65
Creatine	25.98	15.78	53.38	12.22	0.49	-1.04
Creatinine	5.17	11.65	2.89	6.31	1.79	0.84
Glutamine	30.51	11.89	50.79	11.80	0.60	-0.74
Ethanol	0.91	0.61	1.44	0.57	0.63	-0.66
Formate	520.84	593.19	20.48	7.98	25.44	4.67
GABA	8.92	4.90	22.83	4.65	0.39	-1.36
Glycine	13.59	5.03	23.74	4.25	0.57	-0.80
Isoleucine	0.44	0.31	0.54	0.08	0.83	-0.27
Glutamate	12.48	3.17	19.10	3.10	0.65	-0.61
Lactate	56.96	15.92	77.10	28.85	0.74	-0.44
Leucine	1.12	0.17	1.19	0.26	0.95	-0.08
Methanol	14.66	38.23	0.93	0.45	15.84	3.99
2-MA isobutyrate	0.36	0.19	0.43	0.19	0.84	-0.26
Acetylcarnitine	0.29	0.12	0.55	0.16	0.53	-0.93
Phosphocholine	3.86	0.91	5.56	0.96	0.69	-0.53
Propionate	9.10	8.46	2.56	0.98	3.55	1.83
Succinate	1.36	0.27	1.99	0.61	0.68	-0.55
Taurine	271.23	50.37	361.41	70.49	0.75	-0.41
Valine	0.97	0.21	0.99	0.31	0.98	-0.03
myo-Inositol	7.18	3.69	17.61	2.61	0.41	-1.29
GPC	4.97	1.65	8.23	1.40	0.60	-0.73

Table S2 P60 Retina Metabolites Identified and Quantified by NMR: Concentrations, Standard Deviation and Fold Change. 28 metabolites were identified in retinae from 9 CKO and 8 control P60 mice. Column 1 indicates the quantified metabolite, and columns 2 and 3 report the average metabolite concentrations and standard deviations (SD) measured in the retinas from CKO and control mice, respectively. Columns 4 and 5 reports fold change (FC) and Log_2 FC of metabolite concentrations between CKO and control mice. A negative percent value indicates an average lower in CKO mice compared to control mice, and a positive percent value is higher in CKOs compared to controls. Abbreviations: GPC, glycerophosphocholine; GABA, gamma-

aminobutyric acid. AMP, adenosine monophosphate; 2-MA isobutyrate, 2-methylamino isobutyrate.

Name	FC	Log2(FC)	p.adjusted	-log10(p)
myo-Inositol	0.41	-1.30	2.53E-7	6.60
GABA	0.39	-1.35	3.15E-7	6.50
Glycine	0.57	-0.80	7.21E-4	3.14
Glycerophosphocholine	0.60	-0.73	7.21E-4	3.14
Glutamate	0.65	-0.61	7.21E-4	3.14
Glutamine	0.60	-0.73	1.40E-3	2.84
Aspartate	0.62	-0.70	6.29E-3	2.20
Acetylcarnitine	0.52	-0.93	7.35E-3	2.13
Choline	0.64	-0.65	3.26E-2	1.49

Table S3 Volcano plot analysis of P60 retinae metabolite concentrations between CKOs and controls. Volcano plot analysis indicated fold change (FC) and two-sample t-test significance. A FC threshold ≥ 1.5 and a FDR corrected p value < 0.05 were set as the criteria for significance. FC was taken as the ratio of the mean metabolite concentration for the CKO group compared to the control group prior to statistical normalization by log transformation.

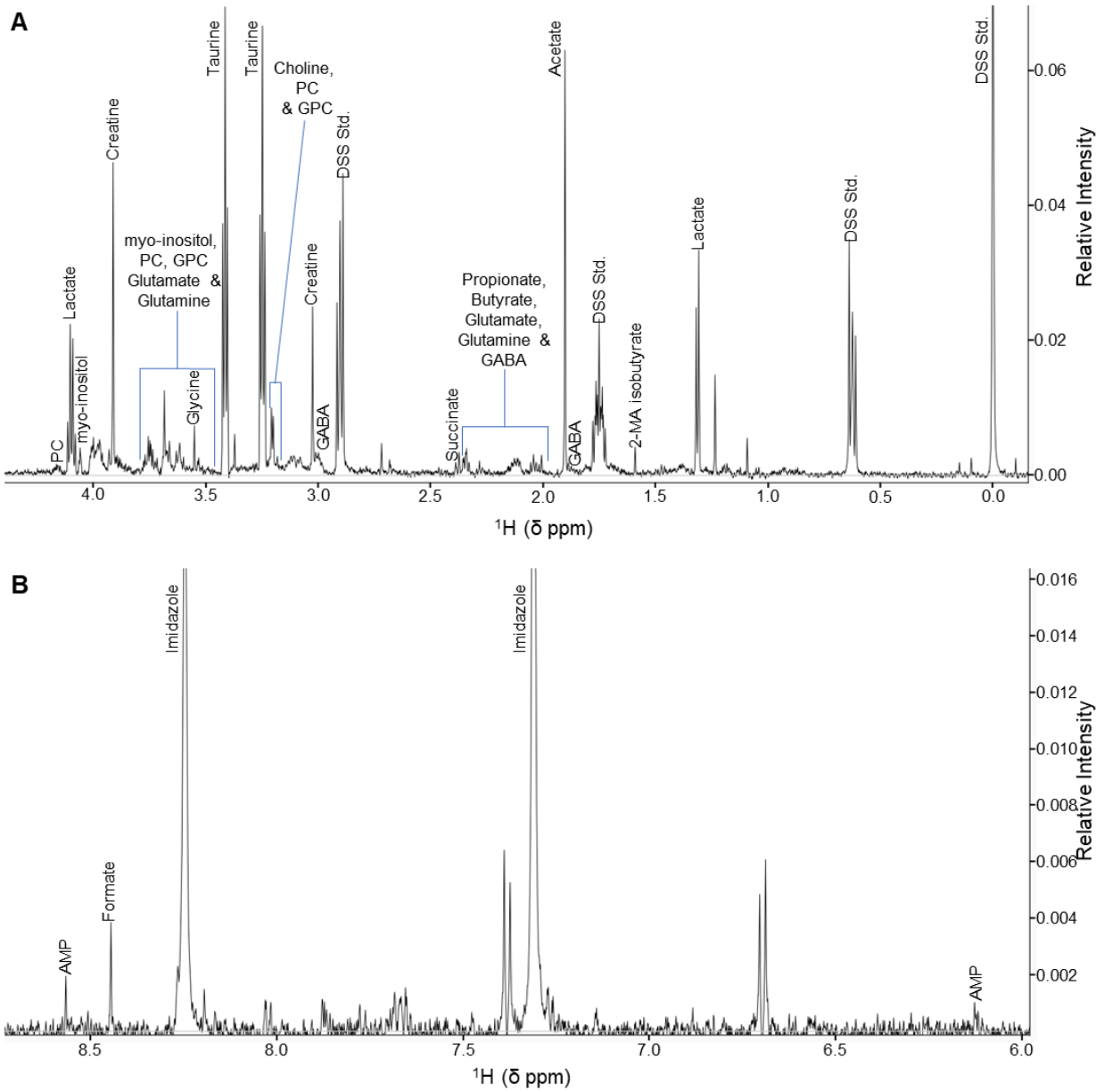


Figure S1 Representative 1D 1H NMR spectrum of retina metabolite extracts from a P60 sample. 1H chemical shift regions corresponding to (A) 0.0 to ~4.5 ppm and (B) 6.0 to ~9 ppm are depicted. Abbreviations denote: DSS, 4,4-dimethyl-4-silapentane-1-sulfonic acid; GPC, glycerophosphocholine; PC, phosphocholine; GABA, gamma-aminobutyric acid. AMP, adenosine monophosphate; 2-MA isobutyrate, 2-methylamino isobutyrate.

Acknowledgements

This research has been funded by the National Institutes of Health, R01-DK117473 (multi-PI R01 award to F.L. and V.C.) and Diversity Supplement 3R01DK117473-02S1 to V.C. and S.M.C. Additional graduate training support to S.M.C. was provided by the Alfred P. Sloan Foundation program and the Montana INBRE Native American Graduate Fellowship P20GM-103474. Support for MSU's NMR Core Facility and NMR instrumentation has been provided, in part, by the NIH Shared Instrumentation Grant (SIG) program (1S10RR13878 and 1S10RR026659), the National Science Foundation (NSF-MRI-DBI-1532078; NSF-MRI-CHE-2018388), the Murdock Charitable Trust Foundation (2015066:MNL) and MSU's Office of the Vice President for Research and Economic Development. Funding for the Montana State Mass Spectrometry Facility used in this publication was made possible in part by the MJ Murdock Charitable Trust, the National Institute of General Medical Sciences of the National Institutes of Health under Award Numbers P20GM103474 and S10OD28650, and the MSU Office of Research and Economic Development. The content is solely the responsibility of the authors and does not necessarily represent the official views of the National Institutes of Health.

References

1. Zanna, C.; Ghelli, A.; Porcelli, A.M.; Karbowski, M.; Youle, R.J.; Schimpf, S.; Wissinger, B.; Pinti, M.; Cossarizza, A.; Vidoni, S.; et al. OPA1 Mutations Associated with Dominant Optic Atrophy Impair Oxidative Phosphorylation and Mitochondrial Fusion. *Brain* **2008**, *131*, 352–367, doi:10.1093/brain/awm335.

2. Sadun, A.A.; Morgia, C.L.; Carelli, V. Leber's Hereditary Optic Neuropathy. *Curr. Treat. Options Neurol.* **2011**, *13*, 109–117, doi:10.1007/s11940-010-0100-y.

3. MacGregor, L.C.; Rosecan, L.R.; Laties, A.M.; Matschinsky, F.M. Altered Retinal Metabolism in Diabetes. I. Microanalysis of Lipid, Glucose, Sorbitol, and Myo-Inositol in the Choroid and in the Individual Layers of the Rabbit Retina. *J. Biol. Chem.* **1986**, *261*, 4046–4051, doi:10.1016/S0021-9258(17)35619-3.

4. Liu, H.; Prokosch, V. Energy Metabolism in the Inner Retina in Health and Glaucoma. *Int. J. Mol. Sci.* **2021**, *22*, 3689, doi:10.3390/ijms22073689.

5. Potilinski, M.C.; Lorenc, V.; Perisset, S.; Gallo, J.E. Mechanisms behind Retinal Ganglion Cell Loss in Diabetes and Therapeutic Approach. *Int. J. Mol. Sci.* **2020**, *21*, 2351, doi:10.3390/ijms21072351.

6. Mendoza-Santiesteban, C.E.; Hedges III, T.R.; Norcliffe-Kaufmann, L.; Axelrod, F.; Kaufmann, H. Selective Retinal Ganglion Cell Loss in Familial Dysautonomia. *J. Neurol.* **2014**, *261*, 702–709, doi:10.1007/s00415-014-7258-2.

7. Mendoza-Santiesteban, C.E.; Hedges, T.R.; Norcliffe-Kaufmann, L.; Warren, F.; Reddy, S.; Axelrod, F.B.; Kaufmann, H. Clinical Neuro-Ophthalmic Findings in Familial Dysautonomia. *J. Neuro-Ophthalmol. Off. J. North Am. Neuro-Ophthalmol. Soc.* **2012**, *32*, 23–26, doi:10.1097/WNO.0b013e318230feab.

8. Ueki, Y.; Ramirez, G.; Salcedo, E.; Stabio, M.E.; Lefcort, F. Loss of Ikbkap Causes Slow, Progressive Retinal Degeneration in a Mouse Model of Familial Dysautonomia. *eNeuro* **2016**, *3*, doi:10.1523/ENEURO.0143-16.2016.

9. Ueki, Y.; Shchepetkina, V.; Lefcort, F. Retina-Specific Loss of Ikbkap/Elp1 Causes Mitochondrial Dysfunction That Leads to Selective Retinal Ganglion Cell Degeneration in a Mouse Model of Familial Dysautonomia. *Dis. Model. Mech.* **2018**, *11*, doi:10.1242/dmm.033746.

10. Mendoza-Santiesteban, C.E.; Palma, J.-A.; Hedges, T.R.; Laver, N.V.; Farhat, N.; Norcliffe-Kaufmann, L.; Kaufmann, H. Pathological Confirmation of Optic Neuropathy in Familial Dysautonomia. *J. Neuropathol. Exp. Neurol.* **2017**, *76*, 238–244, doi:10.1093/jnen/nlw118.

11. Costello, S.M.; Cheney, A.M.; Waldum, A.; Tripet, B.; Cotrina-Vidal, M.; Kaufmann, H.; Norcliffe-Kaufmann, L.; Lefcort, F.; Copié, V. A Comprehensive NMR Analysis of Serum and Fecal Metabolites in Familial Dysautonomia Patients Reveals Significant Metabolic Perturbations. *Metabolites* **2023**, *13*, 433, doi:10.3390/metabo13030433.

12. Cheney, A.M.; Costello, S.M.; Pinkham, N.V.; Waldum, A.; Broadaway, S.C.; Cotrina-Vidal, M.; Mergy, M.; Tripet, B.; Kominsky, D.J.; Grifka-Walk, H.M.; et al. Gut Microbiome Dysbiosis Drives Metabolic Dysfunction in Familial Dysautonomia. *Nat. Commun.* **2023**, *14*, 218, doi:10.1038/s41467-023-35787-8.

13. Ripps, H.; Shen, W. Review: Taurine: A "Very Essential" Amino Acid. *Mol. Vis.* **2012**, *18*, 2673–2686.

14. Castelli, V.; Paladini, A.; d'Angelo, M.; Allegretti, M.; Mantelli, F.; Brandolini, L.; Cocchiaro, P.; Cimini, A.; Varrassi, G. Taurine and Oxidative Stress in Retinal Health and Disease. *CNS Neurosci. Ther.* **2021**, *27*, 403–412, doi:10.1111/cns.13610.

15. Indrieri, A.; Pizzarelli, R.; Franco, B.; De Leonibus, E. Dopamine, Alpha-Synuclein, and Mitochondrial Dysfunctions in Parkinsonian Eyes. *Front. Neurosci.* **2020**, *14*, 567129, doi:10.3389/fnins.2020.567129.

16. Norcliffe-Kaufmann, L.; Slaugenhaupt, S.A.; Kaufmann, H. Familial Dysautonomia: History, Genotype, Phenotype and Translational Research. *Prog. Neurobiol.* **2017**, *152*, 131–148, doi:10.1016/j.pneurobio.2016.06.003.

17. Dietrich, P.; Dragatsis, I. Familial Dysautonomia: Mechanisms and Models. *Genet. Mol. Biol.* **2016**, *39*, 497–514, doi:10.1590/1678-4685-GMB-2015-0335.

18. Slaugenhaupt, S.A.; Blumenfeld, A.; Gill, S.P.; Leyne, M.; Mull, J.; Cuajungco, M.P.; Liebert, C.B.; Chadwick, B.; Idelson, M.; Reznik, L.; et al. Tissue-Specific Expression of a Splicing Mutation in the IKBKAP Gene Causes Familial Dysautonomia. *Am. J. Hum. Genet.* **2001**, *68*, 598–605, doi:10.1086/318810.

19. Chekuri, A.; Logan, E.M.; Krauson, A.J.; Salani, M.; Ackerman, S.; Kirchner, E.G.; Bolduc, J.M.; Wang, X.; Dietrich, P.; Dragatsis, I.; et al. Selective Retinal Ganglion Cell Loss and Optic Neuropathy in a Humanized Mouse Model of Familial Dysautonomia. *Hum. Mol. Genet.* **2022**, *31*, 1776–1787, doi:10.1093/hmg/ddab359.

20. Gastinger, M.J.; Singh, R.S.J.; Barber, A.J. Loss of Cholinergic and Dopaminergic Amacrine Cells in Streptozotocin-Diabetic Rat and Ins2Akita-Diabetic Mouse Retinas. *Invest. Ophthalmol. Vis. Sci.* **2006**, *47*, 3143–3150, doi:10.1167/iovs.05-1376.

21. Kolb, H. Roles of Amacrine Cells. In *Webvision: The Organization of the Retina and Visual System*; Kolb, H., Fernandez, E., Nelson, R., Eds.; University of Utah Health Sciences Center: Salt Lake City (UT), 1995.

22. Kolb, H. Anatomical Pathways for Color Vision in the Human Retina. *Vis. Neurosci.* **1991**, *7*, 61–74, doi:10.1017/s0952523800010944.

23. Witkovsky, P. Dopamine and Retinal Function. *Doc. Ophthalmol. Adv. Ophthalmol.* **2004**, *108*, 17–40, doi:10.1023/b:doop.0000019487.88486.0a.

24. La Morgia, C.; Barboni, P.; Rizzo, G.; Carbonelli, M.; Savini, G.; Scaglione, C.; Capellari, S.; Bonazza, S.; Giannoccaro, M.P.; Calandra-Buonaura, G.; et al. Loss of Temporal Retinal Nerve Fibers in Parkinson Disease: A Mitochondrial Pattern? *Eur. J. Neurol.* **2013**, *20*, 198–201, doi:10.1111/j.1468-1331.2012.03701.x.

25. Hu, Z.-X.; Pu, J.-L.; Zheng, R.; Yan, Y.-Q.; Liu, K.-Y.; Liu, Y.; Zheng, R.; Chen, Y.; Lin, Z.-H.; Xue, N.-J.; et al. Mitochondrial Morphology and Synaptic Structure Altered in the Retina of Parkin-Deficient Mice. *Neurosci. Lett.* **2022**, *790*, 136888, doi:10.1016/j.neulet.2022.136888.

26. Tolman, Z.; Chaverra, M.; George, L.; Lefcort, F. Elp1 Is Required for Development of Visceral Sensory Peripheral and Central Circuitry. *Dis. Model. Mech.* **2022**, *15*, dmm049274, doi:10.1242/dmm.049274.

27. Chen, Y.; Zizmare, L.; Calbiague, V.; Yu, S.; Herberg, F.W.; Schmachtenberg, O.; Paquet-Durand, F.; Trautwein, C. Retinal Energy Metabolism: Photoreceptors Switch between Cori, Cahill, and Mini-Krebs Cycles to Uncouple Glycolysis from Mitochondrial Respiration 2022, 2022.06.20.496788.

28. Country, M.W. Retinal Metabolism: A Comparative Look at Energetics in the Retina. *Brain Res.* **2017**, *1672*, 50–57, doi:10.1016/j.brainres.2017.07.025.

29. Schultz, A.; Cheng, S.-Y.; Kirchner, E.; Costello, S.; Miettinen, H.; Chaverra, M.; King, C.; George, L.; Zhao, X.; Narasimhan, J.; et al. Reduction of Retinal Ganglion Cell Death in Mouse Models of Familial Dysautonomia Using AAV-Mediated Gene Therapy and Splicing Modulators. *Sci. Rep.* **2023**, *13*, 18600, doi:10.1038/s41598-023-45376-w.

30. Midelfart, A.; Dybdahl, A.; Gribbestad, I.S. Detection of Different Metabolites in the Rabbit Lens by High Resolution 1H NMR Spectroscopy. *Curr. Eye Res.* **1996**, *15*, 1175–1181, doi:10.3109/02713689608995153.

31. Santiago, A.R.; Garrido, M.J.; Cristóvão, A.J.; Duarte, J.M.N.; Carvalho, R.A.; Ambrósio, A.F. Evaluation of the Impact of Diabetes on Retinal Metabolites by NMR Spectroscopy. *Curr. Eye Res.* **2010**, *35*, 992–1001, doi:10.3109/02713683.2010.500113.

32. Fuchs, A.L.; Schiller, S.M.; Keegan, W.J.; Ammons, M.C.B.; Eilers, B.; Tripet, B.; Copié, V. Quantitative 1H NMR Metabolomics Reveal Distinct Metabolic Adaptations in Human Macrophages Following Differential Activation. *Metabolites* **2019**, *9*, 248, doi:10.3390/metabo9110248.

33. O'Shea-Stone, G.; Lambert, R.; Tripet, B.; Berardinelli, J.; Thomson, J.; Copié, V.; Garrott, R. 1H NMR Based Metabolic Profiling Distinguishes the Differential Impact of Capture Techniques on Wild Bighorn Sheep. *Sci. Rep.* **2021**, *11*, 11308, doi:10.1038/s41598-021-90931-y.

34. Ramm Sander, P.; Peer, M.; Grandl, M.; Bogdahn, U.; Schmitz, G.; Kalbitzer, H.R. NMR Spectroscopy of Macrophages Loaded with Native, Oxidized or Enzymatically Degraded Lipoproteins. *PLoS ONE* **2013**, *8*, doi:10.1371/journal.pone.0056360.

35. Fuchs, A.L.; Weaver, A.J.; Tripet, B.P.; Ammons, M.C.B.; Teintze, M.; Copié, V. Characterization of the Antibacterial Activity of Bald's Eyesalve against Drug Resistant Staphylococcus Aureus and Pseudomonas Aeruginosa. *PLoS ONE* **2018**, *13*, doi:10.1371/journal.pone.0208108.

36. Mercier, P.; Lewis, M.J.; Chang, D.; Baker, D.; Wishart, D.S. Towards Automatic Metabolomic Profiling of High-Resolution One-Dimensional Proton NMR Spectra. *J. Biomol. NMR* **2011**, *49*, 307–323, doi:10.1007/s10858-011-9480-x.

37. Wishart, D.S.; Feunang, Y.D.; Marcu, A.; Guo, A.C.; Liang, K.; Vázquez-Fresno, R.; Sajed, T.; Johnson, D.; Li, C.; Karu, N.; et al. HMDB 4.0: The Human Metabolome Database for 2018. *Nucleic Acids Res.* **2018**, *46*, D608–D617, doi:10.1093/nar/gkx1089.

38. Xia, J.; Wishart, D.S. Metabolomic Data Processing, Analysis, and Interpretation Using MetaboAnalyst. *Curr. Protoc. Bioinforma.* **2011**, *Chapter 14*, Unit 14.10, doi:10.1002/0471250953.bi1410s34.

39. Pérez-Fernández, V.; Harman, D.G.; Morley, J.W.; Cameron, M.A. Optimized Method to Quantify Dopamine Turnover in the Mammalian Retina. *Anal. Chem.* **2017**, *89*, 12276–12283, doi:10.1021/acs.analchem.7b03216.

40. Keeley, P.W.; Reese, B.E. Role of Afferents in the Differentiation of Bipolar Cells in the Mouse Retina. *J. Neurosci.* **2010**, *30*, 1677–1685, doi:10.1523/JNEUROSCI.5153-09.2010.

41. Voinescu, P.E.; Kay, J.N.; Sanes, J.R. Birthdays of Retinal Amacrine Cell Subtypes Are Systematically Related to Their Molecular Identity and Soma Position. *J. Comp. Neurol.* **2009**, *517*, 737, doi:10.1002/cne.22200.

42. Munteanu, T.; Noronha, K.J.; Leung, A.C.; Pan, S.; Lucas, J.A.; Schmidt, T.M. Light-Dependent Pathways for Dopaminergic Amacrine Cell Development and Function. *eLife 7*, e39866, doi:10.7554/eLife.39866.

43. Yu, D.-Y.; Cringle, S.J.; Yu, P.K.; Su, E.-N. Retinal Energetics: Its Critical Role in Retinal Physiology and Pathology. *Expert Rev. Ophthalmol.* **2011**, *6*, 395–399, doi:10.1586/eop.11.44.

44. Ansar, M.; Ranza, E.; Shetty, M.; Paracha, S.A.; Azam, M.; Kern, I.; Iwaszkiewicz, J.; Farooq, O.; Pournaras, C.J.; Malcles, A.; et al. Taurine Treatment of Retinal Degeneration and Cardiomyopathy in a Consanguineous Family with SLC6A6 Taurine Transporter Deficiency. *Hum. Mol. Genet.* **2020**, *29*, 618–623, doi:10.1093/hmg/ddz303.

45. García-Ayuso, D.; Di Pierdomenico, J.; Hadj-Said, W.; Marie, M.; Agudo-Barriuso, M.; Vidal-Sanz, M.; Picaud, S.; Villegas-Pérez, M.P. Taurine Depletion Causes ipRGC Loss and Increases Light-Induced Photoreceptor Degeneration. *Invest. Ophthalmol. Vis. Sci.* **2018**, *59*, 1396–1409, doi:10.1167/iovs.17-23258.

46. Bonelli, R.; Woods, S.M.; Lockwood, S.; Bishop, P.N.; Khan, K.N.; Bahlo, M.; Ansell, B.R.E.; Fruttiger, M. Spatial Distribution of Metabolites in the Retina and Its Relevance to Studies of Metabolic Retinal Disorders. *Metabolomics* **2023**, *19*, 10, doi:10.1007/s11306-022-01969-6.

47. Jong, C.J.; Azuma, J.; Schaffer, S. Mechanism Underlying the Antioxidant Activity of Taurine: Prevention of Mitochondrial Oxidant Production. *Amino Acids* **2012**, *42*, 2223–2232, doi:10.1007/s00726-011-0962-7.

48. Jong, C.J.; Sandal, P.; Schaffer, S.W. The Role of Taurine in Mitochondria Health: More Than Just an Antioxidant. *Molecules* **2021**, *26*, 4913, doi:10.3390/molecules26164913.

49. Goffena, J.; Lefcort, F.; Zhang, Y.; Lehrmann, E.; Chaverra, M.; Felig, J.; Walters, J.; Buksch, R.; Becker, K.G.; George, L. Elongator and Codon Bias Regulate Protein Levels in Mammalian Peripheral Neurons. *Nat. Commun.* **2018**, *9*, 1–10, doi:10.1038/s41467-018-03221-z.

50. Merckx, C.; De Paepe, B. The Role of Taurine in Skeletal Muscle Functioning and Its Potential as a Supportive Treatment for Duchenne Muscular Dystrophy. *Metabolites* **2022**, *12*, 193, doi:10.3390/metabo12020193.

51. Ohlen, S.B.; Russell, M.L.; Brownstein, M.J.; Lefcort, F. BGP-15 Prevents the Death of Neurons in a Mouse Model of Familial Dysautonomia. *Proc. Natl. Acad. Sci.* **2017**, *114*, 5035–5040, doi:10.1073/pnas.1620212114.

52. Masino, S.A.; Rho, J.M. Mechanisms of Ketogenic Diet Action. In *Jasper's Basic Mechanisms of the Epilepsies*; Noebels, J.L., Avoli, M., Rogawski, M.A., Olsen, R.W., Delgado-Escueta, A.V., Eds.; National Center for Biotechnology Information (US): Bethesda (MD), 2012.

53. Vogel, S. Myo-Inositol Supplementation Augments Visual System Maturation in Mice. Ph.D., Tufts University-Graduate School of Biomedical Sciences: United States -- Massachusetts, 2021.

54. Best, J.G.; Stagg, C.J.; Dennis, A. Other Significant Metabolites. In *Magnetic Resonance Spectroscopy*; Elsevier, 2014; pp. 122–138 ISBN 978-0-12-401688-0.

55. Wensel, T.G. Phosphoinositides in Retinal Function and Disease. *Cells* **2020**, *9*, 866, doi:10.3390/cells9040866.

56. Bar-Shai, A.; Maayan, C.; Vromen, A.; Udassin, R.; Nissan, A.; Freund, H.R.; Hanani, M. Decreased Density of Ganglia and Neurons in the Myenteric Plexus of Familial Dysautonomia Patients. *J. Neurol. Sci.* **2004**, *220*, 89–94, doi:10.1016/j.jns.2004.02.017.

57. Chaverra, M.; George, L.; Mergy, M.; Waller, H.; Kujawa, K.; Murnion, C.; Sharples, E.; Thorne, J.; Podgajny, N.; Grindeland, A.; et al. The Familial Dysautonomia Disease Gene IKBKAP Is Required in the Developing and Adult Mouse Central Nervous System. *Dis. Model. Mech.* **2017**, *10*, 605–618, doi:10.1242/dmm.028258.

58. Grzymajlo, K.; El Hafny-Rahbi, B.; Kieda, C. Tumour Suppressor PTEN Activity Is Differentially Inducible by Myo-inositol Phosphates. *J. Cell. Mol. Med.* **2023**, *27*, 879–890, doi:10.1111/jcmm.17699.

59. Hopkins, B.D.; Hodakoski, C.; Barrows, D.; Mense, S.; Parsons, R.E. PTEN Function, the Long and the Short of It. *Trends Biochem. Sci.* **2014**, *39*, 183–190, doi:10.1016/j.tibs.2014.02.006.

60. Blusztajn, J.K.; Liscovitch, M.; Richardson, U.I. Synthesis of Acetylcholine from Choline Derived from Phosphatidylcholine in a Human Neuronal Cell Line. *Proc. Natl. Acad. Sci. U. S. A.* **1987**, *84*, 5474–5477.

61. Wurtman, R.J. Choline Metabolism as a Basis for the Selective Vulnerability of Cholinergic Neurons. *Trends Neurosci.* **1992**, *15*, 117–122, doi:10.1016/0166-2236(92)90351-8.

62. Hwang, J.-S.; Shin, Y.-J. Role of Choline in Ocular Diseases. *Int. J. Mol. Sci.* **2021**, *22*, 4733, doi:10.3390/ijms22094733.

63. Parisi, V.; Oddone, F.; Ziccardi, L.; Roberti, G.; Coppola, G.; Manni, G. Citicoline and Retinal Ganglion Cells: Effects on Morphology and Function. *Curr. Neuropharmacol.* **2018**, *16*, 919–932, doi:10.2174/1570159X15666170703111729.

64. Mendoza-Santiesteban, C.E.; Palma, J.-A.; Norcliffe-Kaufmann, L.; Kaufmann, H. Familial Dysautonomia: A Disease with Hidden Tears. *J. Neurol.* **2017**, *264*, 1290–1291, doi:10.1007/s00415-017-8486-z.

65. Jin, K.; Jiang, H.; Xiao, D.; Zou, M.; Zhu, J.; Xiang, M. Tfap2a and 2b Act Downstream of Ptf1a to Promote Amacrine Cell Differentiation during Retinogenesis. *Mol. Brain* **2015**, *8*, 28, doi:10.1186/s13041-015-0118-x.

66. Yan, W.; Laboulaye, M.A.; Tran, N.M.; Whitney, I.E.; Benhar, I.; Sanes, J.R. Mouse Retinal Cell Atlas: Molecular Identification of over Sixty Amacrine Cell Types. *J. Neurosci. Off. J. Soc. Neurosci.* **2020**, *40*, 5177–5195, doi:10.1523/JNEUROSCI.0471-20.2020.

CHAPTER FIVE

TUBA1A-CRE^{+}*; ELP1*$^{LOXP/LOXP}$ SUCCINATE SUPPLEMENTATION

Highlighted throughout this dissertation work is the primary issue of mitochondrial dysfunction that imparts cellular stress. The results from our detailed analysis of serum and stool metabolite profiles presented in Chapter 3 of this dissertation indicate additional mechanisms by which metabolic imbalances impart stress on the mitochondria or lead to mitochondrial deficits [1]. Mitochondrial dysfunction in FD patients and mouse model has been characterized by observations of mitochondrial membrane depolarization and fragmentation, increased reactive oxygen species (ROS) production, reduced electron flow through the electron transport chain (ETC), and reduced ATP production [2-5]. In addition to these characteristics, direct evidence of dysfunctional mitochondrial ETC function was found upon examination of an FD patients' muscle biopsy, which revealed functional impairments of the complex 1, 3 and 4 proteins of the ETC, while complex 2 and the coupled function of complex 2 and 3 appeared to remain normal.

Complex 2 of the ETC (succinate dehydrogenase), is the enzyme that facilitates the oxidation of succinate to fumarate, thus producing $FADH_2$ that provides electrons to complex 3 via electron shuttling through coenzyme Q/ubiquinone of the ETC. It was hypothesized that succinate supplementation might provide a compensatory metabolic route to ameliorate mitochondrial dysfunction and to stimulate the production of ATP via the complex2-coenzymeQ-complex 3 axis, potentially mitigating cellular stress. It was postulated that supplementing the water of FD mice with succinate may be a way to examine whether redressing metabolic imbalance could improve energetic deficits underlying cellular networks that are at play in FD, and conceivably perhaps slow or redress progressive neurodegeneration in FD mice.

Towards this goal, *Tuba1a-Cre*$^{+}$*; Elp1*$^{LoxP/LoxP}$ mutant mice, and *Tuba1a-Cre*$^{-}$*;* $^{Elp1+/LoxP}$ control mice were divided into two treatment groups and provided succinate (6.35 mM) water, or regular water, ad libitum. The four treatment groups were designated as mutants treated with water (MW), or succinate (MS), and controls treated with water (CW), or succinate (CS). Mice began supplementation at P90 (postnatal day 90, i.e., 3 months), continued for 3 months, and concluded when mice reached P180 (i.e., 6 months). These experimental parameters were devised based on the onset of phenotypic symptoms, which most consistently presented at P90. Beginning supplementation following phenotypic expression of the disease would allow for a more representative model of what would be the case for treating FD patients, given that patients' median age is 25 and their symptoms are well established at this stage [6-8].

Stool samples were collected at P90, P120, P150, and P180 for both NMR metabolomics analysis and microbiome sequencing. Samples were collected prior to beginning treatment (T0) and each subsequent month following treatment commencement (T1-T3). At the terminal timepoint (T3), serum, liver, brain, and retina samples were collected for NMR metabolomics analyses. Phenotype scores were collected in parallel with stool samples to systematically track the observable progression of the disease over the course of succinate supplementation for both the MS and MW groups. Water consumption was tracked for both mutants and controls either receiving normal water or 6.35 mM succinate water, and it was observed that water consumption by the CW and CS group was not different, but the MS group drank less water than the MW group (Figure 1). The reduced water consumption of the MS group may indicate an improvement in regulating thirst, which is not well regulated in FD patients and leads to excessive water consumption [9]. One week prior to euthanasia, a gut-transit assay was performed for all mice in both treatment groups.

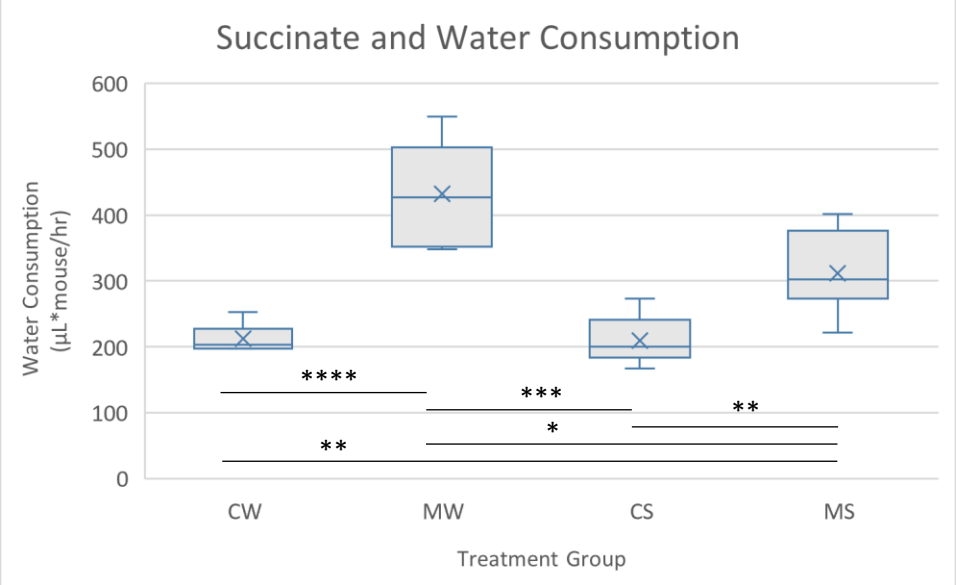


Figure 1 Succinate and water consumption (µL*mouse/hour) for mutants and controls. Treatment groups were graphed by cage, where n = # of cages: CW (n=6), MW (n=6), CS (n=5), MS (n=7). Boxes represent median, and first and third quartiles, whiskers show standard deviation, and x indicates the mean. Significance was determined with a two tailed *t*-test assuming equal variance and the false discovery rate for multiple comparisons was evaluated with the Benjamini-Hochberg procedure, * $p \leq .05$, ** $p \leq .01$, *** $p \leq .001$, **** $p \leq .0001$.

Phenotype Scores

Observing the phenotypic manifestations of the disease throughout the course of the experiment led to an interesting observation that succinate supplementation seemed to positively affect the FD mice, which appeared healthier and stronger, and the females exhibited improved grooming habits, and the males were seemingly more aggressive. Weekly check-ins to monitor the status of water levels revealed that male mutants treated with succinate exhibited a higher frequency of aggression towards cage mates, as seen by visible wounds on littermates. Indeed, this was especially highlighted by the need to re-cage mutants treated with succinate due to fighting, and their increased frequency of bite-attempts while being gently handled. These characteristics were not observed for the mutants treated with water, or mutants from past

experiments, which were both marked by a rather docile nature and compliance while being handled. As a result, excessive fighting may have confounded the phenotypic score for the grooming habits of male MS mice. These observations mostly peaked mid-treatment (P150, T2), and declined in the final month of the experiment, though male mice remained aggressive towards cage mates.

Some of the observations made throughout the experiment were captured in the statistical evaluation and modeling of the phenotype scores. The point classification system previously developed and used by *Cheney et al.* (2023) [10] to numerically score and monitor the disease progression of the Tα mice was used to evaluate the mice in both the MS and MW treatment groups. Hindlimb clasping, lack of grooming, motor function, and size were scoring categories that could receive a 0,1 or 2 based on severity of the observed phenotype. A binary score of either 0 or 1 was assigned for the presence or absence of cataracts, hunch back, tremors, or repetitious jumping. The highest score possible was 12 and indicated the most severe phenotype. T2 showed the most difference between individual parameters of the phenotypic scoring system, with hindlimb clasping, and motor function being the two fields that displayed the most difference between MW and MS groups, which peaked at T2 (P150). Succinate intervention appeared to improve the overall phenotype of the MS mice compared to MW by the end of the experiment, though *t*-test results did not survive Benjamini-Hochberg testing for significance (Figure 2).

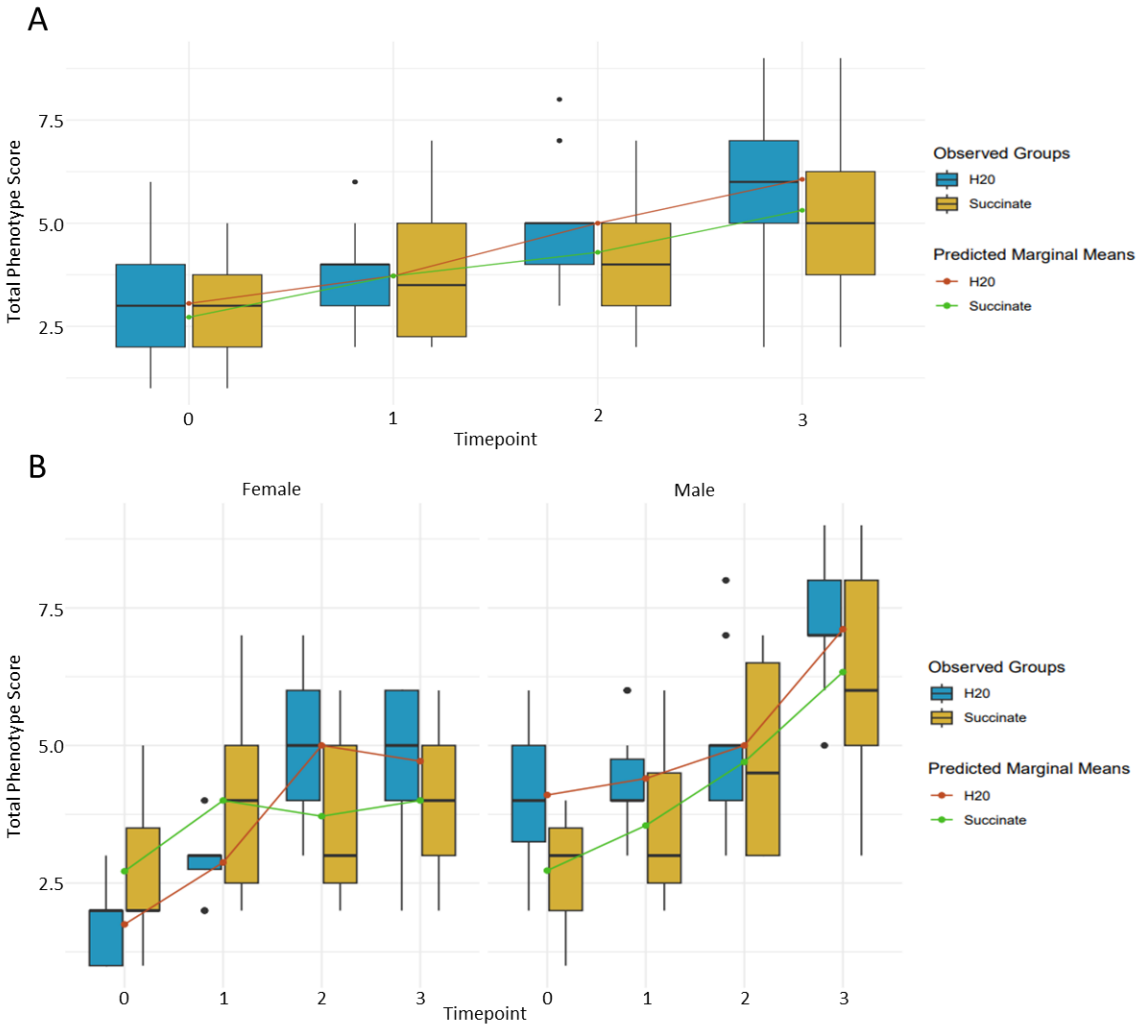


Figure 2. Total phenotype scores for MW and CW groups plotted for each mouse based on (A) treatment group and (B) treatment group partitioned by sex. Observed phenotype score averages for both groups are graphed with boxplots, whereas the predicted marginal means are plotted with the connecting dot-plots. Boxes represent the 1st and 3rd interquartile mean, and median line, whiskers are standard deviation, and dots are outliers. (A) Timepoint 0 and Timepoint 1 MW (n=18), MS (n=18); Timepoint 2 MW (n=17), MS (n=17); Timepoint 3 MW (n=16), MS (n=16). (B) Females Timepoint 0 and Timepoint 1, MW (n=8), MS (n=7); Timepoint 2 and Timepoint 3 MW (n=7), MS (n=7). Males Timepoint 0 and Timepoint 1 MW (n=10), MS (n=11); Timepoint 2 MW (n=10), MS (n=10); Timepoint 3 MW (n=9), MS (n=9).

Gut Transit Assay

The gut transit assay revealed that the MW mice had the shortest gut transit time at an average of 2 hours 38 minutes. The assay also demonstrated that succinate treatment alone increased gut transit time, as the CS group had a slightly longer average gut transit time (3 hours 38 minutes) compared to the CW group (3 hours 17 minutes), though this difference was negligible. The MS group had a gut transit time more comparable to the CW and CS groups, with an average of 3 hours 9 minutes. Groups were evaluated with two-tailed *t*-tests, and the CW vs MW, and MW vs CS were indeed identified to be the most different, though these did not remain significant following FDR correction of the two-tailed *t*-tests. Overall, succinate treatment increased gut transit time, with the MS and CW groups being most similar (Figure 3). The longer gut transit time observed for the mutants treated with succinate suggests a potential improvement in digestion and nutrient absorption.

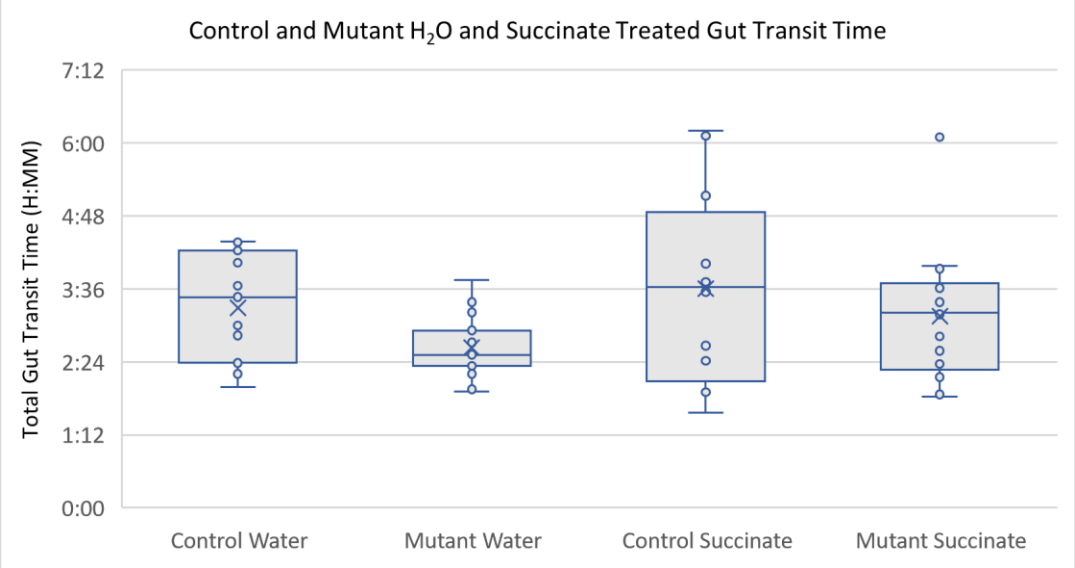


Figure 3. Total gut transit time for mutants and controls treated with either succinate or water. Each dot represents a single mouse, x indicates the mean, boxes represent median and first and third quartiles, whiskers show standard deviation. CW (n=15), MW (n=15), CS (n=12), MS (n=16).

NMR Metabolomics Analysis

Preliminary NMR metabolomics analyses of the serum, liver, and brain samples indicate that succinate treatment impacted both the controls and mutants, with the group variability of an ANOVA analyses being driven predominantly by treatment group rather than genotype. The polar metabolite patterns of retina tissue showed no difference between mutant and controls on water, demonstrating that, though this mouse model exhibits the RGC degeneration characteristic of FD optic neuropathy [5], metabolic differences are not observable, at least at this time point. The lack of impact on the polar metabolite profiles of the retina may be due in part to the lack of *Cre*$^{+}$ penetrance specifically in the retinal neurons, or a slower rate of RGC death in this model.

A detailed metabolic and pathway impact analysis remains to be undertaken for all tissue types and samples collected for the succinate experiment. However, preliminary univariate and

multivariate analyses indicate that treatment group (succinate or H_2O only) prevails over genotype in differentiating groups, and that succinate may have a deleterious effect on the mice, enhancing metabolome differences between MW and CW mice. It was also observed that some metabolite level patterns in the CS group more closely resembled those observed for the MW and MS groups. However, there were instances where ANOVA analyses of the metabolite profiles of brain, liver, and serum samples demonstrated that succinate treatment could return metabolite levels measured in the FD mice to a level more comparable to what had been measured in the control mice receiving water; this included redressing the levels of serine in the brain and taurine in the serum.

In other instances, succinate supplementation seemed to primarily affect the metabolite levels of the FD mice, rather than the control mice on succinate. For instance, the ANOVA analysis of the brain metabolome identified choline levels as being the lowest in the MS group, while the CS, CW, and MW groups all had comparable levels. The brain metabolome ANOVA analysis identified serine to be the most elevated in the MW group, while the CW was the most decreased.

Conclusion

In summary, succinate supplementation appeared to have an impact on the overall health status of the FD and control mice, as reflected in both reduced water consumption, improved phenotypic observations, functional analyses of the gut transit time, and changes in the metabolome of diverse tissue types. A detailed analysis of the metabolomics data is ongoing and aims to provide a better understanding of the cellular networks that have been impacted by succinate supplementation. It would also be very interesting to examine whether succinate

supplementation impacted the gut microbiome of the FD mice and if it could have a positive effect at enhancing gut microbe diversity and abundance. A lot more remains to be accomplished to provide mechanistic insights into the gut-brain-metabolism axis in FD, but this is an exciting area of research to be continued and expanded in the future.

References

1. Costello, S.M.; Cheney, A.M.; Waldum, A.; Tripet, B.; Cotrina-Vidal, M.; Kaufmann, H.; Norcliffe-Kaufmann, L.; Lefcort, F.; Copié, V. A Comprehensive NMR Analysis of Serum and Fecal Metabolites in Familial Dysautonomia Patients Reveals Significant Metabolic Perturbations. *Metabolites* 2023, *13*, 433, doi:10.3390/metabo13030433.

2. Ueki, Y.; Shchepetkina, V.; Lefcort, F. Retina-Specific Loss of Ikbkap/Elp1 Causes Mitochondrial Dysfunction That Leads to Selective Retinal Ganglion Cell Degeneration in a Mouse Model of Familial Dysautonomia. *Dis. Model. Mech.* 2018, *11*, doi:10.1242/dmm.033746.

3. Mendoza-Santiesteban, C.E.; Palma, J.-A.; Hedges, T.R.; Laver, N.V.; Farhat, N.; Norcliffe-Kaufmann, L.; Kaufmann, H. Pathological Confirmation of Optic Neuropathy in Familial Dysautonomia. *J. Neuropathol. Exp. Neurol.* 2017, *76*, 238–244, doi:10.1093/jnen/nlw118.

4. Ohlen, S.B.; Russell, M.L.; Brownstein, M.J.; Lefcort, F. BGP-15 Prevents the Death of Neurons in a Mouse Model of Familial Dysautonomia. *Proc. Natl. Acad. Sci.* 2017, *114*, 5035–5040, doi:10.1073/pnas.1620212114.

5. Ueki, Y.; Ramirez, G.; Salcedo, E.; Stabio, M.E.; Lefcort, F. Loss of Ikbkap Causes Slow, Progressive Retinal Degeneration in a Mouse Model of Familial Dysautonomia. *eNeuro* 2016, *3*, doi:10.1523/ENEURO.0143-16.2016.

6. Dietrich, P.; Dragatsis, I. Familial Dysautonomia: Mechanisms and Models. *Genet. Mol. Biol.* 2016, *39*, 497–514, doi:10.1590/1678-4685-GMB-2015-0335.

7. Ramprasad, C.; Norcliffe-Kaufmann, L.; Palma, J.-A.; Levy, J.; Zhang, Y.; Spalink, C.L.; Khan, A.; Smukalla, S.; Kaufmann, H.; Chen, L.A. Frequency and Burden of Gastrointestinal Symptoms in Familial Dysautonomia. *Clin. Auton. Res. Off. J. Clin. Auton. Res. Soc.* 2021, *31*, 109–116, doi:10.1007/s10286-020-00735-9.

8. Cotrina, M.L.; Morgenstein, B.; Perez, M.; Norcliffe-Kaufmann, L.; Palma, J.-A.; Kaufmann, H. Height, Weight, and Body Mass Index in Patients with Familial Dysautonomia. *PLOS ONE* 2023, *18*, e0293800, doi:10.1371/journal.pone.0293800.

9. Palma, J.-A.; Kaufmann, L.; Fuente, C.; Percival, L.; Mendoza, C.; Kaufmann, H. Current Treatments in Familial Dysautonomia. *Expert Opin. Pharmacother.* 2014, *15*, 2653–2671, doi:10.1517/14656566.2014.970530.

10. Cheney, A.M.; Costello, S.M.; Pinkham, N.V.; Waldum, A.; Broadaway, S.C.; Cotrina-Vidal, M.; Mergy, M.; Tripet, B.; Kominsky, D.J.; Grifka-Walk, H.M.; et al. Gut Microbiome Dysbiosis Drives Metabolic Dysfunction in Familial Dysautonomia. *Nat. Commun.* 2023, *14*, 218, doi:10.1038/s41467-023-35787-8.

CHAPTER SIX

CONCLUSION

Avenues Inspired by the Human Metabolomics Analysis

NMR-based metabolomics techniques were employed to characterize the metabolite profiles of serum and fecal samples from FD patients, and various tissue types and fecal samples from two FD mouse models. The mouse models were engineered to selectively delete *Elp1* in targeted tissues of the central (CNS) and peripheral (PNS) nervous systems (Tα), and retina (Pax6). The detailed fecal metabolomics analysis of FD patients was conducted in parallel with the survey of gut-microbial compositional changes based on 16S ribosomal RNA (rRNA) gene sequencing, and sampled ~14% of FD patients worldwide, along with their relatives who served as controls. This analysis aimed to elucidate the status of the metabolism and gut-microbial networks of FD patients, and pinpoint gut microbiome-metabolism connections [1,2].

The microbiome analysis indicated signs of dysbiosis in FD patients, represented by decreased alpha diversity (species richness and evenness) and increased beta diversity (compositional differences of species compared to controls) [2]. FD patients were also identified to be distinctly different from their control relatives based on their altered fecal metabolite profiles, highlighting altered levels of metabolites associated with the gut microbiome and neuronal signaling [1]. Each of the fecal metabolites of interest open many avenues to further explore the cellular networks underlying the FD disease, with two metabolites (choline and taurine) being of prime focus because of their critical roles in metabolic processes associated with neurodegeneration, biological relevance to physiological phenotypes of FD, gut microbiome association, and the liver-gut-brain axis.

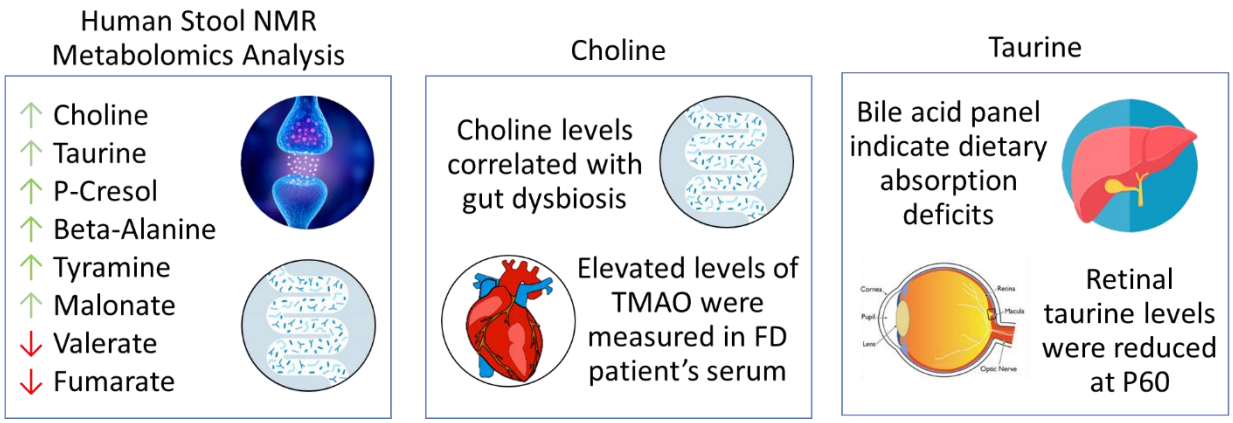


Figure 1. Summary of the NMR metabolomics-based analysis of FD patients' stool samples, and the associated disruptions of choline and taurine metabolism to FD. Eight metabolites indicative of FD were originally identified in the FD patients' stool samples, with the levels of choline, taurine, p-cresol, beta-alanine, tyramine and malonate all elevated, and the levels of valerate and fumarate decreased. The eight metabolites could either be classified as being relevant to either the nervous system, or the gut microbiome. The elevated levels of choline measured in FD patients' stool samples was significantly correlated with the decreased gut-microbiome α-diversity. The gut-microbial mediated conversion of choline to TMA, and ultimately TMAO in the liver, was a metabolic fate of choline that revealed elevated levels of TMAO in the serum of FD patients through a targeted MS analysis, indicating this pathway may be involved in exacerbating cardiovascular disease in FD patients. The association of taurine to both the production of bile acids and eye health lead to the identification of altered bile acids in FD patients' stool samples, and decreased levels of taurine in the Pax6 mutant FD mouse model.

Choline

Elevated choline levels in the stool of FD patients identified this metabolite as one of the most indicative of altered metabolism and relevant to gut health and function. Several avenues were further explored to interrogate the gut-microbial and biological relevance of choline to the pathology and progression of FD. Of primary interest was the gut microbial metabolic conversion of choline to trimethylamine (TMA), an intermediate that is transported to the liver and converted there to trimethylamine N-oxide (TMAO). A targeted liquid-chromatography mass-spectrometry (LC-MS) analysis evaluated levels of these metabolites, and identified only a trend in elevated TMA levels in the fecal samples of FD patients, while elevated levels of TMAO

in the serum of FD patients was significant, highlighting one metabolic fate of choline that is mediated by the gut microbiome of FD patients, suggesting that this compound could play an important role in neurodegeneration and the clinical progression of cardiovascular and kidney disease in FD patients [2].

In addition to the gut microbe-mediated metabolism of choline, this metabolite is a vital dietary substrate used to synthesize phosphatidylcholine, acetylcholine, and betaine. The next step to understanding the implications of elevated levels of choline in the stool samples of FD patients was to characterize the fecal metabolome of the Tα FD mouse model to assess whether the altered patterns of stool metabolites observed in FD patients were recapitulated in the FD mice. Additional aims included identifying if elevated choline levels in stool were due to impairment in absorption or transport of dietary choline due to reduced levels of choline transport proteins. Western blot analyses were undertaken to attempt to measure the levels of choline transport proteins in the large and small intestine, and liver tissue of FD mice.

Luminal scrapings from upper and lower duodenum, jejunum, ileum, and upper and lower colon, and liver were collected from the *Tuba1a-Cre*$^{+}$*; Elp1*$^{LoxP/LoxP}$ and corresponding controls for western blot analysis of the moderate affinity choline transporter-like 1 (CTL1, *Slc44a1*), and low affinity organic cation transporter 1 (OCT1, *Slc22a1*) choline transporters. Western blots of the choline transport proteins proved to be difficult to troubleshoot, with nonspecific binding causing obstructive background signal, distinct bands observed outside the expected molecular weight region, and potential aggregation of target protein within bands (Appendix C). Despite challenges, it was concluded that either choline transport protein levels are expressed normally in the Tα mouse model, or that the ~40% reduction of Elp1 expression in the PNS in this mouse model might not be the best way to evaluate the levels of choline transport

proteins, especially given the variability in measured choline levels in stool samples for this FD mouse model. As such, a different FD mouse model that recapitulate cholinergic neuron deficits and gut tissue alterations more closely, such as the recently generated *ChAT-Cre*$^{+}$*; Elp1*$^{LoxP/LoxP}$ that deletes *Elp1* in all cholinergic neurons, may be a more suitable animal model of FD to examine the dependence of choline transporters on *Elp1* expression.

Taurine

Elevated levels of fecal taurine and reduced trends of serum taurine levels [1], partnered with the deleterious effects of taurine deficits on mitochondrial function and eye health [3-6] led to the postulation that a systemic deficit in taurine may contribute to cellular mechanisms promoting progressive blindness in FD patients. NMR-based extraction methods were adapted to characterize taurine and other high abundant metabolites, and western blots were performed to measure the levels of the taurine transporter (TAUT, *Slc6a6*) protein in retinae from the Pax6 FD mouse model.

Challenges similar to those encountered with the choline transporter western blots were faced when attempting to evaluate the levels of TAUT protein in retina extracts. Given these complications, immunohistochemical staining and visualization present as an alternative method to interrogate whether levels of the taurine transporter are reduced in the Pax6 FD mice. A retina whole-mount and stain for the TAUT protein was conducted as a pilot experiment and indicated that cross sectional analyses of retina tissue (instead of a whole-mount) may be a more effective method to visualize TAUT expression in the tissue layers. Should histological analysis indicate a reduction in taurine transport protein levels, protein quantitation could be achieved using mass-spectrometry (MS) instead of attempting western blot analyses.

Beyond attempting to measure TAUT protein expression using immunohistochemistry methods, targeted MS analyses and comprehensive NMR-based metabolomics methods were employed to assess the metabolic fate of taurine. Taurine is one of two primary constituents that are conjugated to bile acids and can be evaluated via targeted MS analyses using a panel of bile acids as standards. MS studies were conducted on pairs of 24 fecal samples obtained from FD patients and control relatives. The results from these analyses indicated that, out of 14 bile acids measured, levels of taurocholic acid (TCA) ($p = 0.026$) and deoxycholic acid (DCA) ($p = 0.015$) were significantly reduced in the FD patients compared to the levels measured in the samples of control relatives.

Bile acid (BA) metabolism is a cyclical process that involves the production of bile acids in the liver, and secretion of primary BA from the gallbladder into the ileum, where they aid in lipid digestion and are further metabolized by gut microbes to secondary BA, unconjugated BA and their starting constituents, glycine and taurine. The majority (95%) of BA are used for nutrient absorption and re-circulated back to the liver when the gut microbiome is healthy [7]. TCA is a primary bile acid produced by conjugation of cholic acid to taurine, and DCA, along with taurine, is the product generated as a result of gut-microbial de-conjugation of primary and secondary bile acids. Active uptake of bile acids, a mechanism that may be impaired due to reduced gut innervation [8] and potentially indicated by the low BMI of FD patients [9], is necessary to re-absorb bile acids that remain conjugated, while the majority of BA recycling relies on passive reabsorption of unconjugated bile acids [7]. Elevated levels of TCA and reduced levels of DCA support a dysbiotic gut microbiome and impaired gut physiology in FD patients. Together, these impairments may lead to the inefficient deconjugation of TCA to DCA and taurine, and reabsorption, as seen in the elevated levels of TCA and reduced levels of DCA being

excreted in the stool samples of FD patients. Results from this bile acid analysis point to a critical balance between the gut microbiome and metabolic networks, whose homeostasis depends on the healthy function of these two systems to mediate proper absorption of lipids and dietary nutrients.

In addition to their roles in aiding digestion and absorption, BAs modulate diverse metabolic processes including glucose homeostasis and energy metabolism [10], and surprisingly have neuroprotective effects in animal models of Parkinson's disease by improving mitochondrial dysfunction, and modulating JNK (c-Jun N-terminal kinases) activity, which regulates dopaminergic cell death [7]. Even more interesting, recent evidence suggests that BAs may play a therapeutic role in eye disorders, providing cytoprotective effects for retinal ganglion cells [7].

This dissertation work has described the interrogation of taurine specifically in the retina, due to its role in preventing mitochondrial dysfunction and reducing cellular stress. Reduction in taurine levels were found to parallel RGC decline in Pax6 mouse retinae. However, FD patients' stool BA panel further implicates taurine levels in the pathology of FD, including the progressive blindness experienced by FD patients and FD mouse model, and the measured reduced levels of dopamine and dopaminergic amacrine cells in Pax6 mouse retinae. These observations highlight a potential gut-liver-retina metabolic axis which could be mediated by gut microbe production of secondary bile acids, followed by enterohepatic circulation and active absorption, and its impact on the nervous system, which could represent an exciting avenue to explore further regarding FD disease pathology.

Conclusion

Herein, this dissertation work has provided novel findings and answers to original research questions aimed at interrogating the gut-brain-metabolism axis of FD. This includes: 1) identifying distinct and characteristic metabolic profiles of serum and fecal samples of FD patients compared to control relatives. 2) Demonstrating that the GI tracts of FD patients have distinct gut microbial compositions compared to their healthy relative controls. 3) Observing that half of the polar metabolites identified in the fecal metabolomic analysis of FD patients had gut-microbial origins or relevance to the gut microbiome. 4) Demonstrating that gut microbiome dysbiosis appeared to precede metabolic deficits, as observed in the Tα FD mouse model. Results from our study suggest that fecal transplantation may be a valuable therapeutic approach to explore, as re-establishing a healthy gut microbiome may mitigate FD disease severity, or could demonstrate that interventions aimed at redressing impairments in cellular networks other than the neuronal networks of the gut-brain-metabolism axis may be a viable approach to treat FD patients and mitigate their disease symptoms. Lastly, a number of other potential avenues for treatment could be explored based on the identification of altered metabolites in fecal samples of FD patients. Most notably, observations of altered levels of choline and taurine in stool samples of FD patients open new opportunities to further investigate the importance of altered bile acid metabolism in FD. The finding that the levels of these metabolites are also reduced in the retinas of the Pax6 FD mouse model also presents new lines of investigations which could guide the development of promising neurotherapeutic approaches to mitigate ophthalmologic decline or redress eye disease progression in neurodegenerative diseases such as FD.

Though there remain multiple research questions to be answered and studies to be further explored and conducted to fully identify and comprehend modifiable factors that influence the pathology of FD, the work presented in this dissertation has provided new knowledge and a deeper understanding of the crosstalk between the gut microbes, neuronal health, and metabolic homeostasis within the context of the FD disease. Hypotheses that stem from this work present exciting topics and open new research areas to further tease apart the cellular mechanisms that mediate FD disease progression and to complete the interrogation of choline and taurine metabolism in the pathology of FD. This work lays the foundation for the development of potentially valuable metabolism-based interventions and treatment strategies aimed at mitigating neurodegeneration and disease progression both systemically and in targeted tissues. This dissertation work presents a wealth of knowledge that was garnered through a better understanding of the metabolic networks underlying the pathophysiological mechanisms of FD. This work has also contributed to demonstrating that metabolism is an important element of neurodegenerative diseases and presents a powerful and promising cellular system that could be used to redress dysfunction in the gut-brain axis of FD.

References

1. Costello, S.M.; Cheney, A.M.; Waldum, A.; Tripet, B.; Cotrina-Vidal, M.; Kaufmann, H.; Norcliffe-Kaufmann, L.; Lefcort, F.; Copié, V. A Comprehensive NMR Analysis of Serum and Fecal Metabolites in Familial Dysautonomia Patients Reveals Significant Metabolic Perturbations. *Metabolites* **2023**, *13*, 433, doi:10.3390/metabo13030433.

2. Cheney, A.M.; Costello, S.M.; Pinkham, N.V.; Waldum, A.; Broadaway, S.C.; Cotrina-Vidal, M.; Mergy, M.; Tripet, B.; Kominsky, D.J.; Grifka-Walk, H.M.; et al. Gut Microbiome Dysbiosis Drives Metabolic Dysfunction in Familial Dysautonomia. *Nat. Commun.* **2023**, *14*, 218, doi:10.1038/s41467-023-35787-8.

3. Ripps, H.; Shen, W. Review: Taurine: A "Very Essential" Amino Acid. *Mol. Vis.* **2012**, *18*, 2673–2686.

4. García-Ayuso, D.; Di Pierdomenico, J.; Hadj-Said, W.; Marie, M.; Agudo-Barriuso, M.; Vidal-Sanz, M.; Picaud, S.; Villegas-Pérez, M.P. Taurine Depletion Causes ipRGC Loss and Increases Light-Induced Photoreceptor Degeneration. *Invest. Ophthalmol. Vis. Sci.* **2018**, *59*, 1396–1409, doi:10.1167/iovs.17-23258.

5. Jong, C.J.; Azuma, J.; Schaffer, S. Mechanism Underlying the Antioxidant Activity of Taurine: Prevention of Mitochondrial Oxidant Production. *Amino Acids* **2012**, *42*, 2223–2232, doi:10.1007/s00726-011-0962-7.

6. Ansar, M.; Ranza, E.; Shetty, M.; Paracha, S.A.; Azam, M.; Kern, I.; Iwaszkiewicz, J.; Farooq, O.; Pournaras, C.J.; Malcles, A.; et al. Taurine Treatment of Retinal Degeneration and Cardiomyopathy in a Consanguineous Family with SLC6A6 Taurine Transporter Deficiency. *Hum. Mol. Genet.* **2020**, *29*, 618–623, doi:10.1093/hmg/ddz303.

7. Daruich, A.; Picard, E.; Boatright, J.H.; Behar-Cohen, F. Review: The Bile Acids Urso- and Tauroursodeoxycholic Acid as Neuroprotective Therapies in Retinal Disease. *Mol. Vis.* **2019**, *25*, 610–624.

8. Bar-Shai, A.; Maayan, C.; Vromen, A.; Udassin, R.; Nissan, A.; Freund, H.R.; Hanani, M. Decreased Density of Ganglia and Neurons in the Myenteric Plexus of Familial Dysautonomia Patients. *J. Neurol. Sci.* **2004**, *220*, 89–94, doi:10.1016/j.jns.2004.02.017.

9. Cotrina, M.L.; Morgenstein, B.; Perez, M.; Norcliffe-Kaufmann, L.; Palma, J.-A.; Kaufmann, H. Height, Weight, and Body Mass Index in Patients with Familial Dysautonomia. *PLOS ONE* **2023**, *18*, e0293800, doi:10.1371/journal.pone.0293800.

10. Chiang, J.Y.L.; Ferrell, J.M. Bile Acid Metabolism in Liver Pathobiology. *Gene Expr.* **2018**, *18*, 71–87, doi:10.3727/105221618X15156018385515.

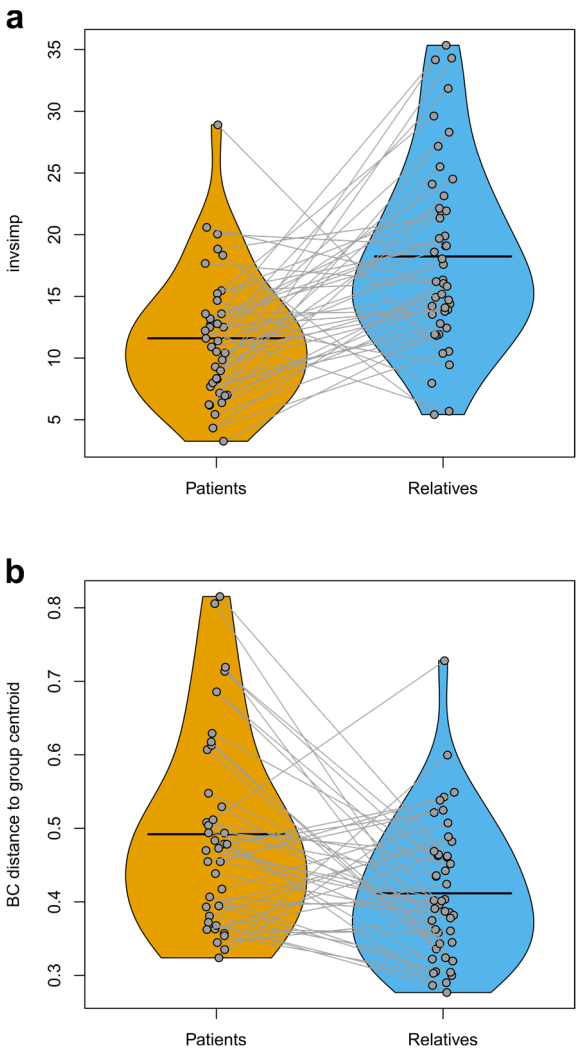
APPENDICES

APPENDIX A

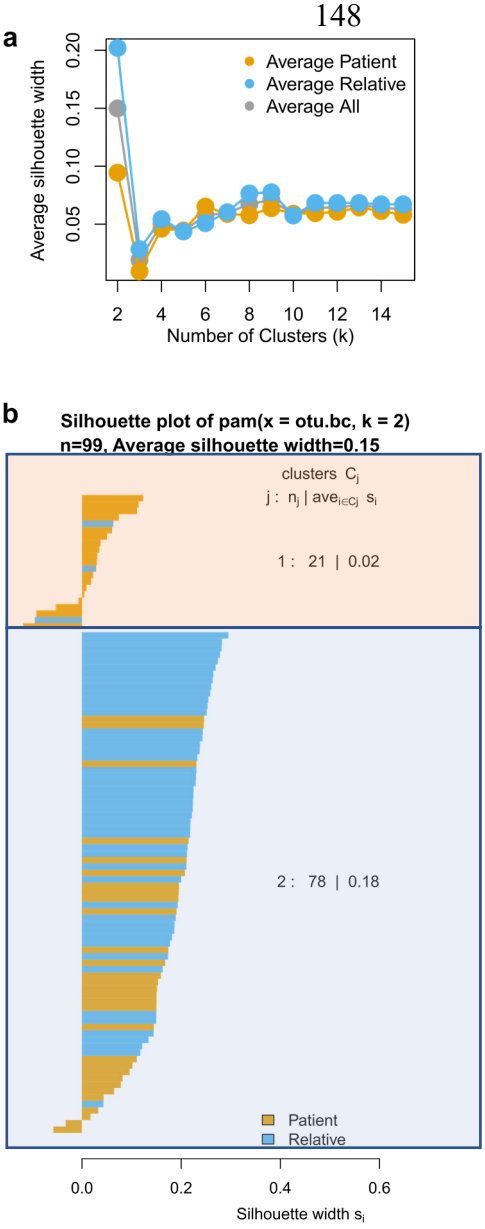
GUT MICROBIOME DYSBIOSIS DRIVES METABOLIC DYSFUNCTION IN FAMILIAL DYSAUTONOMIA: SUPPLEMENTARY MATERIAL

Gut microbiome dysbiosis drives metabolic dysfunction in Familial dysautonomia

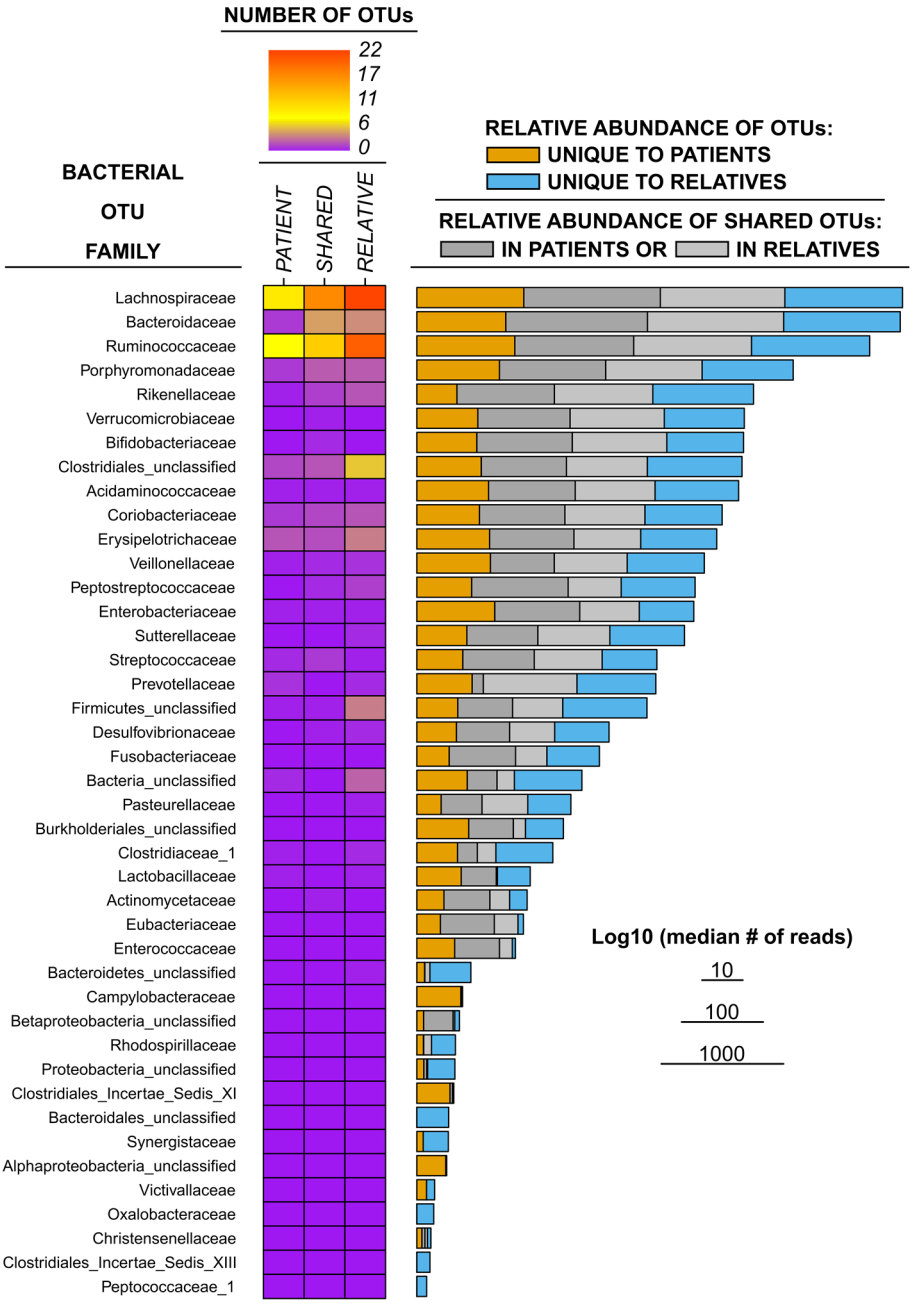
Supplementary Information



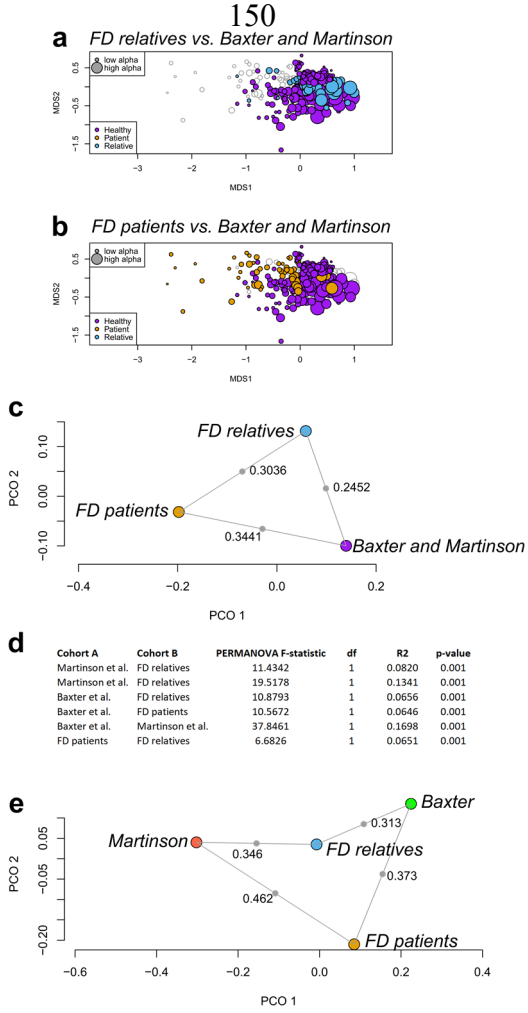
Supplementary Fig. 1. Gut microbiome diversity of FD patients is significantly different from healthy relatives. Alpha diversity (**a,** inverse Simpson's index; patient-relative pairs connected by gray lines; solid black line=mean) and beta dispersion (**b,** Bray-Curtis distance to group centroid; patient-relative pairs connect by gray lines; solid black line=mean) for FD patient-relative pairs. n=**a,b** 29 patient-relative pairs; permutation paired t-testing, two-sided (**a,** mean t-statistic=-4.7136, df=29, mean p<0.0001, mean difference between group means=-6.4263, mean 95% confidence interval of difference between the group means=-9.2128 to -3.6399; **b,** mean t-statistic=2.7016, df=29, mean difference between group means=0.0764, mean 95% confidence interval of difference between the group means=0.0185 to 0.1343).



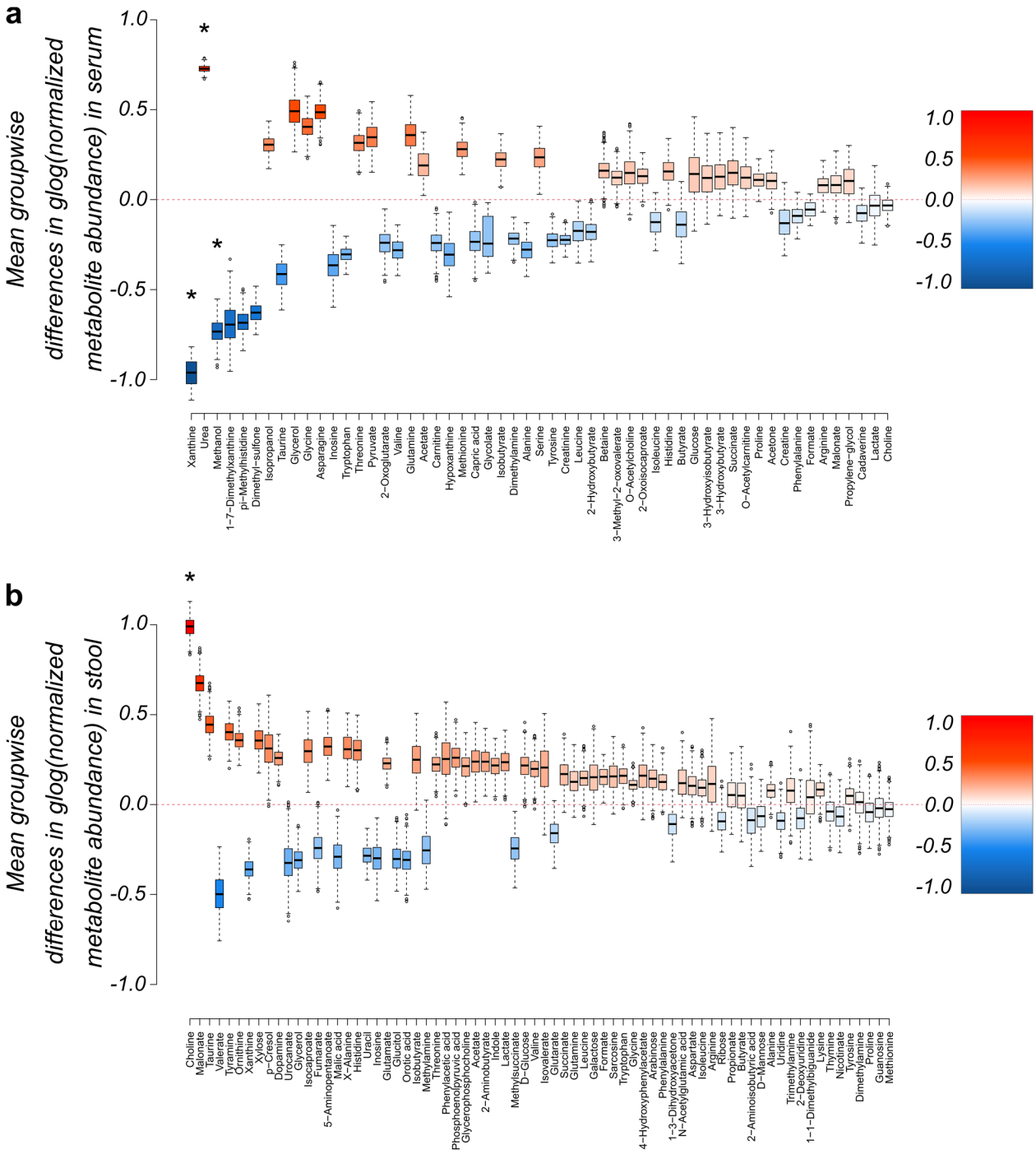
Supplementary Fig. 2. Gut microbiome enterotypes of FD patients. a, Partition around medoids (PAM) clustering of all microbiomes (patients and relatives) supported the presence of two clusters (enterotypes) based on average silhouette width. **b,** FD patients were overrepresented in cluster (enterotype) 1, while most relatives had enterotype 2. Shaded boxes denote samples each enterotype. Colors corresponding to FD patients or relatives shown in legend. n=**a,b** 38 patients, 47 relatives.



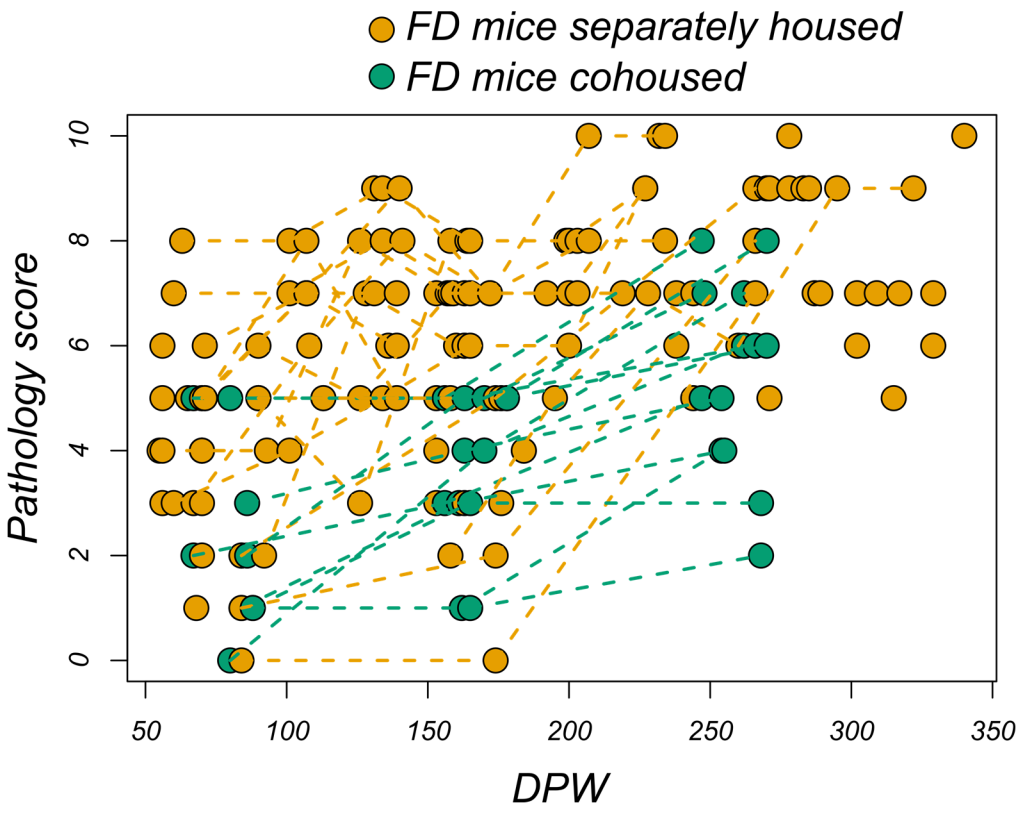
Supplementary Fig. 3. Differentially abundant microbiome members among FD patients and relatives. The heatmap represents the abundance of OTUs at the bacterial family level for FD patients and relatives, including those shared between these groups. For each family, horizontal bars represent the relative abundance of OTUs in each bacterial family that were unique to both FD patients or relatives as well as the relative abundance of shared OTUs within each group.



Supplementary Fig. 4. Gut microbiome diversity of FD relatives and patients compared to two cohorts of healthy adults from other studies. a,b, 16S rRNA sequencing datasets form two previously published human studies (n=182, Baxter et al.[1] and n=8. Martinson et al[2]) were combined and compared via non-metric multidimensional scaling (NMDS) to data from FD patients and their relatives (FD relatives). All samples are shown as circles and plotted in both panels. The size of circles indicates alpha diversity (inverse-Simpson's index; relative legend shown). Only samples involved in the labeled comparisons are colored. Colors correspond to different groups as shown in legends (same for both plots). **c,** Principal coordinates analysis based on beta-diversity (Bray-Curtis dissimilarity) between group centroids (i.e. the "weighted average" microbiome diversity of each group). Microbiomes of healthy subjects from the combined Martinson and Baxter datasets are more similar (smaller BC distances) to the microbiomes of FD relatives than to FD patients. **d,e,** PERMANOVA results (**d**) and principal coordinates analysis (**e**) based on beta-diversity between group centroids for all cohorts. Group centroids are colored according to identical legends in **a** and **b**. BC distances between centroids are labeled at the mid-point of connecting lines between centroids. Centroids of healthy cohorts (Baxter et al., Martinson et al.) are closer to FD relatives than FD patients. PERMANOVA (**a,** FD relatives versus healthy individuals from Baxter et al. and Martinson et al., F=4.360, df=1, p=0.001, R^2=0.0182; **b,** FD patients versus healthy individuals from Baxter et al. and Martinson et al., F=9.072, df=1, p=0.001, R^2=0.037; **d,** details for all pairwise cohort comparisons.

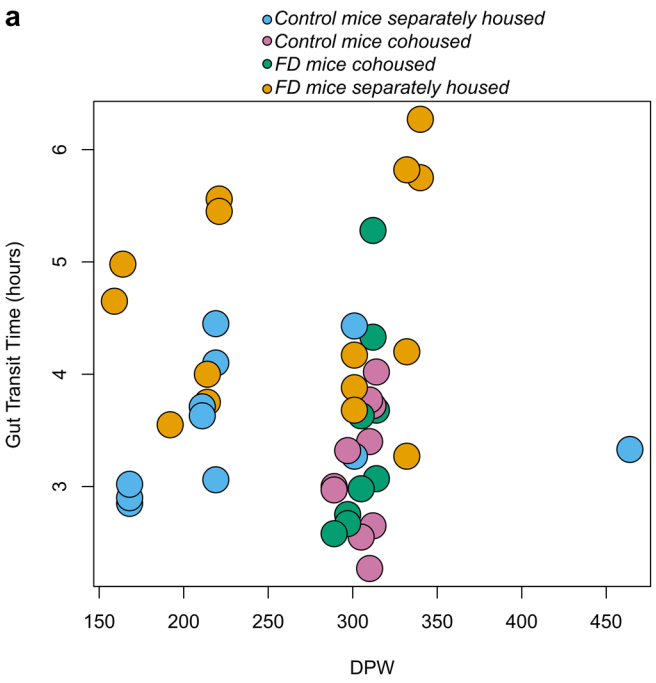


Supplementary Fig. 5. NMR-based metabolomic differences between FD patients and healthy relatives. a,b, Mean difference in serum (**a**) and stool (**b**) metabolites observed in FD patients (relative to healthy relatives) ranked by effect size (mean difference between group means; centrality line=median, boxes=IQR, whiskers=1.5 IQR, circles beyond whiskers=outliers). n=**a,b,** 54 patients, 58 relatives. Permutational paired t-testing (two-sided) with FDR correction (**a,b**). A permutation analysis was conducted where the difference in mean metabolite abundance was calculated between groups of randomly selected patient-relative pairs for 999 permutations. *p<0.05 following FDR correction (see Fig. 2b in the main text for statistical details).



Supplementary Fig. 6. Pathology score for FD mice housed separately or cohoused with control mice. Data for all mice in Figure 4c (main manuscript) are shown. Instead of grouping categorically according to age (DPW) bins, mouse age is displayed here as an ordinal variable. Some mice were sampled multiple times and are connected by dotted lines colored according to group (legend). Separately housed mice had a higher pathology score compared to cohoused mice.

a



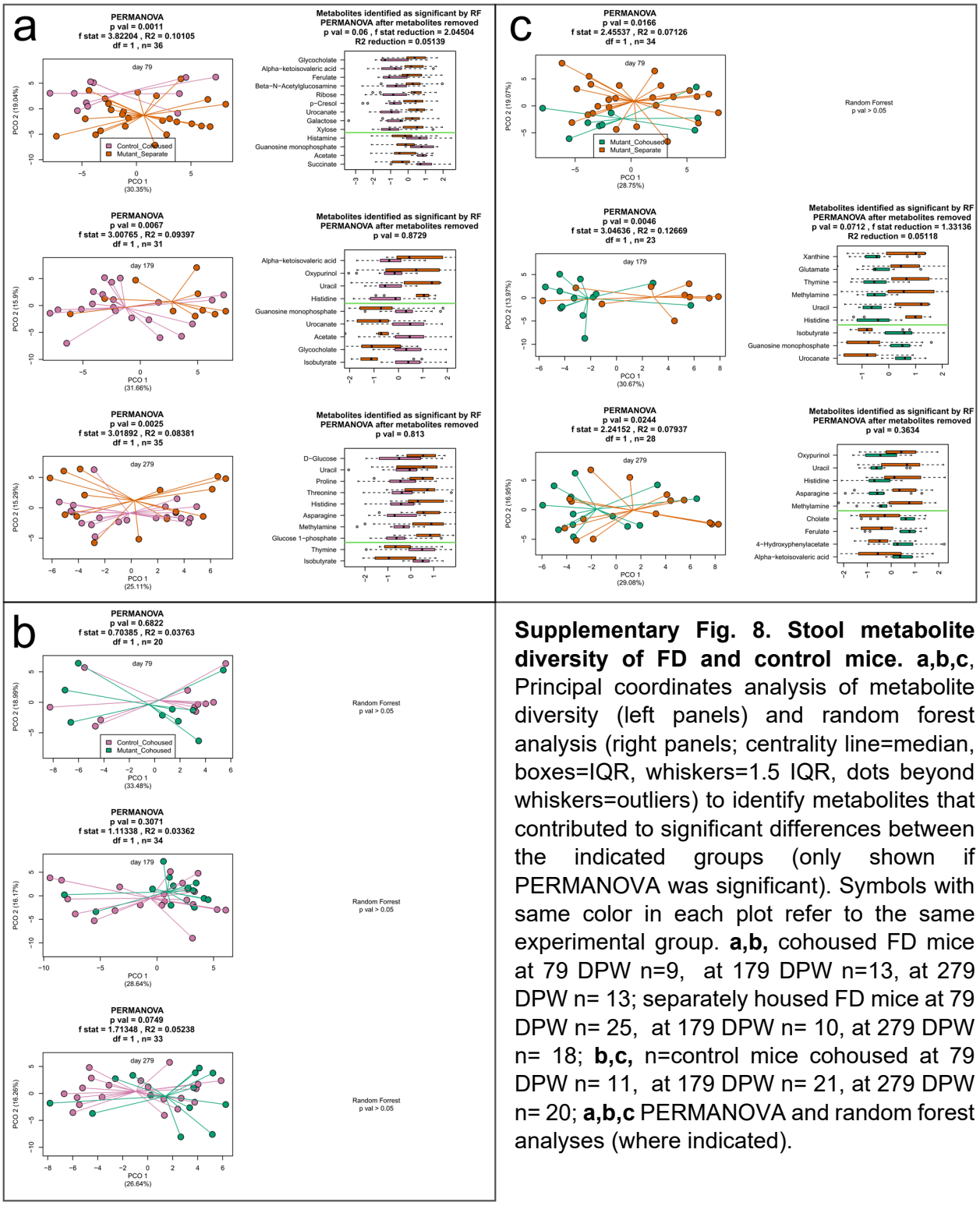
b

Model: lm(formula = gut transit ~ genotype + housing + age)

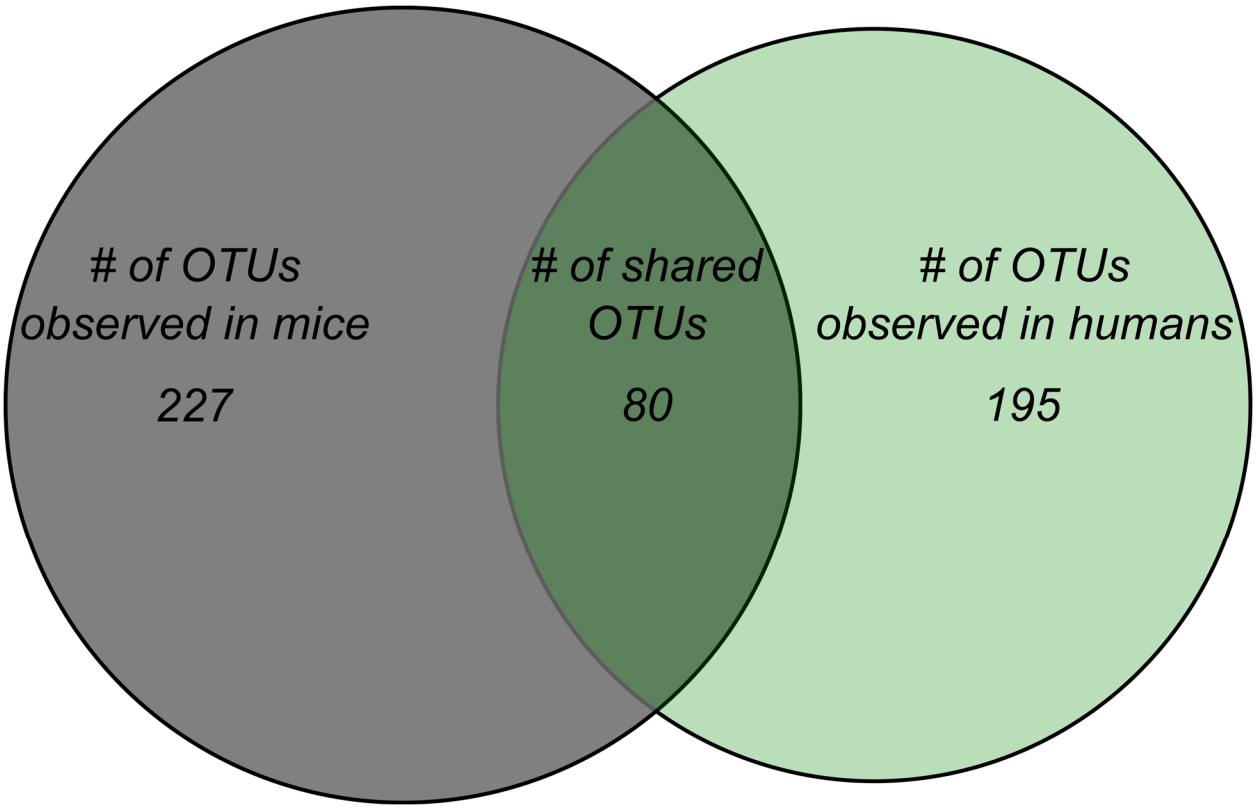
Coefficients:

	Estimate	Standard Error	95% confidence intervals	t value	Pr(>|t|)
Intercept	2.2590	0.6749	0.8961 to 3.6220	3.347	0.0018
genotype (FD)	0.7020	0.2451	0.2069 to 1.1970	2.864	0.0066
house (separately housed)	0.8911	0.2698	0.3462 to 1.4360	3.303	0.0020
age	0.0023	0.0021	-0.0020 to 0.0066	1.082	**0.2858**

Supplementary Fig. 7. Gut transit times for FD mice housed separately or cohoused with control mice. a, Data for all mice in Figure 4d (main manuscript) are shown. Instead of grouping categorically according to age (DPW) bins, mouse age is displayed here as an ordinal variable. **b,** A linear model was used to test the individual effects of mouse genotype (FD vs. WT), housing type (separately housed vs. cohoused), and age (DPW). Age was not a significant factor in gut transit.



Supplementary Fig. 8. Stool metabolite diversity of FD and control mice. a,b,c, Principal coordinates analysis of metabolite diversity (left panels) and random forest analysis (right panels; centrality line=median, boxes=IQR, whiskers=1.5 IQR, dots beyond whiskers=outliers) to identify metabolites that contributed to significant differences between the indicated groups (only shown if PERMANOVA was significant). Symbols with same color in each plot refer to the same experimental group. **a,b,** cohoused FD mice at 79 DPW n=9, at 179 DPW n=13, at 279 DPW n= 13; separately housed FD mice at 79 DPW n= 25, at 179 DPW n= 10, at 279 DPW n= 18; **b,c,** n=control mice cohoused at 79 DPW n= 11, at 179 DPW n= 21, at 279 DPW n= 20; **a,b,c** PERMANOVA and random forest analyses (where indicated).



Supplementary Fig. 9. Unique and shared OTUs observed in laboratory mice and human subjects. Observed OTUs (defined as ≥97% sequence identity at the 16S rRNA encoding gene and corresponding to approximately the bacterial species level) in stool samples of laboratory mice used in this study (WT and FD mice; see methods section in main text) and human subjects (FD patients and healthy relatives). Only n=80 (16%) OTUs were shared in our dataset. To guard against spurious observations, an OTU had to be observed in a minimum of 5 mice or humans to be counted.

Supplementary Table 3. Pathology scoring method used to quantify clinical phenotype in FD (Tuba1a-cre$_{+}$; ELP1$_{loxp/loxp}$) and control (Tuba1a-cre$_{-}$; ELP1$_{+/loxp}$) mice.

Criteria[a]	Value = 0	Value = 1	Value = 2
Hind Limb Clasping[b]	Not observed	Partial	Full
Grooming	Normal coat	Dull coat	Scruffy, matted, or Oily
Cataracts	Not observed	Observed	
Kyphosis[c]	Not observed	Observed	
Motor function[d]	Normal	Obvious loss of function and/or grip but with attempts to correct	Obvious loss of function without attempts to correct
Tremors	Not observed	Observed	
Jumping	Not observed	Observed	
Body condition	No change	Obvious wasting or runted (only one)	Obvious wasting and runted (both)

[a]A total of 12 points was possible where 12 was the most severe, and 0 is considered healthy and normal. All control mice were classified as a score of 0.

[b]The tail of mice was elevated so that the hind legs were raised off the cage floor. A normal response is to extend the hind legs backward parallel to the cage floor. Clasping was evaluated as “Full” if hind limbs fell downward or curled inward toward the body and “Partial” if unsuccessful attempts were made to fully extend hind limbs.

[c]Hunched back or signs of scoliosis.

[d]Mice were removed from the cage and evaluated on top of wire racks that normally hold food (chow) and water bottles. Movement across the rack was observed. A normal response is for mice to move and explore the rack without loss of balance or limbs falling through the space between the wires. Limited movement, loss of balance, or if limbs fell through the space between wires was scored as a “1”. Severe loss of motor function was scored “2” if mice were unable to place feet onto wires (dragging limbs) or unable to pull limbs back up through the space between wires. Grip to wire was also evaluated by pulling mice gently by the tail across the grate. A normal response is for mice to grasp the wire and attempt to pull away. Failure to grasp the wire and/or pull away were scored as a “1”.

References

1 Baxter, N. T., Ruffin, M. T. t., Rogers, M. A. & Schloss, P. D. Microbiota-based model improves the sensitivity of fecal immunochemical test for detecting colonic lesions. *Genome Med* **8**, 37, doi:10.1186/s13073-016-0290-3 (2016).

2 Martinson, J. N. V. *et al.* Rethinking gut microbiome residency and the Enterobacteriaceae in healthy human adults. *ISME J* **13**, 2306-2318, doi:10.1038/s41396-019-0435-7 (2019).

APPENDIX B

A COMPREHENSIVE NMR ANALYSIS OF SERUM AND FECAL METABOLITES IN FAMILIAL DYSAUTONOMIA PATIENTS REVEALS SIGNIFICANT METABOLIC PERTURBATIONS: SUPPLEMENTARY MATERIAL

Supplementary Information:

Title: A comprehensive NMR analysis of serum and fecal metabolites in Familial dysautonomia patients reveals significant metabolic perturbations

Authors: Stephanann M. Costello[†], Alexandra M. Cheney[†], Annie Waldum, Brian Tripet, Maria Cotrina-Vidal, Horacio Kaufmann, Lucy Norcliffe-Kaufmann, Frances Lefcort, and Valérie Copié*

Costello, Cheney et al., Supplementary Table S1

Table S1. Patient and control relative sample and clinical data summary.

Patient Data: **one patient declined to provide info*	**Number**	**Percent**	**Control Relative Data:**	**Number**	**Percent**
Total number of patients enrolled:	50	100%	Total number of control relatives enrolled:	54	100%
Patients only providing stool samples:	7	14%	Controls only providing stool samples:	7	13%
Patients only providing serum samples:	9	18%	Controls only providing serum samples:	8	15%
Patients providing both serum and stool:	34	68%	Controls providing both serum and stool:	39	72%
Total number of patients providing stool:	41	82%	Total number of controls providing stool:	46	85%
Provided second biological stool replicate:	12	24%	Provided second biological stool replicate:	11	20%
Provided third biological stool replicate:	2	4%	Provided third biological stool replicate:	1	2%
Total number of stool samples provided:	54		Total number of stool samples provided:	58	
Total number of patients providing serum:	43	86%	Total number of controls providing serum:	47	87%
Provided second biological serum replicate:	6	12%	Provided second biological serum replicate:	6	11%
Total number of serum samples provided:	49		Total number of serum samples provided:	53	
Female patients	29	58%	Female controls	30	56%
Male Patients	21	42%	Male controls	24	44%
Age group <12 years	8	16%			
Age group 12-17 years	5	10%			
Age group 18-24 years	16	32%			
Age group 25-34 years	16	32%			
Age group 35-44 years	3	6%			
Age group above 45 years	1	2%			
Underweight BMI <18.5	20	40%			
Healthy BMI 18.5-24.9	27	54%			
Overweight BMI 25.0-29.9	2	4%			
Has a gastric tube:	40	80%			
Had a fundoplication:	36	72%			
Can consume food orally:	37	74%			
Can consume liquid orally:	17	34%			
Can consume mixed foods orally:	10	20%			
Can only use gastric tube for consumption:	11	22%			
Received Antibiotics 3 months prior to sample donation	20	40%	Received Antibiotics 3 months prior to sample donation	2	4%

Stool and serum sample collection data for FD patients and control relatives. Patient clinical data was also collected by the Familial Dysautonomia Center at time of collection of samples. Control relatives did not provide clinical data, but it is assumed the age gap is large due to relatives being the parent of the patients. One enrolled patient declined to provide clinical data. The percentage represents the percent out of those enrolled in the study in each group.

Costello, Cheney et al., Supplementary Table S2

Table S2. Human Serum Metabolites Identified and Quantified by NMR: Concentrations and Percent Differences

Metabolites	FD Patients (nmoles/mL)		Control Relatives (nmoles/mL)		Percent Difference
	Mean	Stdev	Mean	Stdev	Mean
1,7-Dimethylxanthine	4.7	4	8.5	10.3	-45
2-Hydroxybutyrate	24.8	18.4	31.8	25.1	-22
2-Oxoglutarate	2.9	1.1	3.1	1.4	-6
2-Oxoisocaproate	19.4	6.7	19.5	6.9	-1
3-Hydroxybutyrate	89.2	99	91.6	115.2	-3
3-Hydroxyisobutyrate	19.6	8	19.2	5.8	2
3-Methyl-2-oxovalerate	18.8	5.5	19.2	6.3	-2
Acetate	79.4	30.4	76.3	52.5	4
Acetone	18.6	11.9	18.3	12.4	2
Alanine	221.2	61.7	247.3	65	-11
Arginine	55.8	19.5	56.4	21.1	-1
Asparagine	27.2	7.2	24.9	6.3	9
Betaine	61.8	30.5	53.2	19.7	16
Butyrate	29.5	14.8	30.2	11.3	-2
Cadaverine	19.2	6.5	20.8	8.5	-8
Capric acid	1315.2	607.3	1446.8	590.2	-9
Carnitine	40.2	10.8	44	12.5	-9
Choline	18.1	12.4	17.3	10.8	5
Creatine	26.8	24.7	25.9	14	3
Creatinine	84.4	73.1	78.4	19.2	8
Dimethyl sulfone	5.2	3	7.2	5.7	-28
Dimethylamine	1	0.6	1.2	0.7	-17
Formate	59.6	27.1	59	29.1	1
Glucose	4465.2	847.4	4380.5	909.6	2
Glutamine	295.4	68.3	271.8	56.3	9
Glycerol	74.6	25.9	65.8	28.7	13
Glycine	167.4	75	136.2	54.9	23
Glycolate	23.4	12.6	34.5	20.4	-32
Histidine	41.7	11.9	40.2	11	4
Hypoxanthine	5.3	2	5.6	2.2	-5
Inosine	4.2	3.1	5.2	3.3	-19
Isobutyrate	7.7	3.4	7.5	3	3

Isoleucine	56.4	20.9	63.2	24.3	-11
Isopropanol	2.6	1.6	2.2	1.2	18
Lactate	1268.5	372.1	1271.3	330.8	0
Leucine	97.7	34.1	111.2	38.9	-12
Malonate	12.9	6.5	12.5	5.8	3
Methanol	14.2	12.2	19.5	11.9	-27
Methionine	19.7	7.4	19.3	5.2	2
O-Acetylcarnitine	3.5	1.6	3.4	1.8	3
O-Acetylcholine	3	0.9	3.1	1.4	-3
Phenylalanine	51.3	13.9	52.5	14.5	-2
Proline	350.1	150.2	342.7	123.5	2
Propylene glycol	122.6	100.1	93.6	27.8	31
Pyruvate	10.8	6	9.4	6.1	15
Serine	129.4	51	114.7	49.8	13
Succinate	7.4	3.8	7.4	4.1	0
Taurine	117	31.1	131.5	34.1	-11
Threonine	123.5	32.1	119.7	32.9	3
Tryptophan	69.5	29.2	74.8	22.2	-7
Tyrosine	56.9	25.7	61.1	18	-7
Urea	13987.3	7670	9718.3	2851.3	44
Valine	159.3	53.7	179.4	53.9	-11
Xanthine	8.6	11.9	16.1	12.6	-47
π-Methylhistidine	9.2	15.9	15.5	15.4	-41

Metabolite concentrations were normalized to serum volume and are reported in nmoles per mL. 55 metabolites were identified across 49 FD patient samples (from 43 patients total) and 53 control relative samples (from 47 control relatives total). Columns 1 and 2 report the mean metabolite concentrations measured in the sera of FD patients and healthy control relatives, respectively, and mean standard deviations. Column 3 reports estimates of percent differences (%) in mean metabolite concentrations between FD patients and healthy controls. A negative percent value indicates a mean lower in FD patients compared to controls, and a positive percent value is higher in FD patients compared to controls.

Costello, Cheney et al, Supplementary Table S3

Table S3. Stool Polar Metabolites Identified and Quantified by NMR: Concentrations and Percent Differences

Metabolites	FD Patients (nMol/g)		Control Relatives (nMol/g)		Percent Difference
	Mean	Stdev	Mean	Stdev	Mean
1,1-Dimethylbiguanide	104.2	263.3	2123.9	12595.8	-95
1,3-Dihydroxyacetone	111.3	149.3	118.5	94.8	-6
2′-Deoxyuridine	34.6	27.5	35.2	24.6	-2
2-Aminobutyrate	571.3	666.9	426.8	431.0	34
2-Aminoisobutyric acid	175.7	114.1	196.1	155.9	-10
4 Hydroxyphenylacetate	249.6	468.9	124.7	84.1	100
5-Aminopentanoate	2223.0	4868.0	987.4	1146.5	125
Acetate	66794.4	39628.5	60482.8	39076.2	10
Alanine	7547.0	6633.5	5945.0	3546.8	27
Arabinose	1379.1	1136.4	1574.2	2127.9	-12
Arginine	544.5	507.1	442.4	365.2	23
Aspartate	4012.5	2258.5	3469.9	1560.4	16
Butyrate	16309.6	11018.9	19333.8	18138.2	-16
Choline	310.3	431.7	91.0	60.8	241
D-Glucose	3207.5	3955.6	2527.8	3180.0	27
D-Mannose	226.3	463.0	259.1	451.9	-13
Dimethylamine	243.1	173.5	230.5	196.5	5
Dopamine	3813.8	25452.7	305.0	338.3	1150
Ethanol	28380.9	79317.3	8978.5	7565.3	216
Formate	2249.0	8536.6	274.4	289.3	720
Fumarate	310.7	624.2	310.7	478.6	0
Galactose	1227.3	715.7	1288.7	921.3	-5
Glucitol	2216.4	6656.0	1411.9	1404.0	57
Glutamate	8803.3	7109.1	7354.0	3990.8	20
Glutamine	1689.8	2220.4	1450.8	1244.8	17
Glutarate	691.9	805.9	936.7	2716.6	-26
Glycerol	4983.5	5504.4	6024.3	5134.1	-17
Glycerophosphocholine	730.1	1302.3	554.7	823.9	32
Glycine	4893.1	4846.3	3499.7	2361.6	40
Guanosine	42.5	64.2	43.0	64.0	-1
Histidine	543.1	887.1	354.2	238.4	53
Indole	265.4	202.6	190.3	95.3	40
Inosine	56.5	87.1	63.0	59.8	-10
Isobutyrate	2606.6	1326.4	2171.5	903.3	20
Isocaproate	566.0	780.2	394.5	193.6	44
Isoleucine	3891.9	3064.7	3159.6	1650.8	23
Isovalerate	2307.3	1472.6	1780.6	905.4	30
Lactate	6911.5	24769.0	648.0	593.6	967
Leucine	5429.8	3886.0	4383.7	2210.6	24

Lysine	5654.6	4223.0	4522.4	2287.1	25
Malic acid	1373.2	921.8	1585.4	962.4	-13
Malonate	3904.5	6925.3	1231.1	1521.4	217
Methionine	1965.9	1199.2	1828.1	980.5	8
Methylamine	382.1	267.5	439.6	379.5	-13
Methylsuccinate	164.4	144.8	222.2	222.5	-26
N-Acetylglutamic acid	394.4	244.5	371.2	221.7	6
Nicotinate	241.4	157.7	250.2	161.7	-4
Ornithine	1802.1	1697.4	1164.7	737.4	55
Orotic acid	458.3	538.1	628.8	886.3	-27
Phenylacetic acid	1726.5	948.9	1397.1	692.5	24
Phenylalanine	2085.4	1969.5	1639.3	916.4	27
Phosphoenolpyruvic acid	241.0	216.6	212.7	156.0	13
Proline	1977.4	2105.7	1620.4	1189.5	22
Propionate	13849.9	7215.2	13774.2	8087.9	1
Ribose	3643.0	2322.7	3818.4	2347.5	-5
Sarcosine	55.7	131.7	38.0	20.8	47
Succinate	7715.5	21266.8	2638.2	6086.3	193
Taurine	2334.7	3285.0	1287.0	2641.5	81
Threonine	2821.2	1853.8	2198.2	1129.8	28
Thymine	471.6	340.3	467.5	345.5	1
Trimethylamine	234.8	318.6	156.1	181.1	50
Tryptophan	576.3	553.3	405.2	227.5	42
Tyramine	182.2	317.8	94.3	57.4	93
Tyrosine	1885.4	1493.1	1565.9	803.4	20
Uracil	1198.3	1097.0	1264.7	909.8	-5
Uridine	137.1	157.1	146.2	126.6	-6
Urocanate	111.8	174.3	98.1	65.7	14
Valerate	2669.9	2655.8	2826.8	1702.0	-6
Valine	5171.5	4509.9	3870.5	2175.1	34
Xanthine	1597.2	1365.5	1877.2	1365.9	-15
Xylose	1426.9	1130.5	1165.6	888.7	22
p-Cresol	740.3	584.3	519.9	295.0	42
β-Alanine	1048.7	2290.6	193.6	309.4	442

Metabolite concentrations were normalized to dry stool mass and are reported in nmoles per gram. 73 metabolites were identified and quantified across 54 FD patient stool samples (from 40 patients total) and 58 control relative stool samples (from 46 control relatives total). Columns 1 and 2 report the mean metabolite concentrations measured in the stool of FD patients and healthy control relatives, respectively, and mean standard deviations. Column 3 reports estimates of percent differences (%) in mean metabolite concentrations between FD patients and healthy controls. A negative percent value indicates a mean lower in FD patients compared to controls, and a positive percent value is higher in FD patients compared to controls.

Costello, Cheney et al., Supplementary Table S4

Table S4. Variable Importance in Projection (VIP) scores associated with components 1, 2, and 3 of the PLS-DA model generated from the distinct serum metabolite profiles of the FD patients and healthy control relatives.

Metabolite	Comp. 1	Comp. 2	Comp. 3
Xanthine	2.80	2.64	2.44
Urea	2.45	2.41	2.18
pi-Methylhistidine	2.08	1.96	1.79
Dimethyl sulfone	1.86	1.76	1.64
1,7-Dimethylxanthine	1.79	1.71	1.65
Methanol	1.79	1.69	1.55
Glycine	1.47	1.39	1.40
Taurine	1.35	1.27	1.21
Alanine	1.31	1.23	1.39
Glycerol	1.22	1.15	1.06
Valine	1.21	1.19	1.23
Glutamine	1.15	1.09	1.09
Glycolate	1.13	1.09	1.03
Asparagine	1.11	1.28	1.16
Leucine	1.11	1.18	1.10
Inosine	1.03	0.99	0.93
Tyrosine	1.00	0.97	1.05
Isopropanol	0.98	0.95	1.08
Tryptophan	0.94	0.97	0.94
Serine	0.92	1.10	1.01
Carnitine	0.89	0.86	1.26
Isoleucine	0.85	0.95	0.95
Dimethylamine	0.82	0.81	1.07
Propylene glycol	0.82	0.78	0.77
Pyruvate	0.78	0.83	0.76
Betaine	0.78	0.75	0.75
Acetate	0.75	0.79	0.75
2-Hydroxybutyrate	0.72	0.68	0.91
Capric acid	0.71	0.76	0.70
Hypoxanthine	0.69	0.65	0.59
Cadaverine	0.65	0.61	0.93
Creatine	0.64	0.79	0.77
Creatinine	0.59	0.59	0.84
Butyrate	0.49	0.46	0.62
Threonine	0.43	0.45	0.76
Histidine	0.42	0.74	0.67

Glucose	0.39	0.37	0.62
O-Acetylcholine	0.31	0.48	0.43
Choline	0.29	0.32	0.50
Phenylalanine	0.28	0.57	0.65
2-Oxoglutarate	0.22	0.31	0.38
Lactate	0.21	0.33	0.38
Succinate	0.17	0.26	0.45
Formate	0.15	0.30	0.40
Malonate	0.13	0.54	0.58
3-Hydroxybutyrate	0.11	0.15	0.33
Isobutyrate	0.10	0.56	0.55
Acetone	0.10	0.15	0.33
3-Methyl-2-oxovalerate	0.09	0.40	0.43
Arginine	0.06	0.15	0.64
O-Acetylcarnitine	0.03	0.04	0.26
2-Oxoisocaproate	0.03	0.45	0.46
Methionine	0.02	0.49	0.58
3-Hydroxyisobutyrate	0.01	0.23	0.21
Proline	0.01	0.54	0.49

Variable importance (VIP) score for all 55 serum metabolites analyzed via PLS-DA. Metabolites with VIP ≥ 1.2 (shaded in gray) are considered to contribute significantly to the separate group clustering observed in the PLS-DA scores plots shown in figure 1 (of the main text).

Costello, Cheney et al., Supplementary Table S5

Table S5. Variable Importance in Projection (VIP) scores associated with components 1, 2, and 3 of the PLS-DA model generated from the distinct stool metabolite profiles of the FD patients and healthy control relatives.

Metabolite	Comp. 1	Comp. 2	Comp. 3
Choline	3.43	2.36	2.29
Malonate	2.61	1.67	1.43
Tyramine	1.72	1.09	0.93
Beta-Alanine	1.66	1.02	0.92
p-Cresol	1.59	0.97	0.86
Phenylacetic acid	1.46	0.89	0.94
Lactate	1.42	0.89	0.81
Taurine	1.39	0.92	0.78
Ornithine	1.39	1.00	0.86
Isovalerate	1.31	0.80	0.79
Threonine	1.29	0.95	1.23
5-Aminopentanoate	1.26	0.95	1.02
Indole	1.24	0.94	1.12
Valerate	1.23	1.14	1.03
Glycerol	1.22	1.39	1.18
Isocaproate	1.22	0.85	1.05
Isobutyrate	1.19	0.91	0.92
Histidine	1.15	0.86	0.73
Dopamine	1.12	0.72	0.61
Xanthine	1.11	1.58	1.51
Inosine	1.11	1.41	1.27
Tryptophan	1.05	1.05	0.90
Formate	1.03	0.76	0.79
Valine	1.02	1.00	0.87
Orotic acid	1.01	1.21	1.03
Xylose	0.95	0.60	1.17
Trimethylamine	0.93	0.95	0.91
2-Aminobutyrate	0.93	0.96	0.99
Acetate	0.90	0.98	0.84
Glycerophosphocholine	0.89	0.70	0.69
Leucine	0.85	1.05	0.90
Ethanol	0.84	0.60	0.52
Phenylalanine	0.80	1.05	0.89
Malic acid	0.80	1.22	1.12
D-Mannose	0.79	0.95	1.06
Methylamine	0.79	1.36	1.29
Succinate	0.74	0.75	0.66

Glutamate	0.71	0.61	0.53
4-Hydroxyphenylacetate	0.71	0.68	0.70
Methylsuccinate	0.70	0.99	1.00
Glycine	0.68	0.59	0.53
Isoleucine	0.67	1.02	0.91
D-Glucose	0.67	0.41	1.63
Glucitol	0.65	0.94	0.85
Urocanate	0.64	1.35	1.56
Alanine	0.62	1.09	0.95
Aspartate	0.61	1.02	0.87
Lysine	0.59	1.01	0.90
Uracil	0.57	1.25	1.31
1,3-Dihydroxyacetone	0.55	0.85	1.00
Tyrosine	0.50	1.11	0.96
Thymine	0.45	0.52	1.32
Arabinose	0.45	0.70	0.93
Propionate	0.44	0.81	0.71
Dimethylamine	0.42	0.44	0.39
Proline	0.41	0.87	0.81
N-Acetylglutamic acid	0.41	1.08	1.07
2'-Deoxyuridine	0.36	1.23	1.07
Phosphoenolpyruvic acid	0.35	0.48	0.54
Fumarate	0.34	0.61	1.07
1,1-Dimethylbiguanide	0.31	0.42	0.36
Sarcosine	0.31	0.47	0.95
Uridine	0.29	1.33	1.19
Methionine	0.28	1.20	1.02
Glutamine	0.25	1.05	0.94
Glutarate	0.18	1.01	0.86
Nicotinate	0.16	0.81	0.83
Guanosine	0.15	0.79	0.68
Ribose	0.13	1.02	1.04
Arginine	0.11	0.60	0.54
Butyrate	0.07	0.94	0.81
2-Aminoisobutyric acid	0.04	0.96	1.09
Galactose	0.03	0.63	0.93

Variable importance (VIP) score for all 74 stool metabolites analyzed via PLS-DA. Metabolites with VIP ≥ 1.2 (shaded in gray) are considered to contribute significantly to the separate group clustering observed in the PLS-DA scores plots shown in figure 1 (of the main text).

Costello, Cheney et al., Supplementary Figure S1

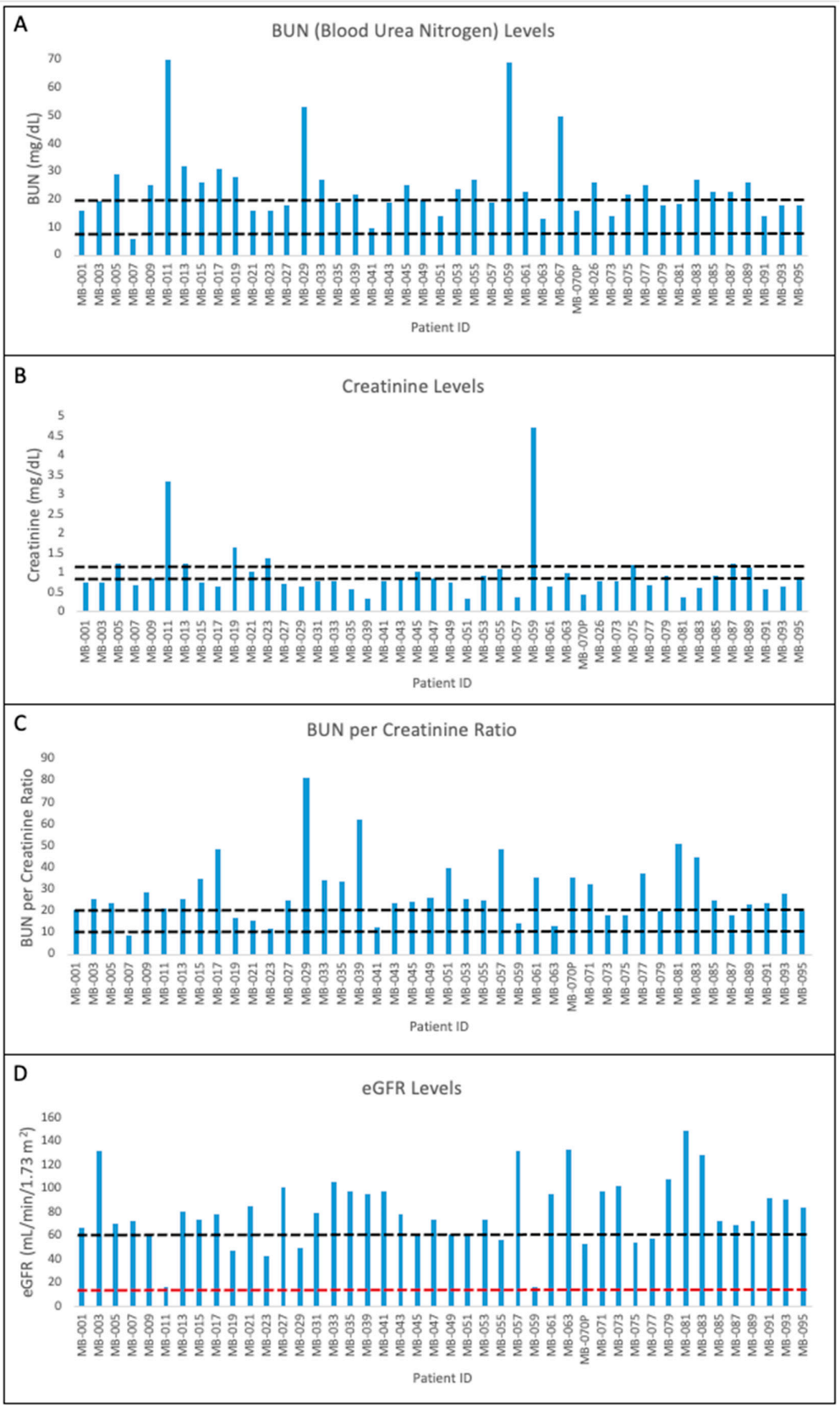


Figure S1. Results from Clinical Blood Tests that measured **(A)** blood urea nitrogen (BUN) levels, **(B)** creatinine levels, **(C)** BUN per creatinine ratio, and **(D)** estimated glomerular filtration rate (eGFR) levels in de-identified FD patient samples. These blood tests assessed the kidney function of FD patients via analysis of blood serum samples. **(A-C)** Levels within the dashed lines were considered normal. In **(D)**, for eGFR levels, levels below the black dashed line suggested chronic kidney disease, and levels below the red dashed line suggests kidney failure. Above the black dashed line indicates clinically normal levels (Mayo Clinic).

Costello, Cheney et al., Supplementary Figure S2

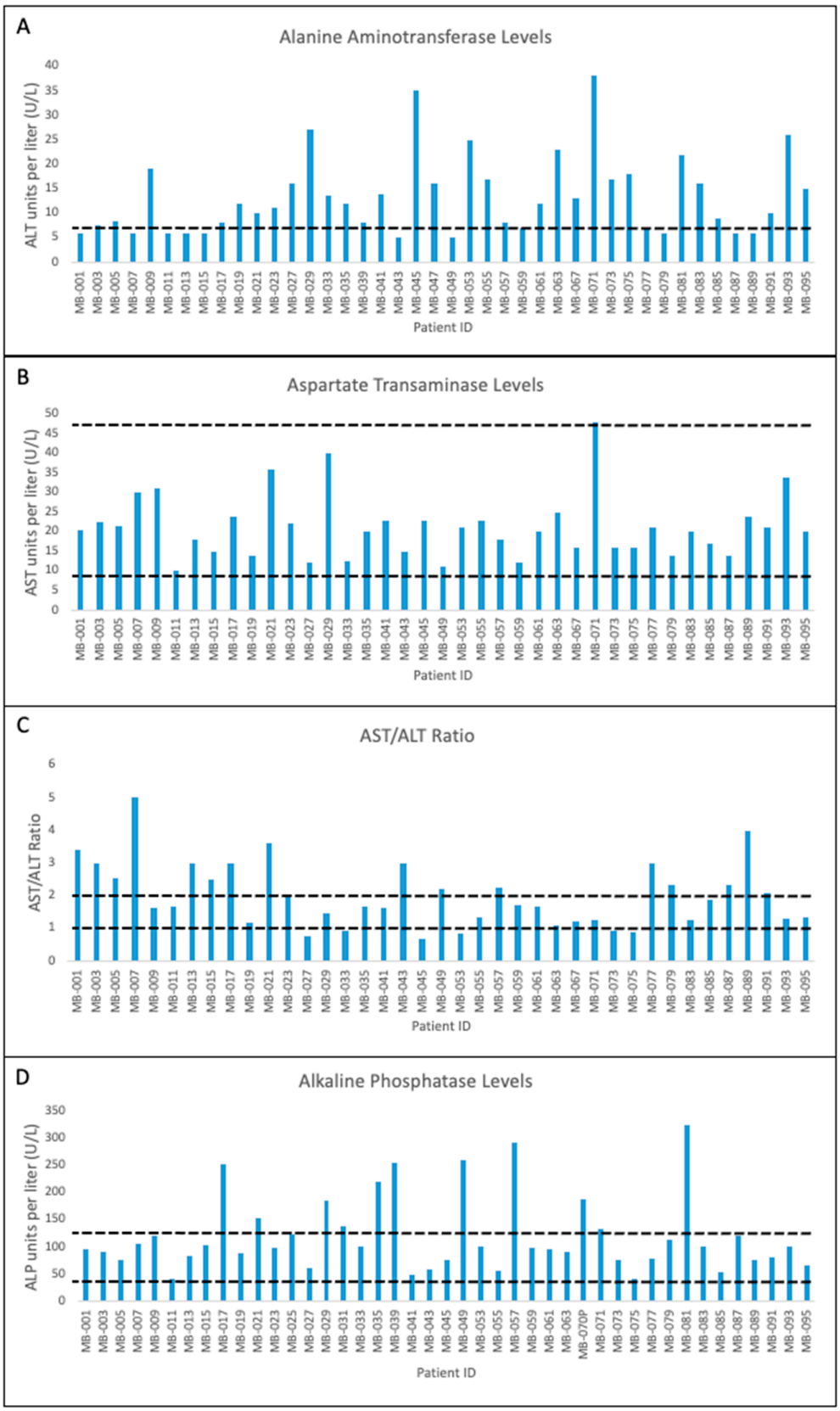


Figure S2. Results from FD patient liver enzyme blood tests and measurements of **(A)** Alanine aminotransferase (ALT) levels; **(B)** aspartate transaminase (AST) levels; **(C)** AST/ALT ratio; and **(D)** alkaline phosphatase levels (ALP). These blood tests assessed liver function by measuring the levels of liver enzymes in blood serum samples of FD patients. In panel **(A)**, values above the dashed line are considered normal ALT levels. In panels **(B-D)**, values between the dashed lines are considered clinically normal (Mayo Clinic). These data were collected on de-identified patient serum samples by clinical staff of the Familial dysautonomia center, at New York University School of Medicine.

Costello, Cheney et al., Supplementary Figure S3

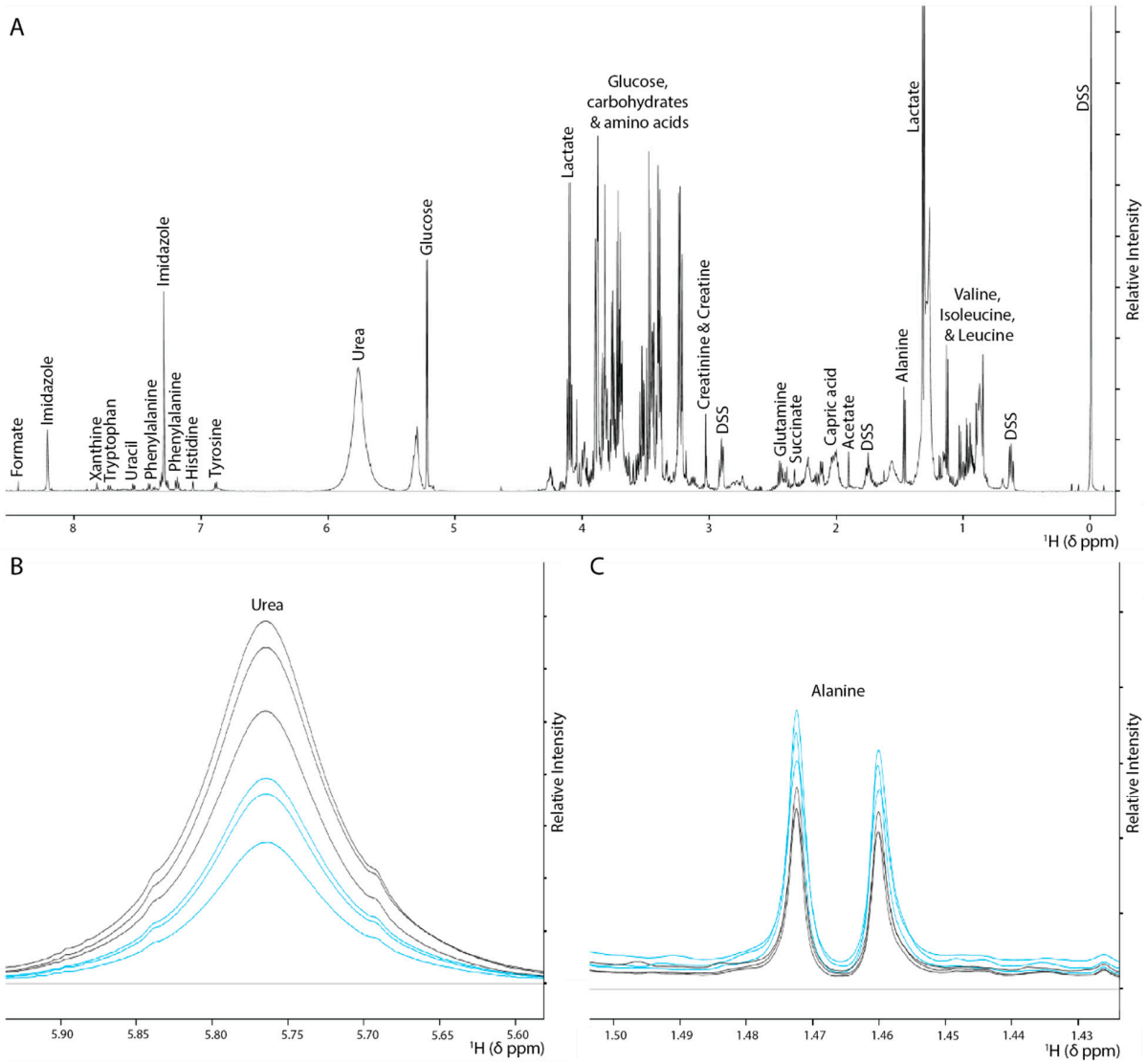


Figure S3. Human serum mixed metabolite 1D ^{1}H-NMR (600 MHz) spectra. **(A)** Overlays of 1D ^{1}H NMR spectra highlighting metabolites identified in serum metabolite mixtures of FD patients and healthy relative controls. Underlined metabolites denote those with multiple signals throughout the 1H chemical shift range. Overlays of ^{1}H NMR spectra from FD patient serum samples (black) and control relative serum samples (blue) are shown in **(B)** for the chemical shift region 5.6-5.9 ppm corresponding to urea, and in **(C)** for the chemical shift region 1.45-1.48 ppm corresponding to alanine.

Costello, Cheney et al., Supplementary Figure S4

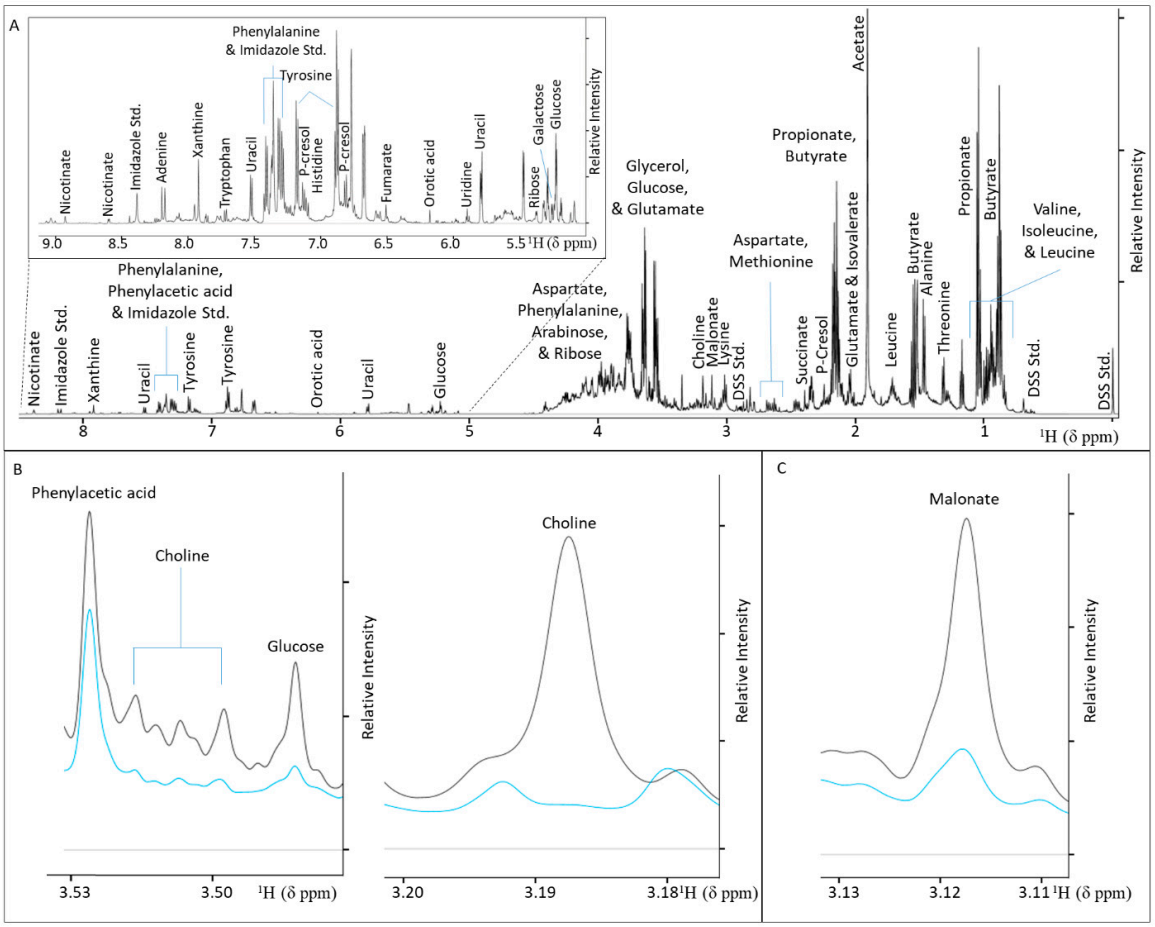
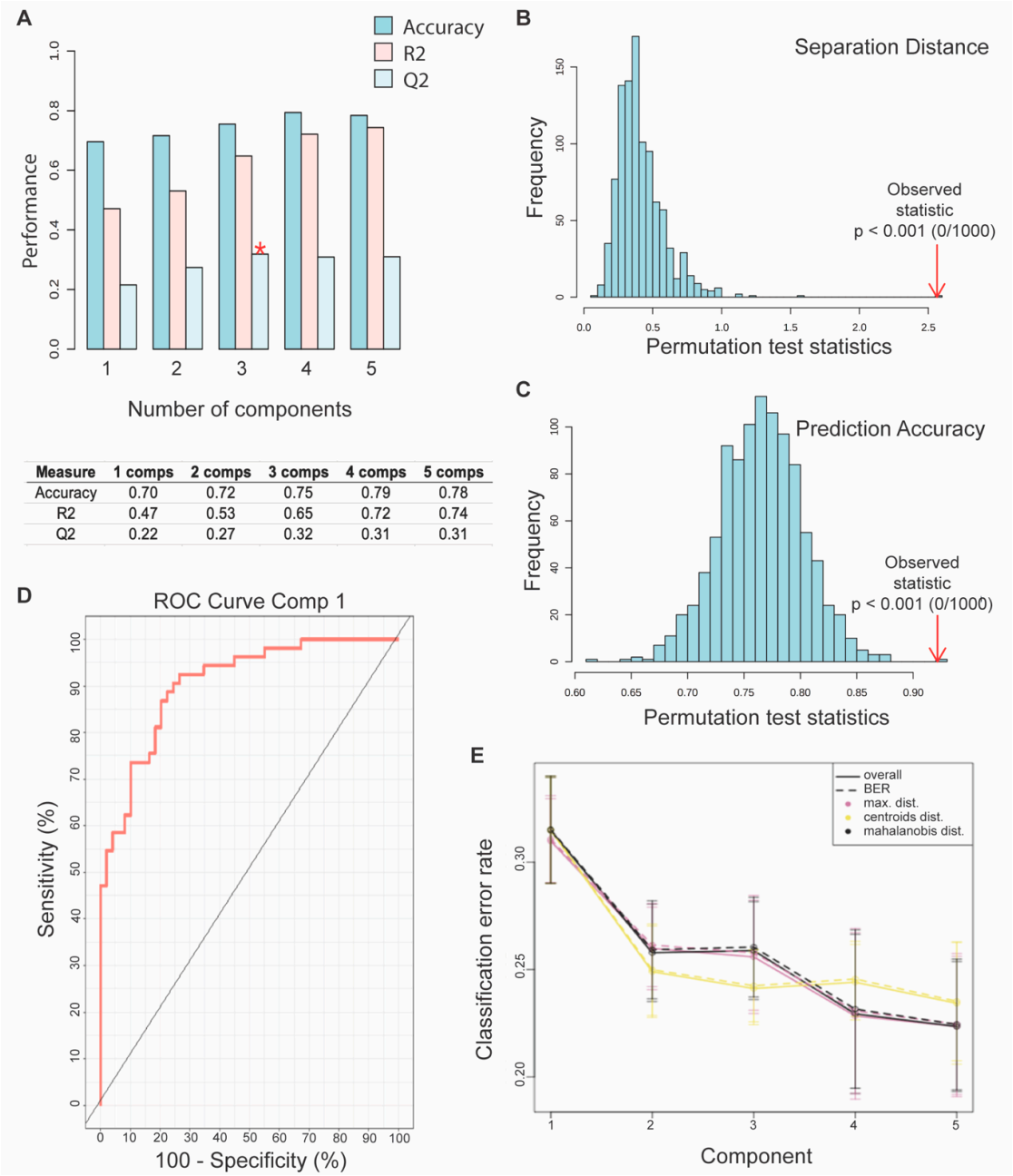


Figure S4. Human fecal metabolite 1D ^{1}H-NMR spectra. **(A)** Overlays of 1D 1H NMR spectra highlighting metabolites identified in the stool metabolite extracts of FD patients and healthy relative controls. Overlays of 1H NMR spectra from FD patient (black) and healthy relative control (blue) stool samples (black) are shown in **(B)** for choline, at chemical shift range 3.18-3.20 ppm, and 3.50-3.53 ppm, and **(C)** for malonate at 3.11-3.13 ppm. Additional peaks (phenylacetic acid and glucose) are annotated in spectral ranges as they appear in **(B)**.

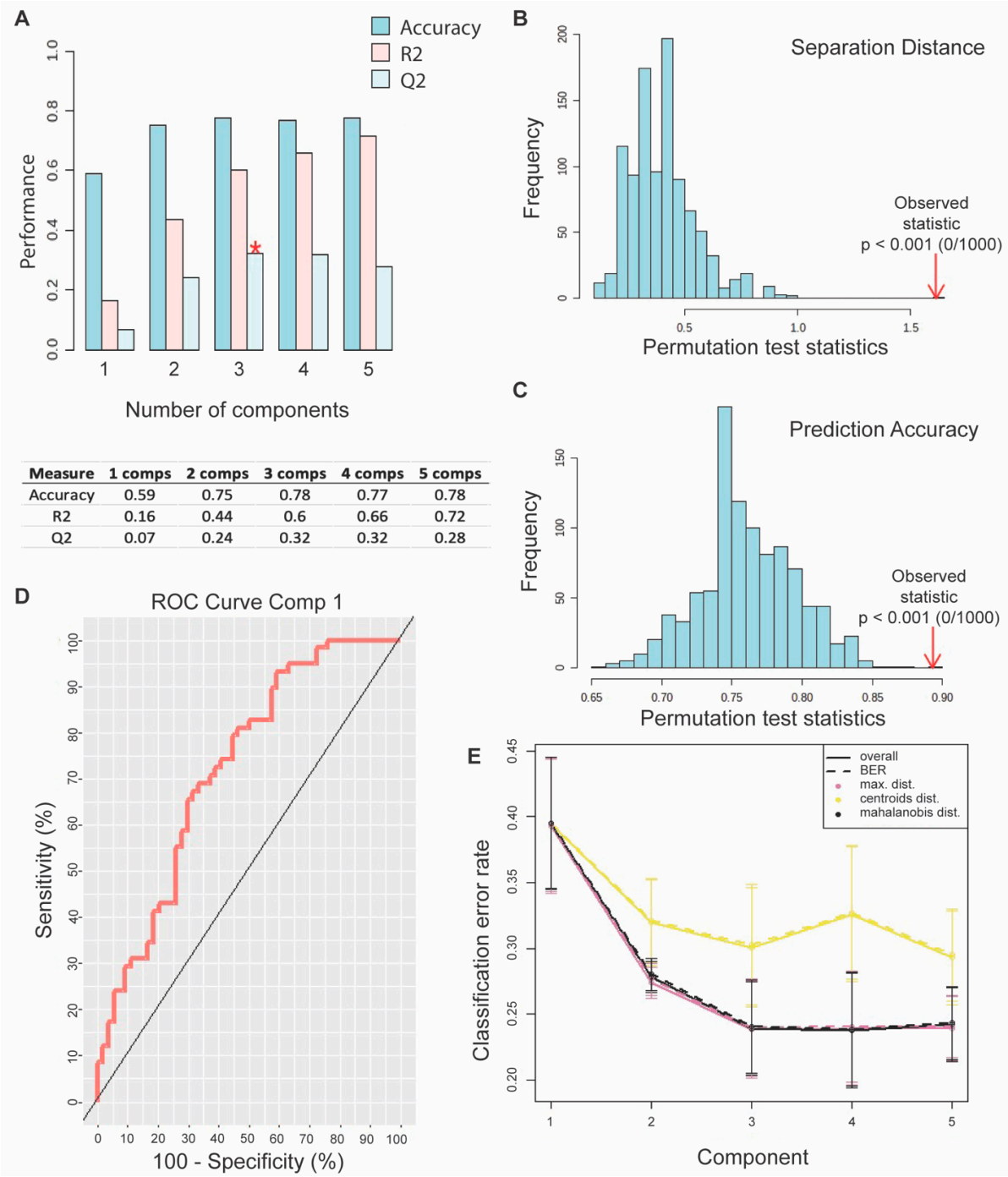
Costello, Cheney et al. Supplementary Figure S5



Measure	1 comps	2 comps	3 comps	4 comps	5 comps
Accuracy	0.70	0.72	0.75	0.79	0.78
R2	0.47	0.53	0.65	0.72	0.74
Q2	0.22	0.27	0.32	0.31	0.31

Figure S5. Validation metrics associated with the PLS-DA modeling of serum metabolite profiles of FD patients and healthy controls. **(A)** Leave-one-out cross validation (LOOCV) plot demonstrated model significance with an accuracy score of 0.75, an R^2 of 0.65, and Q^2 of 0.32, when taking into account the first 3 components of the PLS-DA model. The separation distance **(B)** and prediction accuracy permutation tests **(C)** (n = 1000 tests) yielded significant p-values < 0.001, attesting to the validity and prediction accuracy of the PLS-DA model. **(D)** The area under receiver operating characteristic (AUROC) curves yielded an AUC value of 0.91, demonstrating high model accuracy and specificity for the separate classification of FD patient and healthy control groups. **(E)** Classification error rate (CER) yielded a remaining classification error rate of ~26% for component 3 and less than 25% for component 4 (and beyond) of the PLS-DA model.

Costello, Cheney et al. Supplementary Figure S6



Measure	1 comps	2 comps	3 comps	4 comps	5 comps
Accuracy	0.59	0.75	0.78	0.77	0.78
R2	0.16	0.44	0.6	0.66	0.72
Q2	0.07	0.24	0.32	0.32	0.28

Figure S6. Validation Metrics associated with the PLS-DA modeling of stool metabolite profiles of FD patients and healthy controls. **(A)** Leave-one-out cross validation (LOOCV) plot demonstrated model significance with an accuracy score of 0.78, an R^2 of 0.6, and Q^2 of 0.32, when taking into account the first 3 components of the PLS-DA model. The separation distance **(B)** and prediction accuracy permutation tests **(C)** (n = 1000 tests) yielded significant p-values < 0.001, attesting to the validity and prediction accuracy of the PLS-DA model, demonstrating high model accuracy and specificity for the separate classification of FD patient and healthy control groups. **(D)** The area under receiver operating characteristic (ROC) curves yielded an AUC value of 0.72. **(E)** Classification error rate (CER) yielded a remaining classification error rate of ~25% for component 3 and less than 25% for component 4 (and beyond) of the PLS-DA model.

Costello, Cheney et al. Supplementary Figure S7

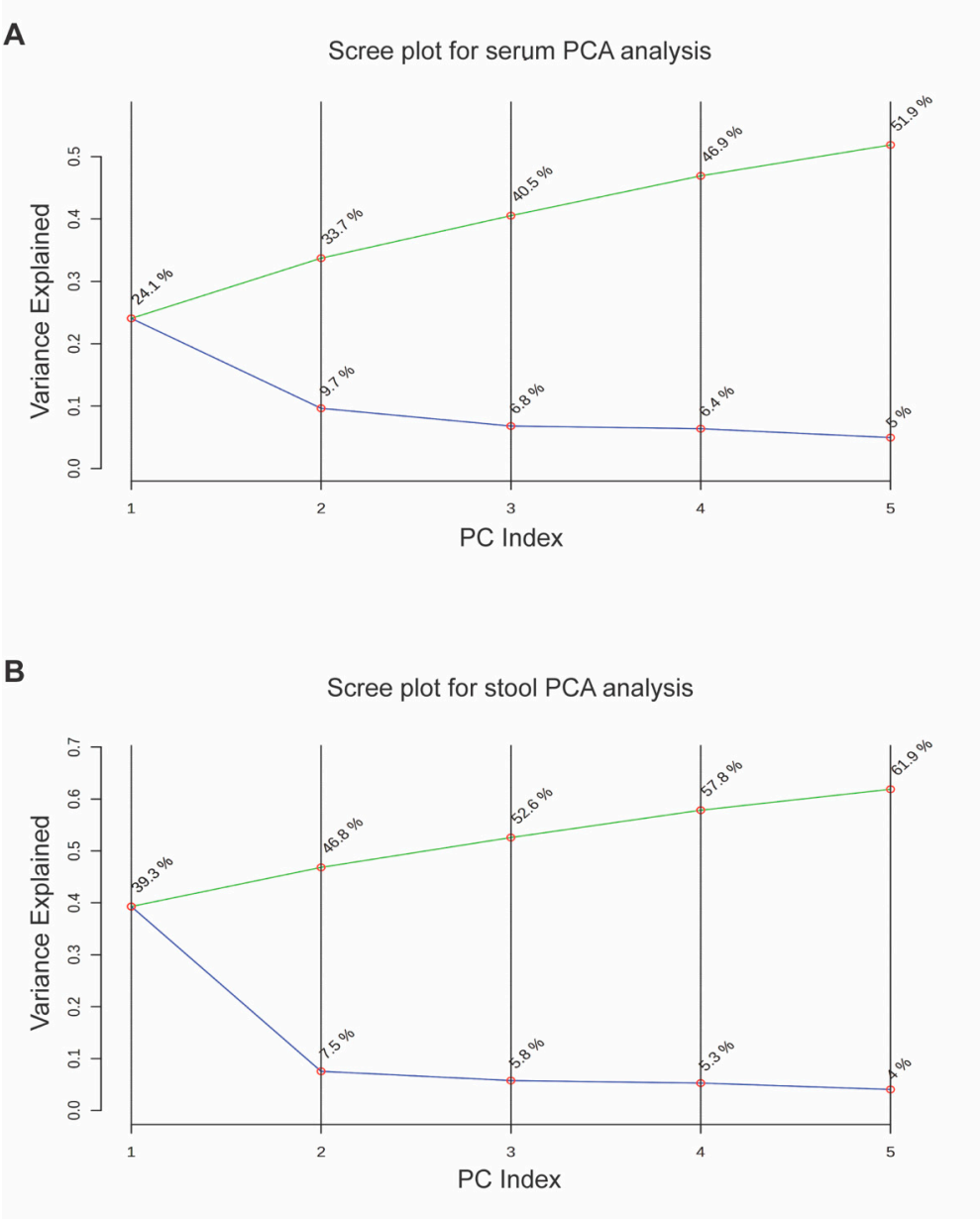


Figure S7. Scree plots associated with unsupervised PCA analyses of **(A)** serum and **(B)** stool metabolite profiles. The plots indicate the percent variance contribution of each principal component (from PC1 to PC5) of the PCA scores plots. The green line represents the total cumulative variance as the percent variance of each PC 1-5 is added. The blue line represents the percent variance accounted for by each PC. The scree plots were generated using the principal component analysis module of MetaboAnalyst v.4.0.

Costello, Cheney et al., Supplementary Figure S8

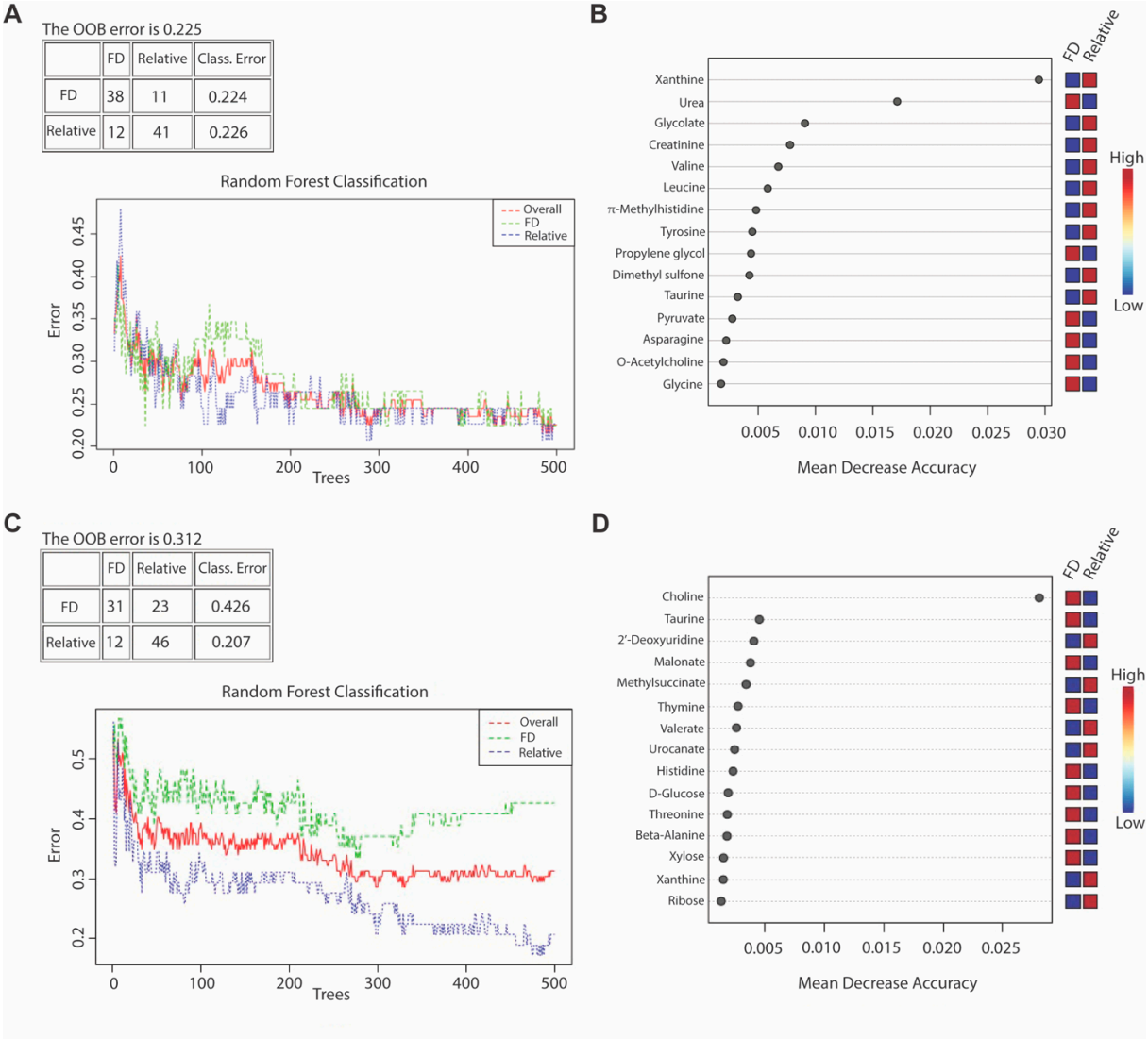


Figure S8. Random forest analysis of the FD patient vs Control relative groups. **(A)** The analysis for serum profiles yielded an overall out-of-bag (OOB) error of 0.225 (22.5%) and classification error rates of 0.224 (22.4%) and 0.226 (22.6%) for the FD and control groups, respectively**. (B)** Mean decrease accuracy values highlighted the top 15 serum metabolites that were found to be important discriminators of the two groups and contributed most to the accuracy of the random forest predictions. **(C)** For the stool profile analyses, the OOB error was 0.312 (31.2%), with the FD class error being 0.426 (42.6%) and the control class error being 0.207 (20.7%). **(D)** The top 15 metabolites of the mean decrease accuracy plot are listed, with their concentration trend in relation to the control group shown to the right. Blue and Red indicate a low and high concentration trend, respectively. Mean decrease accuracy is shown along the bottom.

The random forest analysis of the serum metabolite profiles yielded a comparable classification error rate to that observed in the CER evaluation of the first three components of the PLS-DA model (i.e., a CER value of ~25%) compared to an out-of-bag (OOB) error rate of 22.5% in the random forest analysis (Figures S1E & S3A). Similarly, the random forest analysis of the stool metabolite profiles identified an

overall OOB error rate of 31.2%, which is relatively consistent with a CER of ~25% (Figures S2E & S3C). Additionally, the random forest analysis of the stool metabolome yielded a more accurate classification of the control samples (class error = 20.7%) compared to those of the FD patients (class error = 42.6%), consistent with the greater dispersion observed within the FD patient cluster compared to the control group in the 3D PLS-DA scores plot shown in Figure 1D. This indicates that the stool metabolomes of FD patients are not only different from controls but vary significantly from each other.

Costello, Cheney et al., Supplementary Figure S9

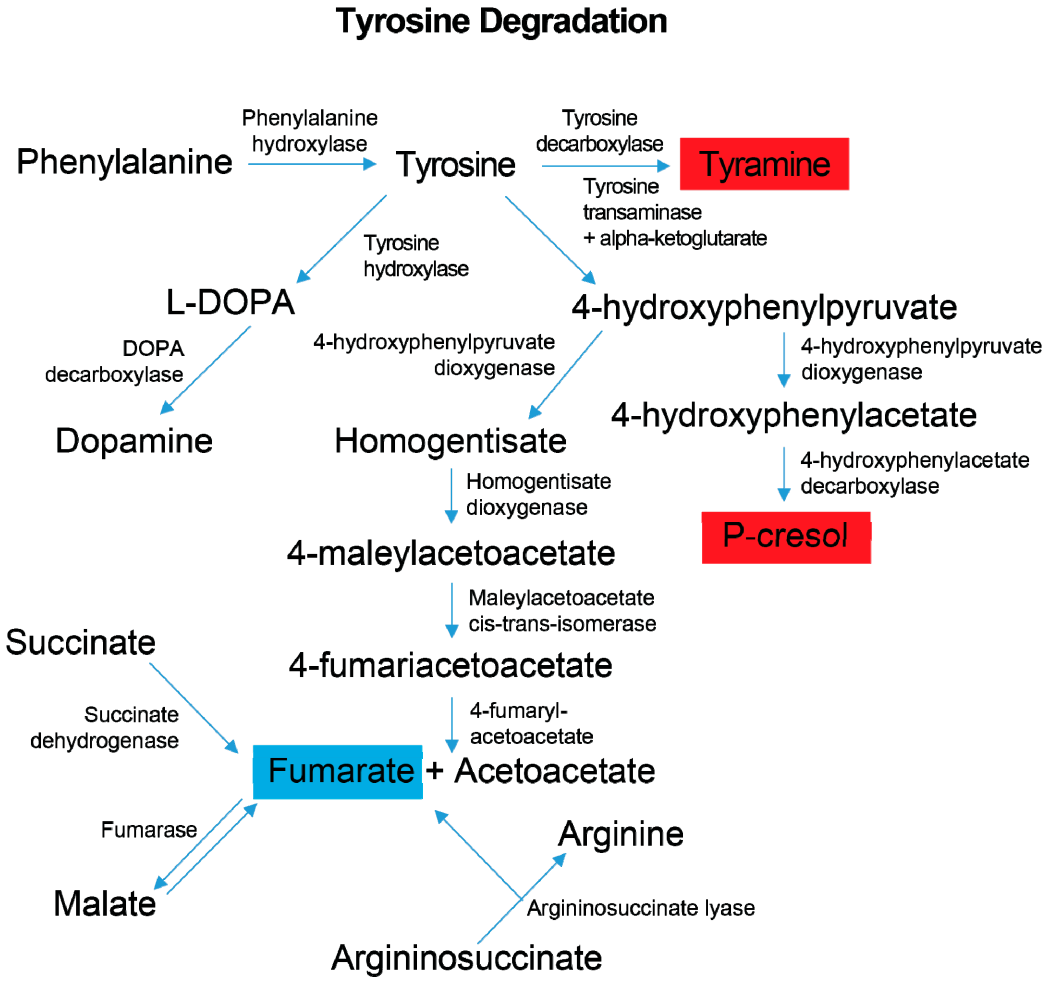


Figure S9. Tyrosine pathways yield tyramine, p-cresol, fumarate, and dopamine. The one-step reaction facilitated by tyrosine decarboxylase converts tyrosine to tyramine. Through a three-step reaction, tyrosine can also be converted to p-cresol. Lastly, fumarate and acetoacetate (linked to the TCA cycle) can be produced by a four-step reaction [1]. In addition to tyrosine metabolism, fumarate is classically produced by the TCA cycle from the conversion of succinate to fumarate via succinate dehydrogenase (Complex II of the ETC). In addition to the metabolites of interest from our study, dopamine, relevant for neurological signaling, is made from the starting substrate tyrosine. Red indicates metabolites with elevated levels in the FD patients stool samples, while blue indicates metabolites that were lower in concentration in the stool samples of FD patients.

Costello, Cheney et al., Supplementary Figure S10

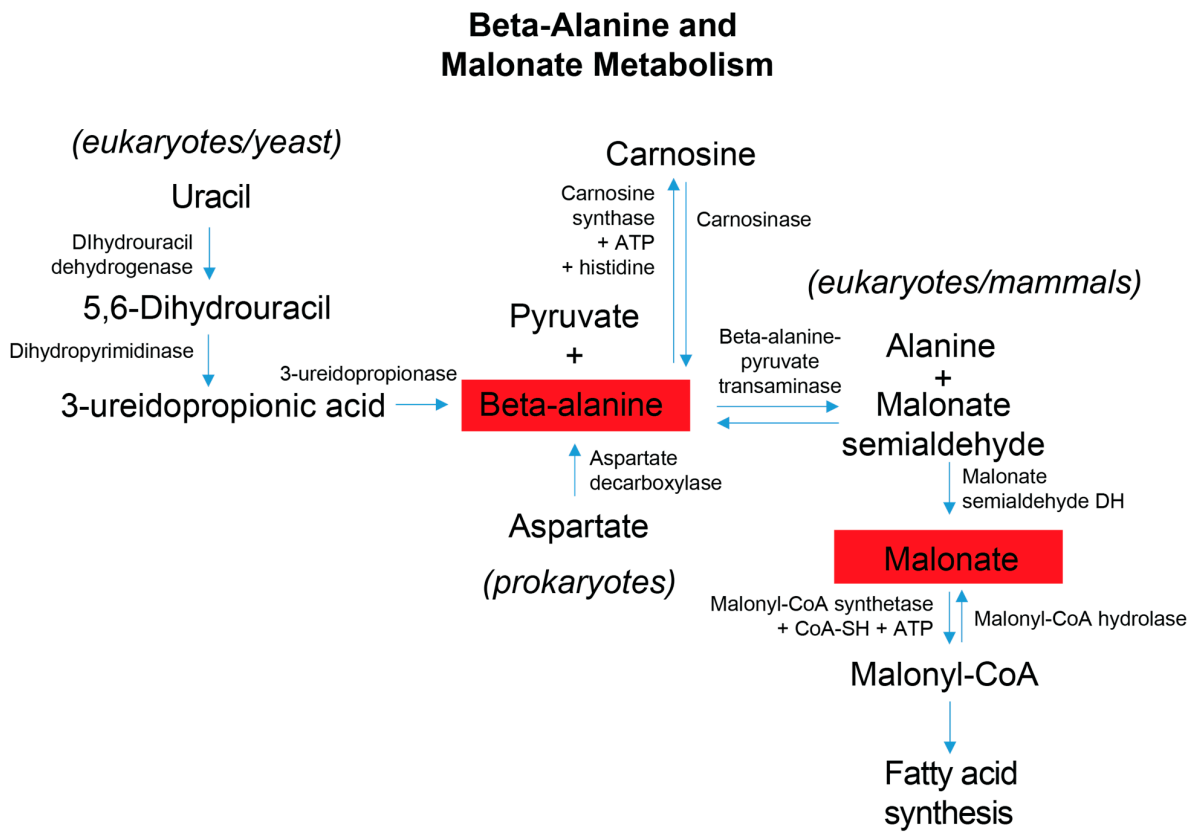


Figure S10. Beta-alanine and malonate metabolism connect via the intermediate malonate semialdehyde. Beta-alanine is produced by the degradation of uracil, decarboxylation of aspartate by gut microbes, carnosine catabolism, and a transaminase reaction using alanine and malonate semialdehyde as substrates [2, 3]. Carnosine is a constituent of muscle, and beta-alanine (in addition to histidine) are produced when muscle carnosine is broken down [4], which take place both when human skeletal muscle and food sources of muscle proteins are degraded. Red indicates metabolites with elevated levels in the FD patients stool samples. Abbreviations: ATP, adenosine triphosphate; DH, dehydrogenase; CoA, coenzyme-A.

Costello, Cheney et al., Supplementary Figure S11

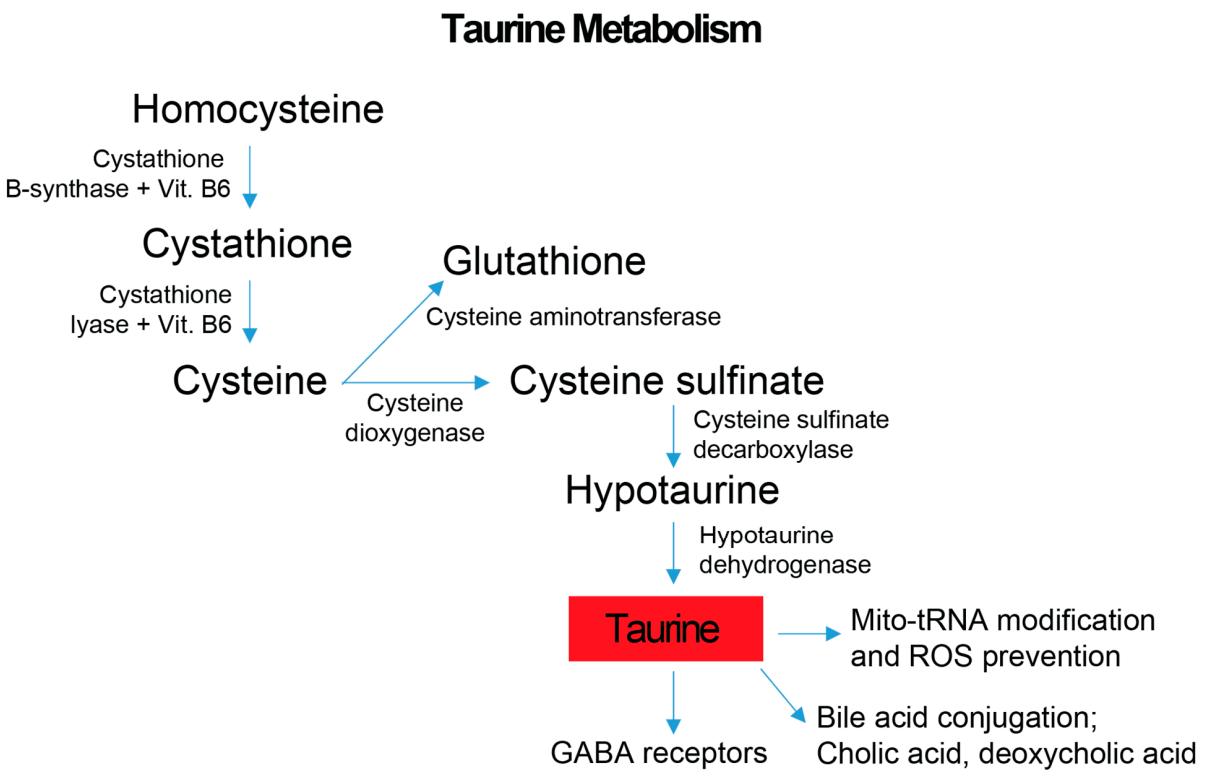


Figure S11. Taurine is obtained primarily from the diet but can also be synthesized endogenously via degradation of homocysteine and participates in 3 primary host metabolic functions. Taurine can conjugate to bile acids, specifically cholic and deoxycholic acid. Taurine functions in the nervous system as an inhibitory signaling molecule as discussed in Figure S13. Lastly, taurine conjugates to mitochondrial tRNA to aid in translation of mitochondrial proteins, specifically enhancing the production of ETC complex 1 protein components and mitigating the production of ROS by facilitating proper complex 1 protein subunit production, and therefore ETC function [5]. Red indicates taurine was elevated in FD patients stool samples. Abbreviations: GABA, gamma-aminobutyric acid; Mito, mitochondria; ETC, electron transport chain; ROS, reactive oxygen species.

Costello, Cheney et al., Supplementary Figure S12

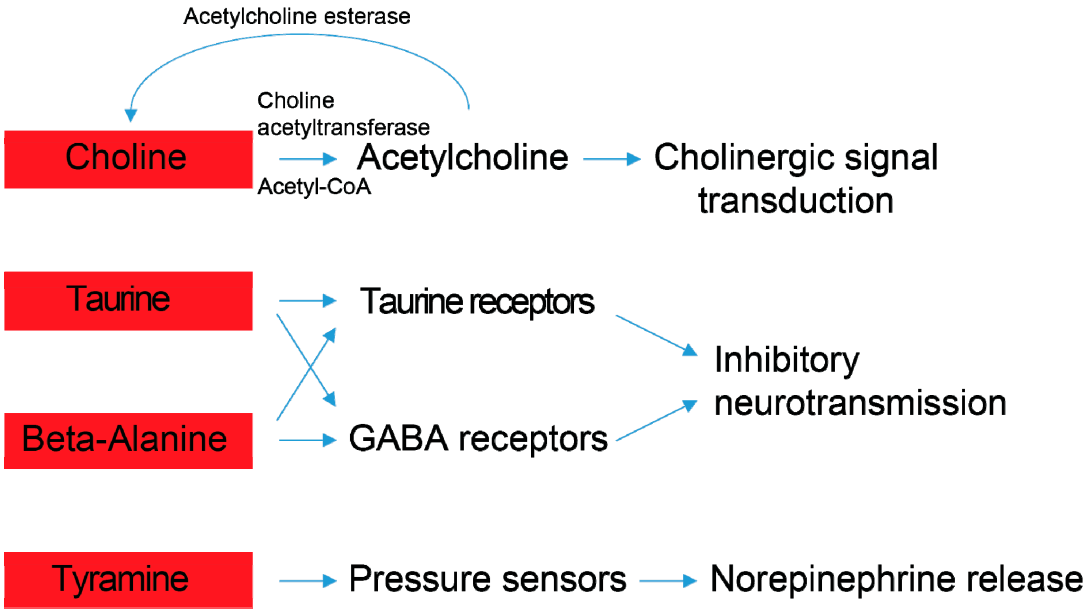


Figure S12. The four neural signaling molecules identified in elevated concentrations in the stool of FD patients compared to their control relatives. Choline is converted to acetylcholine via a one-step reaction requiring acetyl-CoA; this reaction occurs in the pre-synaptic neuron and the product (acetylcholine) is exported to the synaptic cleft of cholinergic neurons where it can bind postsynaptic muscarinic and preganglionic nicotinic receptors [6, 7]. Intra-synaptic acetylcholinesterase terminates the signal and liberates choline from acetylcholine to recycle some choline back into the neuron. Taurine and beta-alanine can both bind GABA receptors to initiate an inhibitory neural signal. Additionally, taurine can elicit neuronal hyperpolarization through its own unique signaling system[8], whereas beta-alanine acts primarily as a "false neurotransmitter", binding GABA receptors and inducing an improper inhibitory response[4]. Tyramine binds pressure sensors and promotes norepinephrine release. Red indicates metabolites in higher concentrations in FD patients stool samples. Abbreviations: GABA, gamma-aminobutyric acid

Supplementary References Cited

1. Stančíková, M., and Rovenský, J. "Metabolism of Aromatic Amino Acids." In *In Alkaptonuria and Ochronosis*, edited by J. Rovensky, Urbanek, T, Boldisova, O., and Gallagher, J., 9-12. Slovakia: Springer, 2015.
2. Eaton, K.K., Howard M., and Hunnisett, A. "Urinary Beta-Alanine Excretion Is a Marker of Abnormal as Well as Normal Gut Fermentation." *J. Nutr. Environ. Medicine* 4, no. 2 (1994): 157-63.
3. Lopez-Samano, M., Lozano-Aguirre Beltran, L.F., Sanchez-Thomas, R., Davalos, A., Villasenor, T., Garcia-Carcia, J.D., Garcia-de los Santos, A. "A Novel Way to Synthesize Pantothenate in Bacteria Involves B-Alanine Synthase Present in Uracil Degradation Pathway." *MicrobiologyOpen* 9(4):e1006 (2020).
4. Tiedje, K. E., K. Stevens, S. Barnes, and D. F. Weaver. "B-Alanine as a Small Molecule Neurotransmitter." *Neurochemistry International* 57, no. 3 (2010): 177-88.
5. Jong, C. J., J. Azuma, and S. Schaffer. "Mechanism Underlying the Antioxidant Activity of Taurine: Prevention of Mitochondrial Oxidant Production." *Amino Acids* 42, no. 6 (2012): 2223-32.
6. Wiedeman, A. M., S. I. Barr, T. J. Green, Z. Xu, S. M. Innis, and D. D. Kitts. "Dietary Choline Intake: Current State of Knowledge across the Life Cycle." *Nutrients* 10, no. 10 (2018).
7. Wurtman, Richard J. "Choline Metabolism as a Basis for the Selective Vulnerability of Cholinergic Neurons." *Trends in Neurosciences* 15, no. 4 (1992): 117-22.
8. Wu, J. Y., and H. Prentice. "Role of Taurine in the Central Nervous System." *J Biomed Sci* 17 Suppl 1 (2010): S1.

APPENDIX C

WESTERN BLOT TROUBLESHOOTING FOR THE CHOLINE TRANSPORTERS

Standard Western Blot Methods

The original method used for the western blot procedure is referred to as the "standard" western blot procedure throughout Appendix C. Steps were modified throughout the troubleshooting process and delineated within the commentary for the Trial that the change was made. Steps that deviate from the standard protocol, and that were found to be useful are annotated throughout the standard procedure as an indented empty bullet point. The protocol was adapted from the procedure outlined by Heini Miettinen.

Protein Extraction from Tissue

- Use 150-200 µL of lysis buffer per sample, dependent on amount of tissue. More lysis buffer can be added after centrifuging, and re-homogenized – goal is to have more supernatant than pellet after centrifuging.
    - 200 µL were used for duodenum segments, jejunum and ileum.
    - 150 µL were used for colon segments.
        - 100 µL can be used for 2 retinas, or 70 µL for one retina.
- Add HALT and PMSF in 1:100 dilutions to the aliquot of lysis buffer that will be added to all samples. Stock concentrations are 100x of PMSF (stored at -20 °C) and 100x HALT (stored at 4 °C); 10% of desired volume of buffer (say 2.5 mL, 10% would be 25 µL) and that is the volume of HALT and PMSF to add each to total volume. Since the volume is so tiny, there is no need to worry about exact dilution factors.
- Homogenize with plastic pestle in microcentrifuge tube directly after removing from storage (at -80 °C or -20 °C), add lysis buffer to samples, and keep on ice whenever possible.

  - Samples can be sonicated with an ultrasonic microcentrifuge sonicator instead to facilitate homogenization.
- Spin down lysates at 13,000 x g for 5 minutes, ideally at 4 °C. If need be, samples can be spun at room temp in a benchtop centrifuge at 13,000 RPM for 5 min.

Bicinchoninic acid (BCA) Assay

The Pierce BCA Assay kit (ThermoFisher Scientific, CAT# 23225) was used according to the manufacturer's instructions with the following notes:

- It is recommended to make 1:10 and 1:30 dilutions of samples using deionized water (dH_2O)
  - For concentrated solutions, make a 1:50 dilution which can be easily diluted to 1:100 if necessary.
- 10% sterile filtered BSA is the stock solution used to make the standards. A 50x dilution of the BSA stock solution is done to make the first standard 2000 µg/mL (20 µL BSA stock + 980 µL dH_2O). Make the standards as delineated in Table 2 using serial dilutions.

Concentration (µg/mL)	BSA	dH_2O (µL)
2000		
1500	300 µL of 2000 µg/mL	100
1000	100 µL of 2000 µg/mL	100
750	100 µL of 1500 µg/mL	100
500	100 µL of 1000 µg/mL	100
250	100 µL of 500 µg/mL	100
125	100 µL of 250 µg/mL	100
62.5	100 µL of 125 µg/mL	100
31.25	100 µL of 62.5 µg/mL	100

Table 1. BCA Assay Standards.

- 25 µL of each sample dilution and standard is loaded into the plate, and 200 µL of BCA assay is subsequently added to all wells. Samples should appear to fall in the middle of the standards color-wise approximately 5-10 min into the incubation period. Add BCA reagent to first sample well of all dilutions being tested, then the 2000 µg/mL standard well, then to remaining wells. If the sample well turns just as dark as the standard, then samples need to be diluted further.
- Incubate for 30 minutes at room temperature (37 °C) on the benchtop.
- Read at 562 nm. Concentration from Spectramax 190 plate reader given in µg/mL, which need to be multiplied by the dilution factor and then convert to µg/µL.

Gel Electrophoresis

- Turn heat block on at the beginning of the gel electrophoresis stage, while pouring the gel and preparing the samples.
- Molecular weight ladder (Precision +) and Laemmli buffer are stored at -20 °C – remove and place on ice to allow to thaw while pouring a gel.
- Prep the gel following the appropriate recipe in Table 2. The recipe for 10 mL of separating gel and 4 mL of stacking gel will make 2 gels. Pick the percentage based on size of protein to be blotted and desired separation. (ex: 61 kDa proteins work well with 10% gels)
    - Check that the buffer dam is inserted properly, and that the unit is not leaking!
    - ***measure how far comb goes in so you will have a stacking gel still***

Separating Gel						
Ingredient	5%	7.5%	10%	12.5%	15%	20%
40% Acrylamide	1.25 mL	1.875 mL	2.5 mL	3.12 mL	3.75 mL	5.0 mL
1.5 M Tris-HCl, pH 8.8	2.5 mL	2.5 mL	2.5 mL	2.5 mL	2.5 mL	2.5 mL
10% SDS	100 µL	100 µL	100 µL	100 µL	100 µL	100 µL
dH_2O	6.09 mL	5.465 mL	4.84 mL	4.22 mL	3.59 mL	2.3 mL
TEMED	10 µL	10 µL	10 µL	10 µL	10 µL	10 µL
10% APS	50 µL	50 µL	50 µL	50 µL	50 µL	50 µL

4% Stacking Gel	
Ingredient	4%
40% Acrylamide	400 µL
0.5 M Tris-HCl, pH 6.8	1.0 mL
10% SDS	40 µL
dH_2O	2.47 mL
TEMED	4 µL
10% APS	80 µL

Table 2. Recipes for 10 mL of Separating gel and 4 mL of 4% Stacking gel.

- Prep protein samples in Laemmli buffer to give a total concentration of 30-50 µg of protein per well. The final volume is achieved with water.
    - Use $M_1V_1 = M_2V_2$ to determine volume of samples to add.
    - Ex: (conc. Of sample) (vol. to add?) = (50 µg/15 µL protein) (Desired vol.)
    - Laemmli buffer should have final conc. of 1x from stock 5x conc. (ex: 10 µL in total vol of 50 µL)
- Heat protein samples for 10 min at ~80 °F to denature.
- Load the gel, with the following total volumes that can be loaded into wells: 30 µL for 10 well gel, 15 µL for 15 well gel.
    - 15 µL total were used for both 10 and 15 well gels.

- Gel lanes should consist of protein samples of interest, Precision + ladder (5 µL for a 15 well gel) and 1x laemmli in any "empty" wells to help the gel run more evenly (load same volume as sample for 1x Laemmli)
- Fill the inner chamber between two gels (or one gel and buffer dam) completely, and the compartment between the gel and electrophoresis box enough to cover the electrodes with running buffer (1x SDS).
- Run at 200 v until dye front gets past the stacking gel, then run at 160 v until dyefront runs off the gel.
- While gel is running, make 5% bovine serum albumin (BSA) solution and Blotto.
    - BSA: 0.75 g BSA in 15 mL 1X TBST – BSA (stored at 4 °C)
    - Blotto: 2.5 g nonfat dry milk in 50 mL 1X TBST

<u>Semi-Dry Transfer and Blot</u>

- Place electrode of Semi-Dry Transfer Unit in fridge to cool while gel is running.
- Crack gel open and transfer to petri dish with 1x Transfer Buffer (stored at 4 °C)
- Activate polyvinylidene difluoride (PVDF) membrane with methanol for ~30 sec.
    - Nitrocellulose is a better membrane to use when proteins are under 20 kDa as these small molecular weight proteins do not transfer as well on PVDF – activate this membrane with transfer buffer.
- Layer the transfer sandwich as follows: Bottom filter -> activated PVDF membrane -> roll bubbles out with a serological pipet or similar -> gel (ladder on left/orientation as loaded) -> top filter -> roll bubbles out.
- Retrieve electrode from fridge and run for 30 min at 12 v.

- Disassemble as was assembled – return filters to respective top and bottom storage containers filled with running buffer, discard gel and put membrane into Blotto.
    - Filters can be reused and stored at 4 °C, though must be distinguished by the filter used for the top or bottom.
    - Clean transfer unit with water and a sponge and allow to air dry.
- Rock in ~10 mL Blotto for 1 hr
    - These parameters are the minimum – blocking can be achieved by rocking overnight at 4 °C to either troubleshoot, or if a stopping point is necessary for the experiment that day.
- After Blotto, wash filter 3 times with 1X TBST (rock for 10 min 3 times)
    - OR wash 6 x for 5 min each
- After washing, cut membrane with razor blade on lid of square petri dish to produce halves of the membrane to allow for primary and loading control antibodies to be applied separately. Place respective halves in primary antibody (AB) to rock overnight in fridge
- Need a minimum of 4 mL to rock in
    - GAPDH is usually used at a 1:20,000 dilution (0.5 uL of AB in 10 mL 5% BSA)
    - Other AB are standardly a 1:1,000 dilution (ex: OCT1 was 5 uL in 5 mL 5% BSA)
- After blotting overnight, wash membrane for 30 min (either 3 x 10 min washes or 6 x 5 min washes) at room temp
    - ***SAVE primary AB in fridge. Can last in fridge until you notice the signal decaying, at which time the antibody solution can be “spiked” by

supplementing the same volume with fresh antibody solution at the same dilution factor. Or, if volume is too low, the antibody solution can be spiked then. AB solution should be discarded immediately if the solution appears cloudy or contaminated.

- Make secondary AB solution (HRP conjugated secondary antibody against the animal the first antibody was produced in).
    - Need a 1:10,000 dilution: 1 uL antibody in 10 mL Blotto, then split into 5 mL for each half of membrane.
- Secondary AB rocks at room temp for 1 hour.
- After secondary AB, wash for 30 min as before w/ 1X TBST
    - Secondary AB are always discarded.

<u>Blot Development on Photopaper</u>

- Leaning the tray so as to facilitate pooling of the remaining wash, then pipette/blot out the wash with a kimwipe.
- ***May want to apply the developing agent in the dark room so as to not waste the strongest signal. Supplies necessary includes:
    - Film + film cassette
    - 3 tubberware containers for developing agents and H_2O
    - Tweezers
    - Tape + aluminum foil to block signal
    - Scissors
    - Plastic wrap

    - Developing agent (Advansta western bright ECL)
    - Tube for developer
    - 1 mL pipette and tips

- Mix the developing agent 1:1 for a total vol of 1.2 mL, i.e.: 600 µL of each A and B reagent.
- Pipette 600 µL directly on membrane where the protein of interest is expected.
- Wait ~2 min.
- Wrap membranes separately in plastic wrap and tape in developing box in the upper right corner to prevent membranes from moving at any point.
- Remove film only in the dark or red light of the dark room. Cut film in half and then cut one corner from the halves. Always try to orient cut corner at bottom left and enabling the film to be realigned with the membrane after development so the Precision + ladder can be drawn on the film.
    - Will likely have to expose GAPDH and protein of interest separately, and as such, tinfoil can be taped over the membrane to block signal from regions other than those of interest.
- To develop film, rock film in developer for ~30s, dip in deionized H_2O to rinse and then place in fixative. The film can remain in the fix solution until all exposures have been complete and developed.
        - After developing, wash film further with deionized H_2O to avoid salt spots; let air dry, then mark ladder on film.

General Troubleshooting Notes:

- If a lot of nonspecific binding is occurring, blotting overnight in the fridge on a rocker in Blotto helps to alleviate this.
- If protein is aggregating or not denaturing properly, test different denaturing temperatures after adding Laemmli buffer. Tests can include ice, room temperature and 37 °C (all 1 hour denaturing periods) and 50 °C, 75 °C, 95 °C (15 min denaturing period). If the same heat block is used for each temperature treatment, samples can be left at room temp after their temperature treatment.
- If primary antibody is not producing signal:
    - Test a different lysis buffer (protein may not be extracted based on tissue)
    - Test temp treatments noted above
    - Refer to the appropriate Genecard, identify a tissue with known high concentrated levels of the targeted protein, and use this tissue type as a positive control while troubleshooting.
    - If activating the PVDF membrane in MeOH causes it to melt, that is not PVDF, its nitrocellulose; That membrane can be activated with the transfer buffer.

Reagents

10x TBS: 1 L H2O, 24.2 g Tris Base (0.2M), 87.7 g NaCl (1.5 M), Adjust pH to 7.4 with HCl (use a 1 mL glass pipette and pipette bulb)

1X TBST: 500 µL Tween20, 50 µL 10x TBS, 450 µL dH2O

Running Buffer (1X SDS): 125 mL H_2O, 25 mL 10x SDS

10x SDS: 30.3 g Tris Base, 144 g glycine, 10 g SDS

1x Transfer Buffer: 100 mL 10x TB (50 mL), 200 mL MeOH (100 mL), 700 mL deionized H_2O (350 mL). *Can also add 0.1% SDS

10x Transfer Buffer (500 mL, no SDS or Methanol, pH 8.3): 29.4 g Tris Base (480 mM), 14.64 g Glycine (390 mM)

Standard Lysis Buffer : 25 mM Tris-HCl 7.5, 150 mM NaCl, -1 mM EDTA, 0.5% NP40, 5% glycerol

Radioimmunoprecipitation assay (RIPA) Lysis Buffer: 150 mM NaCl, 50 mM Tris HCl pH 8.0, 0.1% SDS, 0.5% DOC

Choline Transporters

Gut tissue was of primary interest to measure the choline transport proteins and determine if there were reduced levels of the moderate affinity choline transport like (CTL1, *Slc44a1*) or low affinity organic cation transport (OCT1, Slc22a1) proteins. The liver was also of interest, as this is where dietary choline is delivered, metabolized, and distributed throughout the body from. Gut and liver tissue samples were all collected from *Tuba1a-Cre*$^{+}$*;Elp1*$^{Loxp/Loxp}$ mutant and *Tuba1a-Cre*$^{-}$*;Elp1*$^{+/Loxp}$ control mice.

OCT1/Slc22a1

Trial 1 The first antibody tested was OCT1 (Sigma-Aldrich, Millipore, CAT# AV41516), following the standard western blot procedure detailed above to test efficacy of the method with the antibody. The (other buffer) was used for the protein extraction of the tissue, and the OCT1 AB was used in a 1:1,000 dilution. Figure 1 depicts the results of the first western blot; though significant signal was observed for the loading control GAPDH, no signal was observed for the OCT1 protein in the expected region of 61 kDa. It was hypothesized that a more extreme lysis

buffer should be used when extracting protein lysates from tissue samples. The variable intensity of the signals from GAPDH in Figure 1 also indicates inconsistent loading of samples.

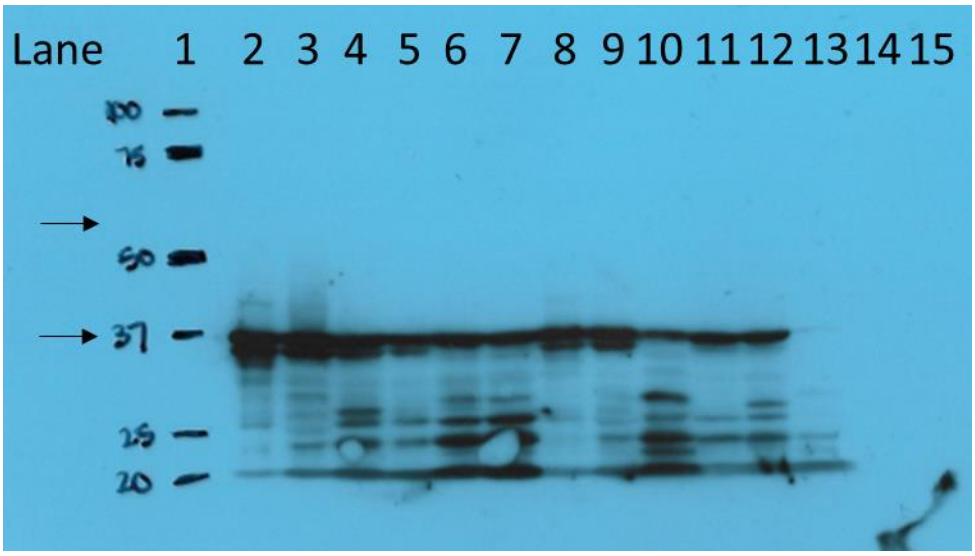


Figure 1. Trial 1 of the OCT1 antibody with an exposure time of ~1 second. Lanes: 1. kDa molecular weight (MW) ladder, 2. Mutant Distal Colon, 3. Mutant Proximal Colon, 4. Mutant Ileum, 5. Mutant Jejunum, 6. Mutant Distal Duodenum, 7. Mutant Proximal Duodenum, 8. Control Distal Colon, 9. Control Proximal Colon, 10. Control Jejunum, 11. Control Ileum, 12. Control Distal Duodenum, 13. Control Proximal Duodenum

Trial 2. The RIPA lysis buffer was used to extract new small and large intestine gut tissue samples collected from a mutant and control. All other methods were kept the same as in Trial 1. Figure 2 A & B depicts the results from trial 2. Given the intensity of the GAPDH signal, the upper region (250-50 kDa) of the blot was exposed separate from the lower region (50-15 kDa). Segments were selectively exposed by covering the segment that was not of interest with tinfoil, thus also preventing any movement of the blot between subsequent exposures.

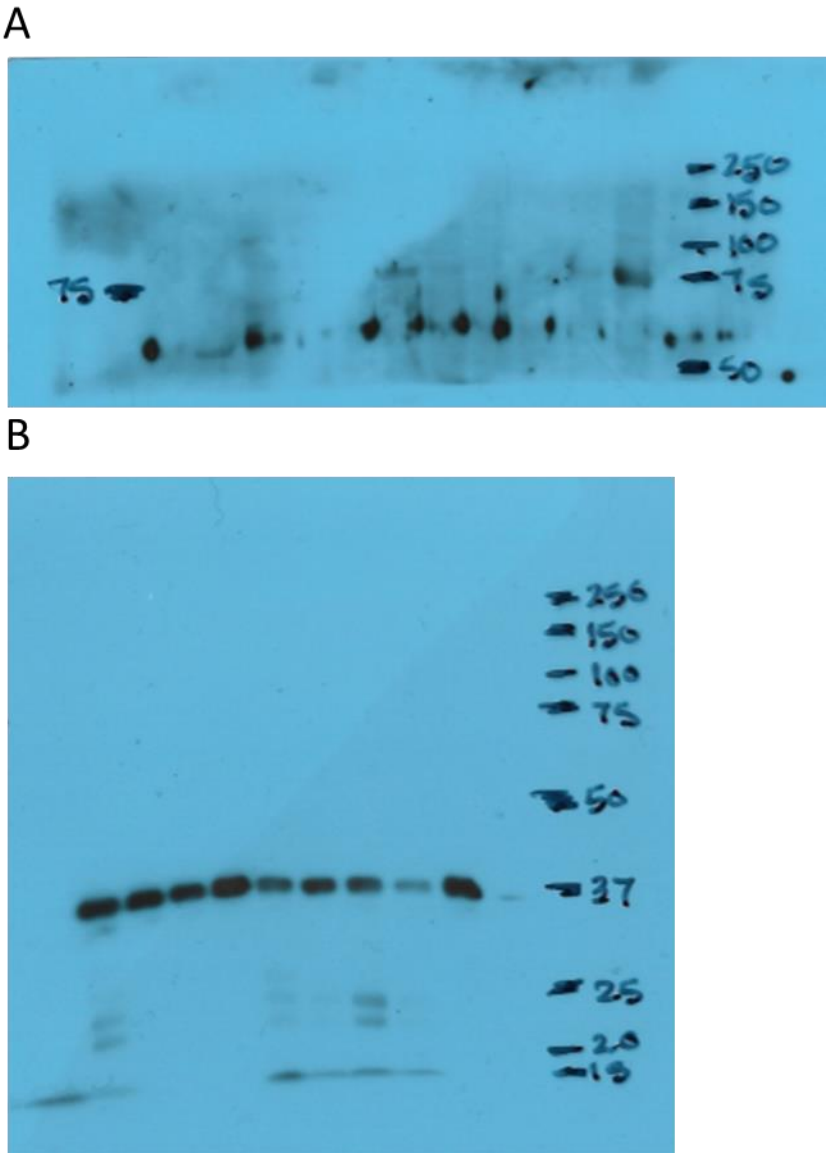


Figure 2. Trial 2 of OCT1 antibody with exposure times of (A) ~45 seconds and (B) < 1 second. Lanes: 3. Mutant Proximal Duodenum, 4. Mutant Distal Duodenum, 5. Mutant Jejunum, 6. Mutant Ileum, 7. Mutant Colon, 8. Control Proximal Duodenum, 9. Control Distal Duodenum, 10. Control Jejunum, 11. Control Ileum, 12. Control Colon, 13. kDa MW ladder.

The exposure of the blot, particularly GAPDH (Figure 2B) revealed the loaded lanes did not run straight, which was due to an error in how the gel was poured. Ample space was not left for the stacking gel and comb, so the gel was essentially comprised of only a separating gel, which likely caused the curvature and unequal travel of the protein through the gel. The

variability of band intensity between the samples for GAPDH also revealed that slightly unequal amounts of protein were loaded for the colon sample of the mutant, and particularly for the jejunum and colon samples from the control.

The upper half of the blot (255-50 kDa) (Figure 2A) did pick up distinct signal around the expected 61 kDa region for the OCT1 protein, though the signals were not distinct uniform bands but instead dots. It was postulated that these dots were a result of protein aggregation, which could potentially be resolved by changing the temperature at which the protein is denatured. Additionally, the upper region of the blot (255-50 kDa) had a lot of background signal, which was extremely apparent upon longer exposure times. It was thought that blocking overnight in Blotto at 4 °C may alleviate the background signal.

Trial 3 The same protein lysates used in trial 2 were used in trial 3, though only mutant and control proximal duodenum samples were used to test the effect of varying temperatures on the denaturing step and ultimately what was believed to be aggregated protein in the region of expected bands. Instead of denaturing the protein at 80 °C for 10 minutes, a range of temperatures with varying times were tested and included: 1) On ice for 1 hour 2) Benchtop room temperature for 1 hour 3) 37 °C for 1 hour 4) 50 °C for 15 minutes 5) 75 °C for 15 minutes and 6) 95 °C for 15 minutes. In addition to the temperature range trial, blocking in 10 mL of Blotto was completed by rocking overnight in Blotto at 4 °C instead of 1 hour at room temperature. The resulting western blot results (Figure 3) did not have the same issues of background signal convoluting the upper region of the blot, but what was believed to be protein aggregates at the 61 kDa region persisted.

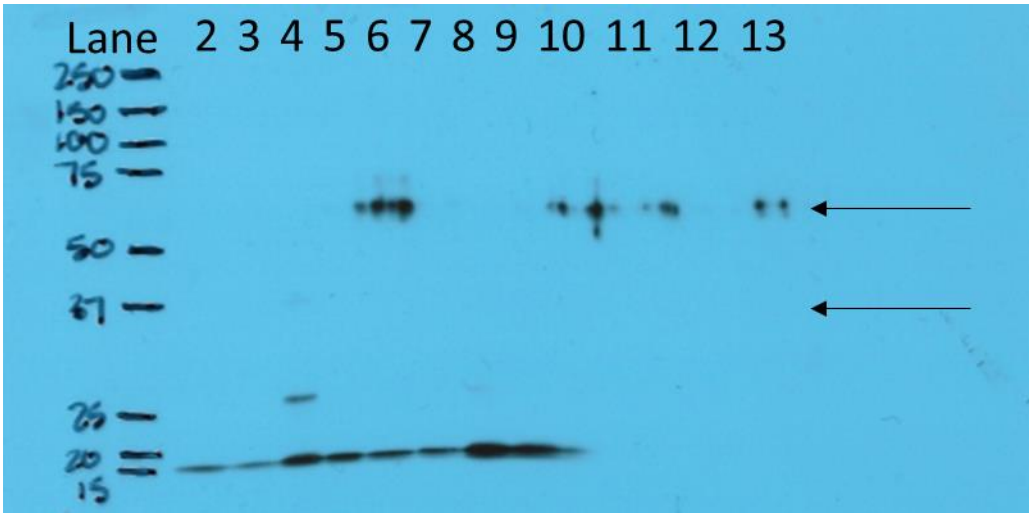


Figure 3. Trial 3 of OCT1 antibody with a 10 second exposure time. Lanes: 1. Protein+ MW ladder 2. M PD Ice >1 hr 3. M PD Room Temp >1 hr 4. M PD 37 °C for 1 hr 5. M PD 50 °C for 15 min 6. M PD 75 °C for 15 min 7. M PD 95 °C for 15 min 8. C PD Ice >1hr 9. C PD Room Temp >1hr 10. C PD 37 °C for 1 hr 11. C PD 50 °C for 15 min 12. C PD 75 °C for 15 min 13. M PD 95 °C for 15 min. Abbreviations: M, mutant; C, control; PD, proximal duodenum. Arrows indicate the 61 kDa region and 37 kDa region where the OCT1 and GAPDH protein bands were expected to be observed.

With the trial 3 bot, presumed protein aggregates were still observed for the anticipated OCT1 61 kDa molecular weight region, though only for some temperatures tested with seemingly varying effects depending on if the proximal duodenum sample was either mutant or control. Lane 6 (mutant PD, 75 °C for 15 min) was the closest signal to representing a distinct band at 61 kDa for all samples and temperature ranges tested. The corresponding control sample treated with the same parameters did not reveal any bands. In addition to the temperature trials being somewhat inconclusive, there was no visible GAPDH registered for any of the samples. The dye front also indicated an unusual pattern in which it appeared that lanes 11-13 did not have any sample loaded at all, though this was not the case.

By reviewing the Genecard for OCT1, it was identified that plasma, liver, and gallbladder contain the highest levels of OCT1 protein. As such, it was determined that a liver sample would perhaps be more suitable for troubleshooting the OCT1 protein.

Trial 4 Concurrently, the CTL1 antibody was also being tested with gut tissue and as such, the CTL1 antibody was the first to be tested using liver samples that were extracted with the modified RIPA, and standard lysis buffers. The same membrane used to test the CTL1 antibody in liver tissue was stripped and re-probed with the OCT1 antibody. Though GAPDH revealed distinct and equal bands, no bands were observed at the 61 kDa molecular weight region. As such, a new membrane was made using the same RIPA and standard lysis buffer extracted liver tissue and probed with the OCT1 antibody solution that had been used up in previous experiments, though it was "spiked" with fresh antibody and BSA to increase the volume of total antibody solution used for incubation. Figure 4 illustrates the results from this western blot.

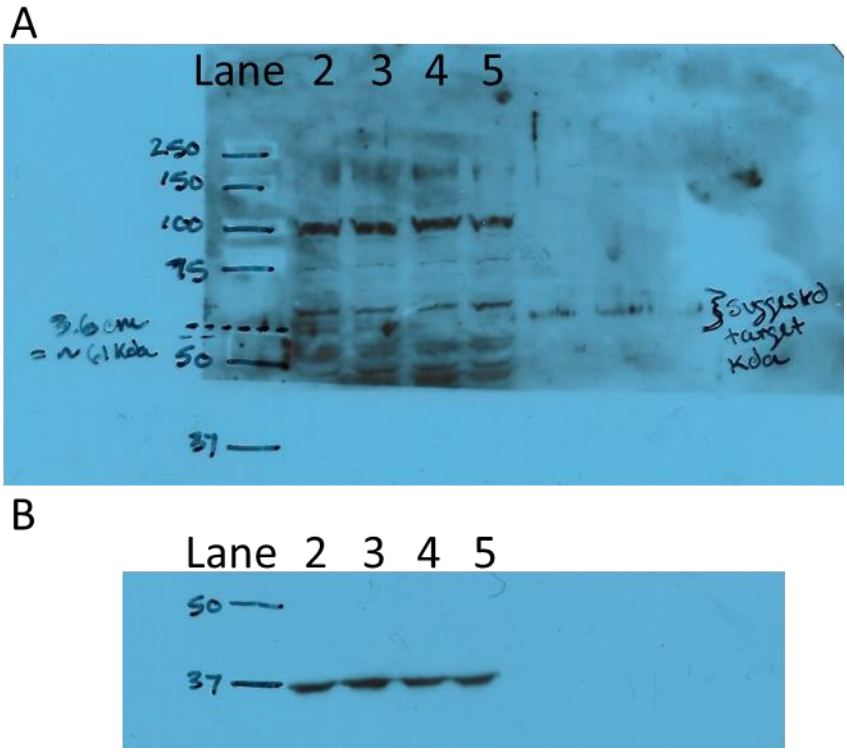


Figure 4. OCT1 western blot for RIPA extracted liver tissue with a (A) 10 minute exposure for OCT1 and (B) a 5 second exposure for GAPDH. Based on the Precision + ladder, the bottom of each MW marker was measured in cm and used to more accurately estimate where the 61 kDa region (dashed line) was located on the blot, and these estimates were annotated on the photopaper. Lanes: 1. Precision + ladder 2. Mutant, RIPA extracted 3. Control, RIPA extracted 4. Mutant, standard lysis buffer extracted and 5. Control, standard lysis buffer extracted.

Distinct bands were observed at the 100 kDa MW region, with additional nonspecific binding throughout each column/well. Thin, though distinct, bands were observed at what was thought to be the expected 61 kDa MW region. Manual measurements of the Precision + ladder in centimeters allowed for a more accurate estimation of where the 61 kDa region was located on the blot, which was measured to be right below the thin distinct bands.

Han *et al.* (2013) [90] used the same OCT1 antibody and tested the binding specificity against human Caco-2 cells, and cross reactivity with mouse Oct1. Chinese hamster ovary cells transfected with human OCT1-3 or mouse mOct1-3, Caco-2 cells, human liver, and mouse liver

and kidneys were used for their westerns blot analysis. Their results demonstrate OCT1 bound to a protein with an apparent molecular mass of ~60 kDa and was equally specific for both human and mouse liver. The full blot and molecular weight protein ladder were not depicted in the results, so it was impossible to determine if nonspecific binding occurred, and this was also not addressed in their paper.

A final trial of OCT1 was conducted once again using mouse liver tissue for a mutant and control to attempt to minimize the nonspecific binding. Three temperatures were tested for the denaturing step (50 °C, 70 °C, 80 °C) as these showed the most promise in trial 3. It was mistakenly identified that the 50 °C temperature had the best results for the mutant PD samples tested in trial 3, and this temperature was used to test the effects of using more protein (100 µg vs 50 µg) in the blot. Additionally, nitrocellulose was used as the membrane instead of PVDF.

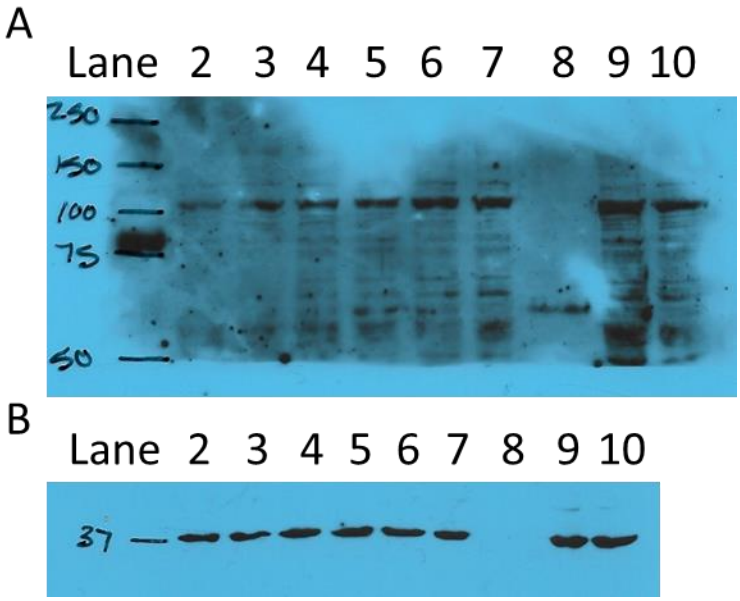


Figure 5. OCT1 western blot for RIPA extracted liver tissue with a (A) 2 minute exposure for OCT1 and (B) a 3 second exposure for GAPDH. Lanes: 1. Precision + Ladder 2. Mutant, 50°, 50 µg protein 3. Mutant, 70°, 50 µg protein 4. Mutant, 80°, 50 µg protein 5. Control, 50°, 50 µg protein 6. Control, 70°, 50 µg protein 7. Control, 80°, 50 µg protein 8. Empty 9. Mutant, RIPA, 50°, 100 µg protein 10. Control, RIPA, 50°, 100 µg protein

Trial 4 revealed a continuation of the nonspecific binding of OCT1 by multiple faint bands being visible in each column/well. Increasing the protein loaded in the wells (Figure 5, lanes 9 and 10) only exasperated this issue. The different temperature treatments appeared to improve the nonspecific binding when denaturing at 50 °C, though it also appeared that less protein was bound with decreasing temperatures tested. GAPDH did not show obvious differences in the amount of protein loaded, though maybe slightly less signal was observed for lanes 2 and 3, which correspond to the 50 °C temperature treatment. The use of a nitrocellulose membrane appeared to have no impact on the nonspecific binding, if not a slightly deleterious effect.

Summary From these experiments conducted to test and troubleshoot the OCT1 antibody in mutant and control mice, gut and liver tissue was used, in conjunction with a variety of modified steps in the western blot procedure. It was concluded that the RIPA lysis buffer should be used for both tissue types otherwise no protein will be obtained in the lysate of gut tissue (Trial 1 vs Trial 2), and the RIPA extraction slightly improves signal when used for liver tissue (Trial 4). The temperature trials concluded that 50-80 °C are all viable for the protein denaturing step. However, Han *et al.* (2013) [1] used 70 °C and achieved good results. The use of a nitrocellulose over PVDF membrane may have marginally worsened the background signal that was observed, though this may have been due to recycling the antibody solution and only supplementing it with fresh BSA and antibody to achieve the volume necessary for blotting. This may have been the most confounding method that was used throughout all the troubleshooting experiments and would likely be the best method to modify in future blots. The antibody solution was recycled due to the expense of purchasing the antibody that is only a very small volume. This technique had been used prior with much success, though perhaps was the most confounding issue throughout the troubleshooting process. The experiments utilizing gut tissue unfortunately led to inconclusive results due to the issue of protein aggregation. The results from the liver tissue western blots indicate distinct binding of the OCT1 antibody to protein in the 100 kDa molecular weight region. Still distinct, though thinner bands were also observed at the expected 61 kDa molecular weight.

Using an antibody against the synthesized oligopeptide of mOCT1, Lee *et al.* (2007) identified bands at ~90 kDa for OCT1 from a western blot of mouse kidney tissue lysates [2]. This is coincidentally very similar to the distinct banding that was observed for the western blots conducted herein on mouse liver tissue lysates. Further troubleshooting to reduce the nonspecific

binding is necessary to definitively determine if OCT1 was reduced in the Talpha liver and gut tissue. If the nonspecific bands that were observed in the liver are valid, these results indicate no difference between mutant and control OCT1 protein levels.

CTL1/Slc44a1

Trial 1 Similar to the OCT1 choline transporter, the CTL1 antibody (EN-627, University of Guelph, Canada) was first tested in gut tissue that was prepped with a RIPA lysis buffer. The antibody was used in a 1:1,000 dilution in BSA, and all parameters of the standard western blot procedure were otherwise followed. As was observed for the OCT1 antibody, a lot of nonspecific binding was also observed for the CTL1 antibody (Figure 6), though only for the distal duodenum, jejunum, and ileum samples from the mutant that corresponded to lanes 5, 6, 7 and 12. Nearly no binding occurring for the proximal duodenum, and colon samples of the mutant, and the proximal and distal duodenum, and jejunum of the control, corresponding to lanes 4 and 8, and 9-12 respectively. The loading control GAPDH revealed comparable levels of protein loaded across samples, though lanes 8-11 may have received slightly less protein. It was interesting to note that the lanes that exhibited nearly no binding on the upper half of the blot (Figure 6A) had many nonspecific bands that were bound in the lower half of the blot (Figure 6B).

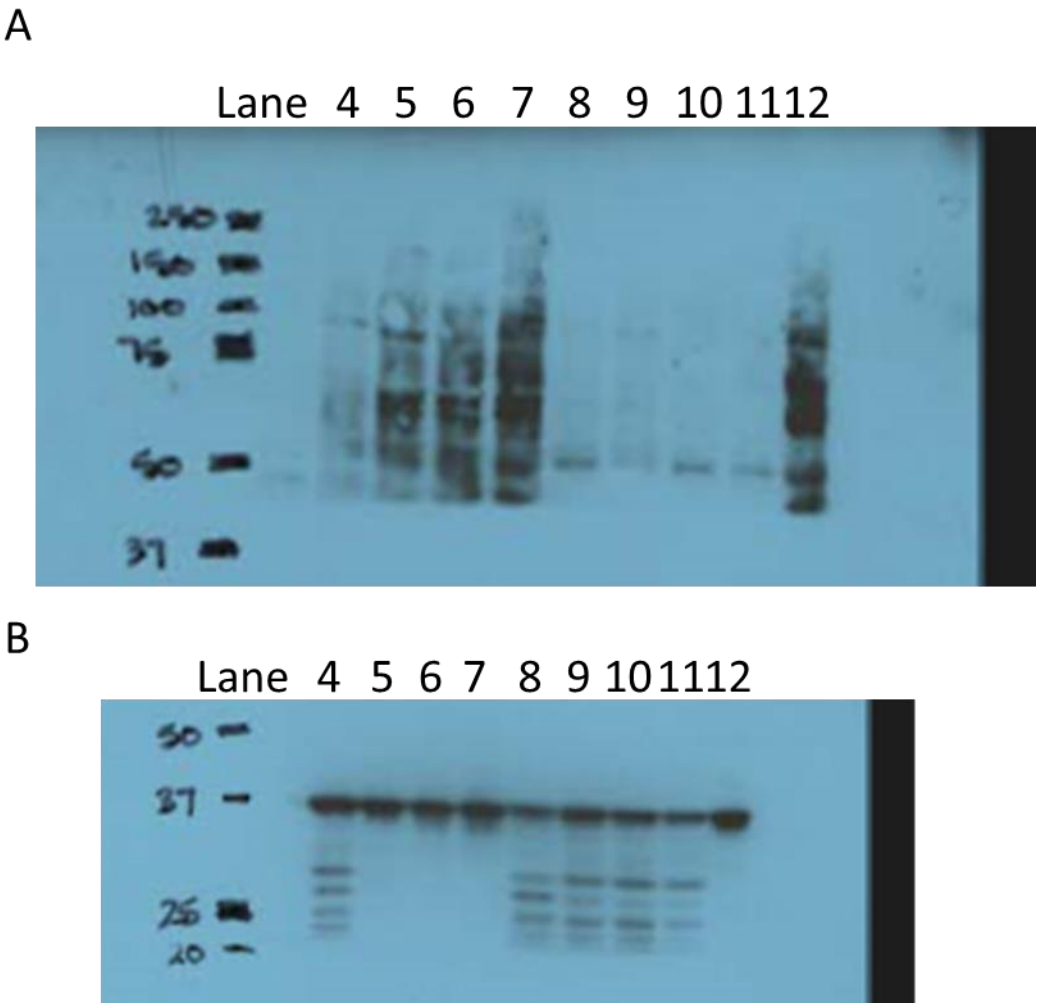


Figure 6. Trial 1 CTL1 western blot for RIPA extracted gut tissue with a (A) ~45 second exposure for CTL1 and (B) a ~15 second exposure for GAPDH. Lanes: 3. Precision + ladder 4. PD, Mutant 5. Distal Duodenum, Mutant 6. Jejunum, Mutant 7. Ileum, Mutant 8. Colon, Mutant 9. PD, Control 10. Distal Duodenum, Control 11. Jejunum, Control 12. Ileum, Control 13. Colon, Control

Trial 2 Following the western blot of gut tissue, the CTL1 antibody was tested against liver tissue that was prepped with RIPA or standard lysis buffers. It was believed that liver would serve as a simpler tissue to extract, and perhaps have more abundant CTL1 transporter protein than gut tissue.

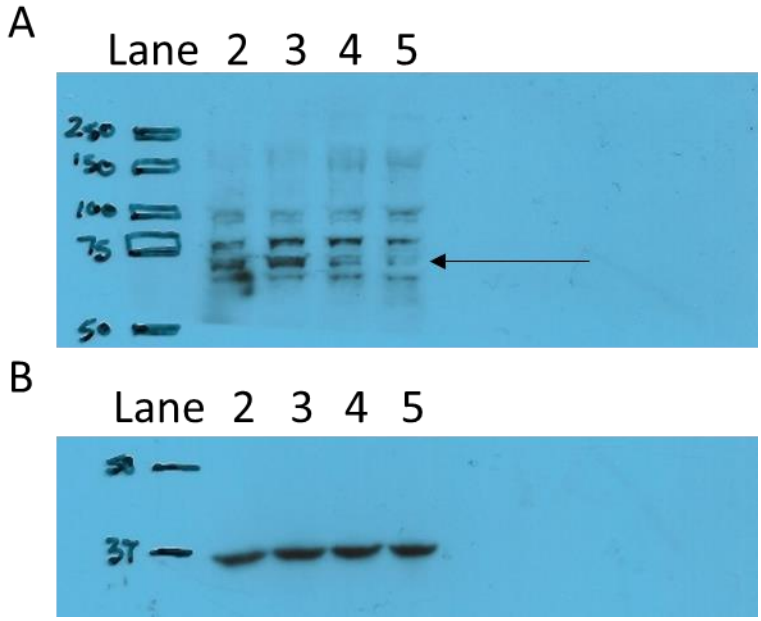


Figure 7. Trial 2 CTL1 western blot for RIPA extracted liver tissue with a (A) 2 minute exposure for CTL1 and (B) a ~1 second exposure for GAPDH. Lanes: 1. Precision + ladder 2. Mutant, RIPA extracted 3. Control, RIPA extracted 4. Mutant, standard extracted 5. Control, standard extracted. The arrow indicates the approximate 72 kDa region where bands were expected.

The liver western blot testing the CTL1 antibody indicated that RIPA lysis buffer was more effective than standard lysis buffer at extracting what was believed to be the CTL1 protein, along with similar molecular weight proteins that were also bound by the primary antibody. Based on visual assessment of lanes 1 and 2 of Figure 7A, the mutant bands were slightly less opaque than those of the control, while the GAPDH loading control was comparable. Though this blot was fairly successful, the nonspecific binding limited relative quantitation of signal intensity, and thus required further troubleshooting.

Trial 3 The CTL1 antibody was gifted from Dr. Marica Bakovic's lab at the University of Guelph, Canada, and the dissertation written by Dr. Vera Michel details the characterization of the antibody used in this work, and summary of methods developed for use of the antibody in a

western blot [3]. It was concluded that the antibody could be used with denaturing and native, non-denaturing conditions, and observe a 72 kDa band under both conditions. However, native conditions were recommended as these parameters prevented any denaturation or degradation of the target protein. Denaturing conditions also appeared to give rise to nonspecific binding of a band just above the target 72 kDa region of the blot. As such, a native page was attempted with the materials on hand and led to inconclusive results. Given the setup available, results seemed more promising when using denaturing conditions.

Trial 4 In conjunction with testing the TAUT antibody, the CTL1 antibody was also tested in retina tissue from control mice for efficacy. Continuing the trend, a lot of nonspecific binding was observed throughout each lane of the western blot, with no individually distinguishable bands observed at 72 kDa. Subsequently, various combinations of long (10 min x 2, 15 min x 2) and short washes (5 min x 6), in conjunction with overnight blotting, revealed much success in the CTL1 blot that was accomplished by extracting retinal tissue with the standard lysis buffer, blocked overnight at 4 °C in BSA, and washed with the long wash combos (Figure 8A). Subsequently, this method was used to test protein concentrations ranging from 50 – 10 ug of protein loaded per well as a means to minimize the GAPDH signal, while maximizing the CTL1 signal. It was determined that 30 ug protein per well was optimal (Figure 8B). From these promising results with retinal tissue lysates, the previous RIPA extracted gut and liver tissue were tested again using the modified parameters of 30 ug/well protein, overnight blocking in BSA, and long washes. Unfortunately, the blot resulting in much nonspecific binding yet again, and unclear results regarding the levels of CTL1 protein in gut and liver tissue.

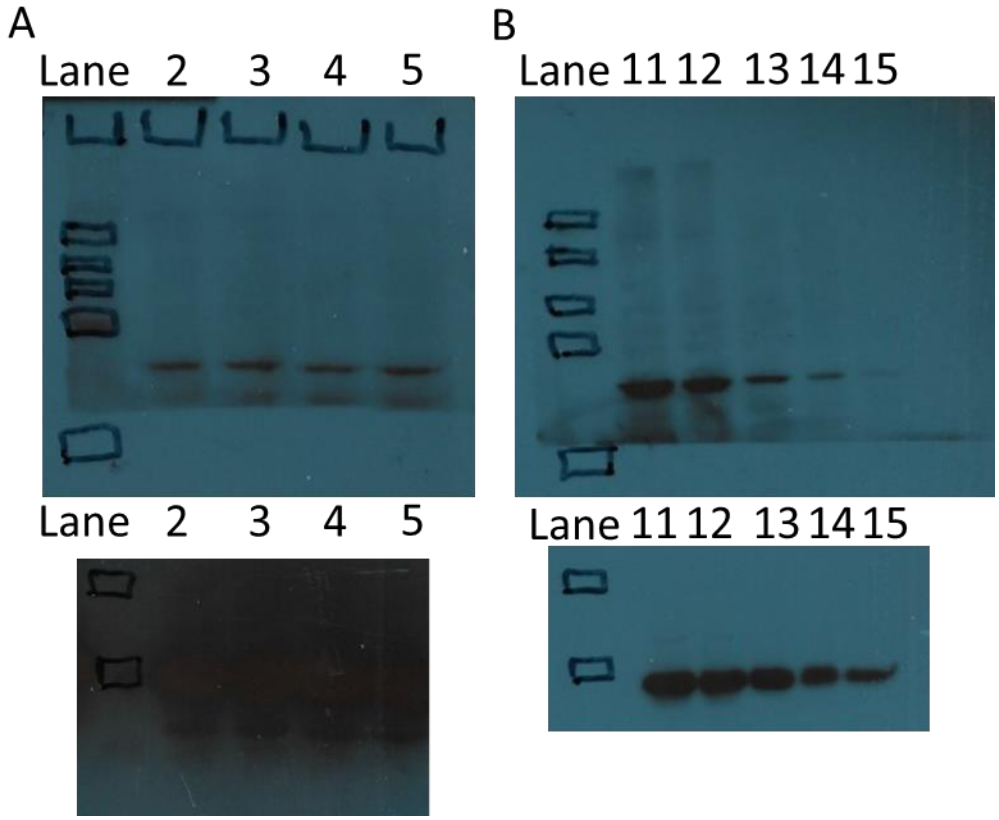


Figure 8. Trial 4 CTL1 western blot for standard extracted retina tissue with a (A) 10 second exposure for CTL1 (upper) and ~1 second exposure for GAPDH (lower) and (B) 1 minute exposure for CTL1 (upper) and ~1 second exposure for GAPDH (lower). (A) Lanes: 1. Precision + ladder 2-5. standard extracted retina tissue. (B) Lanes: 10. Precision + ladder 11. CTL1 50 µg protein 12. CTLW1 40 µg protein 13. CTL1 30 µg protein 14. CTL1 20 µg protein 15. CTL1 10 µg protein.

Summary When testing the CTL1 antibody against both gut and liver tissue samples, distinct bands at the expected 72 kDa molecular weight region are observed, though these are accompanied by nonspecific binding. Gut tissue had much more nonspecific binding (Figure 6) than liver tissue (Figure 7), though both made it difficult to conclude if the protein of interest was bound, and if levels of the protein were reduced in the mutant sample compared to the control. The western blot method recommended from these trials is to use a RIPA lysis buffer and to perform the blot under denaturing conditions. If new reagents and resources were available to

perform a native, non-denaturing western blot, this may be a more viable method to reduce nonspecific binding and achieve good results, as suggested in the original characterization of the antibody [3]. Though, the antibody has been successfully used under denaturing conditions. The difference between those results and mine was that Blotto was used instead of BSA to apply and incubate the CTL1 antibody. This presents as a promising next step, if this western blot were to be attempted again.

Though convoluted by the nonspecific binding, the CTL1 protein may have been reduced in the mutant liver tissue tested compared to the control liver tissue. It was indiscernible if the protein was reduced in the mutant gut tissue. Testing retinal lysates with the CTL1 antibody seems promising though.

References

1. Han, T. (Kevin); Everett, R.S.; Proctor, W.R.; Ng, C.M.; Costales, C.L.; Brouwer, K.L.R.; Thakker, D.R. Organic Cation Transporter 1 (OCT1/mOct1) Is Localized in the Apical Membrane of Caco-2 Cell Monolayers and Enterocytes. *Mol. Pharmacol.* **2013**, *84*, 182–189, doi:10.1124/mol.112.084517.

2. Lee, W.K.; Hwang, J.-S.; Yun, C.-H.; Cha, S.H. Identification of a Kidney-Specific Mouse Organic Cation Transporter like-1 (mOCTL1). *Exp. Mol. Med.* **2007**, *39*, 787–795, doi:10.1038/emm.2007.85.

3. Michel, V.H. Expression, Subcellular Localization and Function of the Solute Carrier 44A1 (SLC44A1), University of Guelph, 2009.

REFERENCES CITED

Abashidze, A., Gold, V., Anavi, Y., Greenspan, H., & Weil, M. (2014). Involvement of IKAP in Peripheral Target Innervation and in Specific JNK and NGF Signaling in Developing PNS Neurons. *PLoS ONE*, *9*(11), e113428. https://doi.org/10.1371/journal.pone.0113428

Adams, J. B., Johansen, L. J., Powell, L. D., Quig, D., & Rubin, R. A. (2011). Gastrointestinal flora and gastrointestinal status in children with autism – comparisons to typical children and correlation with autism severity. *BMC Gastroenterology*, *11*(1), 22. https://doi.org/10.1186/1471-230X-11-22

Addis, L., Ahn, J. W., Dobson, R., Dixit, A., Ogilvie, C. M., Pinto, D., Vaags, A. K., Coon, H., Chaste, P., Wilson, S., Parr, J. R., Andrieux, J., Lenne, B., Tumer, Z., Leuzzi, V., Aubell, K., Koillinen, H., Curran, S., Marshall, C. R., … Pal, D. K. (2015). Microdeletions of ELP4 Are Associated with Language Impairment, Autism Spectrum Disorder, and Mental Retardation. *Human Mutation*, *36*(9), 842–850. https://doi.org/10.1002/humu.22816

Adler, D., Kelly, S. T., Elliott, T. M., & Adamson, J. (2020). *Vioplot: Violin plot v. R package*. CRAN. https://github.com/TomKellyGenetics/vioplot

Ajiro, M., Awaya, T., Kim, Y. J., Iida, K., Denawa, M., Tanaka, N., Kurosawa, R., Matsushima, S., Shibata, S., Sakamoto, T., Studer, L., Krainer, A. R., & Hagiwara, M. (2021). Therapeutic manipulation of IKBKAP mis-splicing with a small molecule to cure familial dysautonomia. *Nature Communications*, *12*, 4507. https://doi.org/10.1038/s41467-021-24705-5

Albright, C. D., Costa, K.-A. da, Craciunescu, C. N., Klem, E., Mar, M.-H., & Zeisel, S. H. (2005). Regulation of Choline Deficiency Apoptosis by Epidermal Growth Factor in CWSV-1 Rat Hepatocytes. *Cellular Physiology and Biochemistry : International Journal of Experimental Cellular Physiology, Biochemistry, and Pharmacology*, *15*(1–4), 59–68. https://doi.org/10.1159/000083653

Allman, B., Biwer, A., Maitland, C. G., DiFabio, B., Coughlin, E., Smith-Ryan, A. E., & Ormsbee, M. (2018). The effect of short term beta alanine supplementation on physical performance and quality of life in parkinson's disease: A pilot study. *Journal of Exercise Physiology Online*, *21*, 1–13.

Anderson, M. V. (2006). Evidenced Based Elimination Diet Restricting Dairy and Tyramine Foods for Familial Dysautonomia (FD) or Riley-Day Syndrome. *Journal of the American Dietetic Association*, *106*(8), A15. https://doi.org/10.1016/j.jada.2006.05.042

Anderson, S. L., Coli, R., Daly, I. W., Kichula, E. A., Rork, M. J., Volpi, S. A., Ekstein, J., & Rubin, B. Y. (2001). Familial Dysautonomia Is Caused by Mutations of the IKAP Gene. *American Journal of Human Genetics*, *68*(3), 753–758.

Anderson, S. L., & Rubin, B. Y. (2005). Tocotrienols reverse IKAP and monoamine oxidase deficiencies in familial dysautonomia. *Biochemical and Biophysical Research Communications*, *336*(1), 150–156. https://doi.org/10.1016/j.bbrc.2005.08.054

Angelis, M. D., Piccolo, M., Vannini, L., Siragusa, S., Giacomo, A. D., Serrazzanetti, D. I., Cristofori, F., Guerzoni, M. E., Gobbetti, M., & Francavilla, R. (2013). Fecal Microbiota and Metabolome of Children with Autism and Pervasive Developmental Disorder Not Otherwise Specified. *PLOS ONE*, *8*(10), e76993. https://doi.org/10.1371/journal.pone.0076993

Ansar, M., Ranza, E., Shetty, M., Paracha, S. A., Azam, M., Kern, I., Iwaszkiewicz, J., Farooq, O., Pournaras, C. J., Malcles, A., Kecik, M., Rivolta, C., Muzaffar, W., Qurban, A., Ali, L., Aggoun, Y., Santoni, F. A., Makrythanasis, P., Ahmed, J., … Antonarakis, S. E. (2020). Taurine treatment of retinal degeneration and cardiomyopathy in a consanguineous family with SLC6A6 taurine transporter deficiency. *Human Molecular Genetics*, *29*(4), 618–623. https://doi.org/10.1093/hmg/ddz303

Antonio, N., Andrea, T., Claudio, T., Beatrice, P., Pamela, C., Chiara, M., Gian, L. de' A., Francesco, D. M., & Tiziana, M. (2018). Digestive disorders and Intestinal microbiota. *Acta Bio Medica : Atenei Parmensis*, *89*(Suppl 9), 47–51. https://doi.org/10.23750/abm.v89i9-S.7912

Arias, N., Arboleya, S., Allison, J., Kaliszewska, A., Higarza, S. G., Gueimonde, M., & Arias, J. L. (2020). The Relationship between Choline Bioavailability from Diet, Intestinal Microbiota Composition, and Its Modulation of Human Diseases. *Nutrients*, *12*(8), Article 8. https://doi.org/10.3390/nu12082340

Ariel, I., & Wells, T. R. (1985). Structural abnormalities of the myenteric (Auerbach's) plexus in familial dysautonomia (Riley-Day syndrome) as demonstrated by flat-mount preparation of the esophagus and stomach. *Pediatric Pathology*, *4*(1–2), 89–98. https://doi.org/10.3109/15513818509025906

Armstrong, C. W., McGregor, N. R., Lewis, D. P., Butt, H. L., & Gooley, P. R. (2016). The association of fecal microbiota and fecal, blood serum and urine metabolites in myalgic encephalomyelitis/chronic fatigue syndrome. *Metabolomics*, *13*(1), 8. https://doi.org/10.1007/s11306-016-1145-z

Awwad, H. M., Geisel, J., & Obeid, R. (2016). Determination of trimethylamine, trimethylamine N-oxide, and taurine in human plasma and urine by UHPLC–MS/MS technique. *Journal of Chromatography B*, *1038*, 12–18. https://doi.org/10.1016/j.jchromb.2016.10.017

Axelrod, F. B., Liebes, L., Gold-von Simson, G., Mendoza, S., Mull, J., Leyne, M., Norcliffe-Kaufmann, L., Kaufmann, H., & Slaugenhaupt, S. A. (2011). Kinetin Improves IKBKAP mRNA Splicing in Patients With Familial Dysautonomia. *Pediatric Research*, *70*(5), 480–483. https://doi.org/10.1203/PDR.0b013e31822e1825

Bar Aluma, B.-E., Norcliffe-Kaufmann, L., Sarouk, I., Dagan, A., Ashkenazi, M., Bezalel, Y., Vilozni, D., Lahad, A., & Efrati, O. (2019). Resting Energy Expenditure in Patients With Familial Dysautonomia: A Preliminary Study. *Journal of Pediatric Gastroenterology and Nutrition*, *68*(3), 422. https://doi.org/10.1097/MPG.0000000000002180

Bar-Shai, A., Maayan, C., Vromen, A., Udassin, R., Nissan, A., Freund, H. R., & Hanani, M. (2004). Decreased density of ganglia and neurons in the myenteric plexus of familial dysautonomia patients. *Journal of the Neurological Sciences*, *220*(1), 89–94. https://doi.org/10.1016/j.jns.2004.02.017

Bates, D., Mächler, M., Bolker, B., & Walker, S. (2015). Fitting Linear Mixed-Effects Models Using **lme4**. *Journal of Statistical Software*, *67*(1). https://doi.org/10.18637/jss.v067.i01

Bauer, F., & Hermand, D. (2012). A coordinated codon-dependent regulation of translation by Elongator. *Cell Cycle*, *11*(24), 4524–4529. https://doi.org/10.4161/cc.22689

Baxter, N. T., Ruffin, M. T., Rogers, M. A. M., & Schloss, P. D. (2016). Microbiota-based model improves the sensitivity of fecal immunochemical test for detecting colonic lesions. *Genome Medicine*, *8*, 37. https://doi.org/10.1186/s13073-016-0290-3

Bento-Abreu, A., Jager, G., Swinnen, B., Rué, L., Hendrickx, S., Jones, A., Staats, K. A., Taes, I., Eykens, C., Nonneman, A., Nuyts, R., Timmers, M., Silva, L., Chariot, A., Nguyen, L., Ravits, J., Lemmens, R., Cabooter, D., Van Den Bosch, L., … Robberecht, W. (2018). Elongator subunit 3 (ELP3) modifies ALS through tRNA modification. *Human Molecular Genetics*, *27*(7), 1276–1289. https://doi.org/10.1093/hmg/ddy043

Berg, R. A. van den, Hoefsloot, H. C., Westerhuis, J. A., Smilde, A. K., & Werf, M. J. van der. (2006). Centering, scaling, and transformations: Improving the biological information content of metabolomics data. *BMC Genomics*, *7*, 142. https://doi.org/10.1186/1471-2164-7-142

Best, J. G., Stagg, C. J., & Dennis, A. (2014). Other Significant Metabolites. In *Magnetic Resonance Spectroscopy* (pp. 122–138). Elsevier. https://doi.org/10.1016/B978-0-12-401688-0.00010-0

Bicknell, B., Liebert, A., McLachlan, C. S., & Kiat, H. (2022). Microbiome Changes in Humans with Parkinson's Disease after Photobiomodulation Therapy: A Retrospective Study. *Journal of Personalized Medicine*, *12*(1), 49. https://doi.org/10.3390/jpm12010049

Blumenfeld, A., Slaugenhaupt, S. A., Liebert, C. B., Temper, V., Maayan, C., Gill, S., Lucente, D. E., Idelson, M., MacCormack, K., Monahan, M. A., Mull, J., Leyne, M., Mendillo, M., Schiripo, T., Mishori, E., Breakefield, X., Axelrod, F. B., & Gusella, J. F. (1999). Precise genetic mapping and haplotype analysis of the familial dysautonomia gene on human chromosome 9q31. *American Journal of Human Genetics*, *64*(4), 1110–1118.

Blusztajn, J. K., Liscovitch, M., & Richardson, U. I. (1987). Synthesis of acetylcholine from choline derived from phosphatidylcholine in a human neuronal cell line. *Proceedings of the National Academy of Sciences of the United States of America*, *84*(15), 5474–5477.

Bo, T.-B., Zhang, X.-Y., Kohl, K. D., Wen, J., Tian, S.-J., & Wang, D.-H. (2020). Coprophagy prevention alters microbiome, metabolism, neurochemistry, and cognitive behavior in a small mammal. *The ISME Journal*, *14*(10), 2625–2645. https://doi.org/10.1038/s41396-020-0711-6

Bonelli, R., Woods, S. M., Lockwood, S., Bishop, P. N., Khan, K. N., Bahlo, M., Ansell, B. R. E., & Fruttiger, M. (2023). Spatial distribution of metabolites in the retina and its relevance to studies of metabolic retinal disorders. *Metabolomics*, *19*(2), 10. https://doi.org/10.1007/s11306-022-01969-6

Bourriaud, C., Robins, R. j., Martin, L., Kozlowski, F., Tenailleau, E., Cherbut, C., & Michel, C. (2005). Lactate is mainly fermented to butyrate by human intestinal microfloras but inter-individual variation is evident. *Journal of Applied Microbiology*, *99*(1), 201–212. https://doi.org/10.1111/j.1365-2672.2005.02605.x

Burns, C., & Kidron, A. (2022). Biochemistry, Tyramine. In *StatPearls*. StatPearls Publishing. http://www.ncbi.nlm.nih.gov/books/NBK563197/

Cameron, B., Lehrmann, E., Chih, T., Walters, J., Buksch, R., Snyder, S., Goffena, J., Lefcort, F., Becker, K. G., & George, L. (2021). Loss of Elp1 perturbs histone H2A.Z and the Notch signaling pathway. *Biology Open*, *10*(9), bio058979. https://doi.org/10.1242/bio.058979

Cani, P. D., Van Hul, M., Lefort, C., Depommier, C., Rastelli, M., & Everard, A. (2019). Microbial regulation of organismal energy homeostasis. *Nature Metabolism*, *1*(1), 34–46. https://doi.org/10.1038/s42255-018-0017-4

Carmi, S., Hui, K. Y., Kochav, E., Liu, X., Xue, J., Grady, F., Guha, S., Upadhyay, K., Ben-Avraham, D., Mukherjee, S., Bowen, B. M., Thomas, T., Vijai, J., Cruts, M., Froyen, G., Lambrechts, D., Plaisance, S., Van Broeckhoven, C., Van Damme, P., … Pe'er, I. (2014). Sequencing an Ashkenazi reference panel supports population-targeted personal genomics and illuminates Jewish and European origins. *Nature Communications*, *5*, 4835. https://doi.org/10.1038/ncomms5835

Castelli, V., Paladini, A., d'Angelo, M., Allegretti, M., Mantelli, F., Brandolini, L., Cocchiaro, P., Cimini, A., & Varrassi, G. (2021). Taurine and oxidative stress in retinal health and disease. *CNS Neuroscience & Therapeutics*, *27*(4), 403–412. https://doi.org/10.1111/cns.13610

Chaverra, M., George, L., Mergy, M., Waller, H., Kujawa, K., Murnion, C., Sharples, E., Thorne, J., Podgajny, N., Grindeland, A., Ueki, Y., Eiger, S., Cusick, C., Babcock, A. M., Carlson, G. A., & Lefcort, F. (2017). The familial dysautonomia disease gene IKBKAP is required in the developing and adult mouse central nervous system. *Disease Models & Mechanisms*, *10*(5), 605–618. https://doi.org/10.1242/dmm.028258

Cheishvili, D., Maayan, C., Smith, Y., Ast, G., & Razin, A. (2007). IKAP/hELP1 deficiency in the cerebrum of familial dysautonomia patients results in down regulation of genes involved in oligodendrocyte differentiation and in myelination. *Human Molecular Genetics*, *16*(17), 2097–2104. https://doi.org/10.1093/hmg/ddm157

Chekuri, A., Logan, E. M., Krauson, A. J., Salani, M., Ackerman, S., Kirchner, E. G., Bolduc, J. M., Wang, X., Dietrich, P., Dragatsis, I., Vandenberghe, L. H., Slaugenhaupt, S. A., & Morini, E. (2022). Selective retinal ganglion cell loss and optic neuropathy in a humanized mouse model of familial dysautonomia. *Human Molecular Genetics*, *31*(11), 1776–1787. https://doi.org/10.1093/hmg/ddab359

Chen, C., Turnbull, D. M., & Reeve, A. K. (2019). Mitochondrial Dysfunction in Parkinson's Disease—Cause or Consequence? *Biology*, *8*(2), 38. https://doi.org/10.3390/biology8020038

Chen, Y., Zizmare, L., Calbiague, V., Yu, S., Herberg, F. W., Schmachtenberg, O., Paquet-Durand, F., & Trautwein, C. (2022). *Retinal energy metabolism: Photoreceptors switch between Cori, Cahill, and mini-Krebs cycles to uncouple glycolysis from mitochondrial respiration* (p. 2022.06.20.496788). bioRxiv. https://doi.org/10.1101/2022.06.20.496788

Chen, Y.-T., Hims, M. M., Shetty, R. S., Mull, J., Liu, L., Leyne, M., & Slaugenhaupt, S. A. (2009). Loss of Mouse Ikbkap, a Subunit of Elongator, Leads to Transcriptional Deficits and Embryonic Lethality That Can Be Rescued by Human IKBKAP. *Molecular and Cellular Biology*, *29*(3), 736–744. https://doi.org/10.1128/MCB.01313-08

Cheney, A. M., Costello, S. M., Pinkham, N. V., Waldum, A., Broadaway, S. C., Cotrina-Vidal, M., Mergy, M., Tripet, B., Kominsky, D. J., Grifka-Walk, H. M., Kaufmann, H., Norcliffe-Kaufmann, L., Peach, J. T., Bothner, B., Lefcort, F., Copié, V., & Walk, S. T. (2023). Gut microbiome dysbiosis drives metabolic dysfunction in Familial dysautonomia. *Nature Communications*, *14*, 218. https://doi.org/10.1038/s41467-023-35787-8

Cheng, W. W.-C., Tang, C. S.-M., Gui, H.-S., So, M.-T., Lui, V. C.-H., Tam, P. K.-H., & Garcia-Barcelo, M.-M. (2015). Depletion of the IKBKAP ortholog in zebrafish leads to hirschsprung disease-like phenotype. *World Journal of Gastroenterology : WJG*, *21*(7), 2040–2046. https://doi.org/10.3748/wjg.v21.i7.2040

Chiang, J. Y. L., & Ferrell, J. M. (2018). Bile Acid Metabolism in Liver Pathobiology. *Gene Expression*, *18*(2), 71–87. https://doi.org/10.3727/105221618X15156018385515

Chiu, C.-Y., Cheng, M.-L., Chiang, M.-H., Kuo, Y.-L., Tsai, M.-H., Chiu, C.-C., & Lin, G. (2019). Gut microbial-derived butyrate is inversely associated with IgE responses to allergens in childhood asthma. *Pediatric Allergy and Immunology*, *30*(7), 689–697. https://doi.org/10.1111/pai.13096

Chong, J., Soufan, O., Li, C., Caraus, I., Li, S., Bourque, G., Wishart, D. S., & Xia, J. (2018). MetaboAnalyst 4.0: Towards more transparent and integrative metabolomics analysis. *Nucleic Acids Research*, *46*(Web Server issue), W486–W494. https://doi.org/10.1093/nar/gky310

Costello, S. M., Cheney, A. M., Waldum, A., Tripet, B., Cotrina-Vidal, M., Kaufmann, H., Norcliffe-Kaufmann, L., Lefcort, F., & Copié, V. (2023). A Comprehensive NMR Analysis of Serum and Fecal Metabolites in Familial Dysautonomia Patients Reveals Significant Metabolic Perturbations. *Metabolites*, *13*(3), 433. https://doi.org/10.3390/metabo13030433

Cotrina, M. L., Morgenstein, B., Perez, M., Norcliffe-Kaufmann, L., Palma, J.-A., & Kaufmann, H. (2023). Height, weight, and body mass index in patients with familial dysautonomia. *PLOS ONE*, *18*(11), e0293800. https://doi.org/10.1371/journal.pone.0293800

Country, M. W. (2017). Retinal metabolism: A comparative look at energetics in the retina. *Brain Research*, *1672*, 50–57. https://doi.org/10.1016/j.brainres.2017.07.025

Cuajungco, M. P., Leyne, M., Mull, J., Gill, S. P., Lu, W., Zagzag, D., Axelrod, F. B., Maayan, C., Gusella, J. F., & Slaugenhaupt, S. A. (2003). Tissue-Specific Reduction in Splicing Efficiency of IKBKAP Due to the Major Mutation Associated with Familial Dysautonomia. *American Journal of Human Genetics*, *72*(3), 749–758.

Culbertson, J. Y., Kreider, R. B., Greenwood, M., & Cooke, M. (2010). Effects of Beta-Alanine on Muscle Carnosine and Exercise Performance: A Review of the Current Literature. *Nutrients*, *2*(1), 75–98. https://doi.org/10.3390/nu2010075

Dalwadi, U., & Yip, C. K. (2018). Structural insights into the function of Elongator. *Cellular and Molecular Life Sciences*, *75*(9), 1613–1622. https://doi.org/10.1007/s00018-018-2747-6

Dammer, E. B., Göttle, M., Duong, D. M., Hanfelt, J., Seyfried, N. T., & Jinnah, H. A. (2015). Consequences of impaired purine recycling on the proteome in a cellular model of Lesch–Nyhan disease. *Molecular Genetics and Metabolism*, *114*(4), 570–579. https://doi.org/10.1016/j.ymgme.2015.02.007

Daruich, A., Picard, E., Boatright, J. H., & Behar-Cohen, F. (2019). Review: The bile acids urso- and tauroursodeoxycholic acid as neuroprotective therapies in retinal disease. *Molecular Vision*, *25*, 610–624.

Dauden, M. I., Kosinski, J., Kolaj-Robin, O., Desfosses, A., Ori, A., Faux, C., Hoffmann, N. A., Onuma, O. F., Breunig, K. D., Beck, M., Sachse, C., Séraphin, B., Glatt, S., & Müller, C. W. (2017). Architecture of the yeast Elongator complex. *EMBO Reports*, *18*(2), 264–279. https://doi.org/10.15252/embr.201643353

Deda, O., Gika, H. G., & Theodoridis, G. A. (2018). Rat Fecal Metabolomics-Based Analysis. In G. A. Theodoridis, H. G. Gika, & I. D. Wilson (Eds.), *Metabolic Profiling: Methods and Protocols* (pp. 149–157). Springer. https://doi.org/10.1007/978-1-4939-7643-0_10

Deda, O., Gika, H. G., Wilson, I. D., & Theodoridis, G. A. (2015). An overview of fecal sample preparation for global metabolic profiling. *Journal of Pharmaceutical and Biomedical Analysis*, *113*, 137–150. https://doi.org/10.1016/j.jpba.2015.02.006

den Besten, G., van Eunen, K., Groen, A. K., Venema, K., Reijngoud, D.-J., & Bakker, B. M. (2013). The role of short-chain fatty acids in the interplay between diet, gut microbiota, and host energy metabolism. *Journal of Lipid Research*, *54*(9), 2325–2340. https://doi.org/10.1194/jlr.R036012

Dietrich, P., & Dragatsis, I. (2016). Familial Dysautonomia: Mechanisms and Models. *Genetics and Molecular Biology*, *39*(4), 497–514. https://doi.org/10.1590/1678-4685-GMB-2015-0335

Dietrich, P., Yue, J., E., S., & Dragatsis, I. (2011). Deletion of Exon 20 of the Familial Dysautonomia Gene Ikbkap in Mice Causes Developmental Delay, Cardiovascular Defects, and Early Embryonic Lethality. *PLoS ONE*, *6*(10), e27015. https://doi.org/10.1371/journal.pone.0027015

Durbin, B. P., Hardin, J. S., Hawkins, D. M., & Rocke, D. M. (2002). A variance-stabilizing transformation for gene-expression microarray data. *Bioinformatics*, *18*(SUPPL. 1), 105–110. https://doi.org/10.1093/bioinformatics/18.suppl_1.S105

Eaton, K. K., Howard, M., & Mphil, A. H. (1994). Urinary Beta-Alanine Excretion Is a Marker of Abnormal as well as Normal Gut Fermentation. *Journal of Nutritional Medicine*, *4*(2), 157–163. https://doi.org/10.3109/13590849409034551

Edgar, R. C., Haas, B. J., Clemente, J. C., Quince, C., & Knight, R. (2011). UCHIME improves sensitivity and speed of chimera detection. *Bioinformatics*, *27*(16), 2194–2200. https://doi.org/10.1093/bioinformatics/btr381

Eley, H. L., Russell, S. T., & Tisdale, M. J. (2007). Effect of branched-chain amino acids on muscle atrophy in cancer cachexia. *The Biochemical Journal*, *407*(Pt 1), 113–120. https://doi.org/10.1042/BJ20070651

Emwas, A.-H., Roy, R., McKay, R. T., Tenori, L., Saccenti, E., Gowda, G. A. N., Raftery, D., Alahmari, F., Jaremko, L., Jaremko, M., & Wishart, D. S. (2019). NMR Spectroscopy for Metabolomics Research. *Metabolites*, *9*(7), Article 7. https://doi.org/10.3390/metabo9070123

Evans, J., & Cushman, S. (2009). Gradient modeling of conifer species using random forests. *Landscape Ecology*, *24*, 673–683. https://doi.org/10.1007/s10980-009-9341-0

Fasullo, M., & Endres, L. (2015). Nucleotide Salvage Deficiencies, DNA Damage and Neurodegeneration. *International Journal of Molecular Sciences*, *16*(5), 9431–9449. https://doi.org/10.3390/ijms16059431

Flockhart, D. A. (2012). Dietary Restrictions and Drug Interactions With Monoamine Oxidase Inhibitors: An Update. *The Journal of Clinical Psychiatry*, *73*(suppl 1), 4461. https://doi.org/10.4088/JCP.11096su1c.03

Forssberg, H. (2019). Microbiome programming of brain development: Implications for neurodevelopmental disorders. *Developmental Medicine & Child Neurology*, *61*(7), 744–749. https://doi.org/10.1111/dmcn.14208

Frolkis, A., Knox, C., & Lim, E. (2010). *SMPDB: The Small Molecule Pathway Database—PMC*. *38*, 480–487.

Fuchs, A. L., Miller, I. R., Schiller, S. M., Ammons, M. C. B., Eilers, B., Tripet, B., & Copié, V. (2020). Pseudomonas aeruginosa Planktonic- and Biofilm-Conditioned Media Elicit Discrete Metabolic Responses in Human Macrophages. *Cells*, *9*(10), 2260. https://doi.org/10.3390/cells9102260

Fuchs, A. L., Schiller, S. M., Keegan, W. J., Ammons, M. C. B., Eilers, B., Tripet, B., & Copié, V. (2019). Quantitative 1H NMR Metabolomics Reveal Distinct Metabolic Adaptations in Human Macrophages Following Differential Activation. *Metabolites*, *9*(11), Article 11. https://doi.org/10.3390/metabo9110248

Fuchs, A. L., Weaver, A. J., Tripet, B. P., Ammons, M. C. B., Teintze, M., & Copié, V. (2018). Characterization of the antibacterial activity of Bald's eyesalve against drug resistant Staphylococcus aureus and Pseudomonas aeruginosa. *PLoS ONE*, *13*(11). https://doi.org/10.1371/journal.pone.0208108

Gaik, M., Kojic, M., Stegeman, M. R., Öncü-Öner, T., Kościelniak, A., Jones, A., Mohamed, A., Chau, P. Y. S., Sharmin, S., Chramiec-Głąbik, A., Indyka, P., Rawski, M., Biela, A., Dobosz, D., Millar, A., Chau, V., Ünalp, A., Piper, M., Bellingham, M. C., … Glatt, S. (2022). Functional divergence of the two Elongator subcomplexes during neurodevelopment. *EMBO Molecular Medicine*, *14*(7), e15608. https://doi.org/10.15252/emmm.202115608

García-Ayuso, D., Di Pierdomenico, J., Hadj-Said, W., Marie, M., Agudo-Barriuso, M., Vidal-Sanz, M., Picaud, S., & Villegas-Pérez, M. P. (2018). Taurine Depletion Causes ipRGC Loss and Increases Light-Induced Photoreceptor Degeneration. *Investigative Ophthalmology & Visual Science*, *59*(3), 1396–1409. https://doi.org/10.1167/iovs.17-23258

Gastinger, M. J., Singh, R. S. J., & Barber, A. J. (2006). Loss of cholinergic and dopaminergic amacrine cells in streptozotocin-diabetic rat and Ins2Akita-diabetic mouse retinas. *Investigative Ophthalmology & Visual Science*, *47*(7), 3143–3150. https://doi.org/10.1167/iovs.05-1376

George, L., Chaverra, M., Wolfe, L., Thorne, J., Close-Davis, M., Eibs, A., Riojas, V., Grindeland, A., Orr, M., Carlson, G. A., & Lefcort, F. (2013). Familial dysautonomia model reveals Ikbkap deletion causes apoptosis of Pax3+ progenitors and peripheral neurons. *Proceedings of the National Academy of Sciences*, *110*(46), 18698–18703. https://doi.org/10.1073/pnas.1308596110

Gibellini, F., & Smith, T. K. (2010). The Kennedy pathway—De novo synthesis of phosphatidylethanolamine and phosphatidylcholine. *IUBMB Life*, *62*(6), 414–428. https://doi.org/10.1002/iub.337

Gillman, P. K. (2018). A reassessment of the safety profile of monoamine oxidase inhibitors: Elucidating tired old tyramine myths. *Journal of Neural Transmission*, *125*(11), 1707–1717. https://doi.org/10.1007/s00702-018-1932-y

Glinton, K. E., & Elsea, S. H. (2019). Untargeted Metabolomics for Autism Spectrum Disorders: Current Status and Future Directions. *Frontiers in Psychiatry*, *10*, 647. https://doi.org/10.3389/fpsyt.2019.00647

Goffena, J., Lefcort, F., Zhang, Y., Lehrmann, E., Chaverra, M., Felig, J., Walters, J., Buksch, R., Becker, K. G., & George, L. (2018). Elongator and codon bias regulate protein levels in mammalian peripheral neurons. *Nature Communications*, *9*(1), 1–10. https://doi.org/10.1038/s41467-018-03221-z

González-Duarte, A., Cotrina-Vidal, M., Kaufmann, H., & Norcliffe-Kaufmann, L. (2023). Familial dysautonomia. *Clinical Autonomic Research*, *33*(3), 269–280. https://doi.org/10.1007/s10286-023-00941-1

Gowda, G. A. N., & Raftery, D. (2023). *NMR Metabolomics Methods for Investigating Disease*. *95*(1), 83–99. https://doi.org/10.1021/acs.analchem.2c04606

Grzymajlo, K., El Hafny-Rahbi, B., & Kieda, C. (2023). Tumour suppressor PTEN activity is differentially inducible by myo-inositol phosphates. *Journal of Cellular and Molecular Medicine*, *27*(6), 879–890. https://doi.org/10.1111/jcmm.17699

Gwak, M.-G., & Chang, S.-Y. (2021). Gut-Brain Connection: Microbiome, Gut Barrier, and Environmental Sensors. *Immune Network*, *21*(3), e20. https://doi.org/10.4110/in.2021.21.e20

Haider, A., Wei, Y.-C., Lim, K., Barbosa, A. D., Liu, C.-H., Weber, U., Mlodzik, M., Oras, K., Collier, S., Hussain, M. M., Dong, L., Patel, S., Alvarez-Guaita, A., Saudek, V., Jenkins, B. J., Koulman, A., Dymond, M. K., Hardie, R. C., Siniossoglou, S., & Savage, D. B. (2018). PCYT1A Regulates Phosphatidylcholine Homeostasis from the Inner Nuclear Membrane in Response to Membrane Stored Curvature Elastic Stress. *Developmental Cell*, *45*(4), 481-495.e8. https://doi.org/10.1016/j.devcel.2018.04.012

Han, J., Antunes, L. C. M., Finlay, B. B., & Borchers, C. H. (2010). Metabolomics: Towards understanding host–microbe interactions. *Future Microbiology*, *5*(2), 153–161. https://doi.org/10.2217/fmb.09.132

Han, T. (Kevin), Everett, R. S., Proctor, W. R., Ng, C. M., Costales, C. L., Brouwer, K. L. R., & Thakker, D. R. (2013). Organic Cation Transporter 1 (OCT1/mOct1) Is Localized in the Apical Membrane of Caco-2 Cell Monolayers and Enterocytes. *Molecular Pharmacology*, *84*(2), 182–189. https://doi.org/10.1124/mol.112.084517

Havelund, J. F., Heegaard, N. H. H., Færgeman, N. J. K., & Gramsbergen, J. B. (2017). Biomarker Research in Parkinson's Disease Using Metabolite Profiling. *Metabolites*, *7*(3), Article 3. https://doi.org/10.3390/metabo7030042

Hensley, K., Kotake, Y., Sang, H., Pye, Q. N., Wallis, G. L., Kolker, L. M., Tabatabaie, T., Stewart, C. A., Konishi, Y., Nakae, D., & Floyd, R. A. (2000). Dietary choline restriction causes complex I dysfunction and increased H2O2 generation in liver mitochondria. *Carcinogenesis*, *21*(5), 983–989. https://doi.org/10.1093/carcin/21.5.983

Hims, M. M., Ibrahim, E. C., Leyne, M., Mull, J., Liu, L., Lazaro, C., Shetty, R. S., Gill, S., Gusella, J. F., Reed, R., & Slaugenhaupt, S. A. (2007). Therapeutic potential and mechanism of kinetin as a treatment for the human splicing disease familial dysautonomia. *Journal of Molecular Medicine (Berlin, Germany)*, *85*(2), 149–161. https://doi.org/10.1007/s00109-006-0137-2

Hims, M. M., Shetty, R. S., Pickel, J., Mull, J., Leyne, M., Liu, L., Gusella, J. F., & Slaugenhaupt, S. A. (2007). A humanized IKBKAP transgenic mouse models a tissue specific human splicing defect. *Genomics*, *90*(3), 389–396. https://doi.org/10.1016/j.ygeno.2007.05.012

Holeček, M. (2018). Branched-chain amino acids in health and disease: Metabolism, alterations in blood plasma, and as supplements. *Nutrition & Metabolism*, *15*, 33. https://doi.org/10.1186/s12986-018-0271-1

Hopkins, B. D., Hodakoski, C., Barrows, D., Mense, S., & Parsons, R. E. (2014). PTEN function, the long and the short of it. *Trends in Biochemical Sciences*, *39*(4), 183–190. https://doi.org/10.1016/j.tibs.2014.02.006

Hu, Z.-X., Pu, J.-L., Zheng, R., Yan, Y.-Q., Liu, K.-Y., Liu, Y., Zheng, R., Chen, Y., Lin, Z.-H., Xue, N.-J., Li, P., & Zhang, B.-R. (2022). Mitochondrial morphology and synaptic structure altered in the retina of parkin-deficient mice. *Neuroscience Letters*, *790*, 136888. https://doi.org/10.1016/j.neulet.2022.136888

Huang, B., Johansson, M. J. O., & Byström, A. S. (2005). An early step in wobble uridine tRNA modification requires the Elongator complex. *RNA*, *11*(4), 424–436. https://doi.org/10.1261/rna.7247705

Hunnicutt, B. J., Chaverra, M., George, L., & Lefcort, F. (2012). IKAP/Elp1 Is Required In Vivo for Neurogenesis and Neuronal Survival, but Not for Neural Crest Migration. *PLoS ONE*, *7*(2), e32050. https://doi.org/10.1371/journal.pone.0032050

Hwang, J.-S., & Shin, Y.-J. (2021). Role of Choline in Ocular Diseases. *International Journal of Molecular Sciences*, *22*(9), 4733. https://doi.org/10.3390/ijms22094733

Indrieri, A., Pizzarelli, R., Franco, B., & De Leonibus, E. (2020). Dopamine, Alpha-Synuclein, and Mitochondrial Dysfunctions in Parkinsonian Eyes. *Frontiers in Neuroscience*, *14*, 567129. https://doi.org/10.3389/fnins.2020.567129

Jackson, M. Z., Gruner, K. A., Qin, C., & Tourtellotte, W. G. (2014). A neuron autonomous role for the familial dysautonomia gene ELP1 in sympathetic and sensory target tissue innervation. *Development*, *141*(12), 2452–2461. https://doi.org/10.1242/dev.107797

Johansen, K. K., Wang, L., Aasly, J. O., White, L. R., Matson, W. R., Henchcliffe, C., Beal, M. F., & Bogdanov, M. (2009). Metabolomic Profiling in LRRK2-Related Parkinson's Disease. *PLOS ONE*, *4*(10), e7551. https://doi.org/10.1371/journal.pone.0007551

Johansson, M. J. O., Xu, F., & Byström, A. S. (2018). Elongator—A tRNA modifying complex that promotes efficient translational decoding. *Biochimica et Biophysica Acta (BBA) - Gene Regulatory Mechanisms*, *1861*(4), 401–408. https://doi.org/10.1016/j.bbagrm.2017.11.006

Jong, C. J., Azuma, J., & Schaffer, S. (2012). Mechanism underlying the antioxidant activity of taurine: Prevention of mitochondrial oxidant production. *Amino Acids*, *42*(6), 2223–2232. https://doi.org/10.1007/s00726-011-0962-7

Jong, C. J., Sandal, P., & Schaffer, S. W. (2021). The Role of Taurine in Mitochondria Health: More Than Just an Antioxidant. *Molecules*, *26*(16), Article 16. https://doi.org/10.3390/molecules26164913

Kang, D.-W., Adams, J. B., Coleman, D. M., Pollard, E. L., Maldonado, J., McDonough-Means, S., Caporaso, J. G., & Krajmalnik-Brown, R. (2019). Long-term benefit of Microbiota Transfer Therapy on autism symptoms and gut microbiota. *Scientific Reports*, *9*, 5821. https://doi.org/10.1038/s41598-019-42183-0

Kang, D.-W., Adams, J. B., Gregory, A. C., Borody, T., Chittick, L., Fasano, A., Khoruts, A., Geis, E., Maldonado, J., McDonough-Means, S., Pollard, E. L., Roux, S., Sadowsky, M. J., Lipson, K. S., Sullivan, M. B., Caporaso, J. G., & Krajmalnik-Brown, R. (2017). Microbiota Transfer Therapy alters gut ecosystem and improves gastrointestinal and autism symptoms: An open-label study. *Microbiome*, *5*, 10. https://doi.org/10.1186/s40168-016-0225-7

Kang, D.-W., Ilhan, Z. E., Isern, N. G., Hoyt, D. W., Howsmon, D. P., Shaffer, M., Lozupone, C. A., Hahn, J., Adams, J. B., & Krajmalnik-Brown, R. (2018). Differences in fecal microbial metabolites and microbiota of children with autism spectrum disorders. *Anaerobe*, *49*, 121–131. https://doi.org/10.1016/j.anaerobe.2017.12.007

Karlsborn, T., Mahmud, A. K. M. F., Tükenmez, H., & Byström, A. S. (2016). Loss of ncm5 and mcm5 wobble uridine side chains results in an altered metabolic profile. *Metabolomics*, *12*(12), 177. https://doi.org/10.1007/s11306-016-1120-8

Karlsborn, T., Tükenmez, H., Chen, C., & Byström, A. S. (2014). Familial dysautonomia (FD) patients have reduced levels of the modified wobble nucleoside mcm5s2U in tRNA. *Biochemical and Biophysical Research Communications*, *454*(3), 441–445. https://doi.org/10.1016/j.bbrc.2014.10.116

Kellingray, L., Gall, G. L., Defernez, M., Beales, I. L. P., Franslem-Elumogo, N., & Narbad, A. (2018). Microbial taxonomic and metabolic alterations during faecal microbiota transplantation to treat Clostridium difficile infection. *Journal of Infection*, *77*(2), 107–118. https://doi.org/10.1016/j.jinf.2018.04.012

Kelly, C. J., Zheng, L., Campbell, E. L., Saeedi, B., Scholz, C. C., Bayless, A. J., Wilson, K. E., Glove, L. E., Kominsky, D. J., Magnuson, A., Weir, T. L., Ehrentraut, S. F., Pickel, C., Kuhn, K. A., Lanis, J. M., Nguyen, V., Taylor, C. T., & Colgan, S. P. (2015). Crosstalk between Microbiota-Derived Short-Chain Fatty Acids and Intestinal Epithelial HIF Augments Tissue Barrier Function. *Cell Host & Microbe*, *17*(5), 662–671. https://doi.org/10.1016/j.chom.2015.03.005

Kępka, A., Ochocinska, A., Chojnowska, S., Borzym-Kluczyk, M., Skorupa, E., Knaś, M., & Waszkiewicz, N. (2021). Potential Role of L-Carnitine in Autism Spectrum Disorder. *Journal of Clinical Medicine*, *10*, 1202. https://doi.org/10.3390/jcm10061202

Kirches, E. (2011). LHON: Mitochondrial Mutations and More. *Current Genomics*, *12*(1), 44–54. https://doi.org/10.2174/138920211794520150

Kojic, M., Gawda, T., Gaik, M., Begg, A., Salerno-Kochan, A., Kurniawan, N. D., Jones, A., Drożdżyk, K., Kościelniak, A., Chramiec-Głąbik, A., Hediyeh-Zadeh, S., Kasherman, M., Shim, W. J., Sinniah, E., Genovesi, L. A., Abrahamsen, R. K., Fenger, C. D., Madsen, C. G., Cohen, J. S., … Wainwright, B. J. (2021). Elp2 mutations perturb the epitranscriptome and lead to a complex neurodevelopmental phenotype. *Nature Communications*, *12*, 2678. https://doi.org/10.1038/s41467-021-22888-5

Kojic, M., & Wainwright, B. (2016). The Many Faces of Elongator in Neurodevelopment and Disease. *Frontiers in Molecular Neuroscience*, *9*. https://doi.org/10.3389/fnmol.2016.00115

Kolb, H. (1991). Anatomical pathways for color vision in the human retina. *Visual Neuroscience*, *7*(1–2), 61–74. https://doi.org/10.1017/s0952523800010944

Kolb, H. (1995). Roles of Amacrine Cells. In H. Kolb, E. Fernandez, & R. Nelson (Eds.), *Webvision: The Organization of the Retina and Visual System*. University of Utah Health Sciences Center. http://www.ncbi.nlm.nih.gov/books/NBK11539/

Konjevod, M., Nikolac Perkovic, M., Sáiz, J., Svob Strac, D., Barbas, C., & Rojo, D. (2021). Metabolomics analysis of microbiota-gut-brain axis in neurodegenerative and psychiatric diseases. *Journal of Pharmaceutical and Biomedical Analysis, 194*, 113681. https://doi.org/10.1016/j.jpba.2020.113681

Kori, M., Aydın, B., Unal, S., Arga, K. Y., & Kazan, D. (2016). Metabolic Biomarkers and Neurodegeneration: A Pathway Enrichment Analysis of Alzheimer's Disease, Parkinson's Disease, and Amyotrophic Lateral Sclerosis. *OMICS: A Journal of Integrative Biology*, *20*(11), 645–661. https://doi.org/10.1089/omi.2016.0106

Kozich, J. J., Westcott, S. L., Baxter, N. T., Highlander, S. K., & Schloss, P. D. (2013). Development of a Dual-Index Sequencing Strategy and Curation Pipeline for Analyzing Amplicon Sequence Data on the MiSeq Illumina Sequencing Platform. *Applied and Environmental Microbiology*, *79*(17), 5112–5120. https://doi.org/10.1128/AEM.01043-13

Krausz, Y., Maayan, C., Faber, J., Marciano, R., Mogle, P., & Wynchank, S. (1994). Scintigraphic evaluation of esophageal transit and gastric emptying in familial dysautonomia. *European Journal of Radiology*, *18*(1), 52–56. https://doi.org/10.1016/0720-048X(94)90367-0

La Morgia, C., Barboni, P., Rizzo, G., Carbonelli, M., Savini, G., Scaglione, C., Capellari, S., Bonazza, S., Giannoccaro, M. P., Calandra-Buonaura, G., Liguori, R., Cortelli, P., Martinelli, P., Baruzzi, A., & Carelli, V. (2013). Loss of temporal retinal nerve fibers in Parkinson disease: A mitochondrial pattern? *European Journal of Neurology*, *20*(1), 198–201. https://doi.org/10.1111/j.1468-1331.2012.03701.x

La Rosa, S. L., Leth, M. L., Michalak, L., Hansen, M. E., Pudlo, N. A., Glowacki, R., Pereira, G., Workman, C. T., Arntzen, M. Ø., Pope, P. B., Martens, E. C., Hachem, M. A., & Westereng, B. (2019). The human gut Firmicute Roseburia intestinalis is a primary degrader of dietary β-mannans. *Nature Communications*, *10*, 905. https://doi.org/10.1038/s41467-019-08812-y

Lamichhane, S., Sen, P., Dickens, A. M., Hyötyläinen, T., & Orešič, M. (2018). An Overview of Metabolomics Data Analysis: Current Tools and Future Perspectives. In *Comprehensive Analytical Chemistry* (Vol. 82, pp. 387–413). Elsevier. https://doi.org/10.1016/bs.coac.2018.07.001

Lee, J. H., Okuno, Y., & Cavagnero, S. (2014). Sensitivity Enhancement in Solution NMR: Emerging Ideas and New Frontiers. *Journal of Magnetic Resonance (San Diego, Calif. : 1997)*, *241*, 18–31. https://doi.org/10.1016/j.jmr.2014.01.005

Lee, W. K., Hwang, J.-S., Yun, C.-H., & Cha, S. H. (2007). Identification of a kidney-specific mouse organic cation transporter like-1 (mOCTL1). *Experimental & Molecular Medicine*, *39*(6), Article 6. https://doi.org/10.1038/emm.2007.85

Lefcort, F., Mergy, M., Ohlen, S. B., Ueki, Y., & George, L. (2017). Animal and cellular models of familial dysautonomia. *Clinical Autonomic Research*, *27*(4), 235–243. https://doi.org/10.1007/s10286-017-0438-2

Lefler, S., Cohen, M. A., Kantor, G., Cheishvili, D., Even, A., Birger, A., Turetsky, T., Gil, Y., Even-Ram, S., Aizenman, E., Bashir, N., Maayan, C., Razin, A., Reubinoff, B. E., & Weil, M. (2015). Familial dysautonomia (FD) human embryonic stem cell derived PNS neurons reveal that synaptic vesicular and neuronal transport genes are directly or indirectly affected by IKBKAP downregulation. *PLoS ONE*, *10*(10), e0138807. https://doi.org/10.1371/journal.pone.0138807

Levitt, M. H. (2013). *Spin Dynamics: Basics of Nuclear Magnetic Resonance*. John Wiley & Sons.

Leylabadlo, H. E., Ghotaslou, R., Feizabadi, M. M., Farajnia, S., Moaddab, S. Y., Ganbarov, K., Khodadadi, E., Tanomand, A., Sheykhsaran, E., Yousefi, B., & Kafil, H. S. (2020). The critical role of Faecalibacterium prausnitzii in human health: An overview. *Microbial Pathogenesis*, *149*, 104344. https://doi.org/10.1016/j.micpath.2020.104344

Li, D., Ke, Y., Zhan, R., Liu, C., Zhao, M., Zeng, A., Shi, X., Ji, L., Cheng, S., Pan, B., Zheng, L., & Hong, H. (2018). Trimethylamine-N-oxide promotes brain aging and cognitive impairment in mice. *Aging Cell*, *17*(4), e12768. https://doi.org/10.1111/acel.12768

Li, H., Uittenbogaard, M., Hao, L., & Chiaramello, A. (2021). Clinical Insights into Mitochondrial Neurodevelopmental and Neurodegenerative Disorders: Their Biosignatures from Mass Spectrometry-Based Metabolomics. *Metabolites*, *11*(4), 233. https://doi.org/10.3390/metabo11040233

Li, N., Chen, H., Cheng, Y., Xu, F., Ruan, G., Ying, S., Tang, W., Chen, L., Chen, M., Lv, L., Ping, Y., Chen, D., & Wei, Y. (2021). Fecal Microbiota Transplantation Relieves Gastrointestinal and Autism Symptoms by Improving the Gut Microbiota in an Open-Label Study. *Frontiers in Cellular and Infection Microbiology*, *11*, 759435. https://doi.org/10.3389/fcimb.2021.759435

Liaw, A., & Wiener, M. (2002). The R Journal: Classification and regression by randomForest. *R News*, *2*(3), 18–22.

Liu, H., & Prokosch, V. (2021). Energy Metabolism in the Inner Retina in Health and Glaucoma. *International Journal of Molecular Sciences*, *22*(7), 3689. https://doi.org/10.3390/ijms22073689

López-Sámano, M., Beltrán, L. F. L.-A., Sánchez-Thomas, R., Dávalos, A., Villaseñor, T., García-García, J. D., & García-de los Santos, A. (2020). A novel way to synthesize pantothenate in bacteria involves β-alanine synthase present in uracil degradation pathway. *MicrobiologyOpen*, *9*(4), e1006. https://doi.org/10.1002/mbo3.1006

Luu, M., Pautz, S., Kohl, V., Singh, R., Romero, R., Lucas, S., Hofmann, J., Raifer, H., Vachharajani, N., Carrascosa, L. C., Lamp, B., Nist, A., Stiewe, T., Shaul, Y., Adhikary, T., Zaiss, M. M., Lauth, M., Steinhoff, U., & Visekruna, A. (2019). The short-chain fatty acid pentanoate suppresses autoimmunity by modulating the metabolic-epigenetic crosstalk in lymphocytes. *Nature Communications*, *10*(1), 760. https://doi.org/10.1038/s41467-019-08711-2

MacGregor, L. C., Rosecan, L. R., Laties, A. M., & Matschinsky, F. M. (1986). Altered retinal metabolism in diabetes. I. Microanalysis of lipid, glucose, sorbitol, and myo-inositol in the choroid and in the individual layers of the rabbit retina. *Journal of Biological Chemistry*, *261*(9), 4046–4051. https://doi.org/10.1016/S0021-9258(17)35619-3

Mächler, M., Rousseeuw, P., Struyf, A., Hubert, M., & Hornik, K. (2012). Cluster: Cluster Analysis Basics and Extensions. In *R packages* (Vol. 1).

Marion, D. (2013). An Introduction to Biological NMR Spectroscopy *. *Molecular & Cellular Proteomics*, *12*(11), 3006–3025. https://doi.org/10.1074/mcp.O113.030239

Markowiak-Kopeć, P., & Śliżewska, K. (2020). The Effect of Probiotics on the Production of Short-Chain Fatty Acids by Human Intestinal Microbiome. *Nutrients*, *12*(4), 1107. https://doi.org/10.3390/nu12041107

Martinson, J. N. V., Pinkham, N. V., Peters, G. W., Cho, H., Heng, J., Rauch, M., Broadaway, S. C., & Walk, S. T. (2019). Rethinking gut microbiome residency and the Enterobacteriaceae in healthy human adults. *The ISME Journal*, *13*(9), 2306–2318. https://doi.org/10.1038/s41396-019-0435-7

Masino, S. A., & Rho, J. M. (2012). Mechanisms of Ketogenic Diet Action. In J. L. Noebels, M. Avoli, M. A. Rogawski, R. W. Olsen, & A. V. Delgado-Escueta (Eds.), *Jasper's Basic Mechanisms of the Epilepsies* (4th ed.). National Center for Biotechnology Information (US). http://www.ncbi.nlm.nih.gov/books/NBK98219/

Mendoza-Santiesteban, C. E., Hedges III, T. R., Norcliffe-Kaufmann, L., Axelrod, F., & Kaufmann, H. (2014). Selective retinal ganglion cell loss in familial dysautonomia. *Journal of Neurology*, *261*(4), 702–709. https://doi.org/10.1007/s00415-014-7258-2

Mendoza-Santiesteban, C. E., Hedges, T. R., Norcliffe-Kaufmann, L., Warren, F., Reddy, S., Axelrod, F. B., & Kaufmann, H. (2012). Clinical Neuro-ophthalmic Findings in Familial Dysautonomia. *Journal of Neuro-Ophthalmology : The Official Journal of the North American Neuro-Ophthalmology Society*, *32*(1), 23–26. https://doi.org/10.1097/WNO.0b013e318230feab

Mendoza-Santiesteban, C. E., Palma, J.-A., Hedges, T. R., Laver, N. V., Farhat, N., Norcliffe-Kaufmann, L., & Kaufmann, H. (2017). Pathological Confirmation of Optic Neuropathy in Familial Dysautonomia. *Journal of Neuropathology and Experimental Neurology*, *76*(3), 238–244. https://doi.org/10.1093/jnen/nlw118

Mendoza-Santiesteban, C. E., Palma, J.-A., Norcliffe-Kaufmann, L., & Kaufmann, H. (2017). Familial dysautonomia: A disease with hidden tears. *Journal of Neurology*, *264*(6), 1290–1291. https://doi.org/10.1007/s00415-017-8486-z

Mercier, P., Lewis, M. J., Chang, D., Baker, D., & Wishart, D. S. (2011). Towards automatic metabolomic profiling of high-resolution one-dimensional proton NMR spectra. *Journal of Biomolecular NMR*, *49*(3–4), 307–323. https://doi.org/10.1007/s10858-011-9480-x

Merckx, C., & De Paepe, B. (2022). The Role of Taurine in Skeletal Muscle Functioning and Its Potential as a Supportive Treatment for Duchenne Muscular Dystrophy. *Metabolites*, *12*(2), 193. https://doi.org/10.3390/metabo12020193

Michel, V. H. (2009). *Expression, subcellular localization and function of the solute carrier 44A1 (SLC44A1)* [University of Guelph]. https://hdl.handle.net/10214/21030

Midelfart, A., Dybdahl, A., & Gribbestad, I. S. (1996). Detection of different metabolites in the rabbit lens by high resolution ^{1}H NMR spectroscopy. *Current Eye Research*, *15*(12), 1175–1181. https://doi.org/10.3109/02713689608995153

Mirzaei, R., Bouzari, B., Hosseini-Fard, S. R., Mazaheri, M., Ahmadyousefi, Y., Abdi, M., Jalalifar, S., Karimitabar, Z., Teimoori, A., Keyvani, H., Zamani, F., Yousefimashouf, R., & Karampoor, S. (2021). Role of microbiota-derived short-chain fatty acids in nervous system disorders. *Biomedicine & Pharmacotherapy*, *139*, 111661. https://doi.org/10.1016/j.biopha.2021.111661

Miyazaki, T., Sasaki, S.-I., Toyoda, A., Wei, F.-Y., Shirai, M., Morishita, Y., Ikegami, T., Tomizawa, K., & Honda, A. (2020). Impaired bile acid metabolism with defectives of mitochondrial-tRNA taurine modification and bile acid taurine conjugation in the taurine depleted cats. *Scientific Reports*, *10*(1), 4915. https://doi.org/10.1038/s41598-020-61821-6

Moreira, P. I., Carvalho, C., Zhu, X., Smith, M. A., & Perry, G. (2010). Mitochondrial dysfunction is a trigger of Alzheimer's disease pathophysiology. *Biochimica et Biophysica Acta (BBA) - Molecular Basis of Disease*, *1802*(1), 2–10. https://doi.org/10.1016/j.bbadis.2009.10.006

Morini, E., Dietrich, P., Salani, M., Downs, H. M., Wojtkiewicz, G. R., Alli, S., Brenner, A., Nilbratt, M., LeClair, J. W., Oaklander, A. L., Slaugenhaupt, S. A., & Dragatsis, I. (2016). Sensory and autonomic deficits in a new humanized mouse model of familial dysautonomia. *Human Molecular Genetics*, *25*(6), 1116–1128. https://doi.org/10.1093/hmg/ddv634

Morini, E., Gao, D., Montgomery, C. M., Salani, M., Mazzasette, C., Krussig, T. A., Swain, B., Dietrich, P., Narasimhan, J., Gabbeta, V., Dakka, A., Hedrick, J., Zhao, X., Weetall, M., Naryshkin, N. A., Wojtkiewicz, G. G., Ko, C.-P., Talkowski, M. E., Dragatsis, I., & Slaugenhaupt, S. A. (2019). ELP1 Splicing Correction Reverses Proprioceptive Sensory Loss in Familial Dysautonomia. *The American Journal of Human Genetics*, *104*(4), 638–650. https://doi.org/10.1016/j.ajhg.2019.02.009

Muddapu, V. R., Dharshini, S. A. P., Chakravarthy, V. S., & Gromiha, M. M. (2020). Neurodegenerative Diseases – Is Metabolic Deficiency the Root Cause? *Frontiers in Neuroscience*, *14*, 213. https://doi.org/10.3389/fnins.2020.00213

Neuwirth, E. (2022). *RColorBrewer: ColorBrewer palettes v. R package version 1.1-3*. CRAN.

Nguyen, L., Humbert, S., Saudou, F., & Chariot, A. (2010). Elongator – an emerging role in neurological disorders. *Trends in Molecular Medicine*, *16*(1), 1–6. https://doi.org/10.1016/j.molmed.2009.11.002

Norcliffe-Kaufmann, L., Slaugenhaupt, S. A., & Kaufmann, H. (2017). Familial dysautonomia: History, genotype, phenotype and translational research. *Progress in Neurobiology*, *152*, 131–148. https://doi.org/10.1016/j.pneurobio.2016.06.003

Ochoa-de la Paz, L., Zenteno, E., Gulias-Cañizo, R., & Quiroz-Mercado, H. (2019). Taurine and GABA neurotransmitter receptors, a relationship with therapeutic potential? *Expert Review of Neurotherapeutics*, *19*(4), 289–291. https://doi.org/10.1080/14737175.2019.1593827

Ogata, H., Goto, S., Sato, K., Fujibuchi, W., Bono, H., & Kanehisa, M. (1999). KEGG: Kyoto Encyclopedia of Genes and Genomes. *Nucleic Acids Research*, *27*(1), 29–34.

Ohlen, S. B., Russell, M. L., Brownstein, M. J., & Lefcort, F. (2017). BGP-15 prevents the death of neurons in a mouse model of familial dysautonomia. *Proceedings of the National Academy of Sciences*, *114*(19), 5035–5040. https://doi.org/10.1073/pnas.1620212114

Oksanen, J., Blanchet, F. G., Friendly, M., Kindt, R., Legendre, P., McGlinn, D., Minchin, P., O'Hara, R., Simpson, G., Solymos, P., Stevens, M., Szöcs, E., & Wagner, H. (2020). *Vegan community ecology package version 2.5-7 November 2020*.

Oksanen, J., Kindt, R., & Simpson, G. (2015, October 29). *Static and Dynamic 3D Plots for the "vegan" Package*. https://www.semanticscholar.org/paper/Static-and-Dynamic-3D-Plots-for-the-%27vegan%27-Package-Oksanen-Kindt/7c637e75d1437150a5adc6edf62b8db25ff1dec4

Oluwatobi, P. E., Ese, I. G., Oluwatumininu, P. A., & Eghosa, M. (2020). Microbiota Gut-Brain Axis and Neurodegenerative Disease. *Romanian Neurosurgery*, 110–116.

O'Shea-Stone, G., Lambert, R., Tripet, B., Berardinelli, J., Thomson, J., Copié, V., & Garrott, R. (2021). 1H NMR based metabolic profiling distinguishes the differential impact of capture techniques on wild bighorn sheep. *Scientific Reports*, *11*(1), Article 1. https://doi.org/10.1038/s41598-021-90931-y

Otero, G., Fellows, J., Li, Y., Bizemont, T. de, Dirac, A. M. G., Gustafsson, C. M., Erdjument-Bromage, H., Tempst, P., & Svejstrup, J. Q. (1999). Elongator, a Multisubunit Component of a Novel RNA Polymerase II Holoenzyme for Transcriptional Elongation. *Molecular Cell*, *3*(1), 109–118. https://doi.org/10.1016/S1097-2765(00)80179-3

Palma, J.-A., Kaufmann, L., Fuente, C., Percival, L., Mendoza, C., & Kaufmann, H. (2014). Current Treatments in Familial Dysautonomia. *Expert Opinion on Pharmacotherapy*, *15*(18), 2653–2671. https://doi.org/10.1517/14656566.2014.970530

Palma, J.-A., Norcliffe-Kaufmann, L., Perez, M. A., Spalink, C. L., & Kaufmann, H. (2017). Sudden Unexpected Death During Sleep in Familial Dysautonomia: A Case–Control Study. *Sleep*, *40*(8). https://doi.org/10.1093/sleep/zsx083

Palma, J.-A., Roda, R., Norcliffe-Kaufmann, L., & Kaufmann, H. (2015). Increased Frequency of Rhabdomyolysis in Familial Dysautonomia. *Muscle & Nerve*, *52*(5), 887–890. https://doi.org/10.1002/mus.24781

Pang, Z., Chong, J., Zhou, G., de Lima Morais, D. A., Chang, L., Barrette, M., Gauthier, C., Jacques, P.-É., Li, S., & Xia, J. (2021). MetaboAnalyst 5.0: Narrowing the gap between raw spectra and functional insights. *Nucleic Acids Research*, *49*(W1), W388–W396. https://doi.org/10.1093/nar/gkab382

Parisi, V., Oddone, F., Ziccardi, L., Roberti, G., Coppola, G., & Manni, G. (2018). Citicoline and Retinal Ganglion Cells: Effects on Morphology and Function. *Current Neuropharmacology*, *16*(7), 919–932. https://doi.org/10.2174/1570159X15666170703111729

Peach, J. T., Wilson, S. M., Gunderson, L. D., Frothingham, L., Tran, T., Walk, S. T., Yeoman, C. J., Bothner, B., & Miles, M. P. (2021). Temporal metabolic response yields a dynamic biosignature of inflammation. *iScience*, *24*(8), 102817. https://doi.org/10.1016/j.isci.2021.102817

Pehar, M., Harlan, B. A., Killoy, K. M., & Vargas, M. R. (2018). Nicotinamide Adenine Dinucleotide Metabolism and Neurodegeneration. *Antioxidants & Redox Signaling*, *28*(18), 1652–1668. https://doi.org/10.1089/ars.2017.7145

Pelletier, C. C., Croyal, M., Ene, L., Aguesse, A., Billon-Crossouard, S., Krempf, M., Lemoine, S., Guebre-Egziabher, F., Juillard, L., & Soulage, C. O. (2019). Elevation of Trimethylamine-N-Oxide in Chronic Kidney Disease: Contribution of Decreased Glomerular Filtration Rate. *Toxins*, *11*(11), 635. https://doi.org/10.3390/toxins11110635

Pérez-Fernández, V., Harman, D. G., Morley, J. W., & Cameron, M. A. (2017). Optimized Method to Quantify Dopamine Turnover in the Mammalian Retina. *Analytical Chemistry*, *89*(22), 12276–12283. https://doi.org/10.1021/acs.analchem.7b03216

Phillips, I. R., & Shephard, E. A. (1993). Primary Trimethylaminuria. In M. P. Adam, J. Feldman, G. M. Mirzaa, R. A. Pagon, S. E. Wallace, L. J. Bean, K. W. Gripp, & A. Amemiya (Eds.), *GeneReviews*®. University of Washington, Seattle. http://www.ncbi.nlm.nih.gov/books/NBK1103/

Pinkham, N. V., & Walk, S. T. (2022). *Gut microbiome dysbiosis drives metabolic dysfunction in Familial dysautonomia v. 1.0.* https://doi. org/10.5281/zenodo.7384390 (2022)

Potilinski, M. C., Lorenc, V., Perisset, S., & Gallo, J. E. (2020). Mechanisms behind Retinal Ganglion Cell Loss in Diabetes and Therapeutic Approach. *International Journal of Molecular Sciences*, *21*(7), 2351. https://doi.org/10.3390/ijms21072351

Praveenraj, S. S., Sonali, S., Anand, N., Tousif, H. A., Vichitra, C., Kalyan, M., Kanna, P. V., Chandana, K. A., Shasthara, P., Mahalakshmi, A. M., Yang, J., Pandi-Perumal, S. R., Sakharkar, M. K., & Chidambaram, S. B. (2022). The Role of a Gut Microbial-Derived Metabolite, Trimethylamine N-Oxide (TMAO), in Neurological Disorders. *Molecular Neurobiology*, *59*(11), 6684–6700. https://doi.org/10.1007/s12035-022-02990-5

Procaccini, C., Santopaolo, M., Faicchia, D., Colamatteo, A., Formisano, L., Candia, P. de, Galgani, M., Rosa, V. D., & Matarese, G. (2016). Role of metabolism in neurodegenerative disorders. *Metabolism - Clinical and Experimental*, *65*(9), 1376–1390. https://doi.org/10.1016/j.metabol.2016.05.018

Purves, D., Augustine, G. J., Fitzpatrick, D., Katz, L. C., LaMantia, A.-S., McNamara, J. O., & Williams, S. M. (2001). The Retina. In *Neuroscience. 2nd edition*. Sinauer Associates. https://www.ncbi.nlm.nih.gov/books/NBK10885/

Quigley, E. M. M. (2017). Microbiota-Brain-Gut Axis and Neurodegenerative Diseases. *Current Neurology and Neuroscience Reports*, *17*(12), 94. https://doi.org/10.1007/s11910-017-0802-6

Ramm Sander, P., Peer, M., Grandl, M., Bogdahn, U., Schmitz, G., & Kalbitzer, H. R. (2013). NMR Spectroscopy of Macrophages Loaded with Native, Oxidized or Enzymatically Degraded Lipoproteins. *PLoS ONE*, *8*(2). https://doi.org/10.1371/journal.pone.0056360

Ramprasad, C., Norcliffe-Kaufmann, L., Palma, J.-A., Levy, J., Zhang, Y., Spalink, C. L., Khan, A., Smukalla, S., Kaufmann, H., & Chen, L. A. (2021). Frequency and burden of gastrointestinal symptoms in familial dysautonomia. *Clinical Autonomic Research : Official Journal of the Clinical Autonomic Research Society*, *31*(1), 109–116. https://doi.org/10.1007/s10286-020-00735-9

Rath, S., Heidrich, B., Pieper, D. H., & Vital, M. (2017). Uncovering the trimethylamine-producing bacteria of the human gut microbiota. *Microbiome*, *5*, 54. https://doi.org/10.1186/s40168-017-0271-9

Riley, C. M., Day, R. L., Greeley, D. MCL., & Langford, W. S. (1949). Central Autonomic Dysfunction with Defective Lacrimation: I. Report of Five Cases. *Pediatrics*, *3*(4), 468–478. https://doi.org/10.1542/peds.3.4.468

Ripps, H., & Shen, W. (2012). Review: Taurine: A “very essential” amino acid. *Molecular Vision*, *18*, 2673–2686.

Roberts, D. (2013). labdsv: Ordination and Multivariate Analysis for Ecology. *CRAN*.

Rognes, T., Flouri, T., Nichols, B., Quince, C., & Mahé, F. (2016). VSEARCH: A versatile open source tool for metagenomics. *PeerJ*, *4*, e2584. https://doi.org/10.7717/peerj.2584

Rohart, F., Gautier, B., Singh, A., & Lê Cao, K.-A. (2017). mixOmics: An R package for 'omics feature selection and multiple data integration. *PLoS Computational Biology*, *13*(11), e1005752. https://doi.org/10.1371/journal.pcbi.1005752

Romano, G., Riccardi, F., Bussani, E., Vodret, S., Licastro, D., Ragone, I., Ronzitti, G., Morini, E., Slaugenhaupt, S. A., & Pagani, F. (2022). Rescue of a familial dysautonomia mouse model by AAV9-Exon-specific U1 snRNA. *The American Journal of Human Genetics*, *109*(8), 1534–1548. https://doi.org/10.1016/j.ajhg.2022.07.004

Romano, K. A., Martinez-del Campo, A., Kasahara, K., Chittim, C. L., Vivas, E. I., Amador-Noguez, D., Balskus, E. P., & Rey, F. E. (2017). Metabolic, Epigenetic, and Transgenerational Effects of Gut Bacterial Choline Consumption. *Cell Host & Microbe*, *22*(3), 279-290.e7. https://doi.org/10.1016/j.chom.2017.07.021

Romano, K. A., Vivas, E. I., Amador-Noguez, D., & Rey, F. E. (2015). Intestinal Microbiota Composition Modulates Choline Bioavailability from Diet and Accumulation of the Proatherogenic Metabolite Trimethylamine-N-Oxide. *mBio*, *6*(2). https://doi.org/10.1128/mBio.02481-14

Roncal, C., Martínez-Aguilar, E., Orbe, J., Ravassa, S., Fernandez-Montero, A., Saenz-Pipaon, G., Ugarte, A., Estella-Hermoso de Mendoza, A., Rodriguez, J. A., Fernández-Alonso, S., Fernández-Alonso, L., Oyarzabal, J., & Paramo, J. A. (2019). Trimethylamine-N-Oxide (TMAO) Predicts Cardiovascular Mortality in Peripheral Artery Disease. *Scientific Reports*, *9*, 15580. https://doi.org/10.1038/s41598-019-52082-z

Rossignol, D. A., & Frye, R. E. (2012). Mitochondrial dysfunction in autism spectrum disorders: A systematic review and meta-analysis. *Molecular Psychiatry*, *17*(3), 290–314. https://doi.org/10.1038/mp.2010.136

Rowland, I., Gibson, G., Heinken, A., Scott, K., Swann, J., Thiele, I., & Tuohy, K. (2017). *Gut microbiota functions: Metabolism of nutrients and other food components—PMC*. *57*(1), 1–24. https://doi.org/10.1007/s00394-017-1445-8

Ruiz-Perez, D., Guan, H., Madhivanan, P., Mathee, K., & Narasimhan, G. (2020). So you think you can PLS-DA? *BMC Bioinformatics*, *21*(1), 2. https://doi.org/10.1186/s12859-019-3310-7

Russo, A., Forest, C., Leone, G. J., Iascone, M., Tenconi, R., Maffei, M., Cersosimo, A., Cordelli, D. M., & Suppiej, A. (2021). ELP2 compound heterozygous variants associated with cortico-cerebellar atrophy, nodular heterotopia and epilepsy: Phenotype expansion and review of the literature. *European Journal of Medical Genetics*, *64*(12), 104361. https://doi.org/10.1016/j.ejmg.2021.104361

Sadun, A. A., Morgia, C. L., & Carelli, V. (2011). Leber's Hereditary Optic Neuropathy. *Current Treatment Options in Neurology*, *13*(1), 109–117. https://doi.org/10.1007/s11940-010-0100-y

Saito, Y., Sato, T., Nomoto, K., & Tsuji, H. (2018). Identification of phenol- and p-cresol-producing intestinal bacteria by using media supplemented with tyrosine and its metabolites. *FEMS Microbiology Ecology*, *94*(9), fiy125. https://doi.org/10.1093/femsec/fiy125

Santiago, A. R., Garrido, M. J., Cristóvão, A. J., Duarte, J. M. N., Carvalho, R. A., & Ambrósio, A. F. (2010). Evaluation of the Impact of Diabetes on Retinal Metabolites by NMR Spectroscopy. *Current Eye Research*, *35*(11), 992–1001. https://doi.org/10.3109/02713683.2010.500113

Savidge, T. C. (2016). Epigenetic Regulation of Enteric Neurotransmission by Gut Bacteria. *Frontiers in Cellular Neuroscience*, *9*, 503. https://doi.org/10.3389/fncel.2015.00503

Schaffer, S., & Kim, H. W. (2018). Effects and Mechanisms of Taurine as a Therapeutic Agent. *Biomolecules & Therapeutics*, *26*(3), 225–241. https://doi.org/10.4062/biomolther.2017.251

Schloss, P. D., Westcott, S. L., Ryabin, T., Hall, J. R., Hartmann, M., Hollister, E. B., Lesniewski, R. A., Oakley, B. B., Parks, D. H., Robinson, C. J., Sahl, J. W., Stres, B., Thallinger, G. G., Van Horn, D. J., & Weber, C. F. (2009). Introducing mothur: Open-Source, Platform-Independent, Community-Supported Software for Describing and Comparing Microbial Communities. *Applied and Environmental Microbiology*, *75*(23), 7537–7541. https://doi.org/10.1128/AEM.01541-09

Schultz, A., Cheng, S.-Y., Kirchner, E., Costello, S., Miettinen, H., Chaverra, M., King, C., George, L., Zhao, X., Narasimhan, J., Weetall, M., Slaugenhaupt, S., Morini, E., Punzo, C., & Lefcort, F. (2023). Reduction of retinal ganglion cell death in mouse models of familial dysautonomia using AAV-mediated gene therapy and splicing modulators. *Scientific Reports*, *13*, 18600. https://doi.org/10.1038/s41598-023-45376-w

Seidel, U., Huebbe, P., & Rimbach, G. (2019). Taurine: A Regulator of Cellular Redox Homeostasis and Skeletal Muscle Function. *Molecular Nutrition & Food Research*, *63*(16), 1800569. https://doi.org/10.1002/mnfr.201800569

Selmer, T., & Andrei, P. I. (2001). P-Hydroxyphenylacetate decarboxylase from Clostridium difficile. *European Journal of Biochemistry*, *268*(5), 1363–1372. https://doi.org/10.1046/j.1432-1327.2001.02001.x

Shao, T., He, Z., Xie, Z., Li, H., Wang, M., & Wen, C. (2016). Characterization of ankylosing spondylitis and rheumatoid arthritis using 1H NMR-based metabolomics of human fecal extracts. *Metabolomics*, *12*(4), 70. https://doi.org/10.1007/s11306-016-1000-2

Simpson, C. L., Lemmens, R., Miskiewicz, K., Broom, W. J., Hansen, V. K., van Vught, P. W. J., Landers, J. E., Sapp, P., Van Den Bosch, L., Knight, J., Neale, B. M., Turner, M. R., Veldink, J. H., Ophoff, R. A., Tripathi, V. B., Beleza, A., Shah, M. N., Proitsi, P., Van Hoecke, A., … Al-Chalabi, A. (2009). Variants of the elongator protein 3 (ELP3) gene are associated with motor neuron degeneration. *Human Molecular Genetics*, *18*(3), 472–481. https://doi.org/10.1093/hmg/ddn375

Sinclair, G. M., Oakes, S. M., Warden, A. C., Paten, A. M., & Jones, O. A. H. (2023). Exploring the potential application of alternative nuclei in NMR based metabolomics. *Metabolomics*, *19*(4), 42. https://doi.org/10.1007/s11306-023-02003-z

Singh, N., Lorbeck, M. T., Zervos, A., Zimmerman, J., & Elefant, F. (2010). The histone acetyltransferase Elp3 plays in active role in the control of synaptic bouton expansion and sleep in Drosophila. *Journal of Neurochemistry*, *115*(2), 493–504. https://doi.org/10.1111/j.1471-4159.2010.06892.x

Slaugenhaupt, S. A., Blumenfeld, A., Gill, S. P., Leyne, M., Mull, J., Cuajungco, M. P., Liebert, C. B., Chadwick, B., Idelson, M., Reznik, L., Robbins, C. M., Makalowska, I., Brownstein, M. J., Krappmann, D., Scheidereit, C., Maayan, C., Axelrod, F. B., & Gusella, J. F. (2001). Tissue-Specific Expression of a Splicing Mutation in the IKBKAP Gene Causes Familial Dysautonomia. *The American Journal of Human Genetics*, *68*(3), 598–605. https://doi.org/10.1086/318810

Soñanez-Organis, J. G., Vázquez-Medina, J. P., Zenteno-Savín, T., Aguilar, A., Crocker, D. E., & Ortiz, R. M. (2012). Prolonged fasting increases purine recycling in post-weaned northern elephant seals. *The Journal of Experimental Biology*, *215*(9), 1448–1455. https://doi.org/10.1242/jeb.067173

Stančíková, M., & Rovenský, J. (2015). Metabolism of Aromatic Amino Acids. In J. Rovenský, T. Urbánek, B. Oľga, & J. A. Gallagher (Eds.), *Alkaptonuria and Ochronosis* (pp. 9–12). Springer International Publishing. https://doi.org/10.1007/978-3-319-15108-3_4

Stempler, S., Yizhak, K., & Ruppin, E. (2014). Integrating Transcriptomics with Metabolic Modeling Predicts Biomarkers and Drug Targets for Alzheimer's Disease. *PLoS ONE*, *9*(8), e105383. https://doi.org/10.1371/journal.pone.0105383

Strug, L. J., Clarke, T., Chiang, T., Chien, M., Baskurt, Z., Li, W., Dorfman, R., Bali, B., Wirrell, E., Kugler, S. L., Mandelbaum, D. E., Wolf, S. M., McGoldrick, P., Hardison, H., Novotny, E. J., Ju, J., Greenberg, D. A., Russo, J. J., & Pal, D. K. (2009). Centrotemporal sharp wave EEG trait in rolandic epilepsy maps to Elongator Protein Complex 4 (ELP4). *European Journal of Human Genetics*, *17*(9), 1171–1181. https://doi.org/10.1038/ejhg.2008.267

Szymańska, E., Saccenti, E., Smilde, A. K., & Westerhuis, J. A. (2012). Double-check: Validation of diagnostic statistics for PLS-DA models in metabolomics studies. *Metabolomics*, *8*(1), 3–16. https://doi.org/10.1007/s11306-011-0330-3

Tang, Z., Ye, W., Chen, H., Kuang, X., Guo, J., Xiang, M., Peng, C., Chen, X., & Liu, H. (2019). Role of purines in regulation of metabolic reprogramming. *Purinergic Signalling*, *15*(4), 423–438. https://doi.org/10.1007/s11302-019-09676-z

Taylor, H., Serrano-Contreras, J. I., McDonald, J. A. K., Epstein, J., Fell, J., Seoane, R. C., Li, J. V., Marchesi, J. R., & Hart, A. L. (2020). Multiomic features associated with mucosal healing and inflammation in paediatric Crohn's disease. *Alimentary Pharmacology & Therapeutics*, *52*(9), 1491–1502. https://doi.org/10.1111/apt.16086

Tiedje, K. E., Stevens, K., Barnes, S., & Weaver, D. F. (2010). β-Alanine as a small molecule neurotransmitter. *Neurochemistry International*, *57*(3), 177–188. https://doi.org/10.1016/j.neuint.2010.06.001

Tolman, Z., Chaverra, M., George, L., & Lefcort, F. (2022). Elp1 is required for development of visceral sensory peripheral and central circuitry. *Disease Models & Mechanisms*, *15*(5), dmm049274. https://doi.org/10.1242/dmm.049274

Torres, P. A., Helmstetter, J. A., Kaye, A. M., & Kaye, A. D. (2015). Rhabdomyolysis: Pathogenesis, Diagnosis, and Treatment. *The Ochsner Journal*, *15*(1), 58–69.

Trifonova, O. P., Maslov, D. L., Balashova, E. E., & Lokhov, P. G. (2023). Current State and Future Perspectives on Personalized Metabolomics. *Metabolites*, *13*(1), Article 1. https://doi.org/10.3390/metabo13010067

Ueki, Y., Ramirez, G., Salcedo, E., Stabio, M. E., & Lefcort, F. (2016). Loss of Ikbkap Causes Slow, Progressive Retinal Degeneration in a Mouse Model of Familial Dysautonomia. *eNeuro*, *3*(5). https://doi.org/10.1523/ENEURO.0143-16.2016

Ueki, Y., Shchepetkina, V., & Lefcort, F. (2018). Retina-specific loss of Ikbkap/Elp1 causes mitochondrial dysfunction that leads to selective retinal ganglion cell degeneration in a mouse model of familial dysautonomia. *Disease Models & Mechanisms*, *11*(7). https://doi.org/10.1242/dmm.033746

Ueland, P. M. (2011). Choline and betaine in health and disease. *Journal of Inherited Metabolic Disease*, *34*(1), 3–15. https://doi.org/10.1007/s10545-010-9088-4

van Kessel, S. P., & El Aidy, S. (n.d.). Bacterial Metabolites Mirror Altered Gut Microbiota Composition in Patients with Parkinson's Disease. *Journal of Parkinson's Disease*, *9*(Suppl 2), S359–S370. https://doi.org/10.3233/JPD-191780

Vascellari, S., Palmas, V., Melis, M., Pisanu, S., Cusano, R., Uva, P., Perra, D., Madau, V., Sarchioto, M., Oppo, V., Simola, N., Morelli, M., Santoru, M. L., Atzori, L., Melis, M., Cossu, G., & Manzin, A. (2020). Gut Microbiota and Metabolome Alterations Associated with Parkinson's Disease. *mSystems*, *5*(5), mSystems.00561-20, e00561-20. https://doi.org/10.1128/mSystems.00561-20

Vogel, S. (2021). *Myo-Inositol Supplementation Augments Visual System Maturation in Mice* [Ph.D., Tufts University-Graduate School of Biomedical Sciences]. https://www.proquest.com/docview/2385652083/abstract/57CA8AFF19A243C5PQ/1

Vogt, N. M., Kerby, R. L., Dill-McFarland, K. A., Harding, S. J., Merluzzi, A. P., Johnson, S. C., Carlsson, C. M., Asthana, S., Zetterberg, H., Blennow, K., Bendlin, B. B., & Rey, F. E. (2017). Gut microbiome alterations in Alzheimer's disease. *Scientific Reports*, *7*, 13537. https://doi.org/10.1038/s41598-017-13601-y

Vogt, N. M., Romano, K. A., Darst, B. F., Engelman, C. D., Johnson, S. C., Carlsson, C. M., Asthana, S., Blennow, K., Zetterberg, H., Bendlin, B. B., & Rey, F. E. (2018). The gut microbiota-derived metabolite trimethylamine N-oxide is elevated in Alzheimer's disease. *Alzheimer's Research & Therapy*, *10*, 124. https://doi.org/10.1186/s13195-018-0451-2

Vujkovic-Cvijin, I., Sklar, J., Jiang, L., Natarajan, L., Knight, R., & Belkaid, Y. (2020). Host variables confound gut microbiota studies of human disease. *Nature*, *587*(7834), Article 7834. https://doi.org/10.1038/s41586-020-2881-9

Wachsmuth, H. R., Weninger, S. N., & Duca, F. A. (2022). Role of the gut–brain axis in energy and glucose metabolism. *Experimental & Molecular Medicine*, *54*(4), Article 4. https://doi.org/10.1038/s12276-021-00677-w

Wang, L., Christophersen, C. T., Sorich, M. J., Gerber, J. P., Angley, M. T., & Conlon, M. A. (2012). Elevated Fecal Short Chain Fatty Acid and Ammonia Concentrations in Children with Autism Spectrum Disorder. *Digestive Diseases and Sciences*, *57*(8), 2096–2102. https://doi.org/10.1007/s10620-012-2167-7

Wang, Q., Alowaifeer, A., Kerner, P., Balasubramanian, N., Patterson, A., Christian, W., Tarver, A., Dore, J. E., Hatzenpichler, R., Bothner, B., & McDermott, T. R. (2021). Aerobic bacterial methane synthesis. *Proceedings of the National Academy of Sciences*, *118*(27), e2019229118. https://doi.org/10.1073/pnas.2019229118

Warnes, G. R., Bolker, B., Lodewijk, B., Robert, G., & Wolfgang, H. (2022). *Various R Programming Tools for Plotting Data Version 3.1.3*. CRAN. https://github.com/talgalili/gplots

Wehrwein, E., Orer, H. S., & Barman, S. (2016). Overview of the Anatomy, Physiology, and Pharmacology of the Autonomic Nervous System. In *Comprehensive Physiology* (Vol. 6, pp. 1239–1278). https://doi.org/10.1002/cphy.c150037

Wensel, T. G. (2020). Phosphoinositides in Retinal Function and Disease. *Cells*, *9*(4), 866. https://doi.org/10.3390/cells9040866

Wickham, H., Francois, R., Henry, L., & Muller, K. (2022). *Dplyr: A grammar of data manipulation v. R package version 1.0.10*. CRAN.

Wiedeman, A. M., Barr, S. I., Green, T. J., Xu, Z., Innis, S. M., & Kitts, D. D. (2018). Dietary Choline Intake: Current State of Knowledge Across the Life Cycle. *Nutrients*, *10*(10). https://doi.org/10.3390/nu10101513

Wing, M. R., Patel, S. S., Ramezani, A., & Raj, D. S. (2016). Gut microbiome in chronic kidney disease. *Experimental Physiology*, *101*(4), 471–477. https://doi.org/10.1113/EP085283

Wishart, D. S. (2008). Quantitative metabolomics using NMR. *TrAC Trends in Analytical Chemistry*, *27*(3), 228–237. https://doi.org/10.1016/j.trac.2007.12.001

Wishart, D. S. (2023). Bioinformatic Tools for Clinical Metabolomics. In A. M. Abdel Rahman (Ed.), *Clinical Metabolomics Applications in Genetic Diseases* (pp. 71–96). Springer Nature. https://doi.org/10.1007/978-981-99-5162-8_4

Wishart, D. S., Cheng, L. L., Copié, V., Edison, A. S., Eghbalnia, H. R., Hoch, J. C., Gouveia, G. J., Pathmasiri, W., Powers, R., Schock, T. B., Sumner, L. W., & Uchimiya, M. (2022). NMR and Metabolomics—A Roadmap for the Future. *Metabolites*, *12*(8). https://doi.org/10.3390/metabo12080678

Wishart, D. S., Feunang, Y. D., Marcu, A., Guo, A. C., Liang, K., Vázquez-Fresno, R., Sajed, T., Johnson, D., Li, C., Karu, N., Sayeeda, Z., Lo, E., Assempour, N., Berjanskii, M., Singhal, S., Arndt, D., Liang, Y., Badran, H., Grant, J., … Scalbert, A. (2018). HMDB 4.0: The human metabolome database for 2018. *Nucleic Acids Research*, *46*(Database issue), D608–D617. https://doi.org/10.1093/nar/gkx1089

Witkovsky, P. (2004). Dopamine and retinal function. *Documenta Ophthalmologica. Advances in Ophthalmology*, *108*(1), 17–40. https://doi.org/10.1023/b:doop.0000019487.88486.0a

Wu, J., An, Y., Yao, J., Wang, Y., & Tang, H. (2010). An optimised sample preparation method for NMR-based faecal metabonomic analysis. *The Analyst*, *135*(5), 1023–1030. https://doi.org/10.1039/b927543f

Wu, J.-Y., & Prentice, H. (2010). Role of taurine in the central nervous system. *Journal of Biomedical Science*, *17*(Suppl 1), S1. https://doi.org/10.1186/1423-0127-17-S1-S1

Wu, L., Han, Y., Zheng, Z., Peng, G., Liu, P., Yue, S., Zhu, S., Chen, J., Lv, H., Shao, L., Sheng, Y., Wang, Y., Li, L., Li, L., & Wang, B. (2021). Altered Gut Microbial Metabolites in Amnestic Mild Cognitive Impairment and Alzheimer's Disease: Signals in Host–Microbe Interplay. *Nutrients*, *13*(1), 228. https://doi.org/10.3390/nu13010228

Wurtman, R. J. (1992). Choline metabolism as a basis for the selective vulnerability of cholinergic neurons. *Trends in Neurosciences*, *15*(4), 117–122. https://doi.org/10.1016/0166-2236(92)90351-8

Xia, J., & Wishart, D. S. (2011). Metabolomic data processing, analysis, and interpretation using MetaboAnalyst. *Current Protocols in Bioinformatics, Chapter 14*, Unit 14.10. https://doi.org/10.1002/0471250953.bi1410s34

Yu, D.-Y., Cringle, S. J., Yu, P. K., & Su, E.-N. (2011). Retinal energetics: Its critical role in retinal physiology and pathology. *Expert Review of Ophthalmology*, *6*(4), 395–399. https://doi.org/10.1586/eop.11.44

Zanna, C., Ghelli, A., Porcelli, A. M., Karbowski, M., Youle, R. J., Schimpf, S., Wissinger, B., Pinti, M., Cossarizza, A., Vidoni, S., Valentino, M. L., Rugolo, M., & Carelli, V. (2008). OPA1 mutations associated with dominant optic atrophy impair oxidative phosphorylation and mitochondrial fusion. *Brain, 131*(2), 352–367. https://doi.org/10.1093/brain/awm335

Zeisel, S. H. (2012). Dietary choline deficiency causes DNA strand breaks and alters epigenetic marks on DNA and histones. *Mutation Research/Fundamental and Molecular Mechanisms of Mutagenesis, 733*(1), 34–38. https://doi.org/10.1016/j.mrfmmm.2011.10.008

Zeisel, S. H., Klatt, K. C., & Caudill, M. A. (2018). Choline. *Advances in Nutrition*, *9*(1), 58–60. https://doi.org/10.1093/advances/nmx004

Zhang, W., Miikeda, A., Zuckerman, J., Jia, X., Charugundla, S., Zhou, Z., Kaczor-Urbanowicz, K. E., Magyar, C., Guo, F., Wang, Z., Pellegrini, M., Hazen, S. L., Nicholas, S. B., Lusis, A. J., & Shih, D. M. (2021). Inhibition of microbiota-dependent TMAO production attenuates chronic kidney disease in mice. *Scientific Reports*, *11*, 518. https://doi.org/10.1038/s41598-020-80063-0